# Advancing Mars Life Detection:

# Insights from a Glaciovolcanic Analogue and Enhanced Rover Survey Techniques


Erin Frances Gibbons

Department of Earth and Planetary Sciences
McGill University, Montréal


November 2023

*Supervised By:*
Dr. Richard Léveillé
Dr. Kim Berlo

A thesis submitted to McGill University in partial fulfillment of the requirements of the degree of Doctor of Philosophy

# ABSTRACT

The notion that Earth and Mars may have hosted similar environmental conditions during their early histories, combined with evidence for the relatively early evolution of life on Earth, has long led to speculation that life could also have emerged on Mars. The search for evidence of such life, either extinct or extant, is now a primary objective for space agencies. This thesis presents a multidisciplinary framework designed to enhance and refine our search strategies.

The first half of the thesis presents a geobiological investigation of an active glaciovolcanic system in Iceland. There is widespread evidence of analogous glaciovolcanic activity on Mars and these warm and wet environments represent some of the most recent potentially habitable niches. However, few studies have investigated the distribution of life in glaciovolcanic regions on Earth, nor the potential of these environments to preserve signs of past life. To address these gaps, this thesis employs a holistic approach encompassing environmental, mineralogical, and lipid studies to assess both habitability and the preservation of biomarkers at the glaciated Kverkfjöll volcano. Physicochemical measurements of the site reveal that interactions between ice and high-temperature magmatic reservoirs result in exceptional environmental heterogeneity, hosting habitats ranging from low to high temperatures, alkaline to acidic pHs, oxic to extremely dysoxic conditions, and with significantly different chemical profiles. Phospholipid fatty acid (PLFA) analyses confirmed viable microorganisms in all samples and provided direct evidence for individual- and population-level responses to the fluctuating environmental conditions. These findings illuminate trends of niche differentiation and divergent adaptation within the system, indicating that the diverse environments created by volcano-ice interactions promote the emergence of varied communities. We also revealed that the native community produces a suite of stable hydrocarbon biomarkers and that the local smectite-dominated mineralogy is favourable for organic preservation. Together, these findings underscore that glaciovolcanic settings have the capacity to preserve signs of life. However, we also document mineralogical variability and evidence for organic preservation biases, both of which could pose challenges in identifying and interpreting Martian biomarkers. These challenges are discussed with recommended solutions to navigate them.

In the latter half of the thesis, the focus shifts towards the purpose-driven development of procedures to augment the operational capacity of Mars rovers, and the scientific return of Mars missions more broadly. We demonstrate that using data fusion from sensors operating in complementary regions of the electromagnetic spectrum can improve the classification of clay minerals. Such minerals are prioritized in astrobiological research, primarily due to their consistent indication of water activity—a quintessential ingredient for life—and their established capability to preserve organic biomarkers for geologically-relevant timescales. Additionally, recognizing that nitrogen (N) is an essential element for life as we know it, we present a comprehensive baseline study on the nature of N emission by the laser-induced breakdown spectroscopy (LIBS) technique, which is available on active Mars rovers. We determine the best emission lines for detection, elucidate specific strategies to maximize quantification accuracy, and provide recommendations for translating these advances to Martian rovers. This contribution lays the foundation for the first remote detection of N on Mars' surface and stands to significantly enhance our capacity to rapidly identify areas of heightened astrobiological interest on Mars.

In sum, this thesis not only deepens our comprehension of potential Martian habitats but also contributes novel data analysis tools to augment the remote survey capabilities of rovers.

# RÉSUMÉ

L'idée que la Terre et Mars ont pu connaître des conditions environnementales similaires au début de leur histoire, combinée aux preuves de l'évolution relativement précoce de la vie sur Terre, a longtemps conduit à la spéculation que la vie aurait également pu émerger sur Mars. La recherche de preuves de l'existence d'une telle vie, qu'elle soit éteinte ou existante, est aujourd'hui l'un des principaux objectifs des agences spatiales. Cette thèse présente un cadre multidisciplinaire conçu pour améliorer et affiner nos stratégies de recherche.

La première moitié de la thèse présente une étude géobiologique d'un système glaciovolcanique actif en Islande. Il existe de nombreuses preuves d'une activité glacio-volcanique analogue sur Mars et ces environnements chauds et humides représentent certaines des niches potentiellement habitables les plus récentes. Cependant, peu d'études ont porté sur la distribution de la vie dans les régions glaciovolcaniques de la Terre, ni sur le potentiel de ces environnements à préserver des signes de vie passée. Pour combler ces lacunes, cette thèse utilise une approche holistique englobant des études environnementales, minéralogiques et lipidiques pour évaluer à la fois l'habitabilité et la préservation des biomarqueurs dans le volcan glaciaire Kverkfjöll. Les mesures physicochimiques du site révèlent que les interactions entre la glace et les réservoirs magmatiques à haute température entraînent une hétérogénéité environnementale exceptionnelle, abritant des habitats dont les températures varient de basses à hautes, les pH alcalins à acides, les conditions oxiques à extrêmement dysoxiques, et dont les profils chimiques sont significativement différents. Les analyses des acides gras phospholipidiques (AGPL) ont confirmé la présence de micro-organismes viables dans tous les échantillons et ont fourni des preuves directes des réponses individuelles et de la population aux conditions environnementales fluctuantes. Ces résultats mettent en lumière les tendances à la différenciation des niches et à l'adaptation divergente au sein du système, indiquant que les divers environnements créés par les interactions entre le volcan et la glace favorisent l'émergence de communautés variées. Nous avons également révélé que la communauté indigène produit une série de biomarqueurs d'hydrocarbures stables et que la minéralogie locale dominée par la smectite est favorable à la préservation organique. Ensemble, ces résultats soulignent que les environnements glaciovolcaniques ont la capacité de préserver des signes de vie. Cependant, nous documentons également la variabilité minéralogique et les preuves

de biais de préservation organique, qui pourraient tous deux poser des problèmes pour l'identification et l'interprétation des biomarqueurs martiens. Ces défis sont discutés et des solutions sont recommandées pour les surmonter.

Dans la seconde moitié de la thèse, l'accent est mis sur le développement ciblé de procédures visant à accroître la capacité opérationnelle des astromobiles martiens et, plus généralement, le retour scientifique des missions martiennes. Nous démontrons que la fusion de données provenant de capteurs opérant dans des régions complémentaires du spectre électromagnétique peut améliorer la classification des minéraux argileux. Ces minéraux sont prioritaires dans la recherche astrobiologique, principalement en raison de leur indication définitive de l'activité de l'eau—un ingrédient quintessentiel pour la vie—et de leur capacité établie à préserver les biomarqueurs organiques sur des échelles de temps géologiquement pertinentes. En outre, reconnaissant que l'azote (N) est un élément essentiel à la vie telle que nous la connaissons, nous présentons une étude de base complète sur la nature de l'émission de N par la technique de spectroscopie d'émission optique de plasma créé par laser («LIBS», signifie *laser-induced breakdown spectroscopy*), qui est disponible sur les astromobiles actifs de Mars. Nous déterminons les meilleures lignes d'émission de l'azote pour la détection, élucidons des stratégies spécifiques pour maximiser la précision de la quantification et fournissons des recommandations pour transposer ces avancées sur les astromobiles martiens. Cette contribution jette les bases de la première détection à distance de l'azote à la surface de Mars et devrait améliorer considérablement notre capacité à identifier rapidement les zones présentant un intérêt astrobiologique accru sur Mars.

En résumé, cette thèse ne se contente pas d'approfondir notre compréhension des habitats martiens potentiels, elle apporte également de nouveaux outils d'analyse de données pour augmenter les capacités de télédétection des astromobiles.

# ACKNOWLEDGEMENTS

I would like to extend my deepest gratitude to my supervisors, Dr. Richard Léveillé and Dr. Kim Berlo. For all the hours, the wisdom, and the confidence you've invested in me, I am grateful. But most of all, I am grateful that you both offered the freedom and encouragement to fully explore my curiosities and find my interests. This has been truly empowering. I am also very thankful to Dr. Greg Slater, whose mentorship during the latter years of my PhD went far beyond any expectations. Your dedication and support have been exceptional. Your insights, constructive feedback, and thought-provoking interpretations consistently challenged me and, in the process, greatly enriched my learning. And thank you also to Dr. Allyson Brady, who played a pivotal role in kindling my passion for astrobiology all those years ago in Idaho. Your extraordinary patience, kindness, and willingness to answer my endless questions were instrumental in helping me find my footing in the laboratory and nurturing my love for chemistry. Thank you for your mentorship and for serving as a remarkable example that I aspire to follow.

Thank you to the Mars 2020 *Perseverance* Science Team, especially the *SuperCam* Team, for the exceptional opportunity to collaborate with a vibrant, international consortium of remarkable scientists. My sincere thanks go to Roger Wiens, whose tireless advocacy paved the way for this once-in-a-lifetime opportunity and whose leadership made the experience so enjoyable. And to Ann Ollila for so patiently showing me the ropes and making my collaboration with NASA seem less intimidating, one email meme at a time.

Many thanks to the many personalities of McGill who filled this journey with laughter and compelling conversation, often over cookies. Thank you especially to Kristy Thornton and Anne Kosowski who shared so much of themselves to make EPS feel like a second home. Thank you to Kyle Henderson for always making time for a picnic, or a walk, or a talk. Thank you to each of my roommates throughout this journey who made Montreal feel like home. Thank you especially to Dinara Karimova and Charlotte Spruzen, whose radiant positivity never ceased to illuminate even the dullest of days and who both somehow made studying seem like a joy. And a big thank you to Hiba Aoid who let me drone on about the joy of lipids at the kitchen table.

Thank you to my dearest friends from Ontario: Kari Van Vliet, Brittany Killingbeck, Kirin Shannon, Craig Rutherford, Brad Coreno, and Emily Reynolds. Your friendship has been a

grounding force in my life, a cherished constant amidst the whirlwind of grad school. I find myself missing each of you more than words can express. Each reunion with The Group, regardless of how brief or far between, is a treat. Our shared laughter and ridiculous moments have been more than just memories; they have been a source of strength and inspiration. In those late nights and challenging times, it was often the thought of our next gathering, the next burst of giggles, the next bowl of Kari's soup with Brad's sourdough, that kept me going. You have all shown me that even amidst the rigors of academic pursuit, there is room for laughter, light, and love. A particular note of appreciation to Craig and Emily (and Spencer) for graciously opening your home to me so that I could learn to be an organic geochemist. Coming home to Bachelorette nights was a thrill I didn't know I needed.

A special mention must be made for my dear and darling partner, Dr. Matthew Svensson. In this intense and sometimes lonely path of academia, you have been there to celebrate my triumphs—no matter how small—and to encourage me through the challenges. Your unwavering support, your patience during my long hours of work, and your belief in the importance of what I was striving for, provided the strength I often needed. I am so grateful for the partnership we have nurtured though this journey, it has blossomed into something more beautiful than I could have ever imagined. Thank you for encouraging me through this final year and thank you for being such an impeccable role model for me to strive after. Your role in this achievement is immeasurable.

My greatest acknowledgments, however, go to my family:

To my dear mother, who joined me on countless walks, patiently listening as I passionately extolled the astonishing beauty of a membrane phospholipid—long before she even knew what a lipid was. Who sat graciously on the couch while I recited my PhD candidacy proposal, word for word. Who gently reminded me of my worth when I felt discouraged.

To my dad, who diligently read numerous scholarship proposals, coached me through composing challenging emails, and encouraged me to pursue ambitious opportunities I thought were out of reach. Who reminded me not to overuse the word 'plethora'. Whose confidence in my abilities never faltered, even when mine did.

To my brother, who somehow managed to show more excitement about my research than I did and consistently reminded me to cherish the joys of discovery. Whose perfectly timed phone calls full of quirky tales provided much-needed distractions during weary moments. Your faith in me was one of my greatest strengths.

To my sister-in-law, who exemplified grace and resilience while completing her own dissertation in a basement during the global pandemic—you inspired me beyond measure.

And finally, to my Space Nerd Uncle, whose regular check-ins never failed to brighten my days and refocus my spirit. It's rare to find someone outside the immediate academic sphere who shows such genuine interest; I am deeply grateful for these conversations and the support they symbolized. Thank you for being an unexpected but cherished part of this journey.

Thank you each for being a part of my village, it was in this shared excitement that I found the true essence of pursuing science. Every page of this work contains a silent note of thanks to you.

Finally, thank you to my funding sources: the European Union's Horizon 2020 research and innovation programme (No 871149), the Canadian Space Agency (CSA) [21EXPCOI1], and the Natural Sciences and Engineering Research Council of Canada (NSERC).

# TABLE OF CONTENTS

# TABLE OF FIGURES

# TABLE OF TABLES

# CONTRIBUTION TO ORIGINAL KNOWLEDGE

I confirm that this thesis presents original scholarship and that the results are my own work, unless otherwise referenced and acknowledged.

The core premise of this thesis was jointly formulated and developed by myself, my supervisors, Dr. Richard Léveillé and Dr. Kim Berlo, and one external mentor, Dr. Greg Slater. A significant influence on the direction of this thesis was my involvement in the operation of two ongoing Mars rover missions—the *Curiosity* and *Perseverance* rovers. These were exceptional experiences that not only broadened the scope of inquiry but also steered the thesis toward addressing critical research objectives that stand to make substantial contributions to the astrobiological community. The refinement of the overarching research goals and aims were guided by my supervisors.

The works presented in this thesis stand as distinct contributions to knowledge. In brief, we present the first comprehensive organic biosignature assessment of a basaltic glaciovolcanic environment. We elucidate novel trends in the biomass distribution, microbial community structure, and adaptive behaviours in these underexplored settings. We describe the taphonomic framework of the system and uncover fossilization trends with important implications for understanding the preservation of organic matter in carbon-poor environments—on Earth and Mars. Coupled with this, we contribute two baseline pilot studies designed to augment the mineralogical and geochemical capabilities of active Mars rover payloads: (1) a new data fusion architecture proposed to enhance the chemometric assessment of clay minerals, and (2) a foundational assessment of nitrogen emission with laser induced breakdown spectroscopy, including instrument optimization and data analysis recommendations.

# CONTRIBUTION OF AUTHORS

This thesis is composed of four manuscripts that I have written as the first author and developed through collaboration with my supervisors, Dr. Richard Léveillé (RL) and Dr. Kim Berlo (KB), as well as one external mentor, Dr. Greg Slater (GS).

Chapters 2 and 3 present work from field studies in a Mars analogue site in Iceland. The manuscripts are each co-authored with RL, KB, and GS. All authors contributed to the design of the methodology and evolution of overarching research goals. I acquired expedition funding and was additionally supported by research funds from my supervisors and mentor. Field work was conducted by myself, RL, and GS. I performed all experiments and analyses (organic analyses were overseen by GS). Experiments were performed by myself, with oversight from GS. I was responsible for data management, analyses, and initial manuscript preparation, including visualizations. RL, KB, and GS contributed commentary and critical revision on the manuscripts.

Chapter 4 is published and may be cited as "Gibbons, E., Léveillé, R., & Berlo, K. (2020). Data fusion of laser-induced breakdown and Raman spectroscopies: Enhancing clay mineral identification. *Spectrochimica Acta Part B: Atomic Spectroscopy*, 170, 105905". All authors contributed to the design of the methodology and evolution of overarching research goals. I was responsible for the provision of study materials, preparation of samples, data collection, data management, and initial data assessment. RL and KB provided funding, access to analytical tools and computing resources, supervision, verification of the analytical methods, and contributed to discussion of the results. I was responsible for manuscript preparation, with commentary and revision from RL and KB.

Chapter 5 is in preparation for submission to *Spectrochimica Acta Part B: Atomic Spectroscopy*. The manuscript is coauthored by myself, RL, and KB. All authors contributed to the design of the methodology and evolution of overarching research goals. All authors contributed to the development of a project proposal which secured funding for the project form the Canadian Space Agency. KB was responsible for the provision of reagents and provided instrumentation, computing resources, and access to analytical tools. I was responsible for the preparation of samples, method validation and refinement, data collection, data management, and initial data assessment. The manuscript was written by myself, in collaboration with RL and KB.

# CHAPTER 1

# Introduction

## 1.1 SEARCHING FOR EXTRATERRESTRIAL LIFE: CONTEXT AND MOTIVATION

The quest for extraterrestrial life has captivated the scientific community and the public alike, inspiring a deep curiosity about our place in the Universe. This pursuit is not merely driven by a sense of wonder; it is rooted in the profound and far-reaching implications that discovering extra-terrestrial life would hold for our philosophies and understanding of basic science.

One of the most monumental outcomes of modern biology is the demonstration that all life on Earth is unified by the same biochemistry and genetic code [1,2]. Whether it be a microbe or a complex eukaryote, every organism is constructed from same chemical units (the "building blocks" of life), consisting of twenty amino acids with left-handed chirality, five nucleotides, a few sugars, and lipids [1]. The universality of DNA and RNA across all life on Earth provides further evidence of a shared lineage, illustrating that we each descended from a common ancient ancestor [2]. However, one of the main goals of astrobiology is to understand life *fundamentally*. It asks: What distinguishes life from non-life? In what conditions can life originate? Are there universal laws of biology, as there are for physics and chemistry? The answers to these questions are difficult to ascertain given the uniformity of Earth's biochemistry—it remains uncertain which characteristics of life are essential, and which are merely coincidences of evolution [3].

The discovery of even the simplest extraterrestrial organisms, or their fossil remains, could revolutionize our comprehension of biochemistry and the prevalence of life in the cosmos. Two major outcomes of a successful search for life are possible [4]. First, we could find that extraterrestrial life shares a hereditary link with life on Earth. These life forms would map onto the evolutionary tree representing the phylogenetic relationships between extant and extinct terrestrial organisms. Such a discovery would provide robust evidence for the panspermia

hypothesis, which suggests that life can be naturally transferred between planets, and possibly between star systems. This would shift our understanding of how life may be distributed in the Universe and challenge concepts of life's resilience in interplanetary space. It would beg the question: Did life originate on Earth and seed other worlds, or vice versa? Indeed, many efforts to understand the origin of life have been framed by the assumption that life began on Earth [5–7] and testing this hypothesis would provide a more robust basis for understanding the conditions that fostered the transition from non-life to life. Additionally, by comparing the similarities and differences between Earth and Martian organisms, we could potentially identify when the two evolutionary paths diverged and explore alternate pathways of biological evolution. Mars has distinct environmental conditions, like its thinner atmosphere, lower gravity, and greater exposure to cosmic radiation, compared to Earth. If it were possible to investigate how life has adapted to these conditions, it would provide a deeper understanding of the flexibility and range of biological adaptation and possibly clarify which biological traits are most essential.

Alternatively, discovering extraterrestrial life with no ties to Earth's biochemistry would be groundbreaking. Such a finding would constitute evidence of an *independent origin of life*. Considering the age and size of the Universe, evidence that life can emerge separately on two distinct bodies in a single star system (or even galaxy), would suggest that the processes precipitating life's origin are not exceptionally rare [4]. It would imply that life is a common cosmic phenomenon (at the very least on rocky planets orbiting yellow dwarf stars). Moreover, examining an independent form of life would refine our understanding of biochemistry, allowing us to ask which biological principles are truly generalizable (e.g., Do these other life forms maintain equilibrium, grow, and replicate? Is Darwinian evolution—the cornerstone of life on Earth—also the driver these life forms? Beyond replication and metabolism, what are the essential traits that define life?). Furthermore, it is possible that evaluating a distinct living system could reveal novel biochemical pathways, mechanisms, and principles. This deeper insight could not only enhance our grasp of a fundamental science but potentially drive progress in fields directly influenced by biochemical knowledge, such as medicine, agriculture, environmental conservation, and food science [8].

In either case—shared or distinct biochemical systems—the act of discovery itself would be only the beginning. The existence of extraterrestrial life would mark the start of a true general biology,

of which Earth's biosphere is simply a special case. We would have a unique opportunity to shed new light on the possible origins of life, its survivability across diverse physical and chemical settings, and its commonality. And if we were to encounter only remnants of life that once thrived but has since gone extinct, it would serve as a poignant cautionary tale of the balances required to sustain life. Lastly, it should also be noted that not finding evidence for life on worlds with conditions thought to be *compatible* with life would not be considered a negative result or a strategic failure. Such a result might reveal limitations of our current methodologies, illuminate specific parameters/conditions that inhibit the emergence of life, provide an empirical basis for estimating the rarity of life, or indicate that current definitions of "life" and "habitability" need refining. Furthermore, on Earth, life seems to have emerged shortly after surface conditions stabilized [9,10], and subsequently coevolved with the planet, mutually influencing and being shaped by geological events, atmospheric composition, and climate shifts [11–13]. This symbiotic relationship makes it challenging to isolate purely geochemical processes from biological influences [14]. A lifeless, but apparently habitable, extraterrestrial world would present an invaluable opportunity to study prebiotic geochemical processes untainted by life's influence, offering a clearer perspective on the standalone evolution of planetary systems and possible conditions surrounding the origin of life.

In brief, the search for life on other worlds is a means to address fundamental (geo)-biological questions that cannot be answered by studying Earth's life. Its potential for catalyzing paradigm-shifting discoveries justifies its high priority amongst scientific objectives in space exploration. Further, advances in launch capabilities, precision landing, and biosignature detection technologies leave us poised, as never before, to conduct this search with scientific rigor. The goal of this thesis is, therefore, to help advance the search for life beyond Earth, with a focus on Mars. Each of the main Chapters describes a distinct avenue of research intended to support optimized exploration strategies. These approaches range from studying how life colonizes Mars-like environments and what fossil remnants are preserved, to introducing advanced spectral approaches for assessing habitability. This work is strongly multi-disciplinary, and the remainder of this Chapter will present essential background information, techniques, and prior research.

## 1.2 THE PREREQUISITES FOR LIFE: HABITABILITY BEYOND EARTH

Our definition of life is necessarily limited by what we know—life on Earth. However, the laws of chemistry and physics have universal principles that underlie life's unique processes, which provide a rough framework for what life needs and therefore where it may be found. Through this notion of universality, a consensus has emerged that life requires three essential components [15,16]: (1) an energy source for metabolic reactions, (2) a liquid solvent to mediate these reactions, and (3) essential elements to build macromolecules. The confluence of these three factors make a world *habitable*. Habitability does not presuppose the existence of life but simply defines whether the necessary criteria exist to allow life to exist, grow, and reproduce.

On geologically active planets, both energy sources (Criteria #1) and a supply of essential elements (Criteria #2) are expected to be relatively common [17]. These planets often feature natural gradients (e.g., gradients of temperature, pH, ion concentration, redox state), which represent inherent potential energy differences that can be harnessed to drive various chemical, biological, and physical processes essential for the emergence and sustenance of life. Indeed, energy harnessed from redox and proton gradients, is believed to have been pivotal in sparking the origins of life on Earth by providing the required energy flux to drive initial metabolisms and growth [7,18]. Regarding the supply of elements, life is assumed to require relatively large molecular structures with sufficient complexity to carry out diverse functions and encode genetic information. On Earth, macromolecules are comprised primarily of six elements: carbon, hydrogen, nitrogen, oxygen, phosphorus, and sulfur ("CHNOPS"), and small amounts of catalytic metals [15,19]. Carbon serves as a scaffolding element, forming stable covalent C-C (and C-H) bonds that form the polymerized backbone of macromolecules [20]. These C-H backbones provide the overall structure and shape of macromolecules but have little chemical function (reactivity) for metabolic activity [21]. And although Si has been proposed as an alternative scaffolding element, Si-Si bonds are less stable and cannot form the same versatility of molecular structures as C [20–22]. The heteroatoms (N, O, P, S) covalently bond with C and the differences in electronegativity provide the reactivity underlying the majority of metabolic reactions occurring in Earth's organisms [23]. The reactive roles played by O, P, S, and less so N, could potentially be substituted by other heteroatoms in extraterrestrial biochemistry. However, given their abundance in the galactic disk and their distinctive bond-forming abilities with C, it has been argued that extraterrestrial life will also use some variation of CHNOPS elements [16,24].

Requirement #2, the availability of a liquid solvent, appears to be the principal factor regulating habitability [25]. Solvents dissolve and transport substrates between reactive sites, allowing life's foundational biochemical reactions to proceed (e.g., energy production and growth); such reactions cannot occur efficiently in a desiccated system [25]. On Earth, water is the only solvent used by life. While alternative solvents have been proposed (e.g., ammonia, organic solvents, sulfuric acid), water is often championed as the most probable solvent for life anywhere in the Universe [20]. This is because of its cosmic abundance (water consists of the first [H] and third [O] most abundant elements in the Universe) and because of its distinct physicochemical properties [20,26]. Indeed, water uniquely offers molecular polarity, broad temperature stability, a capacity to dissolve a wide range of substances (more than any other liquid), and a tendency to expand near freezing [20]. Several independent reports therefore suggest that liquid water is the primary requisite for life [25,27,28]. Without it, other habitability criteria are irrelevant, and water has become the principal metric for identifying habitable worlds beyond Earth.

Lastly, it is important to clarify that, at the time of writing, astrobiology is primarily focused on the search for life "as we know it". Given that no examples of extraterrestrial life or alternative biochemistries have been discovered, it is intellectually more tractable to focus our *initial* search on biochemical systems that we understand and environments in which we know biology can function. This assumes that life is based on carbon chemistry operating in an aqueous environment. As outlined briefly above, and reviewed in detail elsewhere, there are compelling reasons to believe this assumption to be valid and expect extraterrestrial life to use CHNOPS and water [20,21,24], even if their molecular structures and pathways differ.

### 1.3 MARS AS A HABITABLE WORLD

Mars has emerged as a priority target for life detection primarily because its surface is bisected by valley networks and other features suggestive of a past hydrological cycle [29]. While other bodies in our Solar System host liquid water, such as Saturn's moon Enceladus and Jupiter's moon Europa [30], these bodies are extremely distant. Mars is reachable by spacecraft in less than one year, enabling more frequent exploration and adaptive strategies based on previous insights. This section provides an overview of how, and when, Mars has satisfied the basic criteria for life. It briefly reviews plausible sources of energy and nutrients, but primarily focusses on the availability of liquid water given its significance in regulating habitability [27],

and the surrounding debates. The subsequent sections in this Chapter address Martian habitability and putative life in broad, generalizable terms, encompassing the potential for past or current habitation. This intentionally broad approach is maintained due to the current lack of conclusive evidence regarding the existence of life, either in the past or present, on Mars.

### 1.3.1 Viable Energy and Nutrient Sources

Potential energy sources for life on Mars include the direct and indirect use of solar radiation (although this option was likely restricted only to periods when liquid water was available at the surface, see Section 1.3.2), lightning, ionizing radiation, geothermal heat, and various redox couples involving carbon or inorganic compounds [17]. As discussed by Nixon et al. [31], our understanding of the feasibility of potential redox couples on Mars is limited, as very few Martian minerals and only a modest number of meteoritic organics have been chemically examined for their metabolic potential. Nevertheless, a recent review by Cockell et al. [27] highlights several potential redox couples that may have provided viable sources of energy for life on past and present-day Mars. Further, as discussed by Price and Sowers [32], the energy requirements for survival are several orders of magnitude less than the energy required for growth. This concept of survival energy—energy required just for repair of macromolecular damage [33]—implies that life could survive, although not multiply, in a much wider range of environments than previously thought possible [17].

As above, the CHNOPS elements are cosmically abundant. In the case of Earth and Mars, cosmochemical bulk composition models further suggest that both planets formed in a common narrow region of the protoplanetary disk[1], resulting in the accretion of similar material [34,35]. The same elements would accordingly be available for life on both planets unless specific processes on Mars caused their depletion (which may be the case for N [36,37]). Indeed, N has been steadily lost from the Martian atmosphere due to a combination of impact erosion, sputtering by the solar wind, and/or photochemical processes [36–39]. The inventory of bioavailable N retained by the crust is poorly constrained, both in abundance and distribution [40]. This may present an important limiting factor to putative Martian life and remains as one of

[1] The precise origin of this material is still debated. In the classic model of oligarchic growth, the accretion of large (>>km) planetary embryos in the protoplanetary disk was followed by a phase of collisions, leading to the eventual accretion of the rocky inner planets [170]. An alternative hypothesis suggests that planets grow by accreting much smaller fragments (<<km) from the outer solar system, which drift sunward because of gas drag [171]. In either case, Earth and Mars are believed to have formed out of the same material and very close to each other [35,172].

the most important open questions in confirming Mars' habitability [27,38]. Strategies to address this gap in knowledge are discussed in Chapter 5.

Additional, more nuanced differences are observed in the bulk composition of Mars versus Earth and have been largely attributed to differences in oxidation state and subsequent core formation [34]. The most notable compositional difference is the much higher FeO abundance of Mars (18 wt%) compared with that of Earth (8 wt%). The Fe-rich nature of the Martian mantle yields basaltic melts that are also enriched in FeO (13–21 wt%) relative to terrestrial basalts, which typically lie in the 10–15 wt% FeO range [41–43]. There is little reason to assume that the availability of other elements on Mars is significantly different from their availability on Earth.

### 1.3.2 Availability of Liquid Water Through Time

Mars today is a cold, desiccated planet, bathed in UV radiation and with an atmospheric pressure ~1/100 that of the Earth [44]. Present conditions render liquid water unstable at the surface and the existence of viable organisms is considered implausible (although very hardy remnant cells may lie dormant in some areas [45]). However, unlike Earth, Mars lacks plate tectonics, and its ancient crust is incredibly well-preserved, providing a geologic record of planetary processes spanning >4 billion years [29,46,47]. These ancient terrains bear myriad evidence for dramatic climatic evolution through time, including an early period of relative clemency when liquid water is thought to have been abundant [29]. The geological history of Mars is divided into three main periods derived from stratigraphic and crosscutting relationships as well as impact crater statistics: the Noachian Period (4.1-3.7 Ga), the Hesperian Period (3.7-2.9 Ga), and the Amazonian Period (2.9 Ga to present). These periods, reviewed below, broadly parallel the major environmental stages of Martian climatic evolution, and provide a useful framework for understanding the change in Mars' water budget.

#### *1.3.2.1 The Noachian Period, 4.1-3.7 Ga*

Much of the Noachian bedrock is carved by integrated, heavily eroded valley networks [47–50]. These represent the single most important piece of evidence in favour of a radically different climate on ancient Mars [29,51]. Like many drainage basins on Earth, Mars' Noachian-aged valley networks are dendritic and feature tributaries that begin near the peaks of topographic divides. This geomorphology strongly suggests that precipitation (as rain or snow) followed by surface runoff must have occurred, at least episodically, and implicates an active hydrological

cycle [29,49,52]. The valley networks vary dramatically in length and width, with the longest extending thousands of kilometers, and several intersecting basins (e.g., craters) [48,52]. In these topographic lows, deltas or alluvial fans often provide supporting evidence that flowing water sculpted the channels and transported suspended sediment [53–55]. Furthermore, both inlet and outlet valleys are often apparent on basin rims, suggesting that water was sufficiently abundant to over-fill the basins. Some of these lakes are comparable in size to small seas on Earth [48].

Further evidence for liquid water is provided by Mars' mineralogical profile, which has been observed in increasing detail from the 1960s and has been complemented over the last ~20 years by detailed *in situ* observations from rover missions. Iron- and magnesium-rich phyllosilicates (clay minerals) are found extensively across Noachian terrains [56] and implicate the sustained presence of liquid water (although the fluid chemistry is debated [56]). At several locations, the Fe/Mg clays are stratigraphically overlain by Al-clays, such as kaolinite [57,58]. On Earth, such a sequence is often observed in wet weathering environments because mobile Fe and Mg cations are preferentially leached downwards by percolating fluids [59]. Other aqueous minerals, such as hydrated sulfates, chlorides, and silicas are found in more localized regions of the Noachian (and Hesperian) crust, providing additional evidence of water activity [60–62].

Although the geomorphological and geochemical records clearly indicate that Mars' surface was significantly modified by liquid water during the Noachian, the *nature* of the aqueous processes are equivocal. A primary point of uncertainty is related to major unanswered questions of Mars' past climate. Modern climate models predict that the steady-state early Martian climate was far too cold for liquid water to persist (see review by [51]). Indeed, given the distance of Mars from the Sun, and the fact that the young Sun was significantly less luminous than it is today, Mars' Noachian equilibrium surface temperature is estimated to be 210 K (-63.15 °C) [51] (assuming perfect absorption of solar radiation). Elevating Mars' surface to just 0 °C would require a greenhouse effect that is *at least* nine times greater than that of present-day Mars (and around double that of present-day Earth) [51]. Current modeling efforts have been largely unsuccessful in simulating a sufficient gas mixture to achieve such extensive greenhouse warming [51]. This suggests that either we are missing crucial parameters for modeling Mars' warm paleoclimate, or that the ancient climate was indeed predominantly cold. In the latter scenario, the hydrological features likely formed during protracted heating events capable of melting ice masses, which is

consistent with recent work demonstrating that subglacial meltwater drainage contributed significantly to Noachian valley network incision [63]. Several hypotheses have been suggested as a source of heat to initiate ice mass melting on a relatively young Mars:

(1) Catastrophic heat flux into the surface by bolide impacts [64–66], for which there are abundant large craters [67], could melt the base of glaciers or buried permafrost.
(2) Areas of elevated geothermal heating, such as rift zones or magmatic intrusions, could melt local ice [68–70]. For instance, most of the volcanism during the Noachian was likely concentrated in Tharsis, where a volcanic pile approximately 5000 km across and 9 km high may have largely accumulated by the end of the Noachian [71]. The high-elevation domains of the Tharsis mound could have supported an extensive mountain glacier system vulnerable to volcanic melting [72].
(3) Temporary atmospheric changes (e.g., increased temperature, humidity) resulting from impacts, volcanism, or insolation feedbacks, could trigger regional heating [73–75].
(4) High dust concentrations in Mars' snow/ice deposits could increase insolation enough to trigger melting under the modeled daily temperature maxima of the Noachian [74].
(5) Sufficiently thick snowpacks could have experienced pressure-melting at their base [76].

The relative influence of any one of these factors is difficult to predict, but each provides a plausible mechanism that reconciles climate predictions with observations of aqueous activity.

#### *1.3.2.2 The Hesperian Period, 3.7-2.9 Ga*

This period marks a significant shift in Mars' geology. Indeed, geomorphological evidence of large, integrated valley networks declined sharply by the onset of the Hesperian [47]. Localized examples of valley formation are observed, primarily near volcanic centers, but it is clear that the rate and extent of valley formation had changed. Furthermore, both orbital and surface observations indicate that average erosion rates and weathering extent also decreased at the end of the Noachian [29,77]. Indeed, erosion rates derived from data collected by the Mars Exploration Rovers, paired with orbital context mapping, suggest a regional climate shift around the rover landing sites from predominantly wet to dry and desiccating near the Noachian/ Hesperian transition [77]. This shift towards an arid climate regime was permanent and persisted throughout the Late Hesperian and all of the Amazonian, highlighting the Hesperian as the onset of long-term climate change [77]. Further indication of persistently low weathering rates come

from the strong and widespread orbital signatures of olivine, a mineral particularly susceptible to breakdown under moist conditions, in Hesperian bedrock [78,79]. In situ observations confirm that Hesperian-aged blocks are predominantly comprised of primary basaltic minerals (olivine, plagioclase, pyroxene, and magnetite) [80]. The presence of oxidized rock coatings, vugs, and mineralized veins, do indicate ubiquitous aqueous alteration, however the survival of primary minerals suggest that chemical reactions proceeded under low water/rock ratios [80]. Furthermore, the Hesperian marks a transition in the predominant weathering products. Whereas Noachian terrains feature abundant Fe/Mg-phyllosilicates, Hesperian terrains show a predominance of sulfate minerals [29,62,81]. The sulfate-rich deposits sampled by the *Opportunity* rover in Meridiani Planum are predominantly interpreted as evaporative deposits (although other formation mechanisms have been proposed [82,83]), and some require acidic conditions [81]. On this basis, the transition of phyllosilicates into younger sulfate deposits is hypothesized as corroborating evidence for a planetary-scale transition from high water:rock ratio and neutral pH weathering conditions to lower water:rock ratio and lower pH weathering conditions.

However, despite widespread evidence for declining rates of surface water activity, Hesperian-aged terrains are marked by an increased number of large outflow channels. These are interpreted as the products of sudden, catastrophic floods [29,84]. The abrupt start of these outflow channels and the high discharge rates calculated from the channel dimensions [85,86] suggest that these floods formed by the rapid escape of water held under pressure in the subsurface [29]. The sources were likely extensive aquifers sealed below a thick (> km) cryosphere [87,88]. The lack of pressurized floods in the Noachian could be explained by the lack of a sufficiently thick cryosphere in Mars' earliest history to trap and seal subsurface reservoirs [29]. Hesperian floods of such magnitude likely formed lakes and seas, particularly in the low-lying northern plains, but the ponded water would not have been stable for long under the prevailing climate regime [29].

In sum, the geomorphological and mineralogical transitions observed across the Noachian/ Hesperian boundary suggest significant and lasting global climate change, characterized by reduced temperature and atmospheric pressure. Yet, the precise cause(s) of the climatic shift are unknown and likely the culminating result of multiple triggers [89]. One theory, based on patterns of decreasing crustal magnetization through time, posits that Mars' planetary dynamo

ceased near the end of the Noachian [90], precipitating the permanent collapse of Mars' magnetic field [89,91]. In the absence of a magnetic field, Mars' atmosphere would have been left vulnerable to the bombardment of high-energy particles from the solar wind and other cosmic forces. This interaction could lead to the gradual degradation of the atmosphere through a process known as ion sputtering [92,93]. The frequent bolide impacts that characterized Mars' early history could have further exacerbated atmospheric erosion by propelling atmospheric molecules into space [94]. Multiple pieces of evidence indeed suggest that by, the late Noachian or early Hesperian, the Martian atmosphere had undergone substantial volume loss [92,95]. This thinning could have led to persistent cooling and pressure reduction, ultimately resulting in conditions where liquid water could no longer remain stable on the surface. An alternative explanation suggests that volcanically degassed $CO_2$, $SO_2$, and $H_2S$ may have accumulated during the Noachian (likely associated with the emplacement of the Tharsis bulge) and fostered temporary greenhouse conditions conducive to the high water activity early in Mars' history [96,97]. Once the volcanism subsided, the removal of reactive greenhouse gases by photolysis and/or oxidation outpaced their replenishment, triggering declines in global temperatures and atmospheric pressure [96].

Regardless of the cause, the most striking outcome of Mars' climate transition was the rapid and near complete loss of liquid water from the surface. But where did the water go? Leading hypotheses suggest that considerable amounts of water likely permeated into the crust during the wetter Noachian Period, aided by the high permeability of the basaltic crust [29,98]. As Mars cooled into the Hesperian Period, a thick permafrost layer would have formed, trapping the groundwater in the subsurface and creating the pressurized aquifers required to form the catastrophic outflow channels observed in the Hesperian bedrock. It remains unclear whether some confined liquid water aquifers remain in the subsurface today [99,100]. Liquid water not confined to the subsurface or that was subsequently released during flood events, would have either rapidly frozen into growing snowpacks and glaciers, evaporated under the tenuous atmosphere, or (re)infiltrated into the crust to be stored in aquifers or as hydrated minerals [88,101]. With time, even surficial snow/ice deposits at the mid-latitudes would have become unstable and sublimated (unless insulated beneath dust/regolith [102]). Once vaporized, the water would either have migrated towards the poles and precipitated onto the polar ice caps, or it

would have been lost to space through various thermal and non-thermal mechanisms (for a detailed review of water vapour loss mechanisms, see [93]).

#### *1.3.2.3 The Amazonian Period, 2.9 Ga to Present*

The Amazonian Period encompasses two thirds of Mars' history, extending from 2.9 billion years ago, the middle of the Archean Era on Earth, to the present [29]. The Amazonian is characterized by globally low temperatures, low atmospheric pressure, a high radiation flux (a consequence of the thin atmosphere), and minimal surface changes compared with preceding periods. The rates of erosion, weathering processes, and volcanic activity have all remained low [29,77]. Valley and gully formation are also notably scarce, although not entirely absent, suggesting that fluvial activity has been minor and primarily restricted to rare groundwater eruptions and/or the melting of ice emplaced earlier [29,47,103].

In contrast to previous times, the Amazonian Period sees wind and ice as the primary agents of change. The polar ice caps seem to have largely accumulated during this period and most of the mid- and high-latitude surfaces are covered by an ice-cemented soil layer that likely formed <100,000 years ago during a phase of higher obliquity [104,105]. Thicker subsurface deposits of ice may also be present at non-polar latitudes beneath an insulating cover of regolith/dust [102]. Furthermore, evidence for glaciation is observed at mid-latitudes within the last 100-200 million years [106–108], suggesting relatively recent ice activity at the surface. In some of these areas, drainage landforms indicate that episodic melting of the ice body has occurred, likely due to geothermal heat anomalies from rifting or volcanic intrusions [109–112]. The effects of wind are also prevalent, with mega-ripples and dunes evident in almost every orbital image taken of Mars' modern surface [29]. The prevalence of etched surfaces, pedestal craters, wind streaks, venti-facts, and yardangs offer further evidence of the continual movement of loose material across Mars [29]. The loose material is comprised largely of basaltic sand, sulfates, and Fe-oxides and is presumed to derive from mechanical erosion by impact events and past weathering [29].

### 1.3.3 Prospects for Martian Life Throughout Mars' History

The Amazonian surface of Mars is considered inhospitable to life. It is cold, dry, chemically oxidizing, and bathed in solar and cosmic ionizing radiation. However, the geologic history outlined above illustrates a past in which Mars' surface was habitable. This provides constraints on where to look for signs of life and what to look for. Indeed, there is a general consensus that

the Noachian Period—with its clear indications for stable, connected, water-rich environments—provided the most habitable conditions in Mars' entire history [113–115]. Many parallels have been drawn between the aqueous environments of Noachian Mars and the early Earth [115], and, coupled with the early emergence of life on Earth, have fueled speculation that life might have also evolved on Mars. However, the Hesperian-era climate change triggered global degradation of the surface conditions conducive to the proliferation of life [113]. The progressive loss of liquid water would have caused both habitat loss (contraction of water bodies) and habitat isolation (decline of integrated fluvial activity), ultimately restricting the exchange of nutrients and microbes between habitats. These changes would result in a gradual reduction of the diversity and productivity of subaerial habitats over time [113]. The concomitant increase in solar radiation flux associated with atmospheric thinning would have further diminished Mars' surface habitability.

On Earth, as environmental conditions become increasingly hostile, life tends to retreat into progressively restricted pockets ("refugia") where conditions remain locally habitable [116–118]. Several authors have therefore suggested that, if Martian life emerged and proliferated in the habitable Noachian Period, nascent organisms may have sought refuge in areas that insulated them from the full consequences of Mars' climate change [119–121]. Possible refugia on Mars include caves, deep subsurface niches, saturated brines/salt habitats, ice deposits, and areas of glaciovolcanism (any area where magma/lava interacts with ice, firn, or snow [122]) [119,120]. Each of these habitats are hypothesized to have sustained liquid water after Mars' surface dried and potentially extended Mars' habitable window. However, while life could theoretically persist and even evolve within in these isolated niches, it is worth noting that evolution generally advances most significantly in variable (but continuously habitable) environments with ample resources and opportunities for diverse species interactions [123]. Thus, the contraction and fragmentation of habitats on Mars likely inhibited the overall evolutionary progress on Mars; Westall et al. [113] hypothesize that any Martian life would have remained very small, similar in size to Earth's early microbes (<1μm).

Further, the evolution of oxygenic photosynthesis—which precipitated marked increases in body size, biomass production, and population size on Earth [124]—might have been precluded on early Mars [46,113]. On Earth, photosynthesis appeared on a continuously habitable planet with

almost uninterrupted access to energy, carbon, and nutrients, as well as direct access to sunlight in habitable shallow coastal areas [113]. In contrast, Mars' short and spatially discontinuous window of habitability might not have provided sufficiently stable conditions for such a complex process to evolve [46,113]. Indeed, even if life were able to persist within stable refugia, limited access to sunlight in these protected niches would have precluded photosynthesis [27]. Moreover, given Mars' greater distance from the Sun, and the fact that the Sun was fainter during the early phases of its history, there may have never been a strong evolutionary drive for ancient Martian life to develop photosynthesis [51,113]. Thus, in addition to remaining small, it is hypothesized that Martian organisms were predominantly restricted to chemosynthetic and heterotrophic metabolic pathways [46,113,114]. The rate of biomass production through chemosynthesis is generally lower than that achieved through photosynthesis [124]. For instance, Sleep and Bird [125] calculated that less than 0.056 Tmol/year of organic carbon (biomass) would have been buried in sediments on Earth during pre-photosynthetic times, compared with 10 Tmol/y buried today. These authors concluded that chemosynthetic life on Mars would likely leave behind only a sparse and dispersed organic record. Therefore, the main challenge of astrobiologists, and the goal of this thesis, is to develop strategies and instrumentation that focus the search for life towards areas with the highest chance of having hosted life and retaining their sparse organic remains.

## 1.4 HOW WE EXPLORE

### 1.4.1 The Concept of Biosignatures

The crux of any search-for-life mission lies in determining whether an observation can be uniquely attributed to a biological source. A ‘‘biosignature’’ (or “biomarker[2]”) is defined as an object, substance, and/or pattern whose origin specifically requires a biological agent [126]. Their value is evaluated by the probability of life creating it and the improbability of abiotic processes producing it [126]. Although myriad possible biosignatures exist, such as biominerals, cellular fossils, isotopic fractionations, chemical enrichments, biologically-mediated rock structures (e.g., stromatolites, coral), and/or specific organic compounds, this thesis discusses the distribution and preservation of *lipid* biosignatures. Lipids were selected for several reasons.

[2] The terms biosignature and biomarker are used interchangeably throughout the Chapters of this thesis.

First, lipids are vital for life as we understand it. All known organisms are encapsulated by lipid membranes that perform biological functions, including maintaining basic structural integrity, facilitating transport of substrates into and out of the cell, enabling communication, and conserving energy. These functions are absolutely essential to the functioning of a cell and are universal across life on Earth. Thus, if life elsewhere in the universe shares similar biochemical principles, which is a reasonable initial assumption [24], lipids are hypothesized to also play an essential role in extraterrestrial organisms (see review by [127]). Second, biogenic lipids are synthesized through pathways that are unique to biological systems, resulting in distinct molecular patterns that may be used to distinguish them from non-biological molecular compounds [127]. Further, the specific types of lipids produced can be indicative of particular types of organisms or metabolic processes, making lipids an effective biosignature for identifying and characterizing life [128,129]. Third, because lipid membranes form the critical boundary between the inside and outside of a cell, they interact directly with the environment. Organisms are well known to modify the biophysical properties of their membrane to preserve fluidity and integrity in response to environmental factors such as temperature, pH, and salinity [130]. Consequently, the molecular structure of a lipid membrane can offer crucial insights into an organism's conditions and adaptive strategies, making lipids a dynamic biosignature that not only indicates life but also provides insights into the environmental conditions in which that life exists. Lastly, lipid compounds are uniquely recalcitrant. Unlike other organic compounds vital for life—like DNA, proteins, and carbohydrates—lipids are remarkably resistant to degradation, allowing them to accumulate in the sedimentary record, serving as long-term molecular fossils [131]. In fact, our understanding of Earth's early microbial life has been substantially augmented by the detection of lipids, such as hopanes and hydrocarbons, in ancient rocks [132,133]. Hence, lipids offer a promising biosignature in our quest to discover Martian life.

### 1.4.2 Selecting Exploration Sites

Landed planetary missions designed to look for evidence of life are expensive, complex, infrequent expeditions. Exploration sites must be carefully selected to maximize the likelihood of having been inhabited (at some point), as well as the likelihood of *retaining* biosignatures. In the case of Mars, two broad exploration categories stand out: (1) ancient terrains that bear clear evidence of liquid water activity and deposits capable of rapidly entombing and preserving biosignatures (e.g., deltaic fans, phyllosilicate-rich areas), and (2) sheltered refugia that may

have sustained vestiges of Martian life through the global climate transition. Previous (and forthcoming) Mars missions have predominantly focused on category 1, asserting that Noachian and early Hesperian deposits record a time with the greatest probability of widespread microbial colonization and concomitant biosignature production [134–136]. However, there is a growing recognition of the untapped potential that the sheltered refugia hold for astrobiology [119].

Refugia represent the longest sustained habitats on the planet, and thus, the youngest potential biosignature deposits; in some cases, subsurface refugia may remain habitable today and are considered high priority targets for assessing the possibility of *extant* Martian life [119]. Furthermore, drawing parallels to Earth, where refugia have played a critical role in the survival of species through global glaciations [117,137], numerous studies reveal that refugia are marked by elevated taxonomic and genetic diversity [117,118,138]. The underlying mechanism for such biodiversity appears to be the inherent stability of the refugia and their small size. By providing localized oases during adverse climate periods, refugia attract an array of organisms, gradually accumulating diverse species [139] and even catalyzing the emergence of new taxa [140]. Thus, refugia not only serve as late-stage outposts for life, but also as crucibles for biodiversity. If such a pattern holds true for Mars, targeting refugia could greatly enhance our chances of detecting a broad spectrum of relatively recent, and thus less degraded, biosignatures.

Among the various potential refugia on Mars—including caves, the deep subsurface, brines, and glaciovolcanic systems—subglacial volcanic niches stand out as especially compelling targets for exploration. Not only would an ice mass help shield organisms from the planet's harsh surface conditions, but glaciovolcanic interactions could also generate a harmonized ecosystem where life's basic prerequisites are internally generated and sustained. For instance, interactions between volcanic heat and ice/permafrost have the capacity to generate very large volumes of meltwater that can be stored and transported beneath the ice body [141], offering sustained access to liquid water after much of Mars' exposed surface had dried [142]. Meltwater accumulation at the ice-bed interface can additionally promote basal sliding and bedrock comminution [143,144], producing a fine-grained assemblage of freshly exposed, reactive minerals ("rock flour"). On Earth, reactions between meltwater and rock flour liberate an array of bioavailable nutrients via chemical dissolution [145,146] and represent a significant source of sustenance and energy in terrestrial glaciated areas [146,147]. Although the chemical conditions

on Mars would differ due to the lack of atmospheric oxygen and the absence of a vigorous biosphere, comminuted oxidized basalt could still yield key phases necessary for life, such as electron acceptors (e.g., $Mn^{4+}$ and $Fe^{3+}$), electron donors (e.g., $Fe^{2+}$ and organic carbon), and micro/macronutrients (e.g., N, P, Zn, Cu, Ni) [148]. Furthermore, the discharge of reduced volcanic gases such as $H_2S$, CO, $CO_2$, $H_2$, could offer additional redox pairs and introduce inorganic carbon sources, adding to the chemical diversity and energy sources available in these habitats [120,149]. Lastly, glaciovolcanic interactions are also highly conducive to the generation of hydrothermal systems, together with steep thermal and geo-chemical gradients [120]. Such gradients could provide diverse microniches optimized for various organisms, increasing the breadth of lifeforms that could be sustained, whilst also promoting circulation capable of distributing nutrients, removing waste, and transporting organisms [120]. In brief, glaciovolcanic environments not only offer a refuge from Mars' harsh surface, but also deliver a uniquely holistic and dynamic ecosystem where life could thrive.

Importantly, evidence of glaciovolcanic activity spans the Noachian to the Amazonian and is widespread across latitudes, indicating that such areas have been widely available regardless of the climatic regime [120]. Recent (100-200 Myr) glaciovolcanic meltwater deposits have been observed on Mars, suggesting that these sites are well within reach of conventional surface exploration methods, eliminating the need for the intricate technologies that accessing the deep subsurface or caves would demand [106–112]. This thesis therefore focuses on the habitability and biosignature preservation potential of a glaciovolcanic system in Iceland and uses the results to deduce exploration strategies for future exploration (see next section).

### 1.4.3 The use of Terrestrial Field Analogues

Terrestrial field analogues are places on Earth that approximate, in some respect, the geological, environmental, and putative biological conditions on another planetary body, either at the present-day or sometime in the past. They provide a tangible working model of extraterrestrial targets and are, currently, the best way to study the potential habitability of other worlds and develop appropriate exploration strategies.

The composition of Mars' surface has been determined from analysis of Martian meteorites, spectral observations from orbit, and from landed spacecraft. Based on these data, Mars is viewed as being dominantly basaltic, consisting mainly of tholeiites formed by extensive partial

melting [150]. Although much of the surface is covered by unconsolidated regolith, these grains mostly retain the composition of their basaltic precursors [151]. Only a few examples of evolved rocks have been observed in global spectral surveys [152]. Thus, studying how life on Earth colonizes, interacts with, and makes a living on tholeiitic substrates could guide our search for Martian biosignatures.

Tholeiitic basalts that approximate Mars' compositions can be found in various sites on Earth. The Columbia River Basalt Group in the Pacific Northwest of the United States, the Snake River Plain of Idaho, the Deccan Traps in India, Lonar Crater of India, and certain terrains in Hawai'i each exhibit Mars-like geochemistry and have heritage as Mars analogues [153–157]. However, the basaltic environments of Iceland offer an almost unparalleled analogue for Mars due to their unique Fe-rich chemistry [158,159], as well as their exposure to cold climes and slow weathering processes [160]. The interactions between Icelandic basalts and glaciers offer additional unique opportunities to investigate the environmental regimes that dominated much of Mars' history.

It is important to note that tholeiitic basalts also constitute much of our oceanic crust, but their utility as biogeochemical analogues for Mars is contested due to the divergent geological and hydrological histories of Earth and Mars [161]. While marine basalts on Earth support vibrant microbial communities, the degree to which the biomass and biodiversity depends on seawater resources (e.g., organics and ions) or mineral resources from fresh basalts produced at spreading ridges, remains uncertain [162–164]. In contrast, Mars lacks evidence of vast oceans or strong, enduring plate tectonics [29,165], which makes extrapolating findings from Earth's marine environments to Mars challenging. And although some relevant insights can be drawn about microbial survival at low light levels or extreme temperatures, volcanic materials in contact with freshwater are generally considered to be more robust, comprehensive Martian analogues [161].

Relatedly, it is crucial to recognize that no terrestrial analogue provides a flawless representation of Mars, given the myriad differences between the two planets. Each analogue mimics only certain aspects of Mars and it is the cumulative insights gleaned from various complementary studies that facilitate a holistic view capable of propelling the field of astrobiology forward.

### 1.4.4 Rover Missions

Rover-based instrumentation currently remains the most technologically suitable method for the *in situ* exploration of planets in our Solar System. Human exploration, at this stage, is untenable and rovers are designed to be our surrogate 'boots on the ground', enabling us to probe, sample, and analyze a planet's surface (and shallow subsurface). Central to the scientific payload aboard modern rovers is an advanced suite of remote survey instruments, often including panoramic cameras, telescopic lenses, and non-contact spectrometers for stand-off geological analyses [166,167]. These instruments, regularly programmed to operate semi-autonomously, are used throughout a rover's traverse to build comprehensive (chemo)stratigraphic columns.

The value of these consolidated data profiles cannot be overstated [167]. They are the foundation for reconstructing paleoenvironments and assessing whether local or regional conditions favoured the production and preservation of biosignatures. This empowers researchers to develop exploration plans that are informed and targeted, rather than speculative. This is especially crucial for Mars where the organic record is expected to be sparse. By targeting areas with the highest potential for concentrating biosignatures, such as isolated refugia, researchers can optimize the use of limited rover resources, ensuring that every move made on the Martian surface is both purposeful and promising. Further, the geological context afforded by the survey instruments will be critical for the interpretation of any potential biosignature. Environmental context will help determine whether a potential biosignature is a true sign of life or a product of abiotic processes (false positive). Understanding the system hosting any potential biosignature will also provide a more comprehensive picture of how that life may have originated, evolved, and interacted with the environment. In sum, survey instruments are the cornerstone of effective exploration and will be the basis of subsequent interpretation. Therefore, this thesis also aims to enhance the quality of information extracted from remote spectrometers on active and future Mars rovers.

## 1.5 STRUCTURE OF THE THESIS

The body of this thesis is organized in a manner that reflects a strategic progression in astrobiological research. The first half of the thesis, Chapters 2 and 3, present the results of geobiological fieldwork within a glaciovolcanic terrestrial analogue, discussing its habitability and biosignature preservation potential. The latter half of the thesis, Chapters 4 and 5, shift focus

towards the development of techniques designed to improve the scientific output of spectral survey tools on Mars rovers, thus facilitating more insightful strategic planning. Collectively, this organization reflects the essence of astrobiological research: intertwining our existing understanding of life on Earth with the innovation of tools to support investigating the potential for life as we don't know it.

In detail, Chapter 2 uses phospholipid fatty acid lipid biosignatures to investigate the nature of the biological community inhabiting a glaciovolcanic system in Iceland. The study sought to estimate the microbial biomass of the system, elucidate the community structure, and investigate the adaptive strategies employed to withstand the extreme conditions. The findings shed light on the potential for similar Martian glaciovolcanic refuges to support microbial life and provide an empirical framework for developing exploration strategies.

Chapter 3 extends Chapter 2 by examining the production and preservation of recalcitrant biosignatures in this glaciovolcanic system. This involves a comprehensive characterization of sedimentary hydrocarbons, an inert class of lipid previously identified as valuable, degradation-resistant molecular fossils [131]. We discuss the origin of these biosignatures, the biological data they encode, and evaluate their potential for long-term preservation. The hydrocarbon profiles will serve as a valuable reference dataset for future missions that explore analogous sites on Mars. Importantly, this Chapter challenges the common assumption that hydrocarbons are derived from functionalized membrane lipids and discusses the implications of this finding. This Chapter also presents a thorough examination of the system's mineralogy and reveals an abundance of swelling clays, which are known to sorb and store organic biosignatures for geologically relevant timescales. This affirms that glaciovolcanic systems have the capacity to preserve a lasting record of past life. More broadly, given the lack of widespread phototrophic biosignatures, our results offer insight into what a biosignature record might look like if photosynthesis never arose on Mars—a critical unknown highlighted by the Conference on Biosignature Preservation and Detection in Mars Analog Environments in 2016 [168].

Having established this robust empirical framework for investigating glaciovolcanic refugia, Chapters 4 and 5 describe data-driven approaches aimed at expanding the capabilities of remote spectrometers used on Mars rovers. While these innovative tools are pertinent for the exploration

of glaciovolcanic sites, they also hold broader applicability for any astrobiological investigation. Further, as they are designed for survey instruments currently equipped on Mars rovers, the results hold immediate significance, poised to augment the scientific yield of active missions.

Specifically, Chapter 4 introduces a novel approach aimed at enhancing the accuracy of clay mineral identification on Mars, specifically tailored for instruments on the *Perseverance* rover. Given that clay minerals are robust indicators of water activity, and that the mineralogical structure of *some* clays can enhance the preservation of organic biosignatures, this new technique holds great promise in helping to select targets with the greatest potential to retain biosignature organic compounds. This chapter is published in *Spectrochimca Acta Part B: Atomic Spectroscopy* and the technique has since been adapted, by myself and colleagues, to enhance Perseverance's capacity to delineate carbonate minerals—another mineral family that may harbor biosignatures [169].

Chapter 5 presents a comprehensive framework for optimizing the detection and quantification of crustal N on Mars using survey instruments available on active rovers. Enabling remote and accurate surveys of N could address one of the most important outstanding problems in assessing Mars' habitability through time. Further, we found in Chapter 2 that sedimentary N is strongly correlated with biomass, suggesting that N abundance could serve as a key indicator of biomass concentrations on the outcrop-scale and be used to guide rovers towards promising targets.

Chapters 6 and 7 provide a synthesis of the work. These Chapters advocate for an exploration pivot towards Martian refugia with a spotlight on the unique significance of glaciovolcanic areas, exemplified by Kverkfjöll. These Chapters critically assess the exploration challenges identified throughout the thesis, suggesting refined exploration strategies, and emphasizing the value of integrating modern data science techniques with current and future Martian exploration efforts. Moreover, these closing Chapters highlight the broader implications of the thesis findings on our understanding of life in carbon-poor systems on Earth and Mars. Overall, this thesis contributes to ongoing efforts to establish a framework for optimized, data-driven strategies in the pursuit of potential biosignatures on Mars.

# CHAPTER 2

# Organic Biosignatures in Glaciovolcanic Terrains: Implications for Astrobiological Exploration on Mars

Gibbons E.F. [a]*, Slater G. [b], Berlo K. [a], Leveille R.J. [a]

[a] Geotop, Department of Earth and Planetary Sciences, McGill University, 3450 University Street, Montreal, Quebec, Canada, H3A 0E8

[b] School of Earth, Environment & Society, McMaster University, 1280 Main Street West, Hamilton, Ontario, Canada, L8S 4K1

*Corresponding author: *erin.gibbons@mail.mcgill.ca*

**ABSTRACT**

If life emerged on Mars during the Noachian, wet glaciovolcanic environments may have provided protected niches for habitability after Mars lost much of its surface water and atmosphere. To understand the nature of the habitability of these putative refugia, we investigated an active hydrothermal field at the summit of the partially-subglacial Kverkfjöll volcano in Iceland, which features a shallow steam-heated meltwater lake, hot springs, and thermal pools. We used a combined geochemical and lipid biomarker approach to describe the distribution and physiological status of the indigenous microbial community and the hydrothermal fluids that support them.

Our data demonstrate that the volcano-ice interactions generate extensive environmental heterogeneity on a small spatial scale (from kilometer to centimeter), hosting habitats ranging from low to high temperatures (8-87 °C), acidic to alkaline pH (2.9-8.5), extremely dysoxic to oxic

levels, and with significantly variable dissolved ion chemistry. Paired analysis of phospholipid fatty acids (PLFA) reveal that viable microorganisms are present in all samples. No evidence for plant or animal input is observed. We find significant variability in the biomarker profiles across the site, reflecting spatial changes in the community composition as well as biophysical adaptations to extremes of temperature, and possibly pH. These findings illuminate trends of niche differentiation and divergent adaptation within the glaciovolcanic system, indicating that the diverse environments created by volcano-ice interactions are conducive to the emergence of varied communities. PLFA-derived biomass estimates are heterogeneous across the site and strongly correlated with total organic carbon. We propose that biomass becomes concentrated in niches that are conducive to the development of autotrophy, implicating these as potentially valuable targets for future exploration. In sum, we argue that relict glaciovolcanic settings on Mars should be prioritized in future astrobiological exploration and provide recommendations for optimized sampling practices.

## 2.1 INTRODUCTION

Martian glaciovolcanic settings—which refer to any type of volcanic interaction with ice, snow, permafrost, and/or firn—are receiving renewed attention as sites of astrobiological interest [1–3]. These unique interactions generate locally warm and wet conditions at ice-rock interfaces, presenting an integrated ecosystem where life's essential prerequisites (*i.e.*, liquid water, chemical gradients, nutrient supply) are internally generated and maintained [1]. Importantly, these habitable conditions can develop beneath ice sheets or within Mars' frozen subsurface. Thus, even as Mars experienced global desiccation, declining temperatures, and heightened radiation exposure during the post-Noachian era (< 3.7 Ga), glaciovolcanic regions could have created thermal oases, sheltering life from the full consequences of Mars' climate change [1,3]. This hypothesis is supported by extensive evidence that glaciovolcanism has persisted throughout much of Mars' history [1], including the generation of large volumes of meltwater within the last 100 - 200 million years, some of which may have formed habitable englacial lakes persisting for hundreds to thousands of years [3–6]. These environments may, therefore, represent some of the longest sustained and most recently habitable niches near Mars' surface, making them compelling targets in the search for biosignatures. Studies of analogous terrestrial environments will help us understand how life exists in these systems and focus the search for remnant biosignatures in the rock record.

### 2.1.1 Background

Mars' Noachian Period (4.1 - 3.7 Ga), with its widespread evidence for interconnected fluvial activity, is widely considered the most habitable stage of Mars' entire history, after which, increasingly limited access to liquid water and radiation exposure rendered surface conditions largely uninhabitable [7,8]. On Earth, as an area becomes uninhabitable for most species (e.g., during past glacial cycles or in response to human activities) life often retreats to progressively isolated locations in which conditions remain locally favourable [9–13]. These locations, referred to as "refugia", support remnant populations of previously widespread species, often leading to genetic differentiation over time [11]. Similarly, it has been suggested that certain Martian habitats might have functioned as refugia for life forms from the hospitable Noachian Period, providing sustained niches of habitability even after Mars lost much of its surface water and atmosphere [1,14]. Such refugia have been receiving increased attention from the astrobiology community. Not only do these habitats likely represent the longest sustained and most recently habitable niches on the planet, but they may have also acted to concentrate organisms into a relatively constrained region. Identifying refugia could therefore narrow the areas of interest for potential exploration and provide access to the most recent (and thus least degraded) biosignatures.

Glaciovolcanic environments, which refer to any interaction between magma (or its heat) and ice in any form [15], represent particularly compelling potential refugia for Mars for several reasons. First, interactions between volcanism and ice have the potential to satisfy the requirements thought to be necessary for life. Glaciovolcanism can generate and sustain large volumes of meltwater, which provides both the critical solvent for life and creates a range of niches for colonization, such as subglacial lakes, englacial lakes, and/or subsurface water/brine-filled fractures [1]. Moreover, in subglacial systems, meltwater accumulation at the ice-bed interface can promote basal sliding and bedrock comminution, producing fresh and reactive mineral surfaces [16,17]. On Earth, comminuted bedrock is a significant source of bio-essential nutrients and redox couples in glaciated areas [18,19]. While chemical conditions would differ on Mars, comminuted basalt could yield several critical electron acceptors (e.g., $Mn^{4+}$ and $Fe^{3+}$), electron donors (e.g., $Fe^{2+}$, $H_2$, organic matter), and micro/macronutrients required for life (e.g., N, P, Zn, Cu, Ni) [20,21]. The release of reactive volcanic gases, such as $H_2S$, CO, $CO_2$, $H_2$, in some of the habitats would have further strengthened redox gradients and provide an additional carbon

source [22]. Volcano-ice interactions are also highly conducive to the generation of circulating hydrothermal systems, which enhance habitability by clearing waste, redistributing nutrients, transporting microorganisms, and offering diverse physicochemical niches for life to establish a foothold [1,3].

Second, glaciovolcanic processes have likely been a significant feature throughout much of Mars' history (for comprehensive reviews,, see Smellie & Edwards, 2016 [15], and Cousins et al., 2001 [1]). In brief, volcanic activity, evidenced by numerous low shield-like central edifices, large shields, ridged plains, and extensive lava flows, is documented from the Noachian period through to the Late Amazonian [23]. In parallel, signs of significant glaciation are evident across various Martian eras. This includes substantial polar ice caps during the Hesperian period and at present [23,24], as well as strong evidence for mid-latitude glaciation throughout the Amazonian [25,26] and possibly the Noachian [27,28]. Mid-latitude glaciation is inconsistent with ice emplacement under current surface conditions and has instead been linked to past periods of high average obliquity—when Mars' tilt exceeded 30° - 35° [15,29]. During such high-tilt phases, intense polar sublimation is predicted to have caused significant ice loss—up to tens of meters—and atmospheric redistribution of water vapor from the poles to the mid-latitudes [30,31]. Support for this obliquity-driven mid-latitude glaciation process comes from global climate models, which predict cooler equatorial temperatures and consequent ice/snow precipitation at mid-latitudes during past periods of high obliquity [29,32], and from glacial flow modeling which predict broad, extensive, and kilometer-thick ice accumulation in the mid-latitudes under these conditions [33]. Thus, considering the global extent of both volcanic and glacial activities on Mars, it seems highly likely that these processes interacted throughout the planet's history, potentially offering consistent habitable environmental conditions across Mars' climate transition [1]. This hypothesis is increasingly supported by a growing body of geomorphological evidence consistent with volcano-ice interactions occurring from the Late Noachian to the Late Amazonian [1,3,5,6,15,34–37], suggesting that such processes occurred on both sides of Mars' global climate transition. Importantly, recent work has identified geologically young landforms (100-200 Ma) associated with glacial melting, including eskers, streamlined knobs, thrust-block moraines, ribbed moraines [3,6,34,36]. Given that the prevailing cold climatic conditions of the Late Amazonian period do not support ice melting processes, volcanic activity has been invoked to (partially) explain their formation. These late stage glaciovolcanic environments have been

proposed as some of the most recent potentially habitable environments near Mars' surface [1,3,6] and warrant further understanding.

### 2.1.2 Previous Work and Study Objectives

To understand the parameters of habitability and the potential for biosignature preservation in Mars-like glaciovolcanic environments, we studied the summit of the Kverkfjöll volcano in Iceland, including its partially subglacial caldera lake ("Gengissig") and ice-fed hydrothermally-active shoreline. Two prior studies have investigated the biological community here. Marteinsson et al. (2013) [38] used 16S ribosomal RNA gene analysis to characterize the pelagic community of Gengissig, noting a dominance of the betaproteobacterium *Xenophilus*. Cousins et al. (2018) [39] used genomic characterization and stable isotope geochemistry to investigate an acidic hot spring system on the lakeshore. These authors reported a mix of bacteria and thermophilic archaea and highlighted that phototrophy does not play a major role in local primary productivity [39]. Both studies identified exclusively microbial communities with no evidence for inputs from complex organisms; Cousins et al. proposed that the Kverkfjöll summit can serve as a geobiological analogue for Mars [39,40].

Our study builds on this foundation in two significant ways. First, we aimed to present a fuller depiction of the Kverkfjöll ecosystem by monitoring environmental conditions and collecting samples from across the site, including the lakeshore sediments, the lake water column, *and* the lake floor sediments (which have not been sampled previously). Second, we use intact phospholipid-derived fatty acids (PLFA) to query the indigenous community. PLFA are essential components of bacterial and eukaryotic cell membranes that degrade rapidly upon cell death, making them valuable indicators of living (viable) biomass [41]. Further, because their structures vary amongst organism groups and in response to environmental stresses, the suite of PLFA molecular structures ("PLFA profile") can be used as a fingerprint of the community composition and functional status [42].

Specifically, this contribution combines abiotic environmental measurements and PLFA assessment to achieve the following: (1) characterize the environmental gradients in the system, (2) evaluate the source of lipid biomarkers in the system, (3) understand how environmental variables shape the distribution of biomass and/or structural diversity of the community, and (4) ascertain the physiological status and adaptive strategies of this community in response to the local conditions. This study therefore provides a complementary perspective to previous

analyses, contributing novel insights into the diversity, adaptability, and structure of the communities, and the parameters that support them. The results will refine our understanding of Kverkfjöll as a Mars analogue and facilitate more precise extrapolations regarding the habitability potential of Martian glaciovolcanic systems.

## 2.2 GEOLOGICAL CONTEXT

Iceland offers an exceptional natural laboratory for Martian glaciovolcanic processes. An estimated 60% of Icelandic glaciers are underlain by active volcanic systems [43] with predominantly iron-rich tholeiitic deposits of comparable composition to those found on Mars [44,45]. Kverkfjöll is a large, glaciated volcano at the northern margin of the Vatnajökull ice cap. The volcanic system is located along Iceland's neovolcanic zone, which represents a subaerial portion of the mid-Atlantic ridge separating the Eurasian and North American tectonic plates (Figure 2.1a) [46]. Kverkfjöll's main volcanic massif rises to 1900 m altitude, approximately 1000 m above the surrounding area [47] and includes two summit calderas. The northernmost caldera is only partially ice covered (Figure 2.1b), presenting a relatively low-cost opportunity to study the microbial ecology of (partially) subglacial glaciovolcanic systems without the challenges and contamination risks of drilling through a thick ice cover. Notably, because of its geographical isolation and high altitude, the Kverkfjöll summit experiences little disturbance from plants or animals, and no subaerial vegetative cover in the area.

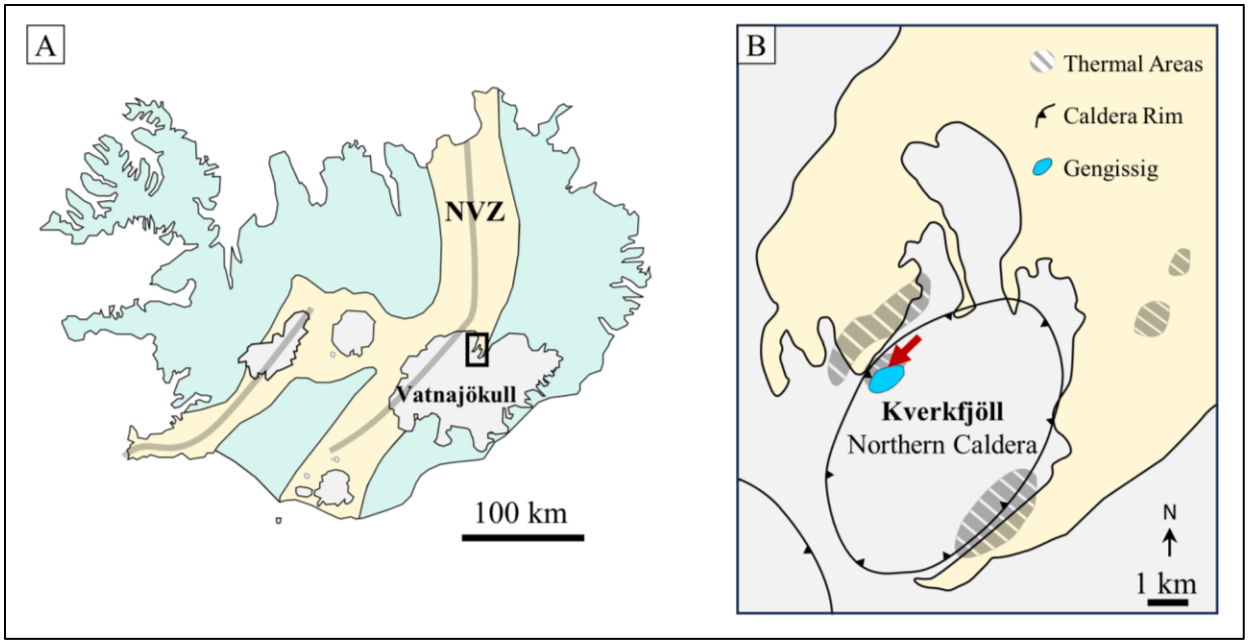


*Figure 2.1: A) Simplified map of Iceland.*

*The neovolcanic zone (NVZ) is depicted in yellow with thick grey lines denoting the approximate locations of active spreading centers. Light grey polygons indicate ice caps/glaciers. A thick black rectangle indicates the location of the Kverkfjöll volcanic area at the northern margin of the Vatnajökull ice cap. B) Study site context map. Volcanic calderas and thermal activity of the Kverkfjöll high-temperature area are shown (adapted with permission from Ólafsson 2001* [47]*). Our study site is located on the north-western shore of lake Gengissig (red arrow).*

Although no eruptions have been recorded within the last 1100 years, Kverkfjöll is located almost directly above the Icelandic hot spot [45,48] and remains one of the country's most active high-temperature geothermal areas [49]. The hydrothermal reservoir fluid averages between 280-300 ± 30 °C, depending on the method of estimation (for a review, see Ranta et al., 2023 [46]), and is sourced mainly from local meteoritic groundwater that has experienced considerable water-rock interaction [46]. Notably, the reservoir is disconnected from marine sources and other subglacial waterbodies elsewhere within Vatnajökull [38,46]. Basaltic terrestrial analogue sites unaffected by seawater influence are rare, and marine-altered basalts are considered less suitable analogues to Mars [50]. Therefore, Kverkfjöll presents a unique opportunity to explore the potential habitability of Mars-like settings in the absence of seawater influence.

The ascending heat and fluids interact with the surficial ice and snow to form a band of intense glaciovolcanic hydrothermal activity. Activity is concentrated on the northwestern flank of the volcanic system within a few well-defined areas [47] (Figure 2.1b). We investigated one of these areas, located south-east of a mapped region known as Hveradalur. The sampling site is

dominated by an ice-damned meltwater lake, locally named Gengissig (or Kverkfjallalón), which formed after a steam eruption in 1959 [49]. At the time of sampling, the lake was surrounded by 30-50 meters high ice walls to the south and to the east, and steep crater rim slopes to the west and north. The lake itself measured approximately 150 meters by 200 meters and was approximately 6 meters deep at its center (cross-sections of the lake's bottom, as reported by Montanaro et al. [51], indicate that the lake's deepest point is near the ice walls, which were not accessed in this study due to safety considerations). Water monitoring data since 1967 highlight substantial variations in water level, occasionally exceeding 25 meters in year-to-year measurements [49]. The lake's shoreline is a dynamic hydrothermal zone, featuring fumaroles, hot springs (>87 °C), thermal streams, boiling mud pots, warm mud pools, and heated ground.

## 2.3 METHODS

### 2.3.1 Field Sampling

Sampling was conducted in May and June of 2022. All samples were collected using nitrile gloves. Sediment samples were collected using various stainless-steel tools (scoopula, shovels, trowels, Petite Ponar® Grab sampler) which were triple rinsed with an ascending series of organic solvents (namely, acetone, dichloromethane, and methanol) before deployment to the field and individually packaged in ashed aluminum foil. Nominally, new collection tools were used for each sample, however, when tools needed to be re-used in the field, they were first ethanol-rinsed and then pre-contaminated in sediment immediately adjacent to the sampling location. Samples for organic analyses (see section 2.3.3 and 2.3.4) were stored in sterile Whirl-Pak bags and frozen in the field using an ice-packed cooler. Samples were lyophilized for 48 to 72 hours upon return to the laboratory.

Shoreline water samples were collected with sterile single-use plastic syringes and lake water samples were collected using a horizontal acrylic Beta™ bottle (solvent rinsed before deployment, as above). Water samples for inorganic aqueous chemistry were stored frozen (samples for anions) or refrigerated (cations) (described in detail in section 2.3.2).

Two distinct areas of thermal activity were visually identified on the north-west shore of lake Gengissig and prioritized for sampling; these are detailed in the following subsections. A summary of samples is provided in Table 2.1 and a sampling map is depicted in Figure 2.2.

#### *2.3.1.1 Sampling Area 1: Spring- Lake Transect*

A vigorously bubbling hot spring was identified on the shore of lake Gengissig (Figure 2.2 and Figure 2.3). Heated waters had overflowed the source pool to create a shallow thermal stream (~90 m long, 1-10 cm depth) that eventually discharged into lake Gengissig. We aimed to collect paired water and sediment samples from the hot spring, along the stream, and into lake Gengissig to evaluate the contextual hydrothermal gradients and their impact on the indigenous community.

On the shoreline, systematic spacing between sampling sites was not possible due to the topography and unconsolidated nature of the stream bank. Instead, end-member localities were prioritized. These included the hot spring source pool (*S_Source_Sed*), the stream's distal end (*S_Distal_Sed*, ~80 m downstream from the source pool), and a mid-point along the stream (*S_Mid_Mat_Sed.*). The mid-point location featured a green filamentous microbial mat, representing the only macroscopic evidence of microbial colonization amongst the samples. This mat spanned about 20 meters of the stream and was confined to a segment with temperatures ranging from 30-47 °C; a sediment sample was collected from the streambed, beneath the mat. At each location where a shoreline sediment sample was taken, a corresponding stream water sample was also collected using sterile syringes (see section 2.3.2).

An inflatable boat was used to traverse the lake along a linear transect from the stream mouth to the lake center (~60 meters from shore). Bottom sediments were collected using a Petite Ponar® Grab sampler (solvent rinsed as above before deployment and cleaned with ethanol between samples). Sediment samples were specifically collected from the central part of the grab sampler to avoid sampling sediment that had come into contact with the walls of the sampler, thus minimizing potential contamination. We attempted to collect samples at 10 meters intervals, however, the coarse grain size of the proximal sediments prevented the grab sampler from closing and capturing a sample. The dominant grain size transitioned from pebble-sized to mud-sized at a position ~50 meters from the lakeshore, allowing successful collection of bottom sediments at positions ~50 and 60 meters from shore. We collected one additional lakebed sample 3 meters from shore where the water was sufficiently shallow to manually close the sampler, despite the coarse grain size. It is important to note that the sediment sample collected at ~50 meters distance from shore (*L_50m_Sed.*) appears to have intersected a subaqueous hot spring as the sediments were hot upon being pulled into the boat, measuring 70 °C using a non-contact infrared temperature gun.

In parallel to the sediment samples, samples of the water column were collected using a a horizontal acrylic Beta™ bottle (solvent rinsed as above before deployment and cleaned with ethanol between samples). Water samples were collected from the near surface (~0.5 m depth) and at the sediment/water interface (at a distance of 3 meters from shore, the water was only 0.5 m deep and only one water sample was collected). These water samples were filtered through sterile 0.45 µm polyvinylidene fluoride (PVDF) filters. The filtered water was retained for dissolved ion analyses (section 2.3.2) and the filters themselves were frozen and retained for PLFA extraction to explore the pelagic community composition. Unfortunately, a water sample could not be collected from the sediment/water interface at the site located ~50 meters from shore (*L_50m_Sed.*) due to high winds.

It is important to note that Cousins et al. (2018) [39] also describe sampling a hot spring and thermal overflow stream on the shore of Lake Gengissig in 2011. However, considering the current spatial distribution of hydrothermal features and the chemical characteristics of the fluids at the site (refer to section 2.4.1), it appears that the Spring-Lake system we studied is either distinct or has undergone significant changes over time.

#### *2.3.1.2 Sampling Area 2: Elevated Mud Pot Area*

In the north-western area, separate from the Spring-Lake Transect, there was an elevated mound of sediment featuring a cluster of mud pools of variable size and temperature (Figure 2.2 and Figure 2.3). The prominent feature was a large quiescent thermal pool, approximately 3 x 7 m in size, lined with viscous and sticky blue-grey mud. Separated from this pool, along its edges, were several small, bubbling, and steaming mud pots, each less than ~20 cm in diameter. Surrounding the active pool and pots, the ground appeared soft and mud-cracked, hosting several shallow depressions. The depressions are interpreted as inactive/semi-dehydrated mud pools. Beneath the mud-cracked surface was a massive deposit of damp blue-grey mud (Figure 2.3c,d). The underlying mud was warm (8-20 °C; at an ambient air temperature of ~4 °C) and showed varying moisture levels between different depressions, suggesting different durations of inactivity.

Sediment and water samples were collected from the large thermal pool (*MP_Pool_Sed.*) and from one representative bubbling, steaming mud pot (*MP_Boil_Sed.*). Additional sediment samples were collected from the inactive mud pots, including a damp and warm (20 °C) hollow interpreted as a recently inactive thermal pool and a cooler (8 °C), mostly dry hollow interpreted

as a longer inactive thermal pool. In the case of the inactive pools, the mud-cracked upper crust was sampled separately from the underlying massive mud.

| | Sample Metadata | | | | Organic Analyses | | Analyses on Paired Water Samples † | |
|---|---|---|---|---|---|---|---|---|
| | **Fig. 2.2 ID #** | **Text ID** | **Sample Type*** | **Sample Description** | **PLFA** | **TOC & TN** | **Phys. Param** | **Aq. Chem** |
| **Spring (S) – Lake (L) Transect** | **1** | **S_Source_Sed.** | Sediment | Bubbling hot spring vent. Grey sediment collected. | ✓ | ✓ | ✓ | ✓ |
| | **2** | **S_Mid_Mat_Sed.** | Sediment | Stream mid-point. Green microbial mat. Underlying sediment collected. | ✓ | ✓ | ✓ | ✓ |
| | **3** | **S_Distal_Sed.** | Sediment | Stream distal end. Gravelly sediment. | ✓ | ✓ | ✓ | ✓ |
| | **4** | **L_3m_Filter** | Filter | Lake filter sample, 3m from shore, ~0.5 m depth. | ✓ | N/A | ✓ | ✓ (one sample) |
| | **5** | **L_3m_Sed.** | Sediment | Lakebed sediment sample, 3m from shore, ~0.5 m depth. | ✓ | ✓ | ✓ | |
| | **6** | **L_50m_TopFilter** | Filter | Lake filter sample, 50m from shore, ~0.5 m depth. | ✓ | N/A | ✓ | ✓ |
| | **7** | **L_50m_Sed.** | Sediment | Lakebed sediment sample, 50m from shore, ~5 m depth. 70 °C at collection. | ✓ | ✓ | ✓ | Not collected; high wind |
| | **8** | **L_60m_TopFilter** | Filter | Lake filter sample, 60m from shore, ~0.5 m depth. | ✓ | N/A | ✓ | ✓ |
| | **9** | **L_60m_DeepFilter** | Filter | Lake filter sample, 60m from shore, ~5 m depth. | ✓ | N/A | ✓ | ✓ (one sample) |
| | **10** | **L_60m_Sed.** | Sediment | Lakebed sediment sample, 60m from shore, ~5 m depth. | ✓ | ✓ | ✓ | |
| **Mud Pot (MP) Area** | **11** | **MP_Pool_Sed.** | Sediment | Large thermal mud pool. Margin sediment collected. | ✓ | ✓ | ✓ | ✓ |
| | **12** | **MP_Boil_Sed.** | Sediment | Small boiling mud pot. Margin sediment collected. | ✓ | ✓ | ✓ | ✓ |
| | **13** | **MP_Recent_Crust_Sed.** | Sediment | Cracked upper crust of damp hollow interpreted as recently inactive mud pool. (Figure 2.3c) | ✓ | ✓ | N/A | N/A |
| | **14** | **MP_Recent_Low_Sed.** | Sediment | Dense, warm underlayer of damp hollow interpreted as recently inactive mud pool. (Figure 2.3c) | ✓ | ✓ | N/A | N/A |
| | **15** | **MP_Old_Crust_Sed.** | Sediment | Cracked upper crust of drier hollow interpreted as long-inactive mud pool. (Figure 2.3d) | ✓ | ✓ | N/A | N/A |
| | **16** | **MP_Old_Low_Sed.** | Sediment | Dense, warm underlayer of drier hollow interpreted as long-inactive mud pool. (Figure 2.3d) | ✓ | ✓ | N/A | N/A |

*Table 2.1: Summary of samples for organic analysis.*

*Samples are given a numeric code corresponding to the labels on Figure 2.2, as well as short informative name that indicates their general collection areas (S=Spring/stream, L=Lake, MP=Mud Pot). Rightmost columns provide a checklist of analyses completed on the samples collected for organic assessment and those collected from the contextual hydrothermal fluids.*
** Sample Type specifies the type of sample used for organic analysis: lyophilized sediment or frozen PVDF filter.*
*†At each subaqueous location where a sediment or filter sample was collected for organic analysis, a paired water analysis was done. "Phys Param." refers to data collected* in situ *at the time of sampling using the YSI Prometer. "Aq. Chem." refers to paired water samples collected for laboratory analyses; only one water sample was collected for each deep-water location. The exception is sample L_50m_Sed., for which winds were too high to collect a water sample for laboratory analysis. Note: No contextual fluid data available for inactive (subaerial) Mud Pots.*

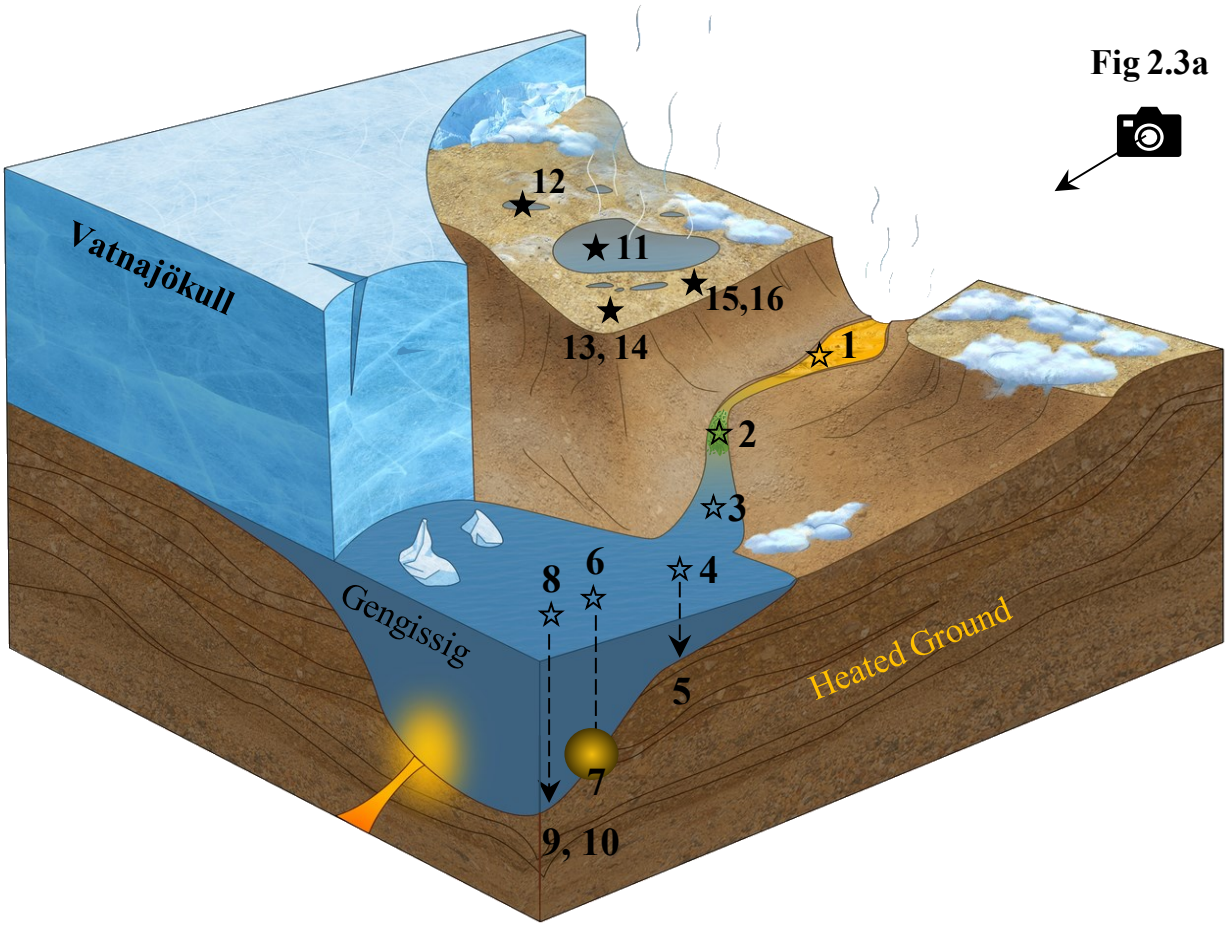


*Figure 2.2: Sampling site map.*

*Simplified site schematic showing the spatial arrangement of major hydrothermal features and sampling sites. Open stars depict sampling sites along the Spring-Lake transect. Filled stars depict sampling sites in the Mud Pot region; see Table 2.1 for sample numbers. The camera icon represents the approximate position of the context photo presented in Figure 2.3A. Drawing not to scale.*

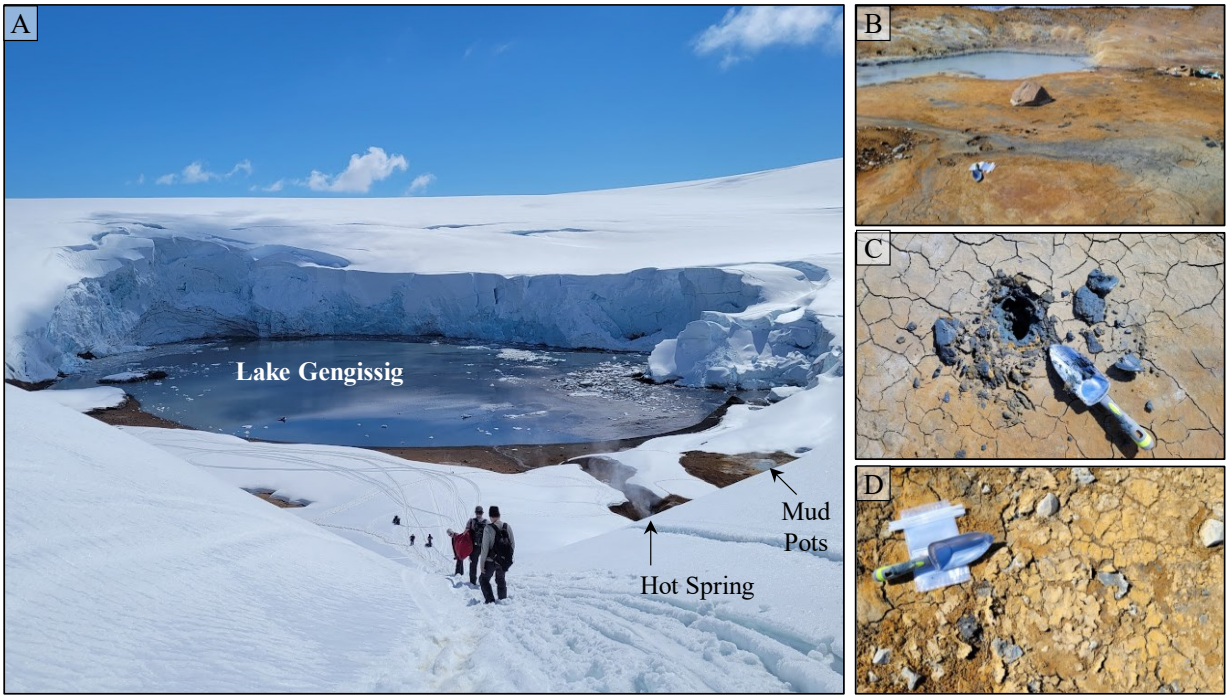


*Figure 2.3: Field photos.*

*A) Context photo of whole study site highlighting the spatial arrangement of various hydrothermal features. B) Contextual photo of Mud Pot region. The large warm pool lies in the background (site of 11.MP_Pool_Sed.), and the soft-sediment hollows interpreted as inactive mud pools life in the foreground, garden trowel for scale. C) Close-up photograph of a recently inactive mud pot. The upper crust is relatively dry, and mud cracked (site of 13.MP_Recent_Crust_Sed.); crust is underlain be warm (~20 °C), damp, massive blue-gray mud (site of 14.MP_Recent_Low_Sed.). D) Close-up photograph of a longer inactive mud pot. The upper crust is very dry, cracked, curled, and oxidized (site of 15.MP_Old_Crust_Sed.); crust is underlain by less warm (~8 °C), dry, massive blue-gray mud (site of 16.MP_Old_Low_Sed.).*

### 2.3.2 Physicochemical Analyses: In-situ Environmental Data & Aqueous Chemistry

All water samples (collected via syringe or Beta-sampler) were filtered in the field through 0.45 µm glass fiber filters and stored in polypropylene bottles with minimal headspace (bottles were pre-cleaned in 10% nitric acid [v/v, $HNO_3$ and Milli Q water] solution as described by the USGS Handbook for Water-Resources Investigations [52]). Sub-samples for cation analyses were acidified with Suprapur nitric acid and frozen upon return to the field base camp. Field blanks of deionized water were collected using identical procedures. Major cations were measured with Inductively Coupled Plasma Optical Emission Spectrometry (Si, Na, Mg, K, Ca, Fe, Mn, Zn, Pb) or Inductively Coupled Plasma Mass Spectrometry (Al, Cr, As, Cu, Ni). Major anions ($F^-$, $Cl^-$, $NO_3^-$, $NO_2^-$, $SO_4^{2-}$, $PO_4^{3-}$) were analyzed by ion chromatography using a Dionex LC20 chromatograph with ED40 electrochemical detector. All analyses were run on samples, field

blanks, standard solutions, and solution blanks. Data were blank subtracted using the response of the field blank (deionized water prepared in the field in the same manner as the samples). Additional methodological details are provided in Appendix A.

Following the collection of each subaqueous sediment sample and pelagic filter sample, physical parameters of the surrounding hydrothermal fluids were measured using a YSI Prometer (including temperature, pH, dissolved oxygen [DO], total dissolved solids [TDS], and salinity). The pH probe was calibrated before deployment, the DO sensor was calibrated daily according to manufacturer instructions. Physical parameters were also measured along an exploratory depth profile (0.5-meter vertical increments) at the center of lake Gengissig to investigate physical gradients through the water column.

### 2.3.3 Untargeted Organic Analyses: Total Organic Carbon and Total Nitrogen

Untargeted organic analyses were performed on all sediment samples at L'Université du Québec à Montréal in the Light Stable Isotope Geochemistry Laboratory; however, due to insufficient material captured on the filters, filter samples were not analyzed. Total carbon and total nitrogen content were determined first. Approximately 10-20 mg of lyophilized sample was measured into separate sterile tin capsules (6 mm x 4 mm, Elemental Microanalysis), crimp-sealed, and analyzed using a Carlo Erba NC 2500™ elemental analyzer. Samples were combusted at 1000 °C with chromium and silver cobaltous oxides (Elemental Microanalysis column B1000) and a pulse of oxygen (Linde, 99.98% purity). Subsequently, gases were reduced over copper at 780 °C. The resulting gases were carried under a helium flux (Linde, 99.999% purity) to a gas chromatography column (Elemental Microanalysis E3003) kept at 50 °C, where gases were separated. Each gas was quantitatively measured on a thermal conductivity detector. On the day of analysis, a calibration curve was performed using acetanilide, cyclohexanone, and atropine (Elemental Microanalysis respectively B2000, B2005 and B2006) with varying weights covering the range of values expected during analysis. A low organic carbon soil (Elemental Microanalysis B2153) was measured as a control. The total organic carbon content was determined in a separate run for the same set of samples using an additional ~10 mg of material weighed into sterile silver capsules (5 mm x 8 mm, Elemental Microanalysis). The open silver capsules were enclosed in a glass container saturated with hydrochloric acid vapour for 48 hours to remove inorganic carbon. The capsules were crimp-sealed and combusted as above. Results

are given in weight percent. The uncertainty is estimated by the long-term average of the control (±0.01% for nitrogen and 0.07% for carbon). C:N ratios are reported using molar concentrations.

### 2.3.4 Phospholipid Fatty Acid Analysis

All glassware was precombusted at 450 °C for 8 hours. Non-combustible equipment was solvent-rinsed 5 times with a sequence of hexane, dichloromethane, and methanol. Total lipids were extracted from representative portions of each sediment sample (between 5 and 50 g) and from each water column filter using a modified Bligh and Dyer protocol [53]. Briefly, the samples were suspended in a solvent mixture of dichloromethane, methanol, and phosphate buffer (pH = 7.4) in a volume ratio of 1:2:0.8, sonicated for 15 minutes, and left to extract overnight on a shaker table (80 rpm). Additional dichloromethane and Milli-Q water were added to adjust the solvent ratio to 1:1:0.9 and trigger a separation of organic and inorganic phases. The solutions were allowed to separate for 3-12 hours at room temperature, after which the organic phase was collected. The complete extraction procedure was repeated on the same subsample using fresh extraction solution, and the resultant organic phases combined. The combined organic extracts were dried under a gentle stream of nitrogen and immediately re-dissolved in a small amount of hexane:dichloromethane (7:3, v/v). Acid-activated copper pellets were added to remove elemental sulfur. The extracts were then separated into different lipid classes using silicic acid column chromatography: hydrocarbons, neutral lipids, glycolipids, and phospholipids were eluted with ~40 mL of hexane, dichloromethane, acetone, and methanol, respectively. The phospholipids isolated in the methanol fraction were evaporated to dryness, redissolved with KOH and a 1:1 toluene:methanol mixture, then heated to 37 °C for an hour to facilitate the conversion of phospholipids to fatty acid methyl esters (FAMEs ) for analysis by gas chromatography-mass spectrometry (GC-MS). The FAMEs were purified via secondary silica gel chromatography (F1 = 4:1 hexane:DCM, F2 = DCM containing PLFA as FAMEs, F3 = MeOH) prior to analysis by GC-MS.

FAMEs were analyzed on an Agilent 7890B GC equipped with an Agilent 7693 auto sampler and an Agilent 5977B high efficiency source Mass Selective Detector (Agilent Technologies, Inc., Santa Clara, CA). Analytical separation of the compounds was accomplished using a 30 m × 0.25 mm × 0.25 um DB-5 MS UI column (J&W Scientific, Folsom, CA) and a column temperature programmed from 50 °C (held for 1 minute), ramped at 20 °C/min to 130 °C, ramped at 4 °C/min to 160 °C, then ramped at 8 °C/min to 300 °C, and held at the final temperature for 5

minutes. The injection port temperature and MS Source temperature were maintained at 300 °C; the MS quadrupole temperature was 150 °C. Electron impact ionization (70 eV) was used, and full scan spectra were obtained by scanning m/z 50–800 at 1 scan/s.

Compound assignment was based on retention time and spectral comparisons with the following certified references: Bacterial Acid Methyl Esters CP Mix (Matreya LLC), Supelco 37 component FAME mixture, 10-methyl palmitic acid methyl ester (10Me-$C_{16:0}$). Additional PLFA were identified using the NIST (National Institute of Standards and Technology) Spectral Library and/or assessment of the mass fragmentation pattern. The abundance of individual FAMEs were quantified in parts per million (ppm) using the integrated area under each chromatographic peak, calibrated according to the five-point external standard curve of the nearest eluting standard (standards included: dodecanoic acid, tetradecanoic acid, hexadecanoic acid, octadecanoic acid, and eicosanoic acid). Chromatographic peak integrations were computed using the Agilent MassHunter Qualitative Analysis software and the *Agile2* integrator.

#### *2.3.4.1 Fatty Acid Nomenclature*

Fatty acids are designated as $C_{X:Y\ (n\text{-}z).}$ X denotes the number of carbons on the longest continuous carbon chain, Y denotes the number of unsaturations by double bonds, and Z represents the position of the first carbon atom of the double bond closest to the methyl end of the chain. If the double bond position is not known, the "n-z" notation is excluded. Where the geometry of the double bond is known, it is additionally labelled with the prefix *cis*- or *trans*- (e.g., α-Linolenic acid: cis-$C_{18:3\ (n\text{-}3)}$). Branched chain fatty acids are identified by a unique prefix: "*i*-" for terminal iso configurations, "*a*-" for terminal anteiso configurations, or by a number indicating the position of the branch from the methyl end of the chain (*i.e.*, 10Me$C_{16:0}$). Methyl branching at undetermined positions is indicated by the generic "br-" prefix. The prefix "cy-" designates fatty acids with a cyclopropane functional group.

#### *2.3.4.2 PLFA Data Processing*

Raw concentration data were converted into a variety of metrics to elucidate patterns of habitation. PLFA concentrations were grouped into the following chemically distinct classes: saturated, monounsaturated, polyunsaturated, mid-chain branched, terminally branched, and cyclopropyl-bearing, fatty acids. Variability in the proportions of these groups can reflect changes in community membership and/or adaptive responses [54,55]. The ratio of *cis* to *trans* monounsaturated fatty acids is used as an indicator of microbial stress, as organisms often

isomerize *cis* compounds to their *trans* configuration under conditions of stress, such as high temperature, organic compound toxicity, starvation, osmotic stress, low pH, and heavy metal toxicity [56]. Generally, unstressed communities exhibit *trans:cis* ratios <0.1, and significantly higher values are considered a marker of stress [57]. Here, the ratio is computed using concentrations of *trans*-$C_{18:1(n-9)}$ and *cis*-$C_{18:1(n-9)}$. Lastly, total PLFA abundances were converted into microbial biomass estimates (cells per unit) using the published conversion factor of Green & Scow (2000): $2x10^4$ cells/pmol PLFA [58].

### 2.3.5 Statistical Analyses

A variety of statistical analyses were applied with a significance level of 0.05. Details of the software packages and data organization are supplied in Appendix A.

To investigate the physicochemical variability of the fluids sampled throughout the study area, dissolved ion chemistry and environmental attributes were subjected to unsupervised Hierarchical Clustering (HC) and Principal Component Analysis (PCA). Prior to analysis, the variables were scaled to unit variance to prevent any potential bias caused by differences in measurement scales or units. In cases where dissolved ions were below the detection limit, the missing values were replaced with a value of one half the instrument limit of detection. However, the following ions were omitted from the analysis because they were not detected in most (or all) samples, resulting in variables with close to 0 variance: Cr, As, Cu, Ni, and Br. The significance of group differences identified by HC and PCA was evaluated using permutational multivariate analysis of variance (PERMANOVA) with the Euclidean measure applied. The same approach (HC, PCA, PERMANOVA) was applied to investigate the variability amongst the PLFA profiles (using data in molar percentage); the Bray-Curtis distance metric was applied in the PERMANOVA due to the use of closed proportional variables.

The Mann-Whitney U test, used to compare two groups, was employed to determine if there were significant variations in organic proxies between the two primary sampling areas (Mud Pot are and Spring-Lake Transect). To further reveal the possible influence of physicochemical factors on the sedimentary microbial community distribution and composition, the Spearman Rank-Order Correlation Coefficient ($r_s$) was computed, which is robust to outliers. Specifically, correlation analysis was used to investigate the relationships between PLFA-derived biomass (pmol/g), TOC (mg), and TN (mg). Additionally, along the Spring-Lake Transect, where each organic sample was paired with an assessment of hydrothermal fluid variables using the YSI

probe, correlation analysis was used to explore the relationships between specific PLFA metrics (e.g., total abundance, *trans:cis* ratio, average chain length, proportion of molecular classes) and environmental variables of the hydrothermal fluids (T, pH, DO, TDS, salinity).

## 2.4 RESULTS

### 2.4.1 Physicochemical Characterization of Hydrothermal Fluids

#### *2.4.1.1 Spatial Patterns*

The hydrothermal fluids across the study area were evaluated based on five key environmental attributes (Table 2.2) and a set of 23 dissolved ions (Appendix A). The environmental parameters, presented in Table 2.2, indicate extensive variability across the site, ranging from low to high temperatures (8-87 °C), acidic to alkaline pH (2.9-8.5), and spanned extremely dysoxic to oxic conditions (DO = 0.4-5.2 mg/L; following the terminology of [59]). Fluids had generally low TDS (0.23-2.2 g/L) and salinity (0.17-1.7 ppt) values, consistent with a freshwater environment.

Notable differences were observed between the two sampling sites. The Mud Pot samples were characterized by lower pH values and a considerably higher load of dissolved ions (Figure 2.4, Table 2.2). Specifically, the chemical profile of the Mud Pot fluids was dominated by $SO_4^-$ (>60% of the total ion load) and elevated proportions of Fe, Mn, Al, and $NH_3$ relative to the Spring-Lake Transect samples (Figure 2.4, Appendix A).

Spatial variability was also apparent along the Spring-Lake Transect. As the distance from the subaerial hot spring source increased, there was a general decline in pH and temperature (except where we encountered a subaqueous vent on the lakebed, *L_50m_Sed.*). Salinity, TDS, and dissolved ion composition were relatively constant within the hot spring source pool and the overflow stream but declined in the lake body (Table 2.2). Specifically, the lake water was relatively depleted in Si, Na, K, and Cl relative to the spring/stream, likely reflecting dilution of the mineral-rich spring effluent by glacial meltwater in the lake basin (Figure 2.4 and Appendix A).

Unsupervised Hierarchical Clustering (HC) and Principal Components Analysis (PCA) were performed to further delineate and visualize this variability (Figure 2.4c,d). Both analyses produced clusters that align with the distinct sampling sites visually identified in the field (*i.e.*, Mud Pot region, spring + overflow samples, lake samples), corroborating the distinct nature of

the hydrothermal fluid profiles between the sites. The difference in physiochemistry between the two areas was confirmed as statistically significant by a PERMANOVA analysis ($p = 0.024$). The PCA loadings highlighted TDS, salinity, and levels of dissolved $SO_4^-$ and Fe ions as key variables differentiating the Mud Pot fluids from Spring-Lake Transect fluids.

| ID # | TDS (g/L) | DO (mg/L) | pH | Temp. (°C) | Salinity (ppt) |
|---|---|---|---|---|---|
| **S_Source_Sed.** | 0.29 | 0.5 | 7.7 | 87.0 | 0.19 |
| **S_Mid_Mat_Sed.** | 0.28 | 4.2 | 8.4 | 37.0 | 0.20 |
| **S_Distal_Sed.** | 0.27 | 3.6 | 8.5 | 34.6 | 0.19 |
| **L_3m_Filter*** | 0.29 | 5.2 | 6.7 | 20.6 | 0.22 |
| **L_3m_Sed.*** | 0.28 | 4.7 | 6.6 | 19.2 | 0.21 |
| **L_50m_SurfFilter** | 0.23 | 4.5 | 6.3 | 8.8 | 0.17 |
| **L_50m_Sed.** | 0.23 | 0.4 | 6.1 | 64.8 | 0.17 |
| **L_60m_SurfFilter** | 0.23 | 4.8 | 6.0 | 10.3 | 0.17 |
| **L_60m_DeepFilter*** | 0.23 | 0.5 | 5.8 | 10.7 | 0.17 |
| **L_60m_Sed.*** | 0.23 | 0.4 | 5.8 | 8.8 | 0.17 |
| **MP_Pool_Sed.** | 1.20 | 3.1 | 3.3 | 43.0 | 0.92 |
| **MP_Boil_Sed.** | 2.24 | 1.0 | 2.9 | 72.0 | 1.68 |

*Table 2.2: In-situ physical parameters of hydrothermal fluids.*

*Measurements were collected in tandem with organic sediment and filter samples. TDS = Total Dissolved Solids, DO = Dissolved Oxygen, Temp. = Temperature.*
** For these sample pairs, physicochemical parameters were measured at the time of each sampling (separate measurements for the filter and sediment sample collection, despite being collected form the same vicinity).*

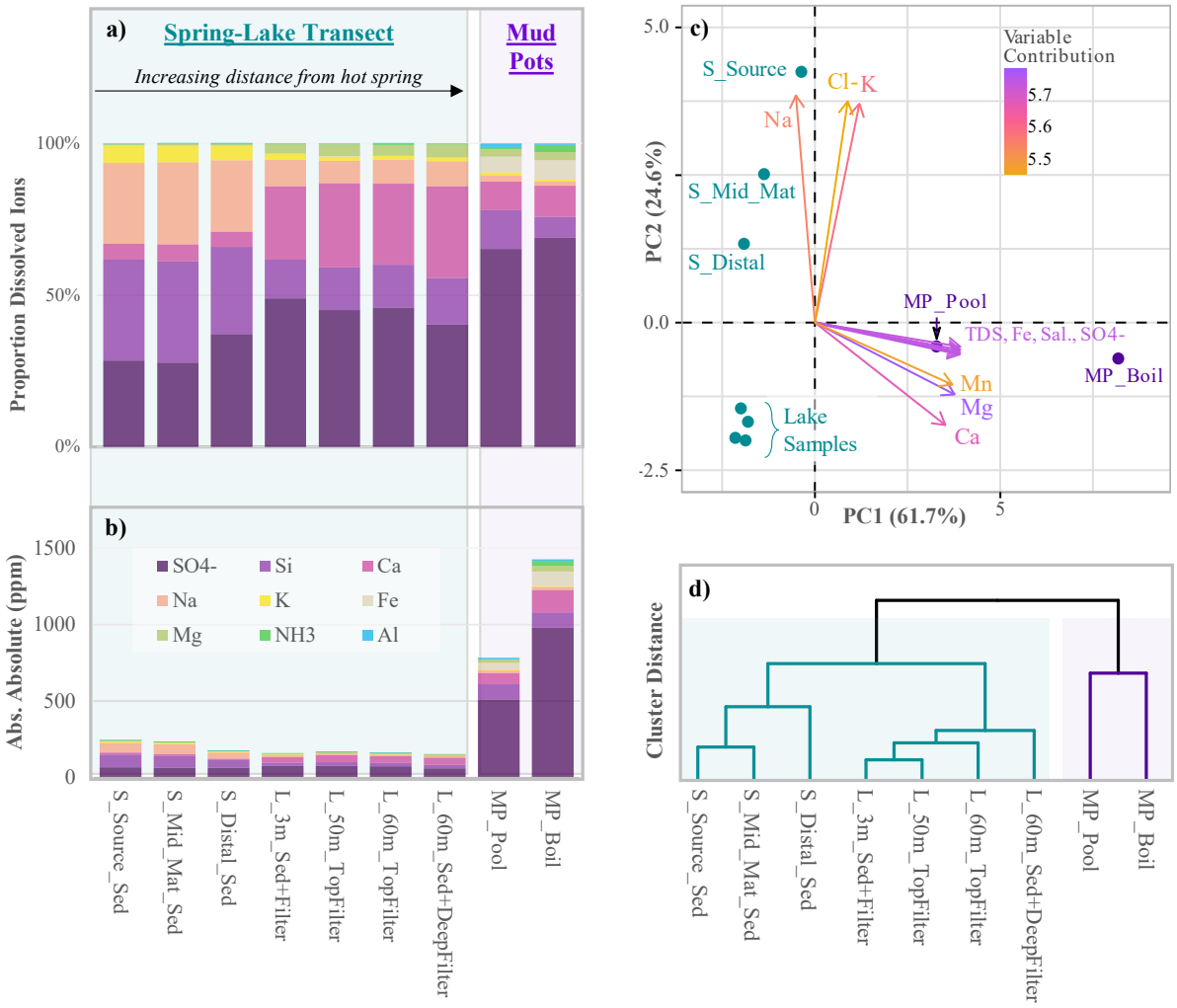


*Figure 2.4: Physicochemical characterization of hydrothermal fluids associated across the sampling area.*

*Panels a and b depict the dissolved ion load of the fluids, presented as relative proportions (a) and absolute abundance (b). For simplicity, only elements accounting for greater than 1% of the distribution are shown. c) PCA of dissolved ion chemistry and physical environmental attributes. The top ten most influential discriminating variables are shown as vectors and coloured according to their relative contribution to the analysis. PC1 accounts for the majority of the physicochemical variance in the system and discriminates the Mud Pot fluids (positive loading) from those sampled along the Spring-Lake Transect (negative loading). d) Unsupervised Hierarchical Clustering dendrogram. The first branching point delineates samples from the two distinct sampling areas identified visually in the field: the Mud Pot region highlighted in purple, and the Spring-Lake Transect highlighted in cyan, validating the physicochemical heterogeneity across the sampling region.*

### *2.4.1.2 Depth Patterns*

The water samples collected across various regions of Lake Gengissig displayed a generally uniform bulk physicochemical profile, as evidenced by their proximity in the PCA coordinate space (Figure 2.4c). A more granular view of environmental parameter variability with depth was

unveiled by YSI ProMeter depth profiles taken at the lake's center (Figure 2.5), with measurements gathered at 0.5 m intervals up to a maximum depth of ~5.5 m (sediment/water interface). It should be noted that variability between the 6 replicate profiles was likely introduced due to the drifting of the boat between the measurements.

A steady decrease in dissolved oxygen was observed with depth, reaching extremely dysoxic conditions near the lakebed. This may reflect oxygen-consuming processes occurring at depth or the influx of oxygen-depleted waters from subaqueous vents. In contrast, temperature, TDS, salinity, and pH remained stable with depth through the top four meters, indicating a well-mixed water column. However, closer to the sediment/water interface, some profiles exhibited dramatic positive excursions in these metrics, deviating from the overall trend. These excursions were not measured consistently across the replicate scans, indicating that the disturbances were highly localized. Given the high temperatures recorded in some profiles (up to 65 °C), we interpret these excursions as evidence of subaqueous springs or vents.

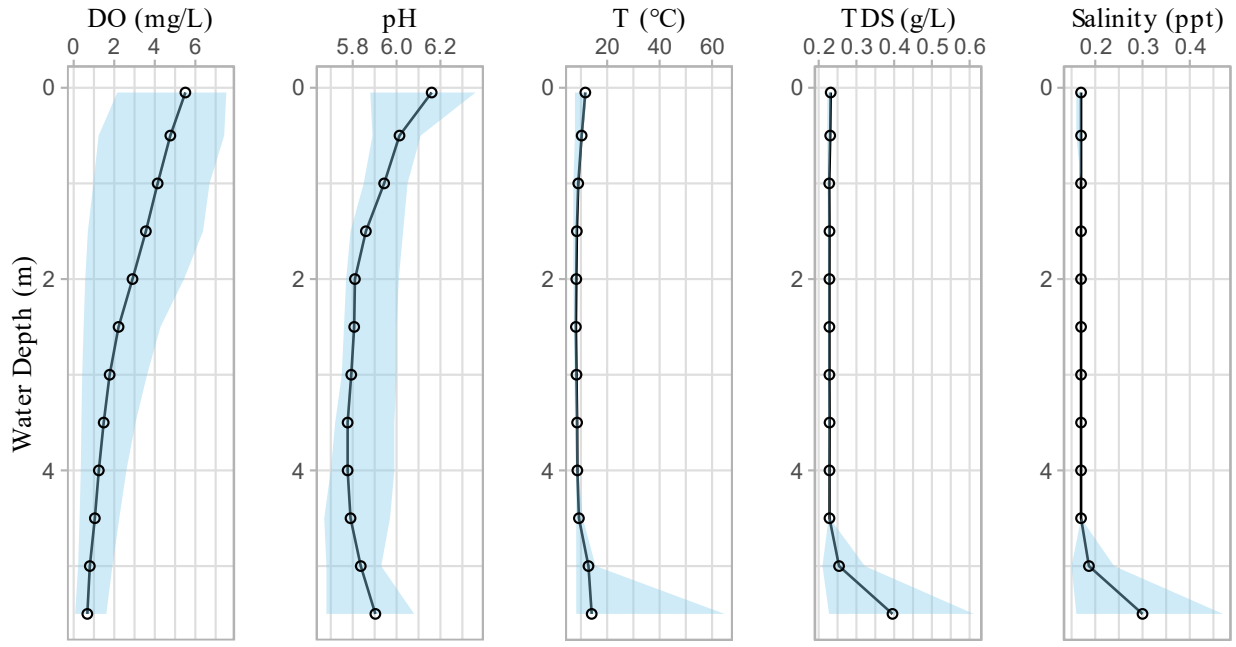


*Figure 2.5: Variability of physical properties with depth in the water column.*

*Data acquired at the approximate center of lake Gengissig. Black line represents the average of 6 replicate scans. Blue polygon displays the minimum and maximum values recorded at each depth interval. Significant positive excursions in temperature (T), total dissolved solids (TDS), and salinity are observed at the sediment/water interface (~5.5 m depth) in some scans and are interpreted as evidence of subaqueous hydrothermal vents.*

### 2.4.2 TOC and TN

Results from the elemental analyzer indicate variable TOC and TN contents in the sediment samples (Table 2.3); filter samples did not retain sufficient material for untargeted organic assessment. The majority of samples had TOC levels below the quantification limit (0.07 %). Of the samples with detectable TOC, values varied widely (0.09-3.14 %), with three samples exhibiting substantially higher TOC levels relative to proximal samples. These included the sample collected adjacent to the visible microbial mat in the stream (*S_Mid_Mat_Sed.*), and the dried upper crusts of both relict mud pots (samples *MP_Recent_Crust_Sed* and *MP_Old_Crust_Sed*).

A comparison between the Spring-Lake Transect sediments and the Mud Pot area sediments revealed consistently higher levels of TOC in the latter; indeed, with the exception of *S_Mid_Mat_Sed,* all samples collected along the Spring-Lake Transect fell below the TOC detection limit. This result illustrates a noteworthy enrichment of organic carbon within the Mud Pot sediments compared to the Spring-Lake Transect.

| | Fig. 2.2 ID # | Sample Text ID | Sample Mass (mg) | TOC (%) (±0.07%) | TN (%) (±0.01%) | C:N |
|---|---|---|---|---|---|---|
| **Spring-Lake Transect** | **1** | **S_Source_Sed.** | 9.212 | n.d | n.d | - |
| | **2** | **S_Mid_Mat_Sed.** | 20.780 | 0.09 | 0.01 | 7.3 |
| | **3** | **S_Distal_Sed.** | 22.080 | n.d | n.d | - |
| | **5** | **L_3m_Sed.** | 21.646 | n.d | n.d | - |
| | **7** | **L_50m_Sed.** | 20.715 | n.d | 0.01 | - |
| | **10** | **L_60m_Sed.** | 20.237 | n.d | 0.01 | - |
| **Mud Pot Area** | **11** | **MP_Pool_Sed.** | 9.645 | 0.35 | 0.04 | 9.3 |
| | **12** | **MP_Boil_Sed.** | 21.025 | n.d | 0.01 | - |
| | **13** | **MP_Recent_Crust_Sed.** | 9.127 | 2.12 | 0.30 | 8.4 |
| | **14** | **MP_Recent_Low_Sed.** | 21.261 | n.d. | 0.02 | - |
| | **15** | **MP_Old_Crust_Sed.** | 9.878 | 3.14 | 0.34 | 10.8 |
| | **16** | **MP_Old_Low_Sed.** | 9.352 | 0.38 | 0.05 | 8.4 |

*Table 2.3: Results of untargeted organic analyses.*

*Tabulation of total organic carbon (TOC), total nitrogen (TN), and the organic carbon to nitrogen molar ratio (C:N). "n.d." = not detected/below level of quantification.*

### 2.4.3 Phospholipid Fatty Acid Analysis

The GC-MS analyses detected PLFA in all samples. Summary metrics for the PLFA analysis are reported in Table 2.4; a complete list of detected compounds is given in Appendix A. However, the sediment sample from the boiling Mud Pot (*MP_Boil_Sed.*) showed siloxane contamination. The siloxane peaks interfered with major PLFA peaks. Consequently, quantification and distribution statistics were not computed for sample *MP_Boil_Sed.* and this sample is excluded from further discussion.

#### *2.4.3.1 Biomass Distribution and Overall Trends*

Analysis of the individual PLFA compounds yielded a total of sixty-seven unique molecular structures (Appendix A). In all samples, chain lengths were predominantly between 12 and 20 carbons long, with an overall average chain length (ACL) of 16.5 (Table 2.4). Longer chain fatty acids, of up to 24 carbons, were detected exclusively in the stream sample with a visible microbial mat, *S_Mid_Mat_Sed,* and in only trace amounts (<1% of the profile). The most abundant PLFA in each sample contained 16 carbon atoms. The on-shore samples, including those from the Mud Pot area and along the spring stream, exhibited a predominance of the saturated $C_{16:0}$. Whereas samples from the lake body, including both lakebed sediment samples and filtered water column samples, were dominated by the monounsaturated *cis*-$C_{16:1\ (n-7)}$.

Overall PLFA abundance, and associated biomass estimates, were heterogeneously distributed across the site. In a manner consistent with the TOC trends, biomass estimates were distinctly different between the two sampling areas, with the Mud Pot samples consistently exhibiting a higher estimated cell abundance (Table 2.4). The Mann-Whitney U test confirmed this difference as statistically significant ($p = 0.03$). Three samples were particularly noteworthy due to their substantially elevated biomass estimates—approximately two orders of magnitude higher than adjacent samples (Table 2.4, Figure 2.6). These included the stream sample near the microbial mat, *S_Mid_Mat_Sed*; and the dried upper crusts of both relict mud pots, *MP_Recent_Crust_Sed*, and *MP_Old_Crust_Sed.* These pronounced biomass concentrations parallel the patchy hotspots observed in the TOC values. Indeed, PLFA-derived biomass strongly correlates with both TOC ($r_s = 0.9$, $p = 9.8 \times 10^{-5}$) and TN content ($r_s = 0.9$, $p = 8.8 \times 10^{-5}$).

#### *2.4.3.2 PLFA Structural Classifications*

A range of chemically distinct PLFA structural families were identified. Monounsaturated, saturated, terminally branched (*iso*- and *anteiso*-), and cyclopropyl-bearing structures were

detected in all samples but showed considerable variability in relative abundance (Figure 2.6). PLFA with mid-chain branches were sparsely present in all *sediment* samples, accounting for ~0.4-8.2% of the profiles but were absent in the filtered lake water column samples (Figure 2.6). This structural family included the detection of one highly branched isoprenoid fatty acid in most sediment samples: 3,7,11,15-tetramethyl hexadecanoic acid (phytanic acid). Phytanic acid eluted at approximately the same time as the unsaturated *cis*-$C_{18:2(n-6)}$, making precise quantification and identification of both compounds difficult in some samples (Appendix A). Polyunsaturated fatty acids, which are typically associated with fungi or photoautotrophic microorganisms (see Section 2.5.1), were found in low abundance (1.6-3.2%) in only three samples, namely *S_Mid_Mat_Sed, MP_Recent_Crust_Sed*, and *MP_Old_Crust_Sed*. Notably, these samples also corresponded to the highest biomass estimates and TOC levels (Table 2.4 and Table 2.3, respectively). Within these, the two Mud Pot crust samples exclusively featured the *cis*-$C_{18:2\ (n-6)}$ polyunsaturated compound, whereas the *S_Mid_Mat_Sed* sample contained multiple polyunsaturated structures, including *cis*-$C_{18:2\ (n-6)}$, $C_{18:2}$, *cis*-$C_{18:3\ (n-6)}$, *cis*-$C_{20:4\ (n-6)}$, *cis*-$C_{20:5\ (n-3)}$ (see Appendix A).

The relative abundance (mol%) of each structural class, serving as a fingerprint of the community composition, varied substantially across the site (Figure 2.6). Unsupervised Hierarchical Clustering analysis of these proportional distributions (the "PLFA profiles") resulted in a dendrogram that clearly separated the PLFA profiles derived from the Mud Pot samples and those obtained from the Spring-Lake Transect (Figure 2.6b), indicating substantial dissimilarities in the biological communities between the two sampling areas. A PERMANOVA test verified these distinctions, indicating that the difference is highly significant ($p = 0.003$). Indeed, the $R^2$ statistic of 0.47 indicated that nearly half of the total variance in the PLFA profiles examined may be ascribed to the differences between the Mud Pot area and the Spring-Lake Transect.

The most striking characteristic of the Spring-Lake Transect PLFA profiles was the consistent predominance of monounsaturated PLFA, which accounted for 39-69% of each PLFA profile. The proportion of these compounds generally increased in the sediments as the distance from the hot spring increased (Figure 2.6). Additionally, all samples of the pelagic lake community (filtered water samples) exhibited substantially elevated levels of unsaturated fatty acids, regardless of distance from the shore (Figure 2.6). In contrast, the Mud Pot sediments displayed approximately equal proportions of monounsaturated, saturated, and terminally branched compounds, with no single class consistently or distinctly dominating over the others.

| | | Fig. 2.2 ID # | Sample Text ID | Chain Length Range | ACL* | Dominant PLFA | Trans: Cis Ratio | Total PLFA (pmol/g or mL) | Total PLFA (µg/g or mL) | Biomass (#cells/g or mL) |
|---|---|---|---|---|---|---|---|---|---|---|
| **Spring-Lake Transect** | **Stream** | **1** | **S_Source_Sed.** | 14 – 20 | 16.9 | $C_{16:0}$ | 1.0 | 1.6E+02 | 0.05 | 3E+06 |
| | | **2** | **S_Mid_Mat_Sed.** | 12 – 24 | 16.7 | $C_{16:0}$ | 0.1 | 1.0E+05 | 29.13 | 2E+09 |
| | | **3** | **S_Distal_Sed.** | 12 – 20 | 16.4 | $C_{16:0}$ | 2.0 | 2.5E+03 | 0.68 | 5E+07 |
| | **Lake Sed.** | **5** | **L_3m_Sed.** | 12 – 20 | 16.4 | $C_{16:0}$ | 1.7 | 1.1E+03 | 0.31 | 2E+07 |
| | | **7** | **L_50m_Sed.** | 14 – 20 | 16.6 | *cis*-$C_{16:1\ (n-7)}$ | 1.1 | 8.6E+02 | 0.24 | 2E+07 |
| | | **10** | **L_60m_Sed.** | 12 – 20 | 16.5 | *cis*-$C_{16:1\ (n-7)}$ | 3.3 | 3.9E+03 | 1.08 | 8E+07 |
| | **Lake Column** | **4** | **L_3m_Filter** | 14 – 18 | 16.1 | *cis*-$C_{16:1\ (n-7)}$ | 5.5 | 1.2E+02 | 0.03 | 2E+06 |
| | | **6** | **L_50m_TopFilter** | 14 – 18 | 16.2 | *cis*-$C_{16:1\ (n-7)}$ | 7.5 | 1.6E+02 | 0.04 | 3E+06 |
| | | **8** | **L_60m_TopFilter** | 14 – 18 | 16.0 | *cis*-$C_{16:1\ (n-7)}$ | 1.9 | 1.1E+02 | 0.03 | 2E+06 |
| | | **9** | **L_60m_DeepFilter** | 14 – 18 | 16.1 | *cis*-$C_{16:1\ (n-7)}$ | 3.6 | 2.1E+02 | 0.06 | 4E+06 |
| **Mud Pot Area** | | **11** | **MP_Pool_Sed.** | 12 – 20 | 16.8 | $C_{16:0}$ | 0.9 | 8.6E+03 | 2.42 | 2E+08 |
| | | **13** | **MP_Recent_Crust_Sed.** | 12 – 20 | 16.6 | $C_{16:0}$ | 0.7 | 5.0E+05 | 138.29 | 1E+10 |
| | | **14** | **MP_Recent_Low_Sed.** | 12 – 20 | 16.6 | $C_{16:0}$ | 1.6 | 4.2E+03 | 1.18 | 8E+07 |
| | | **15** | **MP_Old_Crust_Sed.** | 12 – 20 | 16.6 | $C_{16:0}$ | 1.1 | 6.3E+05 | 175.75 | 1E+10 |
| | | **16** | **MP_Old_Low_Sed.** | 12 – 20 | 16.6 | $C_{16:0}$ | 1.2 | 3.7E+04 | 10.39 | 7E+08 |

*Table 2.4: Summary metrics of PLFA biomarker distributions.*

*Total PLFA and biomass estimates are reported per gram of sediment (dry weight) extracted, or, in the case of the water column filters, per mL of water filtered. The Trans:Cis Ratio for unsaturated fatty acids is an environmental stress marker, where values substantially greater than 0.1 indicate metabolic stress of the biological community.*
**ACL = average chain length of the detected PLFA. ACL = $\sum(i \cdot X_i + \ldots + n \cdot X_n) / \sum(X_i + \ldots + X_n)$, where i is the number of carbons of the smallest PLFA chain, n is the number of carbons of the longest PLFA chain, and X is the concentration in pmole/g.*

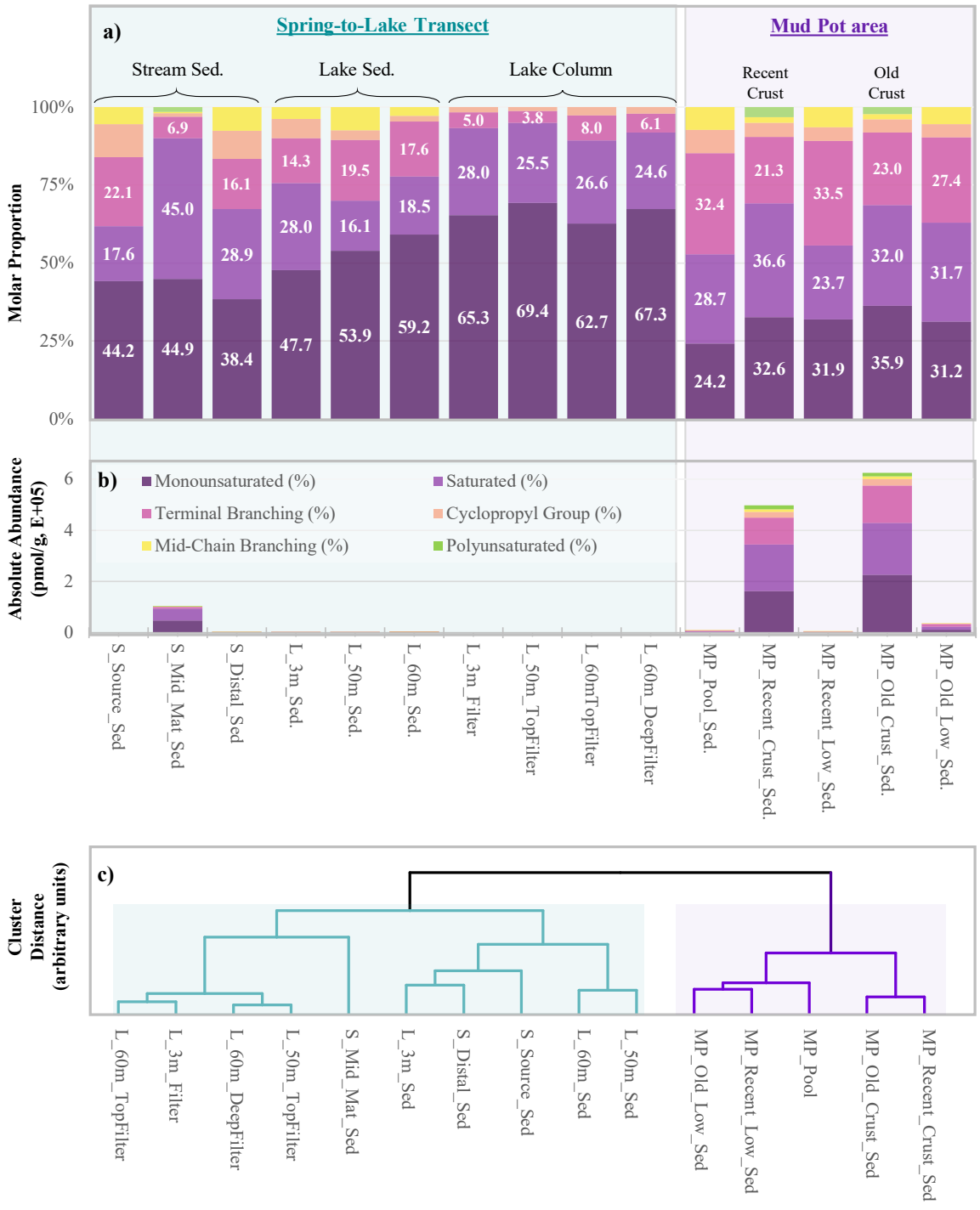


*Figure 2.6: Summary of whole biomarker PLFA profiles.*

*Panels a and b depict the distribution of PLFA molecular classes, presented as (a) relative molar proportions (mol%), and (b) as absolute abundance (pmol/g). Note the distinct profile patterns between the Spring-Lake Transect and the Mud Pot Area, as well as the substantially elevated PLFA abundances in three discrete samples. (c) Unsupervised hierarchical clustering dendrogram of proportional PLFA profiles. The first branching position delineates the PLFA patterns in the Spring-Lake Transect from the Mud Pot region, indicating a first-order difference in community composition between these two sites.*

#### *2.4.3.3 PLFA Variations with Environmental Conditions*

To reveal the possible influences of environmental factors on the microbial community composition, a correlation analysis was made between the PLFA parameters and the physicochemical parameters of the local hydrothermal fluids along the Spring-Lake Transect (namely, T, pH, DO, TDS, and salinity) (Figure 2.7). We focused on the Spring-Lake Transect because it provides a continuous gradient of hydrothermal conditions (Table 2.2) and an interconnected ecosystem, thereby offering a window into how the community responds to the changing environmental variables.

We found that the total PLFA abundance showed no significant correlation with any environmental variables. However, statistically significant relationships were observed with the specific PLFA characteristics. Specifically, temperature was significantly correlated with the average chain length (ACL) and inversely correlated with the *trans:cis* stress ratio and the proportion of monounsaturated fatty acids; pH was also inversely correlated with the proportion of monounsaturated fatty acids. Moreover, both dissolved oxygen and salinity were correlated with the proportion of saturated fatty acids (Figure 2.7). Among the various correlations, those involving temperature were often the most significant.

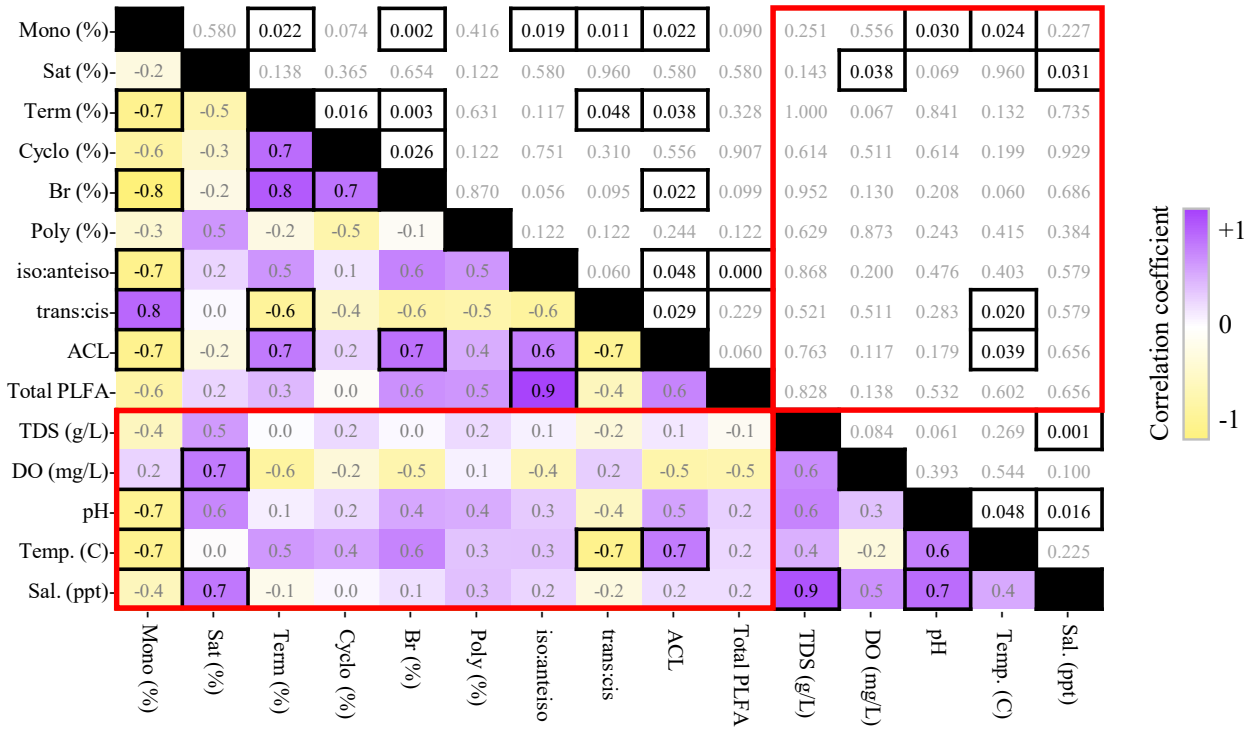


*Figure 2.7: Correlation matrix of PLFA metrics and environmental variables.*

*The matrix is divided diagonally: the lower triangle shows Spearman's Correlation Coefficient ($r_s$), with color intensities reflecting the strength and direction of the correlation; the upper triangle presents the associated p-values. Correlations deemed significant at the $p < 0.05$ level are highlighted with a thicker border and accentuated text colour. Red boxes emphasize the immediate connections between specific PLFA metrics and environmental factors.*
*Abbreviations: Mono = proportion of monounsaturated fatty acids, Sat = proportion of saturated fatty acids, Term = proportion of terminally-branched fatty acids, Cyclo = proportion of cyclopropane fatty acids, BR = proportion of mid-chain branched fatty acids, Poly = proportion of polyunsaturated fatty acids, TDS = Total Dissolved Solids, DO = Dissolved Oxygen, Temp. = Temperature, Sal. = salinity.*

## 2.5 DISCUSSION

### 2.5.1 Source of Organic Matter in Kverkfjöll Glaciovolcanic Sediments

A key motivation for this study was to determine the source of organic biomarkers in the Kverkfjöll system. Both C:N ratios and PLFA profiles have been widely used to identify the sources of organic matter in complex environmental samples [54,60,61].

Herein, the C:N ratios range from 7.3 to 10.8. These ratios align with the known ranges for sedimentary microbes, specifically bacteria (C:N = 3.5-10.4) and fungi (C:N = 5-15, with some instances observed up to 203). This overlap indicates that the C:N ratio alone is not sufficient to distinguish between these microbial sources in sedimentary environments [61–63]. It is

noteworthy that the system does not exhibit C:N ratios above 20, a range often linked with vascular plants due to components like cellulose and lignin [64,65]. This absence aligns with the lack of vegetation observed at the site.

In several samples, the C:N ratios could not be computed because the carbon content was below the level of quantification (0.07%), highlighting a pervasive scarcity of organic carbon. This observation is consistent with the elevated *trans:cis* ratios found throughout the system (average of 2.2; Table 2.4). *Trans:cis* ratios significantly greater than 0.1 are associated with environmental stressors such as high temperatures [66], exposure to toxic organic compounds [66,67], nutrient deprivation [57], osmotic stress [66], low pH [68], and toxic levels of heavy metals (e.g., Cu, Zn, Ni, Pb) [69]. Considering that both organic and heavy metal contents (Appendix A) were consistently low amongst the samples, and that the *trans:cis* stress markers were elevated regardless of variable pH, salinity levels, and temperatures, nutrient deprivation appears to be the chief stress vector. In essence, the low organic carbon content and the heightened *trans:cis* ratios are physiological responses signaling a common environmental stressor—nutrient scarcity.

The biomarker PLFA profiles further reinforce the prevalence of microbial biomass in the system. The bulk of detected PLFAs fall within the 14-20 carbon range, typical of prokaryotes [54,60], whereas eukaryotes commonly generate longer carbon chains [70]. Only one sample, collected adjacent to the microbial mat in the thermal stream (*S_Mid_Mat_Sed.*), contained a low proportion (<1%) of chains exceeding 20 carbons, which may indicate a minor contribution from microeukaryotes or unique bacteria capable of producing long chain fatty acids (e.g., [71–73]).

Specifically, the molecular functional groups extracted from the samples are consistent with a bacterially-dominated community (it is worth noting that archaeal membrane lipids are not efficiently extracted using the PLFA method, and are not considered in this study). Indeed, over half of the quantifiable PLFA extracted from each sample include molecular functional groups typically associated with bacteria, including mono-unsaturations, cyclopropyl groups, *iso*- or *anteiso*-methyl branches, and saturated fatty acids with odd-chain-length (e.g., C15:0, C17:0) [54,60,74,75]. In particular, monounsaturated fatty acids are primarily synthesized by Gram-negative bacteria, while terminally branched fatty acids are associated with Gram-positive bacteria (typically heterotrophic, often sulfate-reducing) [54,60,76]. While such assignments

should be considered as approximate in complex environmental samples [54,77], they suggest a shift in the dominant community membership of the Mud Pot area and Spring-Lake Transect (Figure 2.6). The elevated levels of terminally-branched PLFA in the Mud Pots suggest proportionally more Gram-positive sulfate-reducing bacteria, which is consistent with the high concentrations of dissolved $SO_4^-$ in those fluids. In contrast, the overflow stream and lake body appear to host a greater relative proportion of Gram-negative bacteria.

This latter finding aligns with the reports of Cousins et al. [39] and Marteinsson et al. [38], both of whom noted a predominance of Gram-negative bacteria in this area using 16S RNA techniques. Specifically, Cousins et al. (2018) reported a dominance of *Aquificae* species and *Proteobacteria* species in a hot spring and its overflow stream on the shore of Lake Gengissig. Similarly, Marteinsson et al. (2013) found the lake's water column predominantly composed of a single taxon affiliated with genus *Xenophilus* (phylum*: Pseudomonadota*). Remarkably, this microbial consistency has persisted despite a phreatic eruption that drastically reshaped the area and led to the near-total drainage of Lake Gengissig in the years between these prior studies and our investigation [51]. The persistence of a prominent Gram-negative bacterial community might suggest that these microbes possess robust adaptive capabilities, allowing them to withstand environmental upheavals and change. Similar conclusions were drawn for the predominantly Gram-negative community inhabiting the hostile volcanic system at Poás Crater and Laguna Caliente, Costa Rica, which also experiences periodic phreatic eruptions [78].

The polyunsaturated fatty acids (PUFAs) identified here are typically associated with plants, mammals, fungi, or photoautotrophic microorganisms, such as bacteria, cyanobacteria, algae, or diatoms [79–83]. The $C_{20}$ PUFAs exclusively identified in *S_Mid_Mat_Sed*. are often considered specific markers for phototrophic organisms [79]. An origin associated with plants and mammals is considered improbable given the low C:N ratios, the lack of visual evidence of such complex sources, as well as the geographical isolation, high altitude, and panoply of extreme conditions that would limit these life modes. Notably, PUFAs were solely detected in samples where elevated biomass was also observed, which aligns with the understanding that phototrophic organisms typically generate greater biomass than chemotrophs, providing additional evidence for the presence of phototrophs in these niches [84]. However, the scarcity of the compounds illustrates that phototrophy is not the dominant form of primary production in the ecosystem.

Lastly, isoprenoids in the fatty acid fraction, only represented by phytanic acid, are assigned an archaeal source. Previous environmental studies have interpreted sedimentary phytanic acid as either a derivative of phytol (originally from chlorophyll *a*) [85], or a derivative of archaeol (note, while its recognized that archaeol is found in most archaea, previous environmental studies have specifically linked sedimentary phytanic acid to either methanotrophic archaea participating in the anaerobic oxidation of methane [86,87] or from halophilic archaea [88]). Given the lack of long-chain PUFAs associated with phototrophic organisms and the lack of phototrophic taxa reported by previous investigations of the site using 16S RNA gene analysis [38,39], a phototrophic source seems unlikely. However, the comprehensive genetics report from Cousins et al. (2018) [39] did not report halophilic archaea and ruled out substantial methanogenesis, suggesting that another archaeal source may be responsible or that the community has changed in the intervening years of our analyses. Interestingly, the PLFA preparation methods employed here do not efficiently derivatize archaeal lipids, making their presence in the data unexpected. However, a recent study suggests that heterotrophic bacteria in extreme environments can recycle archaeal isoprenoid cell wall constituents, including archaeol, into their esterified lipids, which may provide an explanation for their presence in the ester-linked fatty acid fraction [89].

Together, the combination of C:N ratios and PLFA profiles provide compelling evidence that microorganisms are the primary source of organic matter, including various bacteria, potential fungi, and archaea. Importantly, our data reveal an absence of complex plant or animal inputs, as well as a limited abundance of phototrophic lipid biosignatures. These factors strengthen Kverkfjöll's relevance as a Mars analogue given that the surface conditions on Mars likely restricted the evolution of large, multicellular organisms or the innovation of phototrophic activity (see section 2.5.4) [90–93]. The isolated hydrothermal area we studied is thus an ideal site for understanding the distribution of Mars-relevant microbes in Mars-relevant niches. Considering that the original distribution of viable organisms is expected to regulate, in part, the eventual distribution of recalcitrant and preservable biosignatures in Mars' relict environments [94], the following sections of this paper concentrate on two key areas of focus. Firstly, we discuss the patterns in biomass distribution (section 2.5.2), and secondly, we discuss molecular structural patterns within the lipid profiles (section 2.5.3). These aspects are critical for understanding how life might have adapted and left traces in this environment, refining our

understanding of potential habitability and laying the groundwork to understand biosignature preservation potential.

### 2.5.2 Overall Patterns in Biomass

Despite the extreme nature of this site, detectable levels of microbial biomass were found in all samples, revealing potential trends linked to temperature gradients, nutrient availability, and autotrophic activity. The lowest biomass estimates corresponded to the samples filtered from the water column, with cell abundances approximately an order of magnitude less than those observed in the lakebed sediments (Table 2.4). The sparse biomass estimated in the water column raises the possibility that migration or detachment of cells from the sediment could be a significant contributor to the pelagic community, as has been suggested for other subglacial Icelandic lakes [95]. This hypothesis is supported by three key observations: First, the PLFA profiles of the water column samples are broadly similar to those of the lake sediment samples, indicating potential shared source communities (Figure 2.6). Second, notably elevated *trans:cis* ratios in the water column samples (average 4.6) signal heightened stress or starvation, suggesting that the cells might have been displaced from their optimal growth environment. Third, the discovery of possible hydrothermal influx on the lakebed provides a plausible source for convection driving the detachment of cells from the benthos and their suspension into the water column. The lake water's notable murkiness, indicative of a high suspended sediment load and active mixing, further corroborates this scenario. Thus, the water column seemingly plays a minimal role in overall ecosystem productivity. This steers our attention towards the sedimentary niches for a more comprehensive understanding of microbial distribution patterns and potential biosignature concentration mechanisms in glaciovolcanic systems.

Amongst the sediment samples, the lowest estimated biomass was observed in the hottest sediments. The subaerial hot spring source (*S_Source_Sed.*) measured 87 °C at the time of sampling and exhibited the lowest estimated biomass overall ($3x10^6$ cells/g). This was followed by the 70 °C lakebed sediment sample collected ~50 meters offshore that apparently struck a subaqueous hot spring (*L_50m_Sed.*; $2x10^7$ cells/g). This implies that high temperatures exert a major control on microbial biomass, corroborating previous findings of biomass and biodiversity dampening at extreme temperatures (high and low) [96–98].

On the other end of the spectrum, three samples exhibited substantially elevated PLFA totals and associated biomass estimates (Figure 2.6b, Table 2.4, respectively). These biomass hotspots

include the sample from the mid-point of the hot spring overflow stream where a green microbial mat was found (*S_Mid_Mat_Sed.*), and the two desiccated upper crusts collected from the inactive Mud Pots (samples *MP_Recent_Crust_Sed.* and *MP_Old_Crust_Sed.*). Notably, these same samples also represent local maxima of TOC levels. In an environment marked by its low organic content, and with an absence of apparent exogenous organic carbon sources, such pronounced and localized enrichments of TOC are strong indicators for *in situ* organic carbon production by autotrophs. The co-occurrence of elevated biomass reflects the ecological advantage autotrophs possess in low-carbon systems. Autotrophic organisms can synthesize organic matter from inorganic sources, bypassing the need to seek out scarce organic molecules for sustenance—a necessity for heterotrophs. This self-sufficiency enables autotrophs to outcompete heterotrophs for inorganic nutrients in carbon-poor settings and permits enhanced productivity (biomass generation) [99–101].

In support of this hypothesis, we find that the three samples with elevated biomass and TOC also lie within specific physicochemical niches uniquely conducive to autotrophic metabolisms. For instance, in the case of the *S_Mid_Mat_Sed.* sample, where we observed a macroscopic green microbial mat and phototrophic PLFA biomarkers, the autotrophic mechanism is apparent. These photoautotrophic indicators occur in a portion of the stream characterized by moderately alkaline pH (~8.4) and warm temperatures (30-44 °C), which are consistent with the optimal growth conditions for several geothermal phototrophic bacteria [102–104]. These observations collectively indicate that this section of the overflow stream constitutes an ecological niche conducive for photoautotrophic processes.

Conversely, the autotrophic potential in the Mud Pot area appears more multifaceted. Distinguished from the Spring-Lake Transect primarily by elevated levels of TDS, salinity, and relative abundance of redox-sensitive elements such as $SO_4^-$, Fe, and Mn, the Mud Pot area provides a notably more concentrated geochemical composition than the more dilute Spring-Lake Transect (Figure 2.4). This profile indicates a heightened capacity for chemical disequilibria within the Mud pots with increased availability of suitable electron donors and acceptors. Such conditions would provide more accentuated differences in potential energy that could be used to drive chemoautotrophic reactions. Importantly, the PLFA-derived biomass (and TOC) hotspots are explicitly linked with the subaerial crust samples (*MP_Recent_Crust_Sed.* and *MP_Old_Crust_Sed*), suggesting a specific advantage conferred by subaerial exposure. This

might imply that the predominant chemoautotrophic mechanisms are oxygen dependent. An alternate interpretation could be that the Mud Pot's concentrated geochemical signature arises from evapoconcentration processes. This could be the result of recurrent wet-dry cycles or continuous evaporation, which would lead to the accumulation of organic and inorganic solutes in the crust, thus amplifying local microbial productivity there. Indeed, fluctuating environments in the form of wet-dry cycles at elevated temperature ranges have long been considered to be possible sources of free energy that could drive life-sustaining reactions [105].

Overall, the interpretation that the Mud Pots, and specifically the subaerial crusts, are amenable to chemoautotrophy aligns with the 16S rRNA gene profiles reported by Cousins et al. (2018) [39]. These authors identified bacterial taxa dominated by the chemolithoautotrophic *hydrogenobaculum* (a thermoacidophilic, aerobic, hydrogen-oxidizing bacterium requiring elemental sulfur for growth) and putative autotrophic sulfur-oxidizing groups in Kverkfjoll's acidic, sulfate-dominated waters. It is also important to note that although the Mud Pots lacked PLFAs diagnostic of phototrophic organisms, the hydrocarbon biomarkers collected from these samples contain cyanobacterial indicators (see Chapter 3). This indicates a latent or historical phototrophic influence in the Mud Pots, but that these processes were not dominant at the time of sampling. Such findings are consistent with reports of "patchy" distributions of phototrophic metabolisms in environments with pH <5 and <56 °C [102], demonstrating that phototrophic communities might sporadically establish in the Mud Pot area, where the hydrothermal fluids were measured to range from pH 2.87 to 3.30 and ~42 to 72 °C.

Lastly, we note that a shared characteristic among these three biomass hotspots is their positioning in moderate thermal zones. They are situated away from the high temperatures proximal to the active springs and the cold temperatures proximal to the glacier or meltwater lake, both of which were associated with lower biomass. These trends are consistent with prior research demonstrating an overall bell-shaped relationship between temperature and microbial diversity, with diversity peaking at moderate temperatures and diminishing at either extreme [96,106]. Nonetheless, since not all intermediary locations with moderate temperatures have high biomass, this thermal control is likely not a primary driver of biomass in the system. In brief, considering that PLFA-derived biomass closely correlates with TOC and is elevated in regions consistent with autotrophic activity, coupled with the absence of significant exogenous organic

carbon sources to sustain heterotrophy, we contend that autotrophy is the key driver of the high biomass concentrations observed in this system.

### 2.5.3 Why do the PLFA Biomarker Profiles Vary Across the Study Area?

We hypothesize that local environmental heterogeneity is the main factor responsible for the observed changes in microbial community composition across the study area. Environmental heterogeneity is recognized as one of the strongest, and universal, determinants of species richness and biodiversity [107–109]. Greater spatial heterogeneity contributes more varied niche spaces, accommodating a broader array of taxa with distinct ecological requirements [107,108]. This not only fosters species coexistence by diversifying available resources and reducing inter-species competition, but also enhances the potential for species diversification due to isolation or environmental adaptation [107–109]. Our data reveal pronounced physicochemical heterogeneities at varying scales (Figure 2.4), which parallel the primary trends in the PLFA profiles (Figure 2.6). Thus, these associations, discussed below, highlight fundamental links between environmental heterogeneity and microbial community structure in the studied system.

In particular, principal component analysis and hierarchical clustering both revealed that the strongest physicochemical differences were observed between the fluids of the Mud Pot area and those of the Spring-Lake Transect (Figure 2.4), demarcating these as distinct habitats. This aligned with the major pattern of the bulk PLFA profiles, which were also principally clustered according to the sampling area (Figure 2.6c); indeed, the distinction between the bulk PLFA profiles of the two sites accounted for nearly half of the total PLFA variability observed in this study as revealed by the PERMANOVA test (see section 2.4.3.1). Variations in bulk PLFA profiles can signal either population-level shifts in the dominant taxa, or biophysical adaptations of individual cells to their environment (or both). Considering that the PLFA-derived biomass estimates and TOC levels were also found to vary significantly between the two areas, it is likely that the variation in the PLFA profiles reflect the same underlying process. We attributed the biomass and TOC enrichments to physicochemical conditions particularly conducive to chemoautotrophy in the Mud Pots (section 2.5.2), and it is plausible that the distinct PLFA profiles reflect a population-level shift in the dominant species that inhabit each site. Such shifts would arise from the specific metabolic capacities that each environment promotes, leading to the divergence of species uniquely adapted to those conditions.

On a more local scale, sharp physicochemical gradients are also observed along the Spring-Lake Transect, with sampling points ranging from high to low temperatures, alkaline to acidic pHs, and oxic to extremely dysoxic conditions. As such, this transect offers a useful lens for directly evaluating how varying physicochemical parameters influence a cohesive microbial community.

We find that the PLFA-derived biomass does not significantly correlate with the environmental heterogeneities along the Transect, but that specific PLFA biomarker metrics do (Figure 2.7). This indicates that although environmental extremes might not dictate microbial survival or overall productivity in the Spring-Lake Transect, they play a pivotal role in shaping the community's composition, functionality, and physiological status. The strongest and most significant correlation is the inverse relationship between the *trans:cis* ratio and temperature ($r_s$ = -0.7, p = 0.020), highlighting an increase in the starvation stress index in colder conditions This aligns with known microbial responses, where lower temperatures are generally associated with reduced enzymatic activity, slowed metabolic processes, and hindered substrate uptake [110,111]. Additionally, temperature also shows a significant inverse correlation with the proportion of monounsaturated fatty acids ("Mono (%)", in Figure 2.7) and a significant positive correlation with the average chain length (ACL). Both of these trends are consistent with well-established biophysical adaptations—known as homeoviscous adaptations—that actively lower the melting point of the fatty acid, thus enabling the cell membrane to remain in a viscous/fluid state under low temperatures [55,111–115]. Specifically, shorter chain lengths have lower melting points than their longer counterparts, and unsaturations introduce 'kinks' into the hydrocarbon chains, which prevent tight packing of fatty acids in the lipid bilayer, thus weakening the van der Waals interactions among fatty acids and enhancing fluidity [55,116]. In summary, this evidence is consistent with an active microbial community within the Spring-Lake Transect that is capable of dynamically adapting its physiological properties to cope with varying temperatures. Our current data do not allow us to definitively determine whether these observed changes represent a physiological response within individual taxa or a broader ecological shift affecting multiple members of the community.

In addition, it is important to note that variations in monounsaturated fatty acid abundance may also reflect changes in the predominant microbial community membership, such as fluctuations in the Gram-negative bacteria population. However, given that other biophysical parameters of the cell (ACL, *trans:cis* ratio) are significantly correlated with temperature, and the fact that the

incorporation of monounsaturated fatty acids is the most prevalent bacterial cold-stress modification [114], we contend that the trends observed in monounsaturated fatty acid abundance mainly indicate homeoviscous adaptation. Distinguishing the effects of homeoviscous adaptations from those of community membership changes would require further analyses, such as DNA sequencing, which will be the focus of future research. Regardless of the mechanism, the strong links between temperature and the composition of the membrane lipids underscores the significant regulatory role of temperature on the structure of the indigenous community.

Other correlations along the Transect are more equivocal. There is a significant relationship between pH and the proportion of monounsaturated fatty acids ($r_s$ = -0.7, p = 0.030). Several studies have demonstrated that bacteria may also modify the biophysical structure of their membranes in response to pH, however the specific modifications do not follow a consistent pattern like temperature-induced responses [114]. While some bacteria synthesize higher proportions of monounsaturated fatty acids in response to acid stress [117], a trend that aligns with our observations, others decrease the amount of unsaturations [118,119]. We also observed a significant positive correlation between pH and temperature (p = 0.048), suggesting that the influence of pH on monounsaturated fatty acids might merely reflect a cross-correlation with temperature fluctuations. As a result, the extent to which pH independently modulates the microbial community structure remains unclear.

Lastly, both salinity and dissolved oxygen are positively correlated with the proportion of saturated fatty acids. Previous research has not identified changes in saturated fatty acid abundance as an adaptive strategy to salinity or oxygen availability. Thus, shifts in the proportion of saturated fatty acids more likely reflect changes in the dominant microbial community membership, rather than adaptive strategies. This interpretation is supported by recent studies indicating that salinity and oxygen availability exert potent selection pressures, triggering shifts in bacterial community composition based on the salt- and oxygen-tolerant traits among species [120,121]. Such findings imply that the environmental heterogeneity at Kverkfjöll introduces selective pressures, fostering niche differentiation and microbial diversity within the system.

Taken together, our findings underscore the profound influence of environmental heterogeneity on microbial community structure in an active glaciovolcanic system. Several aspects of the biomarker PLFA distributions appear to reflect population-level changes of community

membership associated with resource availability or stressors, whilst others reflect biophysical adaptations on the scale of individual cells (*i.e.*, homeoviscous adaptations). The observed homeoviscous adaptations specifically highlight a high level of metabolic and physiological activity within the community considering that biophysical adjustments to fatty acid composition require energy and cellular machinery.

### 2.5.4 Relevance for the search for Life on Mars

Life on Earth has proved to be extraordinarily adaptive through natural selection [122–124]. Despite recurrent environmental changes and numerous global extinction events, life has persisted to occupy every suitable habitat on our planet [122]. If life emerged on Mars, it could likewise be expected to exhibit similar adaptability, adjusting to the global changes that occurred as the planet cooled and desiccated [92,125,126].

In this context, Martian refugia—isolated niches where conditions remain locally habitable—become prime exploration targets. As some of the last remaining locations where organisms could survive, refugia not only act as a natural winnowing mechanism to narrow down the search space for biosignatures, but also hold the potential of retaining the most recent (and possibly intact) biosignatures. Glaciovolcanic environments have been proposed as potential Martian refugia due to their unique ability to create warm and wet niches in an otherwise freezing and desiccating landscape, as well as their persistence through much of Mars' history [1]. Our findings help substantiate this premise by demonstrating that a Mars-like glaciovolcanic site on Earth not only meets the basic requirements for life, but also creates significant environmental heterogeneity at various scales. We find that the biological community profiles, as inferred from PLFA, vary significantly across this environmental mosaic, indicating active and dynamic adaptive responses to localized conditions. These trends illustrate how the environmental dynamicity inherent in these polyextreme settings can foster opportunities for isolation and divergent adaptation, promoting the development of varied biological communities. Consequently, targeting regions recently influenced by glaciovolcanism on Mars offers opportunities to study not just the potential for life, but also the adaptive and evolutionary mechanisms life might employ in response to the diverse and changing conditions of extraterrestrial settings. While active Martian glaciovolcanism is not evident today, there are indications of volcanic heating-induced melting occurring within the last 100-200 million years [3,5,6]. Given that unambiguous biosignatures have been successfully retrieved from much older

environments on Earth (e.g., [127–130]), these Martian sites hold significant potential as targets for uncovering past life signatures.

To enhance the efficacy of future astrobiological missions to these regions, it is imperative to target locations where biosignatures are most likely concentrated [131]. The conclusions we draw in this paper are applicable because the distribution of recalcitrant and preservable biosignatures (e.g., refractory biomolecules, isotopic signatures) in paleohabitats will depend, in part, on the original distribution of biomass [50,94]. Thus, the PLFA-derived biomass estimates presented here can be considered a proxy to identify locations with a higher likelihood of preserving other types of biosignatures based on a higher concentration of biological activity and initial abundance of viable cells [98]. We find that biomass estimates are highest in localized areas that are likely associated with autotrophy but are reduced in extremely high-temperature regions. Notably, biomass estimates are exceptionally high in the Mud Pot area, which is distinguished from the Spring-Lake Transect by its significantly more concentrated geochemical profile. This underscores the potential role of chemical density and disequilibria as pivotal determinants of habitability and autotrophy in such low-energy contexts. This is in alignment with the "follow the energy" perspective on habitability [132], which emphasizes that electron acceptors and donors must be present in large enough quantities, and the energy released needs to be sufficient for life to thrive. In essence, areas of pronounced chemical disequilibria—where differences in potential energy can fuel life-sustaining reactions—are generally more favourable for colonization and can promote (chemo)autotrophy. These factors facilitate the establishment and proliferation of biological communities, and support biomarker production. However, we also found that biomass hotspots were highly localized. In the case of the inactive mud pots, biomass declined ten-fold over centimeter-scales (upper crust versus underlying mud deposit). This heterogenous distribution of biomass is similar to that observed elsewhere in carbon-limited basaltic settings and confirms the needs to collect a large sample suite to avoid overlooking such concentrations [50].

Future missions should therefore prioritize zones with marked geochemical gradients and screen for diverse redox-sensitive species. Signs of past hydraulic activities that favour the accumulation of organic/inorganic substrates, like evapoconcentration mechanisms, could also help direct rovers towards energy-rich locations. Rapin et al. (2023) [133] recently identified erosion-resistant polygonal ridges in Gale crater, interpreted as signs of recurrent wet-dry cycles.

These findings offer a practical model and blueprint for seeking analogous structures in future exploration. Additionally, our findings show a robust linear relationship between biomass, TOC, and TN, indicating that C and N concentrations could serve as reliable indicators for areas of high microbial activity and potential biosignature preservation.

Laser-induced breakdown spectroscopy (LIBS) has the capacity to detect both of these elements and has heritage as a rapid and remote survey instrument on Mars. However, there are difficulties associated with distinguishing sequestered C form atmospheric C (derived from $CO_2$) in the LIBS plasma on Mars and N has intrinsically weak emission lines that have not yet been detected by planetary LIBS instruments [134,135]. A worthy avenue of research, therefore, would be to refine and enhance the sensitivity of LIBS for detecting subtle variations in C and N concentrations on Mars; Chapter 5 presents a baseline study designed to optimize the detection of N with LIBS. Lastly, biomass was substantially dampened in very high-temperature areas, indicating that future missions should prioritize sampling sites that are situated away from vent sources.

#### *2.5.4.1 Broader Significance*

The value of Kverkfjöll as a Mars analogue extends beyond its glaciovolcanic characteristics. Commonly accepted Martian environmental models suggest a history of extended dry and cold periods, punctuated by intervals of warmer, wetter conditions (e.g., [7,136]). Based on our current understanding, life could have gained a foothold under early environmental conditions on Mars [92,93], however, the episodic availability of liquid water and prolonged exposure to harsh conditions on the surface would have posed significant challenges for the development of photosynthesis or the evolution of complex, differentiated organisms [90,91,131]. Consequently, Martian life forms, if they ever existed, were likely restricted to a primitive microbial stage of evolution [91,92].

The Kverkfjöll region mimics some of these key parameters. It is an extremely remote, cold, basaltic environment devoid of subaerial vegetative cover. Our findings confirm that the native biological community is predominantly microbial, with no discernible contributions from complex organisms. Additionally, we observed that phototrophic PLFA markers are scarce and localized, mirroring the presumed constraints on photosynthetic life under Martian conditions. Our study therefore contributes to our understanding of the distribution of viable organisms in a basaltic environment where phototrophy is not the dominant form of primary production and lays

the groundwork for subsequent investigations of the associated distribution of biosignatures and the fidelity of that record (see Chapter 3).

## 2.6 CONCLUSIONS

We investigated the physicochemical and lipid biomarker characteristics of the ice-fed, basalt-hosted glaciovolcanic system at the Kverkfjöll summit. We identified significant variability in the local physicochemical conditions, with hydrothermal fluids ranging from high to low temperatures, alkaline to acidic pH, and oxic to extremely dysoxic conditions. Viable microorganisms were detected across the full range of conditions with no evidence of exogenous plant or animal detritus contributing to the organic pool. This confluence of factors highlights Kverkfjöll as an ideal natural laboratory for understanding microbial colonization and adaptation in glaciovolcanic settings.

We described multiple lines of evidence demonstrating that environmental factors exerted a principal control on shaping the biological community. We found that biomass and organic carbon were elevated in areas that were particularly conducive to the development of autotrophy. We also described distinct differences in bulk PLFA profiles between sampling areas with unique geochemical characteristics, suggesting that population-level trends in community membership are driven by local habitat conditions. Moreover, along the interconnected Spring-Lake Transect, we identified several molecular patterns in the PLFA distributions reflective of homeoviscous adaptation to cold stress, as well as shifts in community membership due to varying oxygen or salinity levels. Collectively, these observations underscore the adaptability and dynamism of the indigenous microbial community and highlight how the environmental heterogeneity intrinsic to glaciovolcanic interactions can foster community variability.

Regions of Mars that have been influenced by glaciovolcanism throughout Mars' history (see Cousins et al., 2011 [1] and Smellie & Edwards, 2016 [15]) could thus offer a similar breadth of resources and environmental heterogeneity, enabling the potential for diverse ecological niche development. Further, considering that these kinds of environments have persisted throughout Mars' history and have been active during the Late Amazonian, they hold significant potential as targets for uncovering past biosignatures. The distribution of biosignatures in such environments (and any Martian paleohabitat) is expected to depend on the original distribution of biomass as well as its potential to be preserved in those environments [94]. Thus, our investigation of

environmental parameters and biomass distribution provides a framework that can guide future astrobiological missions, focusing on areas conducive to autotrophy. Future investigations should focus on the taphonomic considerations relevant to the microbial habitats discussed here.

## 2.7 ACKNOWLEDGEMENTS

This project has received funding from the European Union's Horizon 2020 research and innovation programme under grant agreement No 871149, the Canadian Space Agency (CSA) [21EXPCOI1], and the Natural Sciences and Engineering Research Council of Canada (NSERC).

Special thanks to Magnus Thor Karlsson and Bergur Einarsson for ensuring our safety in the field and generously assisting with sample collection. The authors also thank Magnús Tumi Guðmundsson, Andri Gunnarsson, and the entire team behind the Iceland Glaciological Society (JÖRFÍ) for exceptional logistical support, guidance, patience, and kindness.

## 2.8 REFERENCES

[1] C.R. Cousins, I.A. Crawford, Volcano-ice interaction as a microbial habitat on Earth and Mars, Astrobiology. 11 (2011) 695–710. https://doi.org/10.1089/ast.2010.0550.

[2] I-MIM MDT, Final Report of the International Mars Ice Mapper Reconnaissance/Science Measurement Definition Team, 2022. https://doi.org/10.1016/S0065-2113(08)60505-2.

[3] K.E. Scanlon, J.W. Head, D.R. Marchant, Volcanism-induced, local wet-based glacial conditions recorded in the Late Amazonian Arsia Mons tropical mountain glacier deposits, Icarus. 250 (2015) 18–31. https://doi.org/10.1016/j.icarus.2014.11.016.

[4] S.J. Kadish, J.W. Head, R.L. Parsons, D.R. Marchant, The Ascraeus Mons fan-shaped deposit: Volcano–ice interactions and the climatic implications of cold-based tropical mountain glaciation, Icarus. 197 (2008) 84–109.

[5] F.E. Butcher, M.R. Balme, C. Gallagher, N.S. Arnold, S.J. Conway, A. Hagermann, S.R. Lewis, Recent Basal Melting of a Mid-Latitude Glacier on Mars, J Geophys Res Planets. 122 (2017) 2445–2468.

[6] K.E. Scanlon, J.W. Head, L. Wilson, D.R. Marchant, Volcano-ice interactions in the Arsia Mons tropical mountain glacier deposits, Icarus. 237 (2014) 315–339. https://doi.org/10.1016/j.icarus.2014.04.024.

[7] A.G. Fairén, A.F. Davila, D. Lim, N. Bramall, R. Bonaccorsi, J. Zavaleta, E.R. Uceda, C. Stoker, J. Wierzchos, J.M. Dohm, R. Amils, D. Andersen, C.P. McKay, Astrobiology through the ages of Mars: The study of terrestrial analogues to understand the habitability of Mars, Astrobiology. 10 (2010) 821–843. https://doi.org/10.1089/ast.2009.0440.

[8] F. Westall, F. Foucher, N. Bost, M. Bertrand, D. Loizeau, J.L. Vago, G. Kminek, F. Gaboyer, K.A. Campbell, J.-G. Bréhéret, P. Gautret, C.S. Cockell, Biosignatures on Mars: What, Where, and How? Implications for the Search for Martian Life, Astrobiology. 15 (2015) 998–1029. https://doi.org/10.1089/ast.2015.1374.

[9] J. Davis, A. Pavlova, R. Thompson, P. Sunnucks, Evolutionary refugia and ecological refuges: key concepts for conserving Australian arid zone freshwater biodiversity under climate change, Glob Chang Biol. 19 (2013) 1970–1984.

[10] G. Keppel, K.P. Van Niel, G.W. Wardell-Johnson, C.J. Yates, M. Byrne, L. Mucina, A.G.T. Schut, S.D. Hopper, S.E. Franklin, Refugia: identifying and understanding safe havens for biodiversity under climate change, Global Ecology and Biogeography. 21 (2012) 393–404.

[11] A.B.A. Shafer, C.I. Cullingham, S.D. Côté, D.W. Coltman, Of glaciers and refugia: a decade of study sheds new light on the phylogeography of northwestern North America, Mol Ecol. 19 (2010) 4589–4621.

[12] C.I. Fraser, A. Terauds, J. Smellie, P. Convey, S.L. Chown, Geothermal activity helps life survive glacial cycles, Proc Natl Acad Sci U S A. 111 (2014) 5634–5639. https://doi.org/10.1073/pnas.1321437111.

[13] J. Provan, K.D. Bennett, Phylogeographic insights into cryptic glacial refugia, Trends Ecol Evol. 23 (2008) 564–571.

[14] B.L. Carrier, D.W. Beaty, M.A. Meyer, J.G. Blank, L. Chou, S. Dassarma, D.J. Des Marais, J.L. Eigenbrode, N. Grefenstette, N.L. Lanza, A.C. Schuerger, P. Schwendner, H.D. Smith, C.R. Stoker, J.D. Tarnas, K.D. Webster, C. Bakermans, B.K. Baxter, M.S. Bell, S.A. Benner, H.H. Bolivar Torres, P.J. Boston, R. Bruner, B.C. Clark, P. Dassarma, A.E. Engelhart, Z.E. Gallegos, Z.K. Garvin, P.J. Gasda, J.H. Green, R.L. Harris, M.E. Hoffman, T. Kieft, A.H.D. Koeppel, P.A. Lee, X. Li, K.L. Lynch, R. MacKelprang, P.R. Mahaffy, L.H. Matthies, M.A. Nellessen, H.E. Newsom, D.E. Northup, B.R.W. O'Connor, S.M. Perl, R.C. Quinn, L.A. Rowe, B. Sauterey,

M.A. Schneegurt, D. Schulze-Makuch, L.A. Scuderi, M.N. Spilde, V. Stamenković, J.A. Torres Celis, D. Viola, B.D. Wade, C.J. Walker, R.C. Wiens, A.J. Williams, J.M. Williams, J. Xu, Mars Extant Life: What's Next? Conference Report, Astrobiology. 20 (2020) 785–814. https://doi.org/10.1089/ast.2020.2237.

[15] J.L. Smellie, B.R. Edwards, Glaciovolcanism on Earth and Mars, Cambridge University Press, 2016.

[16] H. Björnsson, Jökulhlaups in iceland: Sources, release and drainage, Megaflooding on Earth and Mars. (2009) 50–64. https://doi.org/10.1017/CBO9780511635632.004.

[17] I.D. Barr, C.M. Lynch, D. Mullan, L. De Siena, M. Spagnolo, Volcanic impacts on modern glaciers: A global synthesis, Earth Sci Rev. 182 (2018) 186–203.

[18] T. Fegel, C.M. Boot, C.D. Broeckling, J.S. Baron, E.K. Hall, Assessing the chemistry and bioavailability of dissolved organic matter from glaciers and rock glaciers, J Geophys Res Biogeosci. 124 (2019) 1988–2004.

[19] H. V. Pryer, J.R. Hawkings, J.L. Wadham, L.F. Robinson, K.R. Hendry, J.E. Hatton, A.M. Kellerman, S. Bertrand, B. Gill-Olivas, M.G. Marshall, R.A. Brooker, G. Daneri, V. Häussermann, The Influence of Glacial Cover on Riverine Silicon and Iron Exports in Chilean Patagonia, Global Biogeochem Cycles. 34 (2020). https://doi.org/10.1029/2020GB006611.

[20] C.S. Cockell, E. Bagshaw, M. Balme, P. Doran, C.P. Mckay, K. Miljkovic, D. Pearce, M.J. Siegert, M. Tranter, M. Voytek, J. Wadham, Subglacial Environments and the Search for Life Beyond the Earth, Antarctic Subglacial Aquatic Environments. (2011) 129–148. https://doi.org/10.1002/9781118670354.ch8.

[21] J. Telling, E.S. Boyd, N. Bone, E.L. Jones, M. Tranter, J.W. MacFarlane, P.G. Martin, J.L. Wadham, G. Lamarche-Gagnon, M.L. Skidmore, Rock comminution as a source of hydrogen for subglacial ecosystems, Nat Geosci. 8 (2015) 851–855.

[22] M. Skidmore, Microbial communities in Antarctic subglacial aquatic environments, Antarctic Subglacial Aquatic Environments. 192 (2011) 61–81.

[23] M.H. Carr, J.W. Head, Geologic history of Mars, Earth Planet Sci Lett. 294 (2010) 185–203. https://doi.org/10.1016/j.epsl.2009.06.042.

[24] J.W. Head, S. Pratt, Extensive Hesperian-aged south polar ice sheet on Mars: Evidence for massive melting and retreat, and lateral flow and ponding of meltwater, Journal of Geophysical Research E: Planets. 106 (2001) 12229–12275. https://doi.org/10.1029/2000je001359.

[25] J.W. Head, J.F. Mustard, M.A. Kreslavsky, R.E. Milliken, D.R. Marchant, Recent ice ages on Mars, Nature. 426 (2003) 797–802.

[26] J.W. Head, G. Neukum, R. Jaumann, H. Hiesinger, E. Hauber, M. Carr, P. Masson, B. Foing, H. Hoffmann, M. Kreslavsky, Tropical to mid-latitude snow and ice accumulation, flow and glaciation on Mars, Nature. 434 (2005) 346–351.

[27] A. Grau Galofre, A.M. Jellinek, G.R. Osinski, Valley formation on early Mars by subglacial and fluvial erosion, Nat Geosci. 13 (2020) 663–668. https://doi.org/10.1038/s41561-020-0618-x.

[28] A. Grau Galofre, K.X. Whipple, P.R. Christensen, S.J. Conway, Valley Networks and the Record of Glaciation on Ancient Mars, Geophys Res Lett. 49 (2022) 1–10. https://doi.org/10.1029/2022GL097974.

[29] J.-B. Madeleine, F. Forget, J.W. Head, B. Levrard, F. Montmessin, E. Millour, Amazonian northern mid-latitude glaciation on Mars: A proposed climate scenario, Icarus. 203 (2009) 390–405.

[30] J. Laskar, A.C.M. Correia, M. Gastineau, F. Joutel, B. Levrard, P. Robutel, Long term evolution and chaotic diffusion of the insolation quantities of Mars, Icarus. 170 (2004) 343–364.

[31] J.W. Head, A.L. Nahm, D.R. Marchant, G. Neukum, Modification of the dichotomy boundary on Mars by Amazonian mid-latitude regional glaciation, Geophys Res Lett. 33 (2006).

[32] F. Forget, R.M. Haberle, F. Montmessin, B. Levrard, J.W. Head, Formation of glaciers on Mars by atmospheric precipitation at high obliquity, Science (1979). 311 (2006) 368–371.

[33] J.L. Fastook, J.W. Head, F. Forget, J.-B. Madeleine, D.R. Marchant, Evidence for Amazonian northern mid-latitude regional glacial landsystems on Mars: Glacial flow models using GCM-driven climate results and comparisons to geological observations, Icarus. 216 (2011) 23–39.

[34] S.Z. Woodley, F.E.G. Butcher, P. Fawdon, C.D. Clark, F.S.L. Ng, J.M. Davis, C. Gallagher, Multiple sites of recent wet-based glaciation identified from eskers in western Tempe Terra, Mars, Icarus. 386 (2022) 115147. https://doi.org/10.1016/j.icarus.2022.115147.

[35] C. Gallagher, M. Balme, Eskers in a complete, wet-based glacial system in the Phlegra Montes region, Mars, Earth Planet Sci Lett. 431 (2015) 96–109. https://doi.org/10.1016/j.epsl.2015.09.023.

[36] F.E.G. Butcher, M.R. Balme, S.J. Conway, C. Gallagher, N.S. Arnold, R.D. Storrar, S.R. Lewis, A. Hagermann, J.M. Davis, Sinuous ridges in Chukhung crater, Tempe Terra, Mars: Implications for fluvial, glacial, and glaciofluvial activity, Icarus. 357 (2021) 114131. https://doi.org/10.1016/j.icarus.2020.114131.

[37] S. Ackiss, B. Horgan, F. Seelos, W. Farrand, J. Wray, Mineralogic evidence for subglacial volcanism in the Sisyphi Montes region of Mars, Icarus. 311 (2018) 357–370. https://doi.org/10.1016/j.icarus.2018.03.026.

[38] V.T. Marteinsson, Á. Rúnarsson, A. Stefánsson, T. Thorsteinsson, T. Jóhannesson, S.H. Magnússon, E. Reynisson, B. Einarsson, N. Wade, H.G. Morrison, E. Gaidos, Microbial communities in the subglacial waters of the Vatnajökull ice cap, Iceland, ISME Journal. 7 (2013) 427–437. https://doi.org/10.1038/ismej.2012.97.

[39] C.R. Cousins, M. Fogel, R. Bowden, I. Crawford, A. Boyce, C. Cockell, M. Gunn, Biogeochemical probing of microbial communities in a basalt-hosted hot spring at Kverkfjöll volcano, Iceland, Geobiology. 16 (2018) 507–521. https://doi.org/10.1111/gbi.12291.

[40] C.R. Cousins, I.A. Crawford, J.L. Carrivick, M. Gunn, J. Harris, T.P. Kee, M. Karlsson, L. Carmody, C. Cockell, B. Herschy, K.H. Joy, Glaciovolcanic hydrothermal environments in Iceland and implications for their detection on Mars, Journal of Volcanology and Geothermal Research. 256 (2013) 61–77. https://doi.org/10.1016/j.jvolgeores.2013.02.009.

[41] Y. Zhang, N. Zheng, J. Wang, H. Yao, Q. Qiu, S.J. Chapman, High turnover rate of free phospholipids in soil confirms the classic hypothesis of PLFA methodology, Soil Biol Biochem. 135 (2019) 323–330.

[42] K.M. Scow, E. Schwartz, M.J. Johnson, J.L. Macalady, Microbial biodiversity, measurement of, in: Encyclopedia of Biodiversity: Second Edition, Elsevier Inc., 2001: pp. 259–270.

[43] H. Björnsson, F. Pálsson, Icelandic glaciers, Jökull. 58 (2008) 365–386.

[44] H.Y. McSween, G.J. Taylor, M.B. Wyatt, Elemental composition of the Martian crust, Science (1979). 324 (2009) 736–739.

[45] B.A. Óladóttir, O. Sigmarsson, G. Larsen, J.L. Devidal, Provenance of basaltic tephra from vatnajökull subglacial volcanoes, iceland, as determined by major- and trace-element analyses, Holocene. 21 (2011) 1037–1048. https://doi.org/10.1177/0959683611400456.

[46] E. Ranta, S.A. Halldórsson, P.H. Barry, S. Ono, J.G. Robin, B.I. Kleine, A. Ricci, J. Fiebig, Á.E. Sveinbjörnsdóttir, A. Stefánsson, Deep magma degassing and volatile fluxes through volcanic hydrothermal systems: Insights from the Askja and Kverkfjöll volcanoes, Iceland, Journal of Volcanology and Geothermal Research. 436 (2023) 107776. https://doi.org/10.1016/j.jvolgeores.2023.107776.

[47] M. Olafsson, H. Torfason, K. Gronvold, Surface exploration and monitoring of geothermal activity in the kverkfjöll geothermal area, central iceland, World Geothermal Congres 2000. (2000) 1539–1545.

[48] G.E. Sigvaldason, S. Steinthorsson, N. Oskarsson, Compositional variation in recent Icelandic tholeiites and the K verkfjoll hot spot, 251 (1974).

[49] M.T. Gudmundsson, Þ. Högnadóttir, Jökullón í Vestari Kverkfjöllum, þróun og jökulhlaupahætta, Skýrsla Til Rannsóknasjóðs Vegagerðarinnar. (2009).

[50] C.S. Cockell, S. McMahon, D.S.S. Lim, J. Rummel, A. Stevens, S.S. Hughes, S.E. Kobs Nawotniak, A.L. Brady, V. Marteinsson, J. Martin-Torres, M.P. Zorzano, J. Harrison, Sample Collection and Return from Mars: Optimising Sample Collection Based on the Microbial Ecology of Terrestrial Volcanic Environments, Space Sci Rev. 215 (2019). https://doi.org/10.1007/s11214-019-0609-7.

[51] C. Montanaro, B. Scheu, M.T. Gudmundsson, K. Vogfjörd, H.I. Reynolds, T. Dürig, K. Strehlow, S. Rott, T. Reuschlé, D.B. Dingwell, Multidisciplinary constraints of hydrothermal explosions based on the 2013 Gengissig lake events, Kverkfjöll volcano, Iceland, Earth Planet Sci Lett. 434 (2016) 308–319. https://doi.org/10.1016/j.epsl.2015.11.043.

[52] F.D. Wilde, D.B. Radtke, J. Gibs, R.T. Iwatsubo, National field manual for the collection of water-quality data, US Geological Survey Techniques in Water-Resources Investigations, Book. 9 (1998).

[53] E.G. Bligh, W.J. Dyer, A rapid method of total lipid extraction and purification, Can J Biochem Physiol. 37 (1959) 911–917.

[54] C. Willers, P.J. Jansen van Rensburg, S. Claassens, Phospholipid fatty acid profiling of microbial communities-a review of interpretations and recent applications, J Appl Microbiol. 119 (2015) 1207–1218. https://doi.org/10.1111/jam.12902.

[55] Y.M. Zhang, C.O. Rock, Membrane lipid homeostasis in bacteria, Nat Rev Microbiol. 6 (2008) 222–233. https://doi.org/10.1038/nrmicro1839.

[56] A. Kaur, A. Chaudhary, A. Kaur, R. Choudhary, R. Kaushik, Phospholipid fatty acid - A bioindicator of environment monitoring and assessment in soil ecosystem, Curr Sci. 89 (2005) 1103–1112.

[57] J.B. Guckert, M.A. Hood, D.C. White, Phospholipid ester-linked fatty acid profile changes during nutrient deprivation of Vibrio cholerae: Increases in the trans/cis ratio and proportions of cyclopropyl fatty acids, Appl Environ Microbiol. 52 (1986) 794–801. https://doi.org/10.1128/aem.52.4.794-801.1986.

[58] C.T. Green, K.M. Scow, Analysis of phospholipid fatty acids (PLFA) to characterize microbial communities in aquifers, Hydrogeol J. 8 (2000) 126–141. https://doi.org/10.1007/s100400050013.

[59] R. V Tyson, T.H. Pearson, Modern and ancient continental shelf anoxia: an overview, Geological Society, London, Special Publications. 58 (1991) 1–24.

[60] L. Zelles, Fatty acid patterns of phospholipids and lipopolysaccharides in the characterisation of microbial communities in soil: A review, Biol Fertil Soils. 29 (1999) 111–129. https://doi.org/10.1007/s003740050533.

[61] C.C. Cleveland, D. Liptzin, C:N:P stoichiometry in soil: Is there a “Redfield ratio” for the microbial biomass?, Biogeochemistry. 85 (2007) 235–252. https://doi.org/10.1007/s10533-007-9132-0.

[62] T. Nagata, Y. Watanabe, Carbon- and nitrogen-to-volume ratios of bacterioplankton grown under different nutritional conditions, Appl Environ Microbiol. 56 (1990) 1303–1309. https://doi.org/10.1128/aem.56.5.1303-1309.1990.

[63] J. Zhang, J.J. Elser, Carbon: nitrogen: phosphorus stoichiometry in fungi: a meta-analysis, Front Microbiol. 8 (2017) 1281.

[64] P.A. Meyers, J.L. Teranes, Sediment organic matter, Tracking Environmental Change Using Lake Sediments: Physical and Geochemical Methods. (2001) 239–269.

[65] P.A. Meyers, Preservation of source identification of sedimentary organic matter during and after deposition, Chem Geol. 144 (1994) 289–302.

[66] H.J. Heipieper, G. Meulenbeld, Q. van Oirschot, J. De Bont, Effect of environmental factors on the trans/cis ratio of unsaturated fatty acids in Pseudomonas putida S12, Appl Environ Microbiol. 62 (1996) 2773–2777.

[67] H.J. Heipieper, B. Loffeld, H. Keweloh, J.A.M. de Bont, The cis/trans isomerisation of unsaturated fatty acids in Pseudomonas putida S12: an indicator for environmental stress due to organic compounds, Chemosphere. 30 (1995) 1041–1051.

[68] E. Bååth, T.-H. Anderson, Comparison of soil fungal/bacterial ratios in a pH gradient using physiological and PLFA-based techniques, Soil Biol Biochem. 35 (2003) 955–963.

[69] Å. Frostegård, A. Tunlid, E. Bååth, Phospholipid fatty acid composition, biomass, and activity of microbial communities from two soil types experimentally exposed to different heavy metals, Appl Environ Microbiol. 59 (1993) 3605–3617.

[70] H.W. Cook, C.R. McMaster, Fatty acid desaturation and chain elongation in eukaryotes, in: New Comprehensive Biochemistry, Elsevier, 2002: pp. 181–204.

[71] Y. Li, S. Wu, L. Wang, Y. Li, F. Shi, X. Wang, Differentiation of bacteria using fatty acid profiles from gas chromatography-tandem mass spectrometry, J Sci Food Agric. 90 (2010) 1380–1383. https://doi.org/10.1002/jsfa.3931.

[72] A.D. Hendricker, C. Abbas-Hawks, F. Basile, K.J. Voorhees, T.L. Hadfield, Rapid chemotaxonomy of pathogenic bacteria using in situ thermal hydrolysis and methylation as a sample preparation step coupled with a field-portable membrane-inlet quadrupole ion trap mass spectrometer, Int J Mass Spectrom. 190–191 (1999) 331–342. https://doi.org/10.1016/s1387-3806(98)14266-5.

[73] F. Basile, M.B. Beverly, K.J. Voorhees, T.L. Hadfield, Pathogenic bacteria: Their detection and differentiation by rapid lipid profiling with pyrolysis mass spectrometry, TrAC - Trends in Analytical Chemistry. 17 (1998) 95–109. https://doi.org/10.1016/S0165-9936(97)00103-9.

[74] T. Kaneda, Iso-and anteiso-fatty acids in bacteria: biosynthesis, function, and taxonomic significance, Microbiol Rev. 55 (1991) 288–302.

[75] H.R. Harvey, S.A. Macko, Catalysts or contributors? Tracking bacterial mediation of early diagenesis in the marine water column, Org Geochem. 26 (1997) 531–544.

[76] T.S. Bianchi, Characterization of organic matter, in: Biogeochemistry of Estuaries, Oxford University Press, 2006.

[77] Å. Frostegård, A. Tunlid, E. Bååth, Use and misuse of PLFA measurements in soils, Soil Biol Biochem. 43 (2011) 1621–1625.

[78] J.L. Wang, N.B. Dragone, G. Avard, B.M. Hynek, Microbial Survival in an Extreme Martian Analog Ecosystem : Poás Volcano, Costa Rica, Frontiers in Astronomy and Space Sciences. 9 (2022) 1–16. https://doi.org/10.3389/fspas.2022.817900.

[79] G.F. Slater, R.K. Nelson, B.M. Kile, C.M. Reddy, Intrinsic bacterial biodegradation of petroleum contamination demonstrated in situ using natural abundance, molecular-level 14C analysis, Org Geochem. 37 (2006) 981–989. https://doi.org/10.1016/j.orggeochem.2006.06.014.

[80] B. Pushparaj, A. Buccioni, R. Paperi, R. Piccardi, A. Ena, P. Carlozzi, C. Sili, Fatty acid composition of Antarctic cyanobacteria, Phycologia. 47 (2008) 430–434.

[81] A. Santana-Sánchez, F. Lynch, S. Sirin, Y. Allahverdiyeva, Nordic cyanobacterial and algal lipids: Triacylglycerol accumulation, chemotaxonomy and bioindustrial potential, Physiol Plant. 173 (2021) 591–602.

[82] A.C. Guedes, H.M. Amaro, C.R. Barbosa, R.D. Pereira, F.X. Malcata, Fatty acid composition of several wild microalgae and cyanobacteria, with a focus on eicosapentaenoic, docosahexaenoic and α-linolenic acids for eventual dietary uses, Food Research International. 44 (2011) 2721–2729.

[83] D.A. Los, K.S. Mironov, Modes of fatty acid desaturation in cyanobacteria: an update, Life. 5 (2015) 554–567.

[84] L.J. Rothschild, The evolution of photosynthesis… again?, Philosophical Transactions of the Royal Society B: Biological Sciences. 363 (2008) 2787–2801.

[85] A.S. Mackenzie, S.C. Brassell, G. Eglinton, J.R. Maxwell, Chemical fossils: The geological fate of steroids, Science (1979). 217 (1982) 491–504. https://doi.org/10.1126/science.217.4559.491.

[86] R.R. Kuechler, D. Birgel, S. Kiel, A. Freiwald, J.L. Goedert, V. Thiel, J. Peckmann, Miocene methane-derived carbonates from southwestern Washington, USA and a model for silicification at seeps, Lethaia. 45 (2012) 259–273.

[87] D. Birgel, J. Peckmann, S. Klautzsch, V. Thiel, J. Reitner, Anaerobic and aerobic oxidation of methane at Late Cretaceous seeps in the Western Interior Seaway, USA, Geomicrobiol J. 23 (2006) 565–577.

[88] R. Anderson, M. Kates, M.J. Baedecker, I.R. Kaplan, R.G. Ackman, The stereoisomeric composition of phytanyl chains in lipids of Dead Sea sediments, Geochim Cosmochim Acta. 41 (1977) 1381–1390.

[89] C. Thomas, V. Grossi, I. Antheaume, D. Ariztegui, Recycling of archaeal biomass as a new strategy for extreme life in Dead Sea deep sediments, Geology. 47 (2019) 479–482.

[90] J.R. Michalski, T.C. Onstott, S.J. Mojzsis, J. Mustard, Q.H.S. Chan, P.B. Niles, S.S. Johnson, The Martian subsurface as a potential window into the origin of life, Nat Geosci. 11 (2018) 21–26. https://doi.org/10.1038/s41561-017-0015-2.

[91] F. Westall, D. Loizeau, F. Foucher, N. Bost, M. Betrand, J. Vago, G. Kminek, Habitability on mars from a microbial point of view, Astrobiology. 13 (2013) 887–897. https://doi.org/10.1089/ast.2013.1000.

[92] D. Schulze-Makuch, L. Irwin, J. Lipps, D. LeMone, J. Dohm, A. Fairén, Scenarios for the evolution of life on Mars, Journal on Geophysical Research. 110 (2005) 12. https://doi.org/10.1029/2005JE002430.

[93] C.S. Cockell, Trajectories of martian habitability, Astrobiology. 14 (2014) 182–203. https://doi.org/10.1089/ast.2013.1106.

[94] S. McMahon, T. Bosak, J.P. Grotzinger, R.E. Milliken, R.E. Summons, M. Daye, S.A. Newman, A. Fraeman, K.H. Williford, D.E.G. Briggs, A Field Guide to Finding Fossils on Mars, J Geophys Res Planets. 123 (2018) 1012–1040. https://doi.org/10.1029/2017JE005478.

[95] E. Gaidos, B. Lanoil, T. Thorsteinsson, A. Graham, M. Skidmore, S.K. Han, T. Rust, B. Popp, A viable microbial community in a subglacial volcanic crater lake, Iceland, Astrobiology. 4 (2004) 327–344. https://doi.org/10.1089/ast.2004.4.327.

[96] C.E. Sharp, A.L. Brady, G.H. Sharp, S.E. Grasby, M.B. Stott, P.F. Dunfield, Humboldt's spa: microbial diversity is controlled by temperature in geothermal environments, ISME J. 8 (2014) 1166–1174. https://doi.org/10.1038/ismej.2013.237.

[97] C.S. Cockell, J.P. Harrison, A.H. Stevens, S.J. Payler, S.S. Hughes, S.E. Kobs Nawotniak, A.L. Brady, R.C. Elphic, C.W. Haberle, A. Sehlke, K.H. Beaton, A.F.J. Abercromby, P. Schwendner, J. Wadsworth, H. Landenmark, R. Cane, A.W. Dickinson, N. Nicholson, L. Perera, D.S.S. Lim, A Low-Diversity Microbiota Inhabits Extreme Terrestrial Basaltic Terrains and Their Fumaroles: Implications for the Exploration of Mars, Astrobiology. 19 (2019) 284–299. https://doi.org/10.1089/ast.2018.1870.

[98] A.L. Brady, E. Gibbons, A. Sehlke, C.J. Renner, S.E. Kobs Nawotniak, D.S.S. Lim, G.F. Slater, Microbial community distribution in variously altered basalts: Insights into astrobiology sample site selection, Planet Space Sci. 194 (2020). https://doi.org/10.1016/j.pss.2020.105107.

[99] M. Svercel, B. Saladin, S.J. van Moorsel, S. Wolf, H.C. Bagheri, Antagonistic interactions between filamentous heterotrophs and the cyanobacterium Nostoc muscorum, BMC Res Notes. 4 (2011) 1–8.

[100] L. Chen, M. Hu, L. Huang, Z. Hua, J. Kuang, S. Li, W. Shu, Comparative metagenomic and metatranscriptomic analyses of microbial communities in acid mine drainage, ISME J. 9 (2015) 1579–1592.

[101] B.J. Baker, J.F. Banfield, Microbial communities in acid mine drainage, FEMS Microbiol Ecol. 44 (2003) 139–152.

[102] E.S. Boyd, K.M. Fecteau, J.R. Havig, E.L. Shock, J.W. Peters, Modeling the habitat range of phototrophs in Yellowstone National Park: toward the development of a comprehensive fitness landscape, Front Microbiol. 3 (2012) 221.

[103] T.L. Hamilton, K. Vogl, D.A. Bryant, E.S. Boyd, J.W. Peters, Environmental constraints defining the distribution, composition, and evolution of chlorophototrophs in thermal features of Yellowstone National Park, Geobiology. 10 (2012) 236–249.

[104] D.M. Ward, R.W. Castenholz, S.R. Miller, Cyanobacteria in geothermal habitats, in: Ecology of Cyanobacteria II: Their Diversity in Space and Time, Springer, 2012: pp. 39–63.

[105] D. Deamer, The role of lipid membranes in life's origin, Life. 7 (2017) 5.

[106] L.R. Thompson, J.G. Sanders, D. McDonald, A. Amir, J. Ladau, K.J. Locey, R.J. Prill, A. Tripathi, S.M. Gibbons, G. Ackermann, A communal catalogue reveals Earth's multiscale microbial diversity, Nature. 551 (2017) 457–463.

[107] M.S. Thomsen, A.H. Altieri, C. Angelini, M.J. Bishop, F. Bulleri, R. Farhan, V.M.M. Frühling, P.E. Gribben, S.B. Harrison, Q. He, Heterogeneity within and among co-occurring foundation species increases biodiversity, Nat Commun. 13 (2022) 581.

[108] A. Stein, K. Gerstner, H. Kreft, Environmental heterogeneity as a universal driver of species richness across taxa, biomes and spatial scales, Ecol Lett. 17 (2014) 866–880.

[109] M. Huston, A general hypothesis of species diversity, Am Nat. 113 (1979) 81–101.

[110] D.B. Nedwell, Effect of low temperature on microbial growth: Lowered affinity for substrates limits growth at low temperature, FEMS Microbiol Ecol. 30 (1999) 101–111. https://doi.org/10.1016/S0168-6496(99)00030-6.

[111] P. De Maayer, D. Anderson, C. Cary, D.A. Cowan, Some like it cold: Understanding the survival strategies of psychrophiles, EMBO Rep. 15 (2014) 508–517. https://doi.org/10.1002/embr.201338170.

[112] M.C. Théberge, D. Prévost, F.P. Chalifour, The effect of different temperatures on the fatty acid composition of Rhizobium leguminosarum bv. viciae in the faba bean symbiosis, New Phytologist. 134 (1996) 657–664. https://doi.org/10.1111/j.1469-8137.1996.tb04931.x.

[113] A. Marr, J. Ingraham, Effect of Temperature on the Composition of Fatty Acids in Escherichia Coli, J Bacteriol. 84 (1962).

[114] M.F. Siliakus, J. van der Oost, S.W.M. Kengen, Adaptations of archaeal and bacterial membranes to variations in temperature, pH and pressure, Extremophiles. 21 (2017) 651–670. https://doi.org/10.1007/s00792-017-0939-x.

[115] N.J. Russell, Cold adaptation of microorganisms, Philosophical Transactions of the Royal Society of London. B, Biological Sciences. 326 (1990) 595–611.

[116] S.M. Murray, R.A. O'Brien, K.M. Mattson, C. Ceccarelli, R.E. Sykora, K.N. West, J.H. Davis, The fluid-mosaic model, homeoviscous adaptation, and ionic liquids: Dramatic lowering of the melting point by side-chain unsaturation, Angewandte Chemie - International Edition. 49 (2010) 2755–2758. https://doi.org/10.1002/anie.200906169.

[117] E.M. Fozo, R.G. Quivey, Shifts in the Membrane Fatty Acid Profile of Streptococcus mutans Enhance Survival in Acidic Environments, Appl Environ Microbiol. 70 (2004) 929–936. https://doi.org/10.1128/AEM.70.2.929-936.2004.

[118] J.L. Brown, T. Ross, T.A. McMeekin, P.D. Nichols, Acid habituation of Escherichia coli and the potential role of cyclopropane fatty acids in low pH tolerance, Int J Food Microbiol. 37 (1997) 163–173.

[119] H.-G. Yuk, D.L. Marshall, Adaptation of Escherichia coli O157:H7 to pH alters membrane lipid composition, verotoxin secretion, and resistance to simulated gastric fluid acid, Appl Environ Microbiol. 70 (2004) 3500–3505.

[120] K.M. Rath, N. Fierer, D. V. Murphy, J. Rousk, Linking bacterial community composition to soil salinity along environmental gradients, ISME Journal. 13 (2019) 836–846. https://doi.org/10.1038/s41396-018-0313-8.

[121] R.L. Spietz, C.M. Williams, G. Rocap, M.C. Horner-Devine, A dissolved oxygen threshold for shifts in bacterial community structure in a seasonally hypoxic estuary, PLoS One. 10 (2015) 1–18. https://doi.org/10.1371/journal.pone.0135731.

[122] L.J. Rothschild, R.L. Mancinelli, Life in extreme environments, Nature. 409 (2001) 1092–1101.

[123] N. Merino, H.S. Aronson, D.P. Bojanova, J. Feyhl-Buska, M.L. Wong, S. Zhang, D. Giovannelli, Living at the extremes: Extremophiles and the limits of life in a planetary context, Front Microbiol. 10 (2019). https://doi.org/10.3389/fmicb.2019.00780.

[124] E. V. Pikuta, R.B. Hoover, J. Tang, Microbial extremophiles at the limits of life, Crit Rev Microbiol. 33 (2007) 183–209. https://doi.org/10.1080/10408410701451948.

[125] A.G. Fairén, J.M. Dohm, E.R. Uceda, A.P. Rodríguez, V.R. Baker, D. Fernández-Remolar, D. Schulze-Makuch, R. Amils, Prime candidate sites for astrobiological exploration through the hydrogeological history of Mars, Planet Space Sci. 53 (2005) 1355–1375. https://doi.org/10.1016/j.pss.2005.06.007.

[126] D. Schulze-Makuch, A. Airo, J. Schirmack, The adaptability of life on earth and the diversity of planetary habitats, Front Microbiol. 8 (2017) 1–10. https://doi.org/10.3389/fmicb.2017.02011.

[127] G. Vinnichenko, A.J.M. Jarrett, J.M. Hope, J.J. Brocks, Discovery of the oldest known biomarkers provides evidence for phototrophic bacteria in the 1.73 Ga Wollogorang Formation, Australia, Geobiology. 18 (2020) 544–559. https://doi.org/10.1111/gbi.12390.

[128] A.J.M. Jarrett, G.M. Cox, J.J. Brocks, E. Grosjean, C.J. Boreham, D.S. Edwards, Microbial assemblage and palaeoenvironmental reconstruction of the 1.38 Ga Velkerri Formation, McArthur Basin, northern Australia, Geobiology. 17 (2019) 360–380. https://doi.org/10.1111/gbi.12331.

[129] J.J. Brocks, R.E. Summons, W. Schlesinger, Sedimentary hydrocarbons, biomarkers for early life, Treatise on Geochemistry. 8 (2005) 63–115.

[130] A.C. Allwood, M.R. Walter, B.S. Kamber, C.P. Marshall, I.W. Burch, Stromatolite reef from the Early Archaean era of Australia, Nature. 441 (2006) 714–718.

[131] R.E. Summons, J.P. Amend, D. Bish, R. Buick, G.D. Cody, D.J. Des Marais, G. Dromart, J.L. Eigenbrode, A.H. Knoll, D.Y. Sumner, Preservation of Martian organic and environmental records: Final report of the Mars biosignature working group, Astrobiology. 11 (2011) 157–181. https://doi.org/10.1089/ast.2010.0506.

[132] T.M. Hoehler, An energy balance concept for habitability, Astrobiology. 7 (2007) 824–838.

[133] W. Rapin, G. Dromart, B.C. Clark, J. Schieber, E.S. Kite, L.C. Kah, L.M. Thompson, O. Gasnault, J. Lasue, P.-Y. Meslin, Sustained wet–dry cycling on early Mars, Nature. 620 (2023) 299–302.

[134] T. Dequaire, P.Y. Meslin, P. Beck, M. Jaber, A. Cousin, W. Rapin, J. Lasne, O. Gasnault, S. Maurice, A. Buch, C. Szopa, P. Coll, Analysis of carbon and nitrogen signatures with laser-induced breakdown spectroscopy; the quest for organics under Mars-like conditions, Spectrochim Acta Part B At Spectrosc. 131 (2017) 8–17. https://doi.org/10.1016/j.sab.2017.02.015.

[135] S. Maurice, S.M. Clegg, R.C. Wiens, O. Gasnault, W. Rapin, O. Forni, A. Cousin, V. Sautter, N. Mangold, L. Le Deit, ChemCam activities and discoveries during the nominal mission of the Mars Science Laboratory in Gale crater, Mars, J Anal At Spectrom. 31 (2016) 863–889.

[136] R.D. Wordsworth, The Climate of Early Mars, Annu Rev Earth Planet Sci. 44 (2016) 381–408. https://doi.org/10.1146/annurev-earth-060115-012355.

# PREFACE TO CHAPTER 3

The preceding Chapter sought to answer the question: *Could Mars' glaciovolcanic refugia offer a habitable environment conducive to sustaining microbial life?* We investigated this by evaluating the ecology of a Mars-analogue environment in Iceland. The results revealed a high degree of environmental heterogeneity, as well as a community of viable microorganisms. Notably, the phospholipid fatty acid profiles showed strong correlations with the environmental parameters, indicating patterns of niche differentiation and divergent adaptation within the indigenous community. We concluded that glaciovolcanic interactions not only provide habitable conditions, but also foster a spectrum of habitats conducive to the emergence of varied communities.

However, when assessing the astrobiological potential of an environment, it is often insufficient to merely demonstrate that the environment is *habitable*. One must also establish whether the environment is favourable to the *preservation* of evidence of inhabitation—its preservation potential. The paleontological term "preservation potential" conventionally refers to the likelihood that a particular species, tissue type, or cell remnant will become part of the fossil record. This potential can be influenced by an array of factors, including those affecting the organisms at the time of death (necrolysis), those operating in the interval between death and final burial (biostratinomic processes), and those impacting the remains after burial (fossil diagenesis). Together, these processes represent preservation filters that govern the degree to which an environment retains a fossil record and how accurately that record reflects the original biological community.

To understand the preservation potential of a Mars-like glaciovolcanic environment, Chapter 3 presents an investigation of the local mineralogy (the preservation environment) and the distribution of hydrocarbons (the fossil biosignatures) at Kverkfjöll. Hydrocarbons were selected for this analysis because they are important biomolecules that can be produced directly by organisms during their lifecycle or by the degradation of functionalized membrane lipids (like the phospholipids studied in Chapter 2) after an organism has died [1,2]. Most importantly, however, is that hydrocarbon biomolecules are relatively inert and are stable for billions of years if they are entombed in intact sedimentary rocks that have experienced only a mild thermal history [3]. The absence of plate tectonics and recent volcanism on Mars [4] increases the probability that rapidly buried, ancient sediments may have been spared intense thermal

alteration that could degrade molecular fossils. Hydrocarbons are therefore powerful tools with which to study potentially ancient life on Mars and its interaction with the environment.

It is important to highlight that we are studying a modern ecosystem. Thus, although hydrocarbons may be stable for billions of years [3,5,6], we cannot assess that enduring potential here. However, the presence and integrity of an ancient molecular fossil record is indeed contingent upon the processes operating in recently deposited sediments. Taphonomic studies of modern ecosystems can lead to an improved understanding of the production of biosignature compounds and how they compare to the profile of modern lipids in the system. This perspective allows us to bridge gaps in our understanding of how contemporary biosignature compounds are translated into the rock record, eventually manifesting as ancient fossils.

It is important to acknowledge, however, that volcanic activity poses a potentially significant threat to the long-term stability and preservation potential of glaciovolcanic environments. These settings are, by their very nature, dynamic and subject to the continuous forces of geological change. Volcanic eruptions could modify or even erase existing biosignature records. However, despite this dynamism, intact morphological evidence of glaciovolcanic activity is widespread through Mars' history and at a range of latitudes [7]. This includes relatively recent (circa. 100-200 million years ago) glaciovolcanism and concomitant meltwater generation [8]. Environments such as these are thus prime targets for exploration where potential organic records could remain intact. Moreover, while volcanic activity might disrupt large sections of the environment, it is plausible that small, sheltered sections of stratigraphy could be spared severe damage. Should biosignatures be encapsulated within organo-mineral complexes in these protected layers, they could remain relatively unaltered. Such pockets would serve as microcosms that still offer significant insights into past life and its interaction with the environment. Lastly, phenomena like jökulhlaups (glacial outburst floods) are potentially capable of transporting glaciovolcanic sediments—and possibly the biosignatures within—away from their original high-temperature environments to expansive flood plains, which might provide a more conducive environment for preservation. Thus, although these environments can experience violent alteration, there are several viable strategies for exploration. By analyzing an active glaciovolcanic environment, we not only gain insights into the processes currently shaping these terrains but also lay a foundational understanding of the records that could potentially endure. In essence, by

understanding the intricacies of current interactions and preservation challenges, we are better positioned to interpret the remnants of ancient life that have withstood the test of time.

Please note that Chapters 2 and 3 are distinct manuscripts. The naming convention for samples is not identical between the Chapters. Further, only the sediment samples were analyzed in Chapter 3 due to analytical issues associated with the hydrocarbon fraction of the filter samples.

**REFERENCES**


[1] J.L. Eigenbrode, Fossil lipids for life-detection: A case study from the early Earth record, Space Sci Rev. 135 (2008) 161–185. https://doi.org/10.1007/s11214-007-9252-9.

[2] N. Ladygina, E.G. Dedyukhina, M.B. Vainshtein, A review on microbial synthesis of hydrocarbons, Process Biochemistry. 41 (2006) 1001–1014. https://doi.org/10.1016/j.procbio.2005.12.007.

[3] J.J. Brocks, R.E. Summons, W. Schlesinger, Sedimentary hydrocarbons, biomarkers for early life, Treatise on Geochemistry. 8 (2005) 63–115.

[4] P. Van Thienen, N.J. Vlaar, A.P. Van den Berg, Plate tectonics on the terrestrial planets, Physics of the Earth and Planetary Interiors. 142 (2004) 61–74.

[5] G. Vinnichenko, A.J.M. Jarrett, J.M. Hope, J.J. Brocks, Discovery of the oldest known biomarkers provides evidence for phototrophic bacteria in the 1.73 Ga Wollogorang Formation, Australia, Geobiology. 18 (2020) 544–559. https://doi.org/10.1111/gbi.12390.

[6] A.J.M. Jarrett, G.M. Cox, J.J. Brocks, E. Grosjean, C.J. Boreham, D.S. Edwards, Microbial assemblage and palaeoenvironmental reconstruction of the 1.38 Ga Velkerri Formation, McArthur Basin, northern Australia, Geobiology. 17 (2019) 360–380. https://doi.org/10.1111/gbi.12331.

[7] C.R. Cousins, I.A. Crawford, Volcano-ice interaction as a microbial habitat on Earth and Mars, Astrobiology. 11 (2011) 695–710. https://doi.org/10.1089/ast.2010.0550.

[8] K.E. Scanlon, J.W. Head, L. Wilson, D.R. Marchant, Volcano-ice interactions in the Arsia Mons tropical mountain glacier deposits, Icarus. 237 (2014) 315–339. https://doi.org/10.1016/j.icarus.2014.04.024.

# CHAPTER 3

# A Case Study on Refractory Lipid Biomarkers for Mars Exploration: The Kverkfjöll Glaciovolcanic System, Iceland

Gibbons E.F. [a]*, Slater G. [b], Berlo K. [a], Leveille R.J. [a]

[a] Geotop, Department of Earth and Planetary Sciences, McGill University, 3450 University Street, Montreal, Quebec, Canada, H3A 0E8

[b] School of Earth, Environment & Society, McMaster University, 1280 Main Street West, Hamilton, Ontario, Canada, L8S 4K1

*Corresponding author*: erin.gibbons@mail.mcgill.ca*

**ABSTRACT**

Glaciovolcanic environments on Mars have been proposed as potential refugia for life, representing some of the longest sustained and recently habitable niches on Mars. However, the production and preservation of biomarkers in analogous settings on Earth remains poorly characterized. Consequently, we investigated the hydrocarbon assemblage of a modern glaciovolcanic area in Iceland with a Mars-like basaltic protolith. We detected two distinct hydrocarbon patterns, both reflective of direct microbial synthesis of hydrocarbons. The first included a predominance of heptadecane and a variety of mid-chain branched heptadecanes diagnostic of cyanobacterial input. The second distribution included an unresolved complex mixture and an unusual distribution of alkane/alkene pairs with a strong even carbon preference (CPI<<1) in the $C_{14}$ to $C_{22}$ range. We interpret the biogenic hydrocarbons as the direct products of

microbial synthesis, rather than the recalcitrant hydrocarbon cores of previously functionalized membrane biolipids. These findings contrast common assumptions made in the field of astrobiology and have important implications for interpreting hydrocarbon patterns in analogous settings on Mars. Overall, our findings show that diverse biogenic hydrocarbons can be recovered from Mars-like glaciovolcanic systems and provide a framework for future *in situ* exploration. Further, the unusual predominance of even alkane/alkene pairs is reported for the first time in a glaciovolcanic setting and thus contributes to the information on the rare occurrence of such distributions in the geosphere.

## 3.1 INTRODUCTION

Evidence of extensive volcanic activity and widespread glaciation is pervasive throughout Mars' history and occurs at a range of latitudes [1–4]. Coupled with the enduring presence of a thick global cryosphere [5], it has long been speculated that magma-ice interactions have consistently impacted the Martian landscape [6–12]. Such interactions can influence the environment in myriad ways [12]. In brief, the enhanced thermal fluxes near magma chambers can heat groundwater and/or melt ice in the cryosphere, creating conditions that are highly conducive to hydrothermal circulation [12]. The heat transfer can also initiate or enhance basal melting of overlying ice to generate large volumes of meltwater, even under climatic conditions that are generally unsuitable for ice melting or water accumulation [6,13]. Basal melting can reduce friction at the ice-bed interface and trigger local ice flow, generating subglacial/englacial lakes and glacial drainage landforms [6,9,12,14,15]. Where magma interacts directly with surface ice, structures akin to Earth's pillow lavas, tuyas, tindars, and rootless cones are expected to form [12]. Where magma intrudes in the form of sills and dikes, it can melt subsurface ice, causing the overlying terrain to collapse, and may trigger explosive releases from previously pressurized aquifers [12].

Morphological evidence of such dynamic processes is apparent across Mars and attests to the important role of magma-ice interaction in sculpting Mars' terrain (see reviews by Cousins et al., 2011 [7], Smellie & Edwards, 2016 [12]). This bears significance for the search for life as several authors have proposed that glaciovolcanic regions represent important astrobiological targets given the confluence of geothermal heat and sustained meltwater generation [6,7,16–18]. In this context, wet subglacial environments may be particularly favourable. These locations

provide a variety of protected subsurface niches that are amenable to colonization, including subglacial caldera lakes, englacial lakes, porous subglacial lava edifices, and/or fluid-filled ice fractures [7]. Under conditions of localized ice flow, diverse bioavailable nutrients and redox couples may be liberated from the fragmentation of bedrock and subsequent meltwater-rock interactions [19]; this is a key source of essential nutrients in terrestrial glaciated settings [20]. The release of volcanic gases (e.g., $H_2$, $H_2S$, CO, $CO_2$) could further strengthen redox gradients and provide an additional carbon source [20–22]. The initiation of hydrothermal circulation would accentuate habitability by providing diverse thermal gradients, dispersing nutrients, purging waste, and potentially transporting organisms throughout the system, enabling proliferation [7].

Indeed, Cousins et al., (2011) [7] postulate that if life gained a foothold during the more widely habitable Noachian Period (4.1-3.7 Ga), glaciovolcanic areas of the Hesperian and Amazonian Periods (<3.7 Ga) may have provided an enduring habitable refuge after Mars lost much of its surface water, potentially extending the window of surface habitability. This concept of glaciovolcanic refugia is empirically supported by terrestrial analogues. On Earth, multiple lines of evidence indicate that diverse life must have persisted throughout the Last Glacial Maximum within areas thought to have been covered by large ice sheets [23–27]. Several disparate studies raise the possibility that volcanic/geothermal areas may have acted as long-term refugia for a range of species, uniquely providing warmth and liquid water within otherwise harsh glaciated regions. These include the inferred persistence of a subterranean amphipod species in geothermally created refugia under the Icelandic ice cap [28], of a Patagonian crab in hot springs [29], of bryophytes on the isolated South Sandwich Islands of the maritime Antarctic [30], of marine life during Snowball Earth glaciations in the Neoproterozoic [31], and of fungal diversity in Antarctica [26]. On Mars, evidence that glaciovolcanism has generated large reservoirs of liquid water into the largely arid late Amazonian periods—in some cases forming englacial lakes stable for hundreds to thousands of years—highlight these sites as some of Mars' youngest habitable environments, and possible refugia for organisms that were more widely distributed during past eras [6,16,32–35]. Exploring glaciovolcanic regions may therefore provide a means to access areas where relatively recent biomarkers could be concentrated and remain minimally degraded. Moreover, as one of the last remaining locations where organisms could survive, Martian glaciovolcanic refugia could act as natural winnowing mechanisms in the search for

biosignatures. By focusing on these areas, astrobiological missions could effectively narrow down their search space, targeting environments where the likelihood of finding preserved biomarkers is higher.

However, few studies have characterized the biomarker record of Mars-like glaciovolcanic regions. In this work, we investigate the production and preservation of organic biomarkers at the summit of a partially subglacial volcano in Iceland where high-temperature activity has generated a caldera meltwater lake and a hydrothermally active shoreline. Prior research has revealed a uniquely isolated, predominantly chemosynthetic microbial ecosystem at this site, proposing it as a high-fidelity geobiological analogue for Mars [36,37]. We aim to: (1) characterize the bulk mineralogy of the site to understand the preservation potential of the sedimentary environment, and (2) characterize the diversity and distribution of hydrocarbon biomarkers. Hydrocarbons were selected because they are universal constituents of the biomolecules synthesized by life on Earth [38]. Further, hydrocarbons are intrinsically refractory and much of their original structure can be stable over billion-year timescales once entombed in sediment, making them powerful molecular fossils for early ecosystems on Earth and possibly other worlds [39–41].

It is important to highlight that our investigation occurs in a contemporary setting and represents the earliest stages of diagenesis—when biological activity is still ongoing, and sediments remain in diffusional contact with water. This perspective offers insight into the extent to which the hydrocarbon assemblage reflects the active biological community. This facilitates the identification of early taphonomic filters that might influence the ultimate presence or quality of the molecular fossil record. It also sheds light on potential organic transport and concentration mechanisms operating in the system. In this context, we hypothesized that hydrocarbon abundance would align with the distribution of viable biomass (as detailed in Chapter 2) and would also become concentrated in the caldera lake basin due to hydraulic transport. Validating these trends can offer valuable guidance for future astrobiological endeavors, directing them towards sites most likely to harbour a rich biomarker record. Although this window does not permit us to directly observe the long-term preservation of the biomarker hydrocarbons, by assessing the molecular stability in conjunction with the environment's mineralogical context, we can make informed predictions about their preservation potential. In sum, our goal is to clarify

the potential for basaltic glaciovolcanic sediments to capture and retain biomarker hydrocarbons and lay a foundation for identifying and interpreting analogous signatures on Mars.

## 3.2 GEOLOGICAL CONTEXT

The ice-capped Kverkfjöll volcano is located along Iceland's tectonic rift zone, a subaerial portion of the divergent plate boundary separating the Eurasian and North American tectonic plates (Figure 3.1a) [42]. The main volcanic massif rises to 1900 m altitude, approximately 1000 m above the surrounding area [43], and lies at the northern margin of the Vatnajökull glacier. Kverkfjöll features two summit calderas, of which the northernmost caldera is only partially covered by the glacier (Figure 3.1b).

Although no eruptions have been recorded within the last 1100 years, Kverkfjöll is located almost directly above the Icelandic hot spot [44,45] and remains one of Iceland's most active high-temperature geothermal areas [46]. The temperature of the hydrothermal reservoir liquid is estimated at ~280 °C and is sourced from a local meteoritic groundwater reservoir that has experienced considerable water-rock interaction [42]. Notably, the hydrothermal environments at Kverkfjöll are largely disconnected from marine reservoirs and other subglacial waterbodies elsewhere within Vatnajökull [37,42], creating a relatively closed hydrological system. Magmatic gases are predominated by $CO_2$ (80-97%), with minor amounts of $H_2$ (1-12%), $H_2S$ (1-12%), $CH_4$ (<0.2%), and Ar (<0.01%) [43]. At the surface, hydrothermal activity is currently concentrated on the western rim of the northern caldera [43], within a few well-defined areas (Figure 3.1b).

In this study, we investigated a thermal area located south-east of a mapped region known as Hveradalur. The area is dominated by a steam-heated lake surrounded by a glacial cauldron melted into the ice cap [43]. The lake, locally named Gengissig (or Kverkfjallalón), measures ~300 m in diameter and ~5 m deep at the center (at the time of sampling in summer 2022). Gengissig originated from a steam eruption in 1959 [46]. The lake remains liquid even when ice-bound due to upwelling heat and gases released from subaqueous vents, and often becomes ice-free in the summer months [43,46]. The lake is surrounded by 30-50 m high ice walls on two sides and steep crater rim slopes to the west and north [46]. The water level has been observed to fluctuate dramatically and Gengissig has experienced major drainage events in the form of jökulhlaups (glacial outburst floods), the most recent of which occurred in 2013 [46,47]. The shore of the lake is itself an active vapor-dominated hydrothermal catchment, featuring steaming

fumaroles, hot springs (>87 °C), boiling mud pots, warm mud pools, and heated ground (see Chapter 2 for details on physiochemistry of the system).

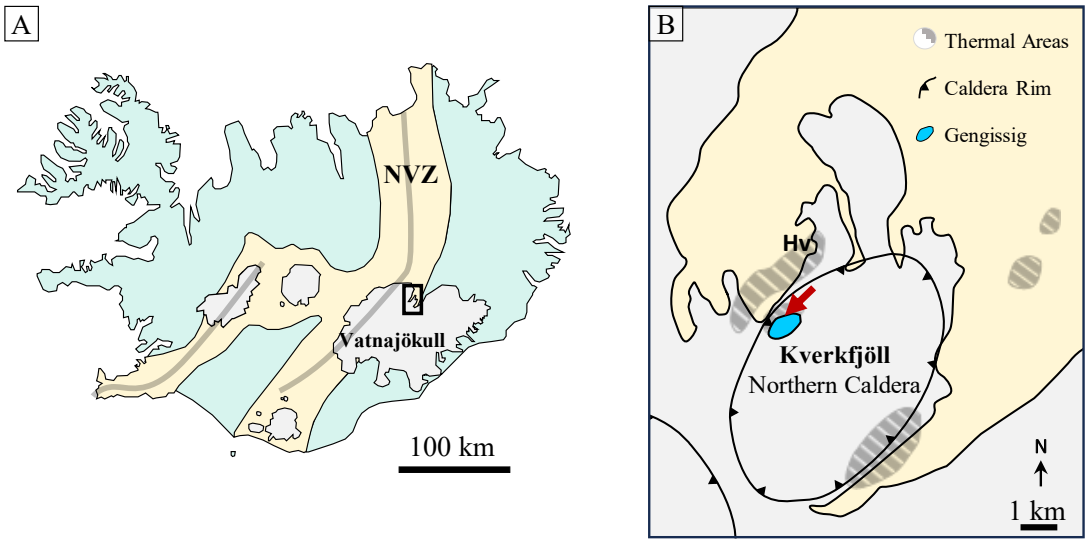


*Figure 3.1: A) Simplified map of Iceland.*

*The neovolcanic zone (NVZ) is depicted in yellow with thick grey lines denoting the approximate locations of active spreading centers. Light grey polygons indicate ice caps/glaciers. A thick black rectangle indicates the location of the Kverkfjöll volcanic area at the northern margin of the Vatnajökull ice cap. B) Study site context map. Volcanic calderas and thermal activity of the Kverkfjöll high-temperature area are shown (adapted with permission from Ólafsson 2001* [43]*). Our study site is located on the north-western shore of lake Gengissig (red arrow). "Hv" marks the approximate location of the Hveratagl area investigated by Moreras-Marti et al. (2021)* [48] *and discussed in section 3.5.5.*

### 3.2.1 Analogy to Mars

The Kverkfjöll hydrothermal catchment is an excellent glaciovolcanic Mars analogue environment for several reasons. First, the primary eruptive materials are basaltic [45]. All environments on Mars originate from basaltic sources due to the lack of large-scale felsic crust [49], and understanding the taphonomy of organic biomarkers within basaltic sedimentary environments is therefore crucial for assessing potential astrobiological targets on Mars. However, it is important to note that Mars and Earth have fundamental chemical and physical differences that impact the nature of volcanism on their surface and, by extension, the composition of their basaltic lavas. A notable distinction is the relative abundance of FeO in their respective mantles; Mars has a much higher FeO content (18.2 wt%) than Earth (8.1 wt%) [49,50]. This Fe enrichment results in basaltic lavas with elevated FeO (13–21 wt%) compared to their terrestrial counterparts (~10–15 wt%) [49–51]. At Kverkfjöll, the primary lavas exhibit FeO contents at the upper end of the terrestrial range (13.83-15.45 wt%), and their bulk igneous composition is similar to that of the Martian crust [45,49]. Considering that reactive Fe-bearing

minerals have specifically been identified as key factors in the long-term storage of organic carbon [52,53], Kverkfjöll offers a relatively unique geochemical opportunity to study glaciovolcanic sediments with a suitably Mars-like chemistry to elucidate their astrobiological potential.

Second, the site presents the opportunity to study a relatively pristine biological community dominated by prokaryotic life-forms. Kverkfjöll is situated in an extremely remote location, with a vast ice sheet on one side and the arid volcanic desert of Iceland's highland region on the other. This harsh, isolated landscape minimizes plant, animal, and anthropogenic activity in the area. Further, the closed hydrothermal reservoir and the lack of overland inflow channels further minimizes external contamination. As a result, the hydrothermal catchment is home to a predominantly prokaryotic community supported primarily by chemotrophic cycling of local volcanic inputs; phototrophy does not play a major role in primary productivity [37,48]. This is important considering that, if it existed, Martian life likely remained in a simple state, possibly analogous to Earth's early cells [54]. It may have never evolved to the point of developing oxygenic photosynthesis [54–56], nor large differentiated tissue structures [57]. Since it remains uncertain whether molecular fossils derived from higher order plants or animals have comparable preservation behaviour to those derived from prokaryotes [58], predominantly prokaryotic analogue sites offer a more realistic simulation of the Martian environment.

## 3.3 METHODS

### 3.3.1 Field Sampling

Sampling was conducted in May and June of 2022. Duplicate sediment samples were collected for mineralogical and organic analyses. All sediment samples were collected using new nitrile gloves and various stainless-steel tools (scoopula, shovels, trowels, Petite Ponar® Grab sampler) which had been triple rinsed with an ascending series of organic solvents (namely, acetone, dichloromethane, and methanol) before deployment to the field and individually packaged in ashed aluminum foil. Nominally, new collection tools were used for each sample, however, when tools needed to be re-used in the field, they were first ethanol-rinsed and then pre-contaminated in sediment immediately adjacent to the sampling location. Samples were stored in sterile Whirl-Pak bags and frozen in the field using an ice-packed cooler. Samples were then lyophilized for 48 to 72 hours upon return to the laboratory.

Two distinct areas of thermal activity were visually identified on the north-west shore of lake Gengissig and prioritized for sampling; these are detailed in the following subsections. A summary of samples is provided in Table 3.1 and a sampling map is depicted in Figure 3.2.

#### *3.3.1.1 Sampling Area 1: Spring-Lake Transect*

The first system compromised a vigorously bubbling hot spring (T = 87.0 °C and pH = 7.7, see Chapter 2 for details) connected to lake Gengissig via a warm, shallow stream (~90 m long, 1-10 cm depth) (Figure 3.2 & Figure 3.3). We aimed to sample along a transect from the spring to the lake center to evaluate changes in the hydrocarbon profile associated with the variable hydrothermal conditions. Given the challenging topography and unstable stream bank, systematic sampling was impractical along the stream. Instead, end-member localities were prioritized. These included the hot spring source pool (*S_Source*), the stream's distal end (*S_Distal*, ~80 m downstream from the source pool), and a mid-point along the stream (*S_Mid_Mat*). The mid-point location featured a green filamentous microbial mat, representing the only macroscopic evidence of microbial colonization amongst the samples. This mat spanned about 20 m of the stream and was confined to a segment with temperatures ranging from 30-47 °C; a sediment sample was collected from the streambed, beneath the mat.

An inflatable boat was used to continue the transect from the stream mouth to the lake center (~60 m from shore). We attempted to collect lake-bed sediment samples at 10-m intervals using the Petite Ponar® Grab sampler, however, the coarse grain size of the proximal sediments prevented the sampler from closing and acquiring a sample. Approximately 50 m from shore, the sediments transitioned to a finer grain-size, enabling successful lakebed sampling at distances of ~50 m (*L_50m*) and ~60 m (*L_60m*) from shore (the sediment from site *L_50m* measured 70 °C with an infrared thermal gun, suggesting that we sampled a submerged hot spring). An additional lakebed sample was taken manually 3 m from the shore using a stainless-steel shovel (*L_3m*).

It is important to note that Cousins et al. (2018) [36] also describe sampling a hot spring and thermal overflow stream on the shore of Lake Gengissig in 2011. However, considering the current spatial distribution of hydrothermal features and the chemical characteristics of the fluids at the site (refer to Chapter 2), it appears that the Spring-Lake system we studied is either distinct or has undergone significant changes over time.

#### *3.3.1.2 Sampling Area 2: Elevated Mud Pot (MP) Area*

The second system was an elevated mound featuring thermal mud pots and pools (Figure 3.2 & Figure 3.3). The prominent feature was a large quiescent thermal pool, approximately 3 x 7 m in size, lined with viscous and sticky blue-grey mud. The pool was characterized by a temperature of ~43 °C and pH ~3.1 (average of four replicate measurements approximately 10 cm below the water surface at pool edge). The area around the active pool was soft and showed mud-crack patterns with shallow depressions. The depressions are interpreted as inactive/semi-dehydrated mud pools. Beneath the mud-cracked crust (<1 cm thick) was a thick layer of moist blue-grey mud (Figure 3.3e). The underlying mud was warm (8-20 °C; at an ambient air temperature of ~4 °C) and showed varying moisture levels between different depressions, suggesting different durations of inactivity. Sediment was sampled from the margin of a large thermal pool, ~10 cm below the water surface (MP 7).

Sediment was collected from the large thermal pool (*MP_Pool*) and from the inactive mud pots, including a damp and warm (20 °C) hollow interpreted as a recently inactive thermal pool and a cooler (8 °C), mostly dry hollow interpreted as a longer inactive thermal pool. In the case of the inactive pools, the mud-cracked upper crust was sampled separately from the underlying massive mud.

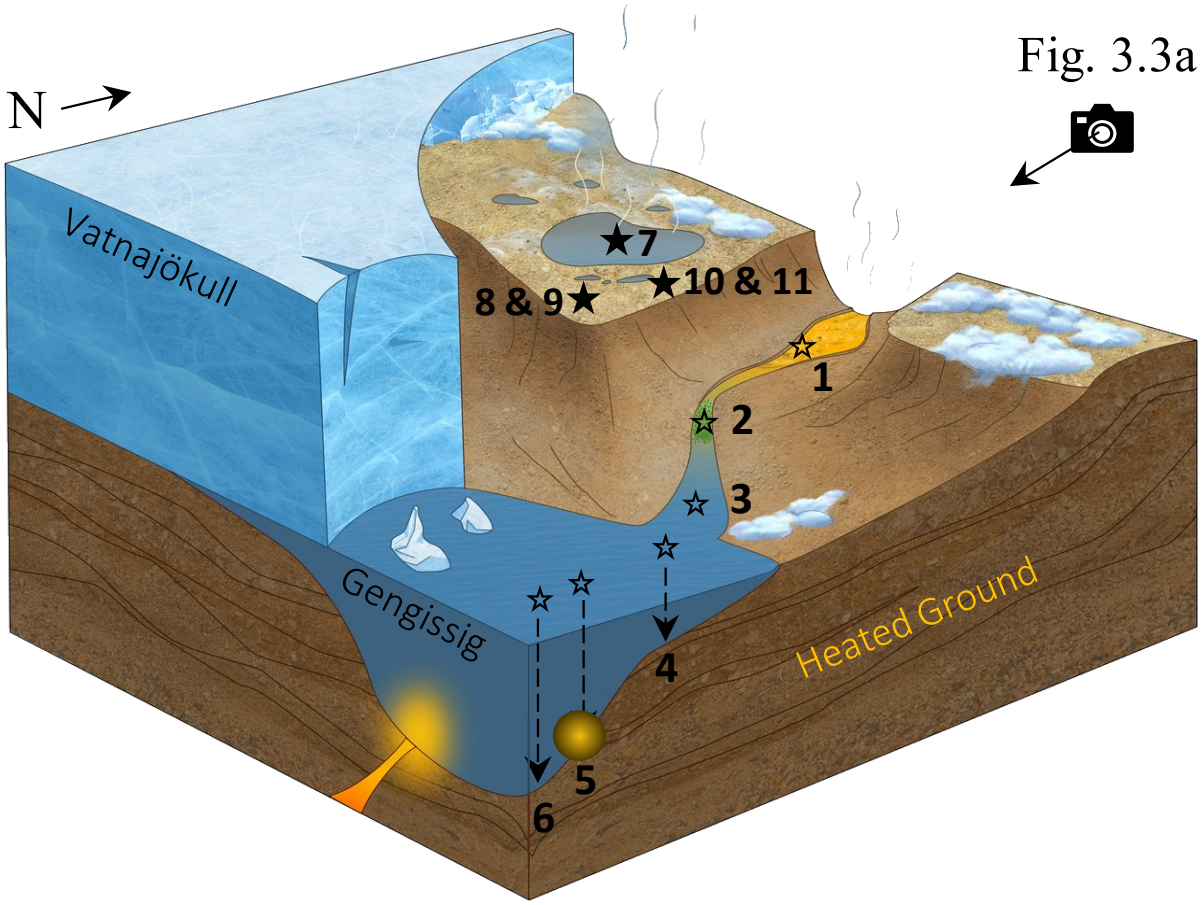


*Figure 3.2: Field sampling sites.*

*Simplified site schematic showing the spatial arrangement of major hydrothermal features and sampling sites. Open stars depict sampling sites along the Spring-Lake transect. Filled stars depict sampling sites in the Mud Pot region; see Table 3.1 for sample numbers. The camera icon represents the approximate position of the context photo presented in Figure 3.3a. Drawing not to scale.*

| | Sample Metadata | | | | Surrounding Fluid Characteristics* | | |
|---|---|---|---|---|---|---|---|
| | **Fig. 3.2 ID #** | **Sample Text ID** | **Sample Description** | **Dominant Grain Size** | **T ( °C)** | **pH** | **DO† (mg/L)** |
| **Spring-Lake Transect** | **1** | **S_Source** | Vigorously bubbling hot spring vent. Subaqueous grey sediment collected. | Clay-coarse sand | 87.0 | 7.7 | 0.5 |
| | **2** | **S_Mid_Mat** | Stream mid-point. Green microbial mat. Underlying sediment collected. (Figure 3.3b) | Coarse sand-pebbles | 37.0 | 8.4 | 4.2 |
| | **3** | **S_Distal** | Distal end of stream before meeting lake Gengissig (~80 m downstream). Gravelly sediment. | Coarse sand-pebbles | 34.6 | 8.5 | 3.6 |
| | **4** | **L_3m** | Lakebed sediment sample, 3m from shore, ~0.5 m depth. | Coarse sand-pebbles | 19.2 | 6.6 | 4.7 |
| | **5** | **L_50m** | Lakebed sediment sample, 50m from shore, ~5 m depth. 70 °C at collection. | Clay | 64.8 | 6.1 | 0.4 |
| | **6** | **L_60m** | Lakebed sediment sample, 60m from shore (lake center), ~5 m depth. | Clay | 8.8 | 5.8 | 0.4 |
| **Mud Pot Area** | **7** | **MP_Pool** | Large thermal mud pool. Sediment collected ~10 cm below water surface. | Clay | 43.0 | 3.3 | 3.1 |
| | **8** | **MP_Recent_Crust** | Cracked upper crust of damp hollow interpreted as recently inactive mud pool. (Figure 3.3e) | Clay-fine sand | N/A | N/A | N/A |
| | **9** | **MP_Recent_Low** | Dense, warm underlayer of damp hollow interpreted as recently inactive mud pool. (Figure 3.3e) | Clay | N/A | N/A | N/A |
| | **10** | **MP_Old_Crust** | Cracked upper crust of drier hollow interpreted as long-inactive mud pool. (Figure 3.3f) | Clay-fine sand | N/A | N/A | N/A |
| | **11** | **MP_Old_Low** | Dense, warm underlayer of drier hollow interpreted as long-inactive mud pool. | Clay | N/A | N/A | N/A |

*Table 3.1: Summary of samples for organic analysis.*

*Samples are given a numeric code corresponding to the labels on Figure 2.2, as well as short informative name that indicates their general collection areas (S=spring/stream, L=Lake, MP=Mud Pot).*
**Physicochemical data of the surrounding hydrothermal fluids collected concurrently with subaqueous sediment samples. Note: No contextual fluid data available for inactive (subaerial) Mud Pots. Data are reproduced from Chapter 2.*
*† DO = Dissolved Oxygen*

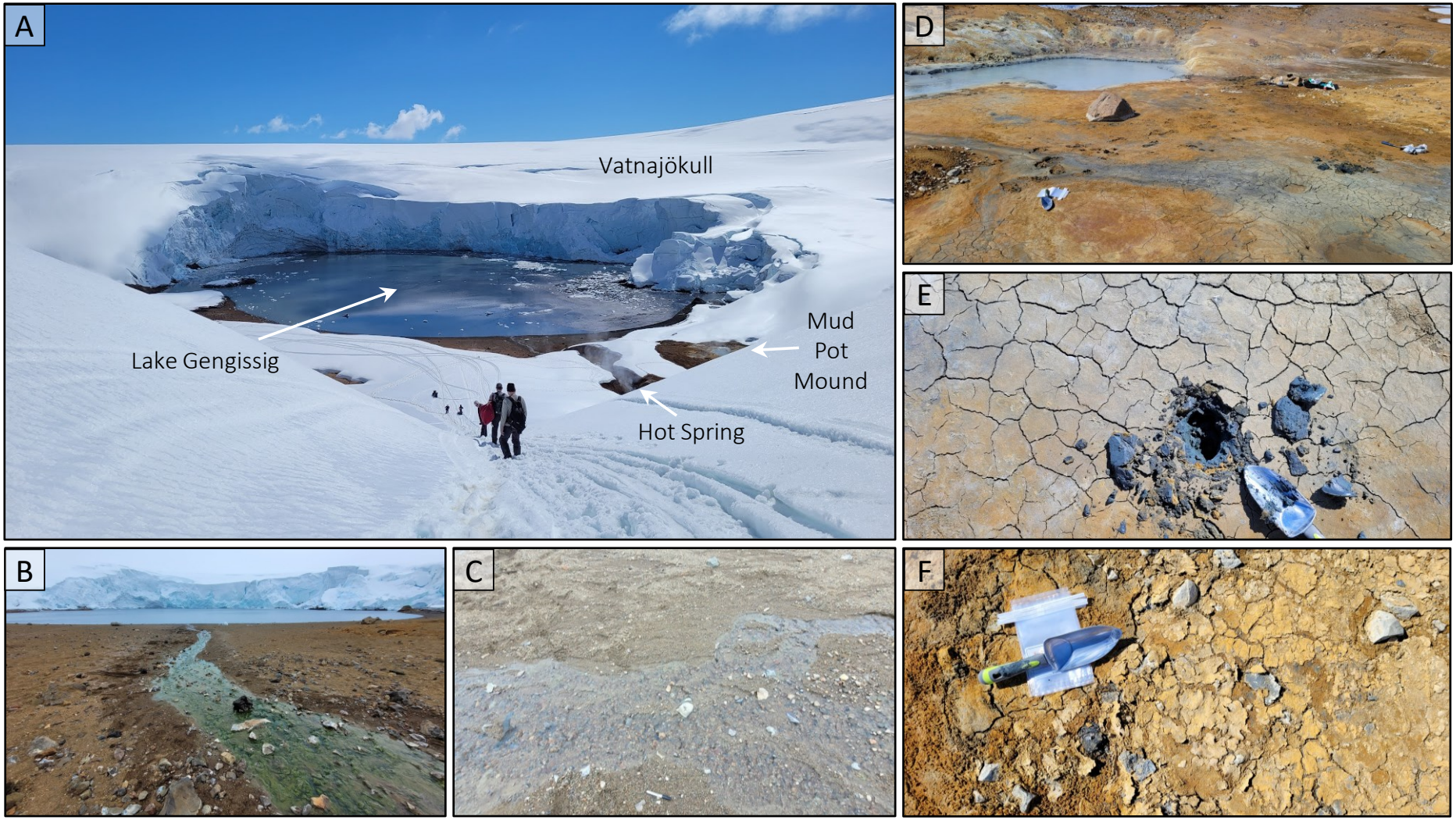


*Figure 3.3: Field photographs.*

*A) Context photo of whole study site highlighting the spatial arrangement of various hydrothermal features. B) Photo of the green filamentous microbial mat in hot spring stream, approximate location of sample 2.S_Mid_Mat. C) Distal portion of the hot spring overflow stream, showcasing the clarity of the spring water; approximate location of sample 3.S_Distal. D) Contextual photo of the Mud Pot area, showing the large pool in the background (7.MP_Pool) and the damp, mud cracked hollows interpreted as inactive mud pools. E) Close-up photograph of a recently inactive mud pot. The upper crust is relatively dry, and mud cracked (site of 8.MP_Recent_Crust.); crust is underlain be warm (~20 °C), damp, massive blue-gray mud (site of 9.MP_Recent_Low). F) Close-up*

*photograph of a longer inactive mud pot. The upper crust is very dry, cracked, curled, and oxidized (site of 10.MP_Old_Crust); crust is underlain by less warm (~8 °C), dry, massive blue-gray mud (site of 11.MP_Old_Low).*

### 3.3.2 Bulk X-Ray Diffraction

Sediment samples were dried at 50 °C for 1-5 days and hand-ground to <50 μm using an agate mortar and pestle without the addition of liquids. The random oriented powders were prepared using the "razor tamped surface" technique described by [59]. Analyses were conducted at the McMaster Analytical X-Ray Diffraction Facility (Ontario, Canada) using a Bruker D8 DISCOVER equipped with a 2.5 Axial Soller slit and EIGER2 R 500K Detector. The instrument was operated in 1D mode with a Co-tube (1.79 Å), 0.02° 2θ step size, 2.5 s/step, and 5-83° 2θ scan range. Mineral phases were identified using the Bruker EVA software, with the International Centre for Diffraction Data Powder Diffraction Files (ICDD PDF) 4+ database for comparison. This software matches the measured diffraction pattern (peak positions and relative peak heights) against the patterns of mineral phases for which structural information is available in the database, suggesting likely matches.

### 3.3.3 Hydrocarbon Analysis

#### *3.3.3.1 Extraction*

Sedimentary samples for lipid analyses were lyophilized for 48 to 72 hours to remove excess water and subsequently homogenized by light grinding in a solvent-cleaned agate mortar and pestle. All glassware was precombusted at 450 °C for 8 hours. Non-combustible equipment was solvent-rinsed five times with a sequence of hexane, dichloromethane, and methanol.

Total lipids were extracted from representative aliquots of each sample (between 5 and 50 g of sediment) using a modified Bligh and Dyer protocol [60]. In detail, each sample was suspended in a monophasic solvent solution of dichloromethane, methanol, and 50 mM phosphate buffer (adjusted to pH = 7.4 using HCl) in a ratio of 1:2:0.8 by volume. The suspensions were sonified for 15 minutes to ensure complete penetration of the solution into the sediment and allowed to extract overnight at room temperature on a shaker table set to 80 rpm. The extraction solutions were then decanted and filtered through solvent-rinsed 1.5 μm binder-free VWR® glass fiber filters into glass separatory funnels. Total lipid extracts were collected after phase partitioning by adding dichloromethane and Milli-Q water to the funnel to achieve a final solvent ratio of 1:1:0.9 by volume. Following the methods of [61], the total lipid extracts were dried under a gentle stream of nitrogen and immediately re-dissolved in a small amount of hexane:dichloromethane solution (7:3, v/v). The complete extraction procedure was repeated on the same sediment aliquot and the total extracts combined. Acid-activated and solvent-cleaned copper pellets were added

and allowed to react overnight to remove elemental sulfur. The S-treated total extract was concentrated to a small volume under nitrogen gas. Hydrocarbons were isolated using silicic acid column chromatography, eluted with 40 mL of hexanes. The purified hydrocarbon fractions concentrated under a nitrogen and stored at 4 °C until analysis. One extraction blank was prepared for every six sediment extractions to monitor contamination.

#### *3.3.3.2 Gas-Chromatography/Mass-Spectrometry*

Hydrocarbons were analyzed on an Agilent 7890B GC equipped with an Agilent 7693 auto sampler and an Agilent 5977B high efficiency source Mass Selective Detector. Analytical separation of the compounds was accomplished using a 30 m × 0.25 mm × 0.25 um DB-5 MS UI column (J&W Scientific, Folsom, CA). Helium was the carrier gas, in a constant-flow mode. The column temperature was programmed from 50 °C to 120 °C at 10 °C/min, then to 310 °C at 5 °C/min, and then held for 20 min. The MS was operated under the following conditions: the injection port temperature was 3000 °C, the MS source temperature was 300 °C, and the MS quadrupole temperature was 150 °C. Electron impact ionization (70 eV) was used, and full scan spectra were obtained by scanning m/z 50–800 at 1 scan/s.

Compound assignment was based on co-elution with the Supelco® $C_7$-$C_{40}$ Saturated Alkanes Standard and assessment of the fragmentation pattern with comparisons to literature and the NIST (National Institute of Standards and Technology) mass spectral database. Individual compounds were quantified using the response of 5-point external calibration curves consisting of standards of hexadecane, octadecane, eicosane, and tetracosane. Where applicable, the concentration of the unresolved complex mixture was semi-quantitatively determined by integrating the total area of the chromatographic 'hump' and using the average response factor of octadecane standard curve.

#### *3.3.3.3 Lipid Nomenclature*

A common shorthand nomenclature is used throughout this paper to designate aliphatic lipid molecules. The alkyl chain is designated as $C_{X:Y}$, where X is the number of carbons on the longest continuous carbon chain and Y is the number of unsaturations, if present. Straight and saturated chains are designated as "normal" and are labelled with the prefix *n*- (e.g., *n*-$C_x$). For mid-chain methyl-branched alkanes, we adopt the common abbreviations for monomethylaklanes (MMA), dimethylakanes (DMA), and trimethylalkanes (TMA).

#### *3.3.3.4 Data Processing*

Quantified hydrocarbons are reported per gram of sediment extracted (dry weight). A number of indices were calculated to characterize the biomarker distributions and elucidate their source (See Appendix B for specific calculation details). These include:

- *Chain Length Range* is simply the range of the most abundant carbon chain lengths observed in hydrocarbon molecules extracted from environmental samples. Specific ranges are often characteristic of groups of organisms and are used, in part, to determine the sources and composition of sedimentary organic matter ([62], and references therein). For instance, short-chain *n*-alkanes ($<C_{20}$) are mainly derived from bacteria, algae, and/or planktons as well as other possible marine sources (in phytoplankton and zooplankton, these short chains are characterized by a predominance of odd numbers of carbon atoms [$C_{15}$, $C_{17}$, or $C_{19}$], while bacterial origins are dominated by even numbers [58,62]; see *CPI* below). Middle-length chained *n*-alkanes (*i.e.*, $C_{20}$-$C_{25}$) are dominant components of submerged and floating aquatic macrophytes. Long-chain *n*-alkanes ($C_{25}$-$C_{35}$), especially with a strong odd-to-even carbon preference (see *CPI*), mainly have terrestrial sources (e.g., higher plants).
- *Average Chain Length* (ACL) is defined as the average number of carbons in the hydrocarbon chains extracted from a given sample. The ACL parameter has been used to distinguish hydrocarbons associated with higher plants (ACL ≈ 30), from those of algae (ACL ≈ 29), or microorganisms (ACL ≲ 20), as well as to identify petrogenic hydrocarbon inputs (ACL ≈ 28) [58,62].
- *Low Molecular Weight (LMW) to High Molecular Weight (HMW) ratio* (LMW/HMW) is computed here as the sum of *n*-alkanes with chains of 23 carbons or less, over the sum of *n*-alkanes with chains of 24 carbons or greater [63]. Similar to the ACL, this ratio enumerates the general trend of chain lengths observed in a sample and has been used to assess prokaryotic versus eukaryotic inputs, where prokaryotes generally biosynthesize proportionally more LMW compounds (e.g., [64,65]).
- *Carbon Preference Index* (CPI) is defined as the ratio of odd-numbered carbon chains to even-numbered carbon chains. We calculate the CPI for two ranges: the low molecular weight range, $<C_{23}$ ($CPI_{LMW}$) and the high molecular weight range, $>C_{25}$ ($CPI_{HMW}$). A CPI value of ~ 1 is frequently considered as an indication of abiotic hydrocarbons or of

very mature (degraded) fossil matter; values which differ significantly from 1 indicate biological input or modification [65–67].

Lastly, to investigate possible correlations between hydrocarbon abundance and estimates of biomass or total organic carbon, Spearman's Correlation Coefficient ($r_s$) was computed using PAleontological STatistics (PAST) v.4.09. A p-value of 0.05 was set as the threshold for significance.

## 3.4 RESULTS

### 3.4.1 Mineralogical Characterization of the Substrate

The bulk XRD patterns (Figure 3.4) are similar across the site. The data reveal the ubiquitous presence of abundant phyllosilicate, marked by a strong, broad, and asymmetric 001 diffraction peak extending from ~12 to 17 Å. This is reflective of the large interlayer spacing within a 2:1 smectite [68,69]. Although this broad range of 001 diffraction is common to a variety of phyllosilicates, the breadth of the peak and the absence of other well-defined peaks, such as an 002 peak at 5 Å (~20.6 2θ), indicate that the presence of well-crystallized phyllosilicates like mica or illite is unlikely. Additionally, there is no evidence of the sharp diffraction peaks for kaolinite or chlorite-group minerals at 7 Å (~14.6 2θ). The smectite 060 reflections display peak apex positions ranging from 72.706-73.062 2θ, or d-spacings of 1.509-1.503 Å. Such values are consistent with dioctahedral smectite species [68]. Specific identification of the smectite species is ongoing.

The composition of the crystalline mineral assemblage was also largely identical across the site, with all samples comprising abundant heulandite (Ca/Na zeolite) and pyrite, with lesser relative amounts of plagioclase, low-quartz, and anatase. Gypsum was identified in three samples only: the upper and lower layers of the mostly dry mud pot (*10.MP_Old_Crust* & *11.MP_Old_Low*) and the dry upper layer of the damp mud pot (*9.MP_Old_Crust*), suggesting that it is the product of subaerial alteration. Calcite was identified as the primary constituent of the rock coatings proximal to the subaerial hot spring vent, but only minor calcite peaks were detected in the sediments of the overflow stream.

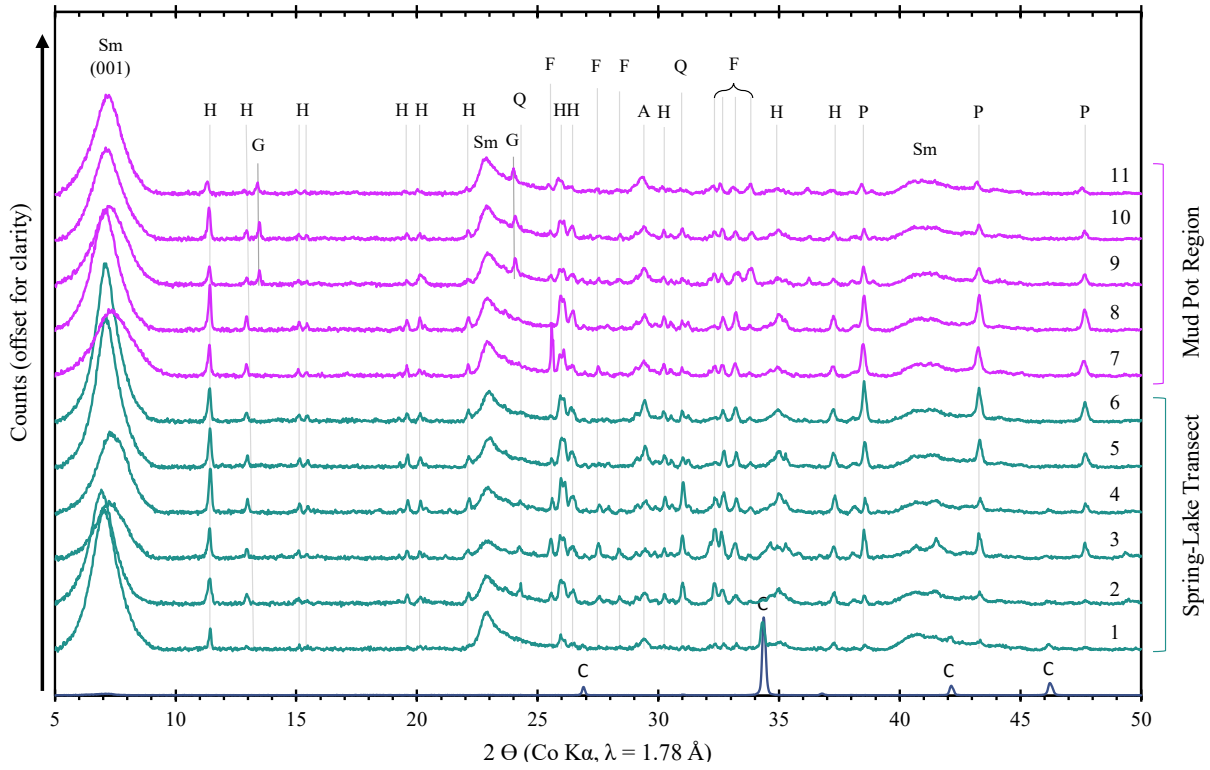


*Figure 3.4: Background-subtracted XRD patterns of bulk sediments.*

*Offset vertically for clarity. Samples are labelled on the right according to the numeric code listed in Table 3.1. Major peaks of identified minerals are labelled: Sm – smectite (the 001 peak near 7˚ 2Θ is asymmetric before background subtraction), H – heulandite, Q – low quartz, F – plagioclase feldspar, A – anatase, P – pyrite, G – gypsum, C – calcite. Labels for minor peaks of the same mineral are omitted for simplicity.*

### 3.4.2 Extracted Hydrocarbon Profiles

GC-MS analysis revealed a variety of hydrocarbon compounds. The total yields and descriptive indices of these hydrocarbons are documented in Table *3.2* (a complete list of identified compounds with retention times is included in Appendix B). Two distinct hydrocarbon assemblages were observed throughout the system, referred to as Group 1 and 2. These patterns are detailed below. Notably, two samples (*S_Mid_Mat* and *MP_Recent_Low*) exhibited characteristics of both Group 1 and Group 2, indicating a mixture of the two end-member distributions in these particular samples. Biomarker isoprenoid alkanes, such as pristane and phytane (often linked to chlorophyll degradation [39]), as well as crocetane and squalane (commonly associated with archaea [64]), were not detected in any samples.

#### *3.4.2.1 Group 1 Distribution*

Four samples from the mud pot region exhibited a profile with a narrow range of hydrocarbons in the low molecular weight range (*n*-$C_{14}$ to *n*-$C_{20}$) (Figure 3.5). These distributions were characterized by a high abundance of heptadecane (*n*-$C_{17}$), which accounted for 11-28% of the identifiable hydrocarbons. Additionally, these samples contained various mono-, di-, and tri-methylheptadecanes (MMH, DMH, and TMH, respectively). The relative retention times and mass fragmentographic responses were used to tentatively identify several specific methyl-branching positions, including the 7-, 6-, 5-, and 4-MMHs; the 4,5-, 5,12-, and 5,13-DMHs; and the 4,5,13-TMH. Other chromatographic peaks were assigned to the DMH suite based on retention time, but the positions of branching could not be confirmed.

#### *3.4.2.2 Group 2 Distribution*

Although local physicochemical parameters such as temperature, pH, and dissolved oxygen showed significant variation at the time of collection, most samples from the Spring-Lake Transect exhibited a strikingly similar hydrocarbon profile that is distinct from the Group 1 profile (Figure 3.6a). This distribution includes a convex baseline in the GC retention region of *n*-$C_{16}$ to *n*-$C_{24}$, known as an "unresolved complex mixture" (UCM). The UCM is unimodal with a maximum at ~*n*-$C_{19\text{-}20}$. Several specific hydrocarbon peaks are visible above the UCM bulge; normal alkanes were identified through comparison with the Supelco® $C_7$-$C_{40}$ Saturated Alkanes Standard and normal alkenes were identified by their fragmentation pattern and elution characteristics. Several compounds could not be confidently identified.

The *n*-alkanes ranged from *n*-$C_{12}$ to *n*-$C_{31}$ with a pronounced predominance of compounds shorter than *n*-$C_{23}$ (LMW/HMW>>1). The *n*-alkane suite also showed a strong even carbon-number preference in the *n*-$C_{14\text{-}22}$ range, with 2-4 maxima per sample (typically *n*-$C_{16}$, *n*-$C_{18}$, *n*-$C_{20}$, and/or *n*-$C_{22}$) (Figure 3.6b). Heptadecane (*n*-$C_{17}$) was abundant in all samples, slightly offsetting the prevailing even-over-odd character (Figure 3.6b). However, the $CPI_{LMW}$ values were consistently less than 1, ranging from 0.57 – 0.85, highlighting a marked even-carbon preference amongst the short-chained compounds, despite the co-occurring abundance of *n*-$C_{17}$. Higher molecular weight *n*-alkanes were present in only trace amounts and exhibited no carbon chain length preference ($CPI_{HMW}$ was consistently near unity).

A homologous series of even-numbered *n*-alkenes were also detected at high concentrations, including *n*-$C_{14:1}$, *n*-$C_{16:1}$, *n*-$C_{18:1}$, *n*-$C_{20:1}$, and *n*-$C_{22:1}$. The most abundant was *n*-$C_{18:1}$. Although

the exact position of the double bond could not be determined by our methods, the *n*-alkenes consistently eluted immediately before the corresponding even-numbered *n*-alkane, forming a striking alkane/alkene pair in the chromatogram (Figure 3.6a). Neither high-molecular weight *n*-alkenes, nor odd-numbered *n*-alkenes were observed.

Lastly, it is important to highlight that samples exhibiting the Group 1 and Group 2 profiles were collected and analyzed following an identical protocol. This consistent methodology implies that the distinct hydrocarbon profiles observed are inherent to the samples, not artifacts of our analytical process. Therefore, contamination as a source for the observed patterns is unlikely, reinforcing the authenticity of these distinct profiles.

| Sample Text ID | Dist.[a] | TOC (%)[b] | Biomass Estimate (#Cells/g)[b] | Total Identified HCs (pmol/g) | Total Identified HCs (ug/g) | UCM (ug/g) | Chain Length Range | ACL | CPI $_{LMW}$[c] | CPI $_{HMW}$[d] | LMW/ HMW |
|---|---|---|---|---|---|---|---|---|---|---|---|
| **MP_Pool** | Group 1 | 0.35 | 2E+08 | 5.73E+04 | 14.97 | n.d. | 15 – 20 | 18 | N/A | N/A | N/A |
| **MP_Recent_Crust** | | 2.12 | 1E+10 | 1.16E+05 | 29.06 | n.d. | 14 – 20 | 18 | N/A | N/A | N/A |
| **MP_Old_Crust** | | 3.14 | 1E+10 | 1.65E+05 | 42.60 | n.d. | 15 – 20 | 18 | N/A | N/A | N/A |
| **MP_Old_Low** | | 0.38 | 7E+08 | 3.99E+04 | 10.18 | n.d. | 14 – 19 | 18 | N/A | N/A | N/A |
| **MP_Recent_Low** | Mixed | n.d. | 8E+07 | 1.70E+03 | 0.44 | 0.13 | 12 – 29 | 19 | N/A | 1.1 | 5.5 |
| **S_Mid_Mat** | | 0.09 | 2E+09 | 1.82E+04 | 4.53 | n.d. | 13 – 30 | 18 | 1.3 | 1.1 | 18.3 |
| **S_Source** | Group 2 | n.d. | 3E+06 | 3.73E+03 | 0.97 | 8.03 | 12 – 29 | 18 | 0.9 | 1.0 | 13.8 |
| **S_Distal** | | n.d. | 5E+07 | 3.68E+03 | 1.01 | 8.00 | 12 – 31 | 20 | 0.6 | 1.1 | 4.8 |
| **L_3m** | | n.d. | 2E+07 | 1.60E+03 | 0.46 | 2.92 | 14 – 31 | 21 | 0.6 | 1.0 | 3.6 |
| **L_50m** | | n.d. | 2E+07 | 1.85E+03 | 0.51 | 4.83 | 14 – 31 | 20 | 0.6 | 1.1 | 5.1 |
| **L_60m** | | n.d. | 8E+07 | 1.13E+03 | 0.32 | 3.65 | 14 – 31 | 20 | 0.6 | 1.0 | 6.1 |

*Table 3.2: Compositional summary of lipid hydrocarbon (HC) distribution.*

*Samples are labeled using the short informative name that indicates their general collection areas (S=Spring/stream, L=Lake, MP=Mud Pot).*

*[a] 'Dist.' Denotes the distribution group to which each sample's hydrocarbon distribution broadly aligns. Samples have been categorized into two main distribution groups based on their hydrocarbon patterns, see Section 3.4.2.*

*[b] Total Organic Cabron (TOC) and biomass estimates are reprinted from Chapter 2. Uncertainty is ±0.07%.*

*[c] Carbon Preference Indec for Low Molecular Weight Compounds ($CPI_{LMW}$) could not be calculated for samples with a strong Group 1 or mixed distribution since the n-$C_{18}$ compound could not be verified or quantified – see text for details.*

*[d] Carbon Preference Indec for High Molecular Weight Compounds ($CPI_{HMW}$) and the Low Molecular Weight to High Molecular Weight ratio (LMW/HMW) could not be calculated for samples without hydrocarbons in the HMW range (>$C_{23}$).*

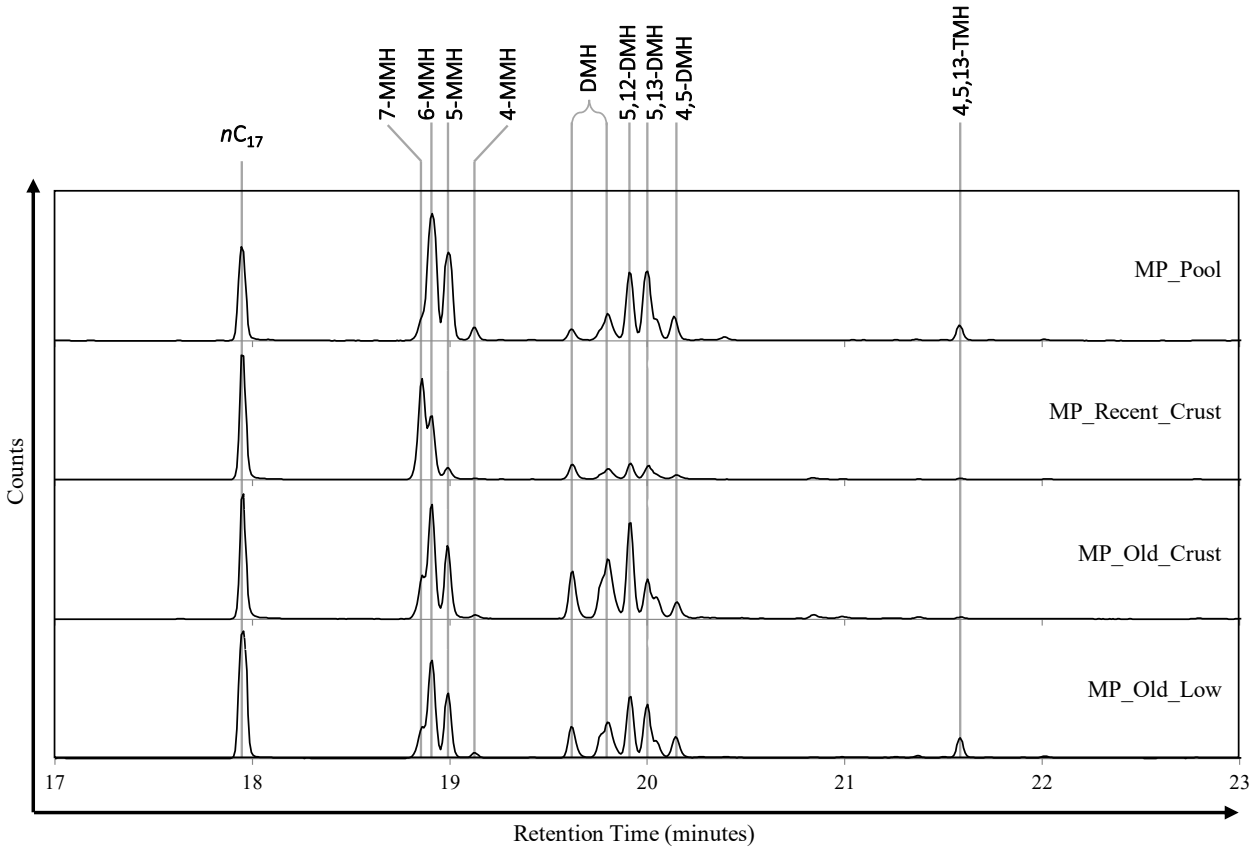


*Figure 3.5: Total ion current GC-MC chromatograms of samples showing the Group 1 Distribution.*

*The Group 1 Distribution is characterized by a strong heptadecane signal, and a suite of mid-chain branched heptadecane compounds. X-axis is truncated to show predominant compounds. Y-axis is not constant across panels as the objective of this figure is to show the distribution of various compounds. MMH = monomethylheptadecane, DMH = dimethylheptadecane, TMH = trimethylheptadecane.*

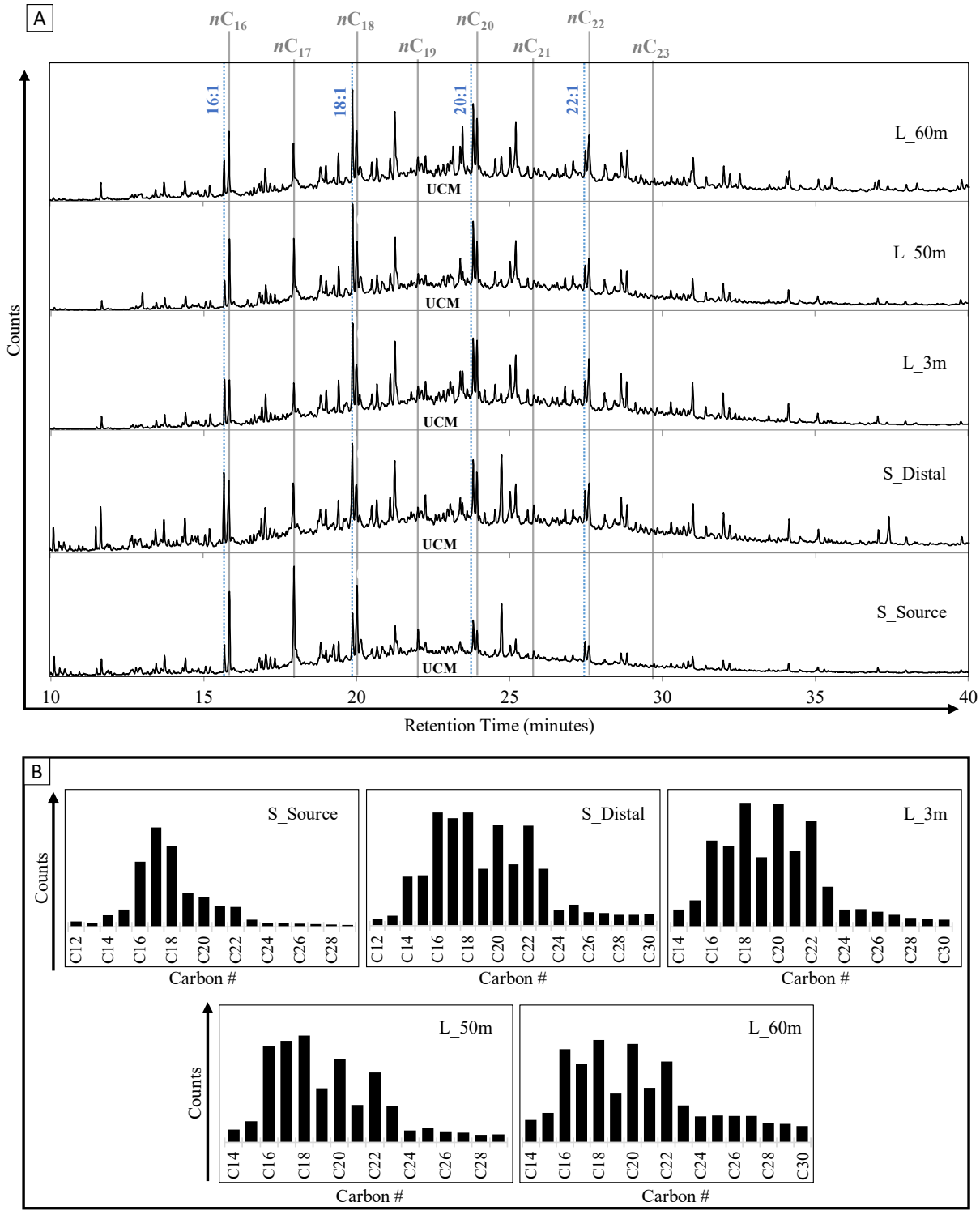


*Figure 3.6: A) Total ion current of GC-MS chromatograms of samples bearing the Group 2 Distribution.*

*The Group 2 Distribution is characterized by a pronounced UCM, alkanes (gray lines) with an even carbon preference, and a series of even-numbered alkenes (blue dotted lines). Y-axis is in arbitrary units of intensity; it is not constant between panels as the objective of this figure is to showcase the overall pattern of the distribution. B) Relative abundance of n-alkanes in each sample exhibiting the Group 2 Distribution to exemplify the pronounced even-over-odd carbon preference in the low molecular weight compounds (<$C_{23}$).*

## 3.5 DISCUSSION

### 3.5.1 Interpretation: Biogenicity of Observed Hydrocarbons

#### *3.5.1.1 Group 1: Attributed to Cyanobacteria*

The composition of alkanes in the Group 1 profiles closely aligns with the alkane assemblage typically reported for cyanobacteria [81–85]. Notably, heptadecane (*n*-$C_{17}$), which is the most commonly observed hydrocarbon in freshwater cyanobacteria, including both unicellular and filamentous strains [70–73], is among the most prominent compounds of the Group 1 hydrocarbons. However, *n*-$C_{17}$ is also present in many aquatic algae, as well as both photosynthetic and non-photosynthetic bacteria [74]. Biological markers that are more diagnostic for a cyanobacterial origin are mid-chain branched alkanes, including mono-, di-, and tri-methylalkanes (MMA, DMA, TMA), specifically those within the $C_{17}$-$C_{20}$ chain length range [70,75–77]. These robust biomarkers for cyanobacterial input constituted a significant portion of the Group 1 hydrocarbon profile (64-88% of the identifiable compounds) (Figure 3.5; Appendix B). In particular, the 6- and 7-methylheptadecanes or 5,12-dimethylheptadecane are generally the most abundant branched alkanes. The high concentration of these specific branched heptadecanes is consistent with previous descriptions of Icelandic hot spring microbial mats dominated thermophilic cyanobacteria [77], suggesting a similar biological source for our samples.

#### *3.5.1.2 Group 2: Attributed to Diverse Microorganisms*

The Group 2 hydrocarbon distribution is less specific than the Group 1 distribution but exhibits multiple complementary lines of evidence for a biogenic origin.

The first line of evidence is the observed predominant chain lengths. Specifically, we observe a unimodal distribution of hydrocarbon chains with a relatively narrow bulge corresponding to high concentrations of chains in the *n*-$C_{14\text{-}22}$ range (LMW/HMW>1) (Figure 3.6a). Biological systems often synthesize hydrocarbons within specific chain length ranges tailored to their physiological needs. For instance, microorganisms typically synthesize short (LMW) *n*-alkanes in the *n*-$C_{12\text{-}20}$ range [62]. Conversely, middle-length chains (*i.e.*, $C_{20}$-$C_{25}$) are dominant components of aquatic macrophytes, and long chains (*i.e.*, $C_{25}$-$C_{35}$) mainly have terrestrial sources, such as higher plants [58,62]. Thus, the specific length range of hydrocarbons we observed are most consistent with a predominantly microbial source. The minimal presence of

middle- and long-chain hydrocarbons in our samples implies a non-dominant role for these sources (further insights on the origin of hydrocarbons >$C_{20}$ are discussed later).

The second line of evidence arises from the observed predominance of even-carbon number homologs in the LMW range ($CPI_{LMW}$<1). Biological hydrocarbon synthesis typically involves the polymerization of simple monomers, such as acetate (containing 2 carbons) or isoprene (containing 5 carbons), due to enzymatic specificities of the biosynthetic pathways [58,78]. As a result, biogenic hydrocarbon profiles frequently display specific and repeated patterns in chain length, such as a disproportionate level of either even- or odd-numbered chains, reflecting synthesis based on acetate units [38,58]. This manifests as a saw-tooth patten in the alkane profile, which is apparent in the Group 2 distributions (Figure 3.6b). In contrast, non-biological synthesis mechanisms, including Fischer-Tropsch processes, polymerize hydrocarbons one carbon at a time [79,80]. This yields smooth alkane distributions that approximately follow a statistical function called the Anderson–Schulz–Flory relationship [79]; these distributions bear no obvious carbon-number preference and are thus distinct from biological patterns [80]. It is important to note that these samples also contain abundant *n*-$C_{17,}$ which diverges from the prevailing even-over-odd pattern (nonetheless, $CPI_{LMW}$ remains significantly below 1, underscoring the pronounced preference for even carbon numbers). While *n*-$C_{17}$ is often associated with cyanobacteria, the absence of other distinct cyanobacterial markers in these profiles suggests a different origin. Notably, *n*-$C_{17}$ is synthesized in high concentrations by various microorganisms, including photosynthetic and non-photosynthetic bacteria [74,81], leading us to interpret it here as a general marker of microbial input, rather than a specific indicator of any one type.

However, although the pronounced even-over-odd pattern of the Group 2 distributions is consistent with a biological influence, the precise origin is more enigmatic. The source of even-over-odd hydrocarbon patterns in environmental samples, which is reported less frequently than odd-over-even patterns, is a matter of debate and must be considered in the context of the formation environment. Leading hypotheses include: (1) the reduction of membrane fatty acids (e.g., phospholipid fatty acids) from expired organisms under anoxic conditions, resulting in *n*-alkanes having the same number of carbon atoms as the initial fatty acid, which are themselves

often even-numbered [82], (2) microbial alteration of algal detritus [83], or (3) direct and preferential synthesis of even-numbered *n*-alkanes by specific microorganisms [81,84–86].

Our data are not consistent with the first two hypotheses. With regards to hypothesis 1, the composition of the even *n*-alkanes does not parallel the membrane phospholipid fatty acids (PLFA) having the same carbon-number range, which were described in Chapter 2. Specifically, while the even-carbon *n*-alkanes in Group 2 displayed multiple local maxima at *n*-$C_{16}$, *n*-$C_{18}$, *n*-$C_{20}$, and/or *n*-$C_{22}$ (Figure 3.6b), the PLFA fraction was universally dominated by compounds with 16 carbons and contained only very low concentrations of compounds with 20 or more carbons (refer to Chapter 2). In fact, only a single sample contained PLFA with 22 carbons (*S_Mid_Mat*, collected near the visible microbial mat). Since significantly different patterns are found in the Group 2 hydrocarbon profile, a diagenetic source of fatty acids is unlikely. Additionally, the well oxygenated waters measured at the time of sampling (Table 3.1) raise additional difficulties for invoking an anoxic reductive formation mechanism. Concerning hypothesis 2, the validity is also challenged by the PLFA profiles detailed in Chapter 2. The PLFA profiles of the Group 2 samples did not contain fatty acids characteristically synthesized by algae (e.g., $C_{16:3(n-3)}$, $C_{16:4(n-3)}$, $C_{18:3(n-3)}$) [87,88], suggesting that algae are not significant components of the modern community and are unlikely to be the source of the even *n*-alkanes. While it is possible that algae existed prior to our sampling and contributed fossil biomarker hydrocarbons, a more parsimonious explanation is provided by the third hypothesis: the direct and preferential synthesis of even-numbered *n*-alkanes by microorganisms.

Indeed, multiple studies have demonstrated that several bacteria produce *n*-alkanes in the $C_{12}$-$C_{22}$ range, often with strong maxima of one of two even-numbered compounds [74,81,84,86]. It is therefore plausible that a mixture of such bacteria could account for the range of even-numbered *n*-alkanes observed in our samples. Notably, many types of bacteria producing even carbon-numbered *n*-alkanes below *n*-$C_{22}$ also synthesize low concentrations of *n*-alkanes with no carbon predominance in the *n*-$C_{23\text{-}34}$ range [81,84,89], which aligns with our observation that the carbon preference index of the HMW *n*-alkanes is near unity in all samples (Table *3.2*). Moreover, while some fungi and yeast have also been reported to biosynthesize even-numbered alkane chains [89,90], the PLFA profiles extracted from these samples (detailed in Chapter 2), revealed high concentrations of diverse bacterial biomarkers, such as monounsaturated fatty acids associated

with Gram-negative bacteria and multiple isomers of iso- and anteiso-branched fatty acids associated with gram-positive bacteria. Contrarily, fungal or yeast biomarkers (e.g., $C_{16:1\ (n-5)}$, $C_{18:2\ (n-6)}$) were absent or present at only low concentrations (see Chapter 2), implicating bacteria as the predominant sources of the observed biomarker hydrocarbons.

The concomitant appearance of *n*-alkenes with the even-carbon *n*-alkanes is an unusual distribution that also demands an explanation. While alkenes are known to have diverse biological sources, none of the commonly reported sources match the observed distribution. For instance, higher plants produce abundant alkenes and are regularly observed in environmental samples, but these are of high molecular weights (>*n*-$C_{22:1}$) and are typically odd-numbered [91]. Short chain *n*-alkenes (<*n*-$C_{22:1}$) have been reported as intracellular components of algae, phytoplankton, and/or zooplankton, but alkene from these sources are also generally dominated by odd-numbered compounds (e.g., *n*-$C_{15:1}$, *n*-$C_{17:1}$, *n*-$C_{19:1}$) [92,93], and thus do not match the distribution observed here. It is also important to note that Ekpo et al. (2012) [94] reported a distribution of even-predominated *n*-alkenes from *n*-$C_{16}$ to *n*-$C_{26}$ within organic solvents that had been contaminated by leachates from the plastic bottles in which they were stored. However, this contamination source is unlikely in our study for the following reasons: (1) our solvents were of high purity and stored exclusively in glass bottles, (2) we exclusively used pre-combusted glassware for the extractions (no plastics or plastic derivatives), (3) we did not detect *n*-alkenes in the solvent blanks that were analyzed in parallel, and (4) although we did use plastic Whirl-Pak bags for sample collection, we not detect *n*-alkenes in other sediment samples (e.g., the Mud Pot samples) which were collected with an identical protocol (a sampling blank will be extracted in the near future to confirm this).

Significantly, a *paired* elution of short-chain *n*-alkanes and *n*-alkenes with an even carbon preference has only been reported in a handful of environmental studies [85,95–98]. These studies unanimously suggest that the unique alkene/alkane pairs are associated with microbial activity, however no specific biogenic source has been described. Some reports propose that the pattern arises from petroleum-derived compounds reworked by microorganisms inhabiting an oil-polluted environment [95,96,98]. However, in samples from the Gulf of Gabes in Tunisia, Aloulou et al. [97] reported that the alkane/alkene pairs were not detected in crude oil samples or samples with high anthropogenic input, suggesting instead that they are directly produced by

certain microbial communities. In either case, even-numbered alkene/alkane pairs certainly do not fit the profile produced by non-biological hydrocarbon synthesis processes and have so far been exclusively assigned a biogenic origin, implicating them as a unique biomarker. Indeed, Grimalt et al. [85] suggest that the remarkable similarity between the *n*-alkane and *n*-alkene distributions in sediment samples could suggest a common biological origin for both distributions.

Lastly, the bell-shaped UCM in all Group 2 chromatograms may supply further evidence for the biogenicity of this distribution. UCMs, typically interpreted as mixtures of many structurally complex isomers that cannot be resolved by capillary GC columns [99], arise either from catagenic decomposition of organic matter [100,101] or microbial breakdown of labile organics [102–105]. Catagenically produced mixtures are usually defined by a very broad hump with a maximum ≥*n*-$C_{25}$, whereas biologically produced mixtures commonly elute with a narrower profile between *n*-$C_{16}$ and *n*-$C_{22}$, sometimes extending up to ~*n*-$C_{25}$ [100,102,103]. We observed a UCM eluting between *n*-$C_{16}$ and *n*-$C_{24}$, suggesting a microbial origin. While we cannot dismiss the potential influence of catagenesis from the deep hydrothermal system, the elution characteristics combined with the well-established microbial markers (e.g., predominance of LMW alkanes and strong carbon-number preference) suggests the heterotrophy has left a strong imprint on the hydrocarbon record. Moreover, the absence of steranes and hopanes in the samples may provide corroborating evidence of intense heterotrophic reworking of the original biomass, as suggested by Pawlowska et al. (2013) [106] and Vinnichenko et al. (2020) [40].

### 3.5.2 From Organisms to Molecular Fossils: Preservation Potential of Hydrocarbons

Understanding the potential of basaltic glaciovolcanic environments to capture and preserve fossil biomarkers is of vital importance in assessing their astrobiological potential for Mars. Our investigation occurs during the early diagenetic window—where a biological community is still active and where sediments are still in diffusional contact with water. This window does not permit us to directly observe the long-term preservation of the compounds, however, by assessing the intrinsic molecular stability of the detected hydrocarbons, in conjunction with the environment's mineralogical context, we can make informed predictions about their preservation potential.

All hydrocarbon assemblages extracted from the Kverkfjöll sediments were predominantly comprised of normal and mid-chain branched alkanes. These compounds are amongst the most recalcitrant hydrocarbon compounds and do not experience major alterations during diagenesis once entombed in sediment [99]. Thus, they are considered important molecular fossils for life-detection on the early Earth and, potentially, other worlds (e.g., [39,107]). Further, the pronounced unresolved complex mixture (UCM) observed in the Group 2 distribution is generally understood to consist of a complicated assemblage of linear and branched compounds [99]. These mixtures are thus similarly resistant to degradation and have a propensity to accumulate in sediments over geologically significant periods [99]. Indeed, the co-occurrence of normal alkanes, methyl-branched alkanes, and a large UCM, have been used to infer past biological activity and help reconstruct paleoenvironmental conditions from Earth's mid-Proterozoic eon (1.8-0.8 Ga) [40,41,106,108], highlighting both the informative nature of these compounds as well as their potential for preservation.

The *n*-alkenes observed in the Group 2 distribution, however, are less likely to be preserved intact. The sensitivity of the double bond(s) to oxidation renders alkenes more reactive than alkanes and more susceptible to degradative processes [109], although sub-oxic conditions may increase their preservation potential [110]. As a consequence, alkenes are rarely reported in sedimentary deposits and are unlikely to be a robust biomarker for ancient settings. Nonetheless, it is noteworthy that the diagenetic loss of the double bond often occurs without a change in the number of carbon atoms and can lead to the relative enrichment of the associated saturated chain. This enrichment could serve to enhance the even-over-odd predominance amongst the saturated *n*-alkanes, thereby potentially strengthening one biomarker signal despite the loss of another.

In addition to the intrinsic molecular stability of a compound, interactions between organic carbon and the mineral matrix play an integral role in the preservation potential of biomarkers [111–113]. At Kverkfjöll, the mineralogical assemblage is universally dominated by dioctahedral smectite(s) and heulandite. These minerals are not significant products of cold (~0 °C) subglacial chemical weathering in mafic regions [114]. Instead, they are emblematic of hydrothermal influence [10,115]. Within this context, the smectite group minerals serve as indicators of the initial stages of hydrothermal alteration paragenesis, representing the argillic alteration facies [115]. They form through hydrolysis reactions at the expense of silicate phases under low

temperatures (<160 °C) and generally near-neutral pH values (~5.5–7) [115], although more acidic pH formation conditions are possible [116]. Under these conditions the smectites regularly co-occur with zeolites. The omnipresence and dominance of these minerals throughout the system could be attributed either to a consistent hydrothermal alteration influence or to sediment mixing and homogenization processes occurring in the subglacial environment or during periods of elevated lake stands.

This mineralogical assemblage holds significant promise for the preservation of organic biomarkers, as smectites are considered a favourable group for forming stable organo-mineral complexes [117]. Smectites are the phyllosilicate minerals with the highest surface area and cation exchange capacity, which impart several advantageous features for concentrating and preserving organic molecules. Firstly, the high specific surface area and layer charge of smectites results in a greater availability of reactive sites for organo-mineral interactions, facilitating more opportunities for the adsorption of organic molecules. Consequently, specific surface area can be a strong predictor of the organic carbon content in sediments [118–120]. Second, smectites have been shown to interact with organics particularly strongly [121], making them more resistant to desorption compared to other minerals and extending the residence time of intact organic compounds [113]. Third, once organic compounds are effectively sorbed to the smectite structure, especially within the interlayer, individual mineral particles or mineral aggregates provide physical protection from degradation by minimizing oxygen diffusion and preventing microbial attack [112]. Lastly, the fine-grained nature of smectites can decrease permeability, further enhancing preservation by reducing exposure to migrating fluids, gases, and radiation. Indeed, the tendency for smectite-containing sediments to contain elevated organic contents in terrestrial environments (e.g., [120,122–125]) underscores their effectiveness in concentrating and preserving organic biomarkers.

The pervasive presence of smectites throughout the field study area indicates that these preservation advantages are uniformly distributed across the various microenvironments, increasing the likelihood that a high-fidelity organic record is captured and retained. Importantly, the preservative properties of smectite arise from the intrinsic characteristics of its mineral structure and it is widely accepted that these advantages would extend to the Martian context [57,117,126]. This assertion is supported by recent findings from the *Mars Science Laboratory*.

Data from the Sample Analysis at Mars (SAM) instrument pyrolysis and wet chemistry experiments (derivatization and thermochemolysis) revealed that the clay-bearing Glen Torridon unit contained the most diverse and abundant sulfur-organic molecules and aromatic compounds discovered on Mars to date [127]. These authors suggest that the presence of dioctahedral smectite and sulfate minerals likely played a key role in enhancing the preservation of these compounds relative to other geological units explored in Gale crater [127].

However, while our study concentrated on the local mineralogy and its capacity to immediately capture and retain organic biomarkers, sample selection strategies for paleoenvironments on Mars must also consider the effects of prolonged post-burial diagenesis on organic matter. In the Martian context, the potential preservative effects of geopolymerization (organic macromolecular matrices) have been identified as a likely contributor to long-term organic matter preservation (in tandem with mineral interactions and permeability factors) [128]. While this process was not directly examined in our research at Kverkfjöll, it represents an important area of interest in understanding the long-term potential for preservation.

Indeed, on Earth, the preservation of labile organic compounds in sedimentary environments is greatly enhanced through polymerization and condensation reactions that fuse small individual molecules together to form macromolecular networks. If these networks are extensive enough, the product is insoluble and is termed kerogen [129]. Kerogen is extremely refractory and constitutes the largest reservoir of organic carbon on Earth's surface [130]. The refractory nature of kerogen arises, in part, because it forms from the very small fraction of organic compounds that evade degradation in surface carbon cycles [129,131,132], thereby incorporating compounds that have already demonstrated a certain level of stability and resistance to environmental degradation. Furthermore, the macromolecular structure of kerogen offers inherent resistance to degradation because the organics on the surface act as a protective shield for the internal structures, guarding against the impacts of radiation, oxidation, and thermal degradation [132–134]. This resistance to various degradative forces makes kerogen of great relevance for understanding the preservation of molecular biomarkers on Mars.

Yet, although kerogen has been studied extensively, the reactions involved in kerogen synthesis are manifold and their individual relevance is still debated (see review by Vandenbroucke & Largeau, 2007 [129]). In addition, the geological context of Mars is markedly different from that

of the Earth, and the extent to which terrestrial kerogen-forming mechanisms can be applied to Martian environments is uncertain. Nevertheless, the organic molecules detected *in situ* by the Mars Science Laboratory and within Martian meteorites are consistent with the presence of macromolecular material akin to terrestrial kerogens [127,128,135]. Notably, the diversity and abundance of sulfur-bearing organics in Mars' sedimentary rocks led Eigenbrode et al. (2018) [128] to highlight the potential importance of natural sulfurization (sometimes referred to as vulcanization) for macromolecular carbon formation/preservation on Mars. In this process, organic molecules react with and incorporate inorganic sulfur or sulfur-containing compounds, leading to the formation of organosulfur macromolecular matrices [136–138]. Sulfurization is thought to enhance the refractory state of sedimentary organic matter by eliminating energy-yielding functional groups, increasing the molecular weight of the organic matter, and potentially altering structures to make them less compatible with enzymatic degradation, all of which reduce reactivity and bioavailability of the organic compounds [136]. The potential role of sulfurization suggests that some processes similar to Earth's kerogen-forming processes might also be at play on Mars. The Kverkfjöll site contains abundant inorganic sulfur in the local waters and minerals (see Chapter 2 and Cousins et al., 2023 [139]) and exploring the potential for sulfurization in this context presents a promising direction for future research.

In sum, the preceding discussion highlights a favourable preservation framework at Kverkfjöll whereby a range of intrinsically refractory hydrocarbons (including alkanes, alkenes, and UCM) exhibiting clear biogenic signatures are produced within an environment that has a preservative mineralogical context. The lack of tectonic activity on Mars [140] minimizes the thermal pressures that could degrade an entombed molecular record, further enhancing its potential longevity. In this context, it is crucial to emphasize that recent research has identified potentially habitable glaciovolcanic environments on Mars as young as 100-200 million years [6,16,34,35]. This recency further limits the window of degradation, and it is worth noting that hydrocarbons akin to those detailed here have been retrieved from far older sediments on Earth [40,41,106,108]. Hence, if microbial life had gained a foothold in these geologically young niches, producing refractory hydrocarbons, the molecular remnants of such life could remain intact. We therefore recommend glaciovolcanic areas as high priority astrobiological targets.

### 3.5.3 Preservation Biases Observed During Initial Diagenesis

Our analysis reveals a pronounced preservation bias which becomes evident when considering the biological production of hydrocarbons, especially alkanes and alkenes. Broadly, there are two main categories of biosynthesized hydrocarbons. The first category consists of intracellular or extracellular hydrocarbons generated directly by organisms as independent biomolecules [73,141,142]. These compounds can exhibit straight, branched, or unsaturated configurations, but do not contain functional groups with heteroatoms, making them intrinsically refractory. We refer to these here as "primary hydrocarbons". The second category includes hydrocarbons that are synthesized as structural elements of larger, more complex, and functionalized biomolecules—such as the hydrocarbon "tails" of fatty acids. In this latter scenario, the functionalized components of the biomolecule are reactive/labile and are degraded over time, potentially leaving the more stable hydrocarbon constituents to be incorporated into the geological record [39,99,107]. These hydrocarbon remnants are referred to here as "derivative hydrocarbons".

The geobiology (and astrobiology) literature is dominated by discussions of the derivative pathway, whereby membrane lipids of expired organisms become buried and diagenetically reduced to their fossil hydrocarbon cores [39,58,107,143–145]. During this process, the hydrocarbon can retain much of the architecture of the original functional biomolecule, thus encoding information about the source organism into the geologic record [39,107]. Further, there is extensive evidence that organisms modulate the hydrocarbon constituents of their membrane lipids to maintain fluidity under variable environmental conditions [146,147], or in response to stress [148,149], suggesting that derivative hydrocarbons could also be informative indicators of past environments. However, the biogenic hydrocarbons observed here are interpreted exclusively as *primary hydrocarbons*. This begs the question: Why are the hydrocarbon derivatives of membrane lipids not detected? And in turn, what is the potential impact of such selective preservation on the interpretation of the resultant hydrocarbon record?

Regarding the first question, our leading hypothesis is that, upon cell death, the functionalized membrane lipids in this environment are preferentially and rapidly metabolized, preventing the accumulation of their hydrocarbon derivatives in the sediments. Indeed, membrane lipids are energy-rich, atomically diverse compounds that often contain phosphate, a limiting nutrient, and can therefore serve as vital sources of energy and nutrients in oligotrophic systems [150]. This makes them favourable substrates for heterotrophic recycling [150]. Further, Harvey et al. (1986)

[151] found that the rate of heterotrophic recycling of free membrane lipids is most rapid in environments with low total organic carbon (≤0.7% w/w humic acid) and slows when other organic carbon sources are more abundant. These results demonstrate that heterotrophic recycling is uniquely stimulated in organic-poor environments. Importantly, these authors also observed that membrane lipid degradation can begin in as little as one hour, and that the vast majority of the original lipid is metabolized fully to $CO_2$ [151]. Such rapid and exhaustive degradation illustrates how membrane lipids (including their constituent hydrocarbons) can be quantitatively removed from a carbon-poor system.

With this context, two key observations outlined in Chapter 2 suggest that conditions are indeed unfavourable for the preservation of membrane lipids in our study area: (1) low total organic carbon values (frequently below the precision limit), and the (2) elevated trans:cis ratios of unsaturated fatty acids (>>0.1), indicating nutrient deprivation/starvation [148]. Together, these metrics underscore the carbon-poor nature of the Kverkfjöll environment. It is therefore plausible that heterotrophic microorganisms preferentially, and exhaustively, recycled the pool of energy-rich membrane lipids at our study site, leaving the comparatively inert primary hydrocarbons to accumulate. The presence of a heterotrophically-derived UCM in many samples provides supporting evidence for heterotrophy within the system.

This preservation bias exposes a critical gap in knowledge for interpreting lipid records in carbon-poor settings—on Mars and on Earth. This is primarily due to our limited understanding of the physiological function of microbial primary hydrocarbons [73,141,142]. For instance, amongst cyanobacteria, there are speculative theories suggesting that mid- to long-chain alkanes might influence cell morphology, aid cell division, maintain membrane fluidity, and/or help the organism tolerate environmental stresses [73,142]. However, these hypotheses are tentative, and the relative significance of each proposed function is unclear [73,141]. For other microbes, the functions are even more enigmatic. Various microbes produce primary hydrocarbons intracellularly and/or extracellularly with possible functions related to membrane integrity, nutrient accumulation, or cellular adhesion [141]. These roles, however, appear to differ across species or metabolic preferences, and a unified theory for the role of microbial hydrocarbons is lacking [141]. This ambiguity limits the information that may be derived from these compounds

beyond merely assigning them a biogenic origin and could severely limit palaeobiological reconstructions in environments dominated by primary hydrocarbons.

Regarding Mars, these limitations are relevant beyond the glaciovolcanic analogy. For instance, the *Mars Science Laboratory* recently analyzed lacustrine mudstones purported to be favourable for the preservation of organics, revealing a refractory organic carbon content of 273 ± 32 μg C/g (0.00027%) [152]. Although this value represents a minimal amount given that several lines of evidence point to incomplete combustion, it is well below the carbon contents observed at Kverkfjöll and is more comparable to carbon contents in arid, low-life places on Earth, such as the Atacama Desert and the Antarctic [153,154]. It is therefore plausible that Mars' sedimentary environments could be similarly inhibitive towards the preservation of energy-dense (and informative) membrane-derived hydrocarbons. These limitations are exacerbated considering that primary intracellular hydrocarbons comprise only 0.005 to 2.69% of the dry cell weight (DCW) of terrestrial bacteria [141], whereas functionalized membrane lipids like fatty acids account for a much larger portion, ranging from roughly 1% DCW to over 40% DCW in certain oleaginous microorganisms [155–157]. Thus, if Mars' sediments have a degradation bias towards functionalized lipids analogous to that at Kverkfjöll, the biogenic lipid reservoir may be much lower than previously hypothesized. This underscores the importance of identifying and targeting locations where such hydrocarbons could be concentrated.

### 3.5.4 Distribution Patterns of Hydrocarbon Biomarkers

#### *3.5.4.1 What Drives Hydrocarbon Concentration in the System?*

We theorized that areas with a higher viable biomass, as estimated in Chapter 2, would have more hydrocarbons due to the greater initial abundance of cells. Indeed, we find a significant correlation between the viable biomass and the hydrocarbon concentrations ($r_s = 0.7$, $p = 0.01$). Notably, three samples exhibited substantially elevated hydrocarbon concentrations relative to surrounding samples—"hydrocarbon hotspots". These include the sample from the mid-point of the hot spring overflow stream where a green microbial mat was observed (*S_Mid_Mat*), and the two desiccated upper crusts from the inactive mud pots (samples *MP_Recent_Crust* and *MP_Old_Crust*). These samples also yielded the greatest viable biomass estimates in Chapter 2.

However, the factors underlying the correlation between viable biomass and hydrocarbon abundance appear to be more complex than the original hypothesis implies. Indeed, the

hydrocarbon hotspots are each characterized by a strong Group 1 pattern, indicative of cyanobacterial input (see section 3.5.1.1). This suggests a direct causal relationship between the presence of cyanobacteria and heightened hydrocarbon accumulation, which is aligned with the understanding that photosynthetic processes typically support a greater biomass output than chemosynthetic ones [158,159]. Regarding the *S_Mid_Mat* sample, the link between the hydrocarbon concentration and viable cyanobacterial biomass is supported by visual evidence of green phototrophic pigments, visible filamentous morphologies, and the detection of specific phospholipid fatty acids (PLFA) characteristic of cyanobacteria and/or phototrophic metabolisms (e.g., $C_{18:3(n-6)}$, $C_{20:4(n-6)}$, $C_{20:5(n-3)}$ [160,161]) (reported in Chapter 2). In contrast, the two desiccated Mud Pot crust samples, as well as all other Group-1-bearing Mud Pot samples, lacked visible evidence of phototrophic pigments and did not feature the characteristic PLFA above. This suggests that viable cyanobacteria may have been absent from these samples, complicating the presumed link between the viable community and the sedimentary hydrocarbons. This discrepancy in the Mud Pot samples warrants an explanation.

One possibility is that viable cyanobacteria were present in the Mud Pot area during sampling but did not produce the noted PLFA. Indeed, while certain PLFA can be characteristic of particular groups, they are not necessarily ubiquitous across all species [161]. This explanation, however, is not favoured given the concomitant lack of visible phototrophic pigments and the detection of cyanobacterial hydrocarbons within the lower subsurface Mud Pot samples (*MP_Recent_Low* and *MP_Old_Low*). These samples were collected ~10 cm below the surface from an extremely dense and viscous mud deposit. Given the density of the mud, sunlight penetration is highly unlikely, making it improbable that the cyanobacterial hydrocarbons were being actively deposited by a living cyanobacterial community.

Alternatively, the cyanobacterial hydrocarbons could be “fossil” remnants of a past community, likely active when the (now dried) Mud Pots were inundated and amenable to solar penetration. Such a scenario would explain both the observed distribution of hydrocarbons and the absence of pigments and phototrophic PLFA. Indeed, as the mud pots dehydrated, native cyanobacterial communities would have likely become concentrated in the diminishing water levels near the surface. Once these communities expired—potentially due to seasonal shifts [162–164] or alterations in the physicochemical environment that made phototrophy untenable [165]—the

more labile pigments and PLFA would have degraded. This sequence of events would be expected to produce: (1) a high level of refractory cyanobacterial biomarkers in the mud pot upper crusts, representing the last vestiges of the concentrated community, (2) reduced/diluted biomarker concentration in the lower mud pot body, and (3) an absence of cyanobacterial PLFAs and pigments throughout. These outcomes align with our findings.

Yet, if we accept that these hydrocarbons denote a *past* cyanobacterial presence in the Mud Pots, it raises the question of why there remains a robust correlation with the estimated biomass of the *current* community (which is presumably not cyanobacterial). This suggests that the Mud Pots might present particularly fertile conditions that promoted another productive community to colonize the area and contribute biomass after the disappearance of the local cyanobacteria. It is conceivable that this new community colonized the Mud Pot area specifically because of the concentration of cyanobacterial hydrocarbons, leveraging the fossil carbon as a nutrient and/or energy source. It is important to note, however, that we do not observe a UCM in these samples, which may argue against significant heterotrophic activity, or suggest that insufficient time has elapsed for such intermediates to accumulate. Conversely, the unique inorganic physiochemistry of the Mud Pots might foster heightened local productivity. Notably, in comparison to the Spring Lake Transect, the Mud Pot fluids exhibit a more enriched geochemical profile, characterized by elevated TDS, salinity, and redox-sensitive elements (see Chapter 2). This richer supply of electron donors and acceptors could be exploited to drive autotrophy and contribute elevated biomass, or simply provide a supply of nutrients required to support a productive community.

In sum, although we find a strong correlation between the estimated viable biomass and the pool of refractory hydrocarbons, the causal link is unclear. What is clear, however, is that cyanobacteria have left a strong imprint on the hydrocarbon record, and that their distribution is a principal driver of hydrocarbon concentration within the system. Factors like subaerial exposure, along with temperature and pH conditions favourable to phototrophy [165], therefore emerge as key predictors of hydrocarbon distribution. Moreover, the collective evidence suggests that the Mud Pots are hotspots of dynamic productivity. Initially supporting a cyanobacterial community capitalizing on sunlight, the area seems to have become a haven for another productive, presumably non-photosynthetic community, potentially harnessing chemical energy from legacy hydrocarbons or autotrophically from the geochemically enriched environment. This highlights

the complexity and potential overlap of different energy pathways, suggesting that the confluence of geochemically enriched conditions, nutrients, and diverse available energy sources create a localized environment that promotes productivity.

#### *3.5.4.2 Transport of Hydrocarbon Biomarkers*

We also hypothesized that the fine-grained muds at the center of lake Gengissig would serve as a biomarker sink, amalgamating the hydrocarbon residues from the surrounding hydrothermal catchment. This hypothesis was grounded in the understanding that organic matter is typically less dense than water and can be transported with fine sediments to accumulate in depositional basins [112,166]. This principle has motivated the proposals for, and selection of, several exploration sites on Mars (e.g., [167,168]).

However, this hypothesis was not supported by the data at Kverkfjöll and the fine-grained samples from the lake center exhibited some of the lowest levels of resolvable hydrocarbon biomarkers. Moreover, despite a direct hydraulic connection with the microbial mat on the shore (*S_Mid_Mat*)—which displayed a pronounced Group 1 cyanobacterial signature—the downstream sediments lacked any evidence for the characteristic branched heptadecanes indicative of cyanobacteria. This indicates that either these compounds were quantitatively degraded during transit, or they were not effectively transported by the stream flow. The degradation of the cyanobacterial hydrocarbons over such a short distance (~20 m to the next downstream sample) is improbable given their inert nature and their apparent capacity to endure initial diagenesis in the Mud Pot area. We therefore favour the explanation that the stream flow was insufficient to transport these compounds; this assertion is supported by the clarity of the stream water which indicates minimal fine sediment suspension (Figure 3.3c). In either case, the distribution of the Group 1 compounds remains highly localized, and the crater lake does not accrue a complete record of biomarkers from the local catchment.

#### *3.5.4.3 A Homogenous Sedimentary Signature*

In contrast to the Group 1 cyanobacterial signature (preceding sections), the Group 2 microbial signature (defined by even *n*-alkanes, alkenes, and a prominent UCM) is more pervasive and does not appear to be regulated by physicochemical constraints. Take, for instance, the Spring-Lake Transect where the Group 2 signature is most prevalent. This Transect encompasses a broad spectrum of environmental conditions, including temperature extremes (8-87 °C), varying pH (8.5-5.8), extreme dissolved oxygen shifts (0.4-4.7 mg/L DO), and variable aqueous chemistry

(see Chapter 2 for details). Despite such environmental diversity, the hydrocarbon profiles extracted across the Transect were strikingly consistent (Figure 3.6) (with the exception of sample *S_Mid_Mat* near the microbial mat, where a mixed Group 1 and 2 signal was observed). This uniformity suggests that the Group 2 pattern is largely independent of contemporary physiochemistry.

To account for this apparent environmental independence, we propose that the Group 2 hydrocarbon profile represents a temporally integrated record of biological activity, making it less reliant on current conditions. Glaciovolcanic regions often exhibit shifting local environmental conditions [46,47], influenced by changes in the hydrothermal reservoir, fluctuations in subsurface fluid flow, and/or varying interactions with snow and ice [42,169]. A striking example of this variability at Kverkfjöll can be seen when comparing our observations of the Gengissig shoreline to those made by Cousins et al. [26] in 2011. These authors document three large (~10 meter in diameter) interconnected hydrothermal pools with moderate temperatures (<68 °C) and sulfate-dominated geochemistry. Based on the published fluid chemistry data and site photographs, we infer that the Mud Pot area described here is the remnant of this expansive pool system. Cousins et al. [36] did not note the hot spring (>87 °C) and associated thermal overflow stream that we observed. Collectively, these observations underscore the dynamic nature of the site. As a consequence, any field measurement of local physiochemistry is only a snapshot of an evolving environmental narrative. In contrast, the refractory hydrocarbon pool is enduring and has the potential to aggregate fingerprints from ecosystems that were active under different conditions. The ubiquitous presence of a pronounced UCM in the Group 2 pattern, which suggests heterotrophic recycling, reinforces that the Group 2 signature reflects a somewhat aged component of the organic pool that is mature enough to have experienced degradation.

But what accounts for the striking uniformity of the signal across such a broad area? We propose three potential explanations, though they are not necessarily mutually exclusive. First, fluctuations in the Gengissig lake level could have homogenized the biomarker record. Water monitoring data since 1967 highlights significant variations, occasionally exceeding 25 m in year-to-year measurements [46]. These water level shifts could serve as a potent homogenizing force on the biomarker record, blending previously isolated niches and leading to a reduction of

taxonomic distinctness in the benthic communities (e.g., [170]). Additionally, sediment resuspension during these shifts might amalgamate organic traces from various timelines, creating a more unified "fossil" organic record.

Alternatively, the pervasive Group 2 pattern could indicate the presence of a generalist microbial community. This possibility may be supported by the spatial consistency of the mineralogical assemblage, which indicates either a relatively uniform hydrothermal influence across the site (at least integrated over time) or extensive sediment mixing during high lake stands. In either case, such homogenous mineralogy could provide a consistent substrate for microbial growth and adhesion across the site. If these microbes could withstand transient physicochemical changes within the limits of the argillic alteration regime (<160 °C, circumneutral pH), then these niches could plausibly have been occupied by a relatively consistent community, resulting in a consistent biomarker pattern throughout. However, this hypothesis seems less likely in light of the varied PLFA community profiles detected across the site, which were interpreted (in part) to reflect population-level shifts in community membership. Genetic data would be essential for a definitive conclusion.

A final potential explanation for the prevalent Group 2 signal is that it represents a highly degraded vestige of a once more diverse biomarker record. Considering the inherent dynamism of the environment, including a history of phreatic eruptions [47] and the evidence for widespread heterotrophic activity, many original biomarkers may have been obliterated or substantially altered. In such a scenario, the observed consistency in biomarkers across the study site might not reflect mixing or a uniform biological community, but rather a universal degradation pathway that preferentially preserves a narrow subset of the original biomolecular diversity at low concentration.

Regardless of the uncertain origin of the Group 2 hydrocarbon signature, its pervasive spatial dispersion across diverse environmental conditions is noteworthy. Such a pattern indicates that, despite the volcanic history and the transient nature of certain niches, the system as a whole consistently preserves some enduring record of biological history.

### 3.5.5 Synthesis and Considerations for Future Mars Missions

Glaciovolcanic environments have been proposed as potential Martian refugia because of their unique and enduring habitability advantages [6,7,16,171,172]. Our findings advance this

narrative by demonstrating that an assemblage of stable hydrocarbon biomarkers is produced by the indigenous community and are deposited within a mineralogical framework conducive to preservation. Crucially, we identified multiple distinct patterns of biogenicity in the refractory compounds, which not only increases confidence in the biogenic interpretation, but also increases the likelihood that at least one molecular biomarker pattern will be preserved over time. These factors thus indicate that Mars-like glaciovolcanic sediments have the capacity to preserve an enduring record of inhabitation and should be considered as priority exploration targets.

However, our findings also illuminate several potential challenges that must be considered for future sampling and analysis in such environments. First, although our field site hosts a smectite-dominated mineral assemblage that could enable long-term preservation, it is essential to highlight that approximately two km north, a separate hydrothermal field (Hveratagl, Figure 3.1) exhibits a markedly different hydrothermal alteration assemblage. At Hveratagl, the mineralogical assemblage is dominated by kaolinite (with only trace amounts of smectite) [48]. Kaolinite forms at the expense of smectites when hydrothermal alteration advances into the intermediate argillic regime (~150–300 °C, pH 4.5-6), indicating that Hveratagl sediments have experienced more intense alteration than our site [115]. This is important because kaolinite adsorbs substantially less organic carbon than smectite and does not bind it as effectively, resulting in more rapid turnover [113,173]. This suggests that the potential for organic preservation in glaciovolcanic systems can vary significantly over relatively short distances (kilometer scale), even if hydrothermal alteration is driven by the same reservoir. Forthcoming missions investigating hydrothermal glaciovolcanic deposits should begin with widespread mineralogical surveys, subsequently narrowing their focus to regions dominated by smectite for more detailed investigation.

Another critical consideration comes from the evidence for selective preservation, which could severely limit the quantity of organic matter conferred to the geologic record, regardless of the mineral assemblage. Although this issue is likely not exclusive to glaciovolcanic settings and may need to be considered during *any* future organic investigation on Mars (see section 3.5.3), it does impose constraints on glaciovolcanic exploration strategies. For example, previous workers have proposed that the distal flood deposits formed when ice-damned glaciovolcanic lakes drain

in events referred to as jökulhlaups could be promising exploration targets. The idea is that these flood deposits would serve as an indirect means for accessing biomarker compounds originally produced in the subglacial source habitat [7,172,174]. This carries appeal because jökulhlaups create vast, low-relief flood plains that can be described from orbit and easily traversed by a rover [7,172]. However, our investigation of Lake Gengissig, which is a jökulhlaup source [47], reveals some reservations. For instance, we observed that the cyanobacterial hydrocarbon biomarkers were highly localized and not effectively dispersed within the source area. Thus, jökulhlaup releases might not transport the complete biomarker record of a glaciovolcanic source region to the flood plain. Such transport biases could accentuate the existing molecular preservation biases, potentially reducing the overall organic signal further and also compromising the fidelity of the final record. It is more likely that a hydrocarbon assemblage akin to the Group 2 pattern—which was uniquely pervasive across the study area—would be transported during a jökulhlaup release. Yet, this pattern was relatively weak and not fully representative of the native biodiversity. This pattern would likely be further diluted during a flood event. Nevertheless, the actual dynamics of jökulhlaups in transporting biomarkers remain unexplored and further research is needed to assess the feasibility of these outburst floods to transport organic records from subglacial niches to more accessible surface locations.

Consequently, the source region emerges as the most promising locale for accessing an authentic and concentrated repository of glaciovolcanic biomarkers. Recent work has exposed several promising candidates. For instance, Amazonian-aged landforms indicative of subglacial eruptions and subsequent meltwater generation have been identified near the Tharsis Montes volcanic edifices [6,16]. Scanlon et al. (2014) estimate that the volume of meltwater produced in the construction of such landforms would have generated glacial lakes large enough to persist for hundreds to thousands of years [6]. These could represent some of the most recent potentially habitable environments on Mars. Unfortunately, the fine-scale features of the region are obscured by glacial debris and dust, which hinders mineralogical assessment and the determination of hydrothermal activity; a worthy avenue of future research would be *in situ* reconnaissance of this compelling region. The Sisyphi Planum region presents another promising area for exploration with multiple landforms indicative of subglacial eruptions [10]. Although the putative glaciovolcanic landforms here are more ancient (late Noachian to late Hesperian), spectral data reveal an assemblage of smectites, zeolites, and iron oxides consistent with low temperature

hydrothermal alteration at high water:rock ratios [10]. Coexisting spectral signatures of gypsum and polyhydrated sulfate are interpreted to reflect either subaerial hydrothermal activity or subglacial weathering. The similarities between the mineral assemblages of Sisyphi Planum and the smectite-zeolite composition found in our study underscores Kverkfjöll's significance as a prime analogue for understanding the astrobiological potential of such environments.

Lastly, our investigation of the distribution of hydrocarbons throughout the system underscores the importance of autotrophy in biomarker generation. We observed that the Group 1 hydrocarbon signal, uniquely associated with cyanobacterial influence, was consistently stronger than the Group 2 signal, and was notably elevated in the Mud Pot area. The heightened hydrocarbon signal in the Mud Pot area is likely attributable to their unique combination of geochemically enriched conditions, nutrient availability, and varied potential energy sources, which collectively support autotrophy. In settings where carbon is limited, autotrophy allows organisms to independently overcome the scarcity of raw materials in the environment and remain productive. The association between autotrophic metabolisms and biomarker signals, both as biomass and refractory biolipids, motivates a “follow the energy” exploration approach within the glaciovolcanic source area [175]. This approach emphasizes targeting sites where liquid water co-existed with energy sources capable of meeting biological requirements. While the precise energy requirements of potential Martian organisms remain unknown, the fundamental principal that the quantity of biomass that can be formed and supported within a system depends on energy availability, provides a valuable direction for targeting future missions. However, even if energy-rich niches cannot be identified during future missions, our discovery of the spatially pervasive Group 2 pattern is promising. Though this pattern is less pronounced than the cyanobacterial pattern, its prevalence throughout the system implies that traces of biological activity can become dispersed throughout dynamic glaciovolcanic terrains.

## 3.6 CONCLUSION

Previous studies have identified Martian glaciovolcanic areas as potentially compelling astrobiological targets [6,7,16–18,172]. Drawing parallels with Earth, where volcano-ice interactions have played a critical role in the maintenance of life during periods of intense climatic change [23–27], Martian glaciovolcanic regions may have similarly extended Mars's window of (near)surface habitability as the climate became increasingly arid and cold. Thus,

such environments could represent some of the last habitable areas on Mars, potentially acting as a natural winnowing mechanism and narrowing down the search area for (relatively recent) biomarkers. Focusing on these environments could thus significantly enhance the efficiency and success of missions aimed at uncovering evidence of past life on Mars.

In this work, we investigated the mineralogy and distribution of refractory biomarkers (alkanes, alkenes, and UCM) produced within a modern basaltic glaciovolcanic setting in Iceland to understand the biomarker preservation potential of analogous environments on Mars. All samples comprised volumetrically abundant smectite and exhibited hydrocarbon patterns indicative of biological activity, evidenced by some combination of: (1) carbon-number preference, (2) specific structural modifications, (3) a narrow chain length range, and/or (4) a UCM with elution characteristics attributed to microbial heterotrophy. Drawing parallels with Earth's ancient record, hydrocarbons similar to those described here can remain intact for geologically significant time scales [39]. Our work therefore provides critical depth to the consideration of glaciovolcanic settings as astrobiological targets, revealing a mineralogical assemblage amenable to preservation and a suite of chemically refractory biomarkers; we therefore recommend glaciovolcanic areas as high priority exploration sites.

Guided by our findings, future Martian missions should target glaciovolcanic source regions where biomarkers are most likely to be concentrated and remain in their ecological context. These missions would benefit from regional, *in situ* mineralogical surveys aimed at identifying locations of low temperature hydrothermal alteration conducive to smectite formation. Subsequently, adopting a "follow the energy" strategy could further improve the identification of localized biomarker concentrations. However, it is important to note that diagenesis by radiation or oxidation may have impacted the preservation of potential energy sources, and missions would benefit from prioritizing regions with indications of limited diagenesis. This comprehensive approach aims to maximize the discovery potential in some of Mars' most recent habitable zones, balancing the quest for biomarkers with the realities of their preservation and alteration in the Martian environment.

## 3.7 ACKNOWLEDGEMENTS

This project has received funding from the European Union's Horizon 2020 research and innovation programme under grant agreement No 871149, the Canadian Space Agency (CSA)

[21EXPCOI1], and the Natural Sciences and Engineering Research Council of Canada (NSERC).

Special thanks to Magnus Thor Karlsson and Bergur Einarsson for ensuring our safety in the field and generously assisting with sample collection. The authors also thank Magnús Tumi Guðmundsson, Andri Gunnarsson, and the entire team behind the Iceland Glaciological Society (JÖRFÍ) for exceptional logistical support, guidance, patience, and kindness.

### 3.8 REFERENCES

[1] M.H. Carr, J.W. Head, Geologic history of Mars, Earth Planet Sci Lett. 294 (2010) 185–203. https://doi.org/10.1016/j.epsl.2009.06.042.

[2] J.S. Kargel, R.G. Strom, Ancient glaciation on Mars, Geology. 20 (1992) 3–7.

[3] M.B. Wyatt, H.Y. McSween, K.L. Tanaka, J.W. Head, Global geologic context for rock types and surface alteration on Mars, Geology. 32 (2004) 648–654. https://doi.org/10.1130/G20527.1.

[4] P.R. Christensen, H.Y. McSween Jr, J.L. Bandfield, S.W. Ruff, A.D. Rogers, V.E. Hamilton, N. Gorelick, M.B. Wyatt, B.M. Jakosky, H.H. Kieffer, Evidence for magmatic evolution and diversity on Mars from infrared observations, Nature. 436 (2005) 504–509.

[5] S.M. Clifford, J. Lasue, E. Heggy, J. Boisson, P. McGovern, M.D. Max, Depth of the Martian cryosphere: Revised estimates and implications for the existence and detection of subpermafrost groundwater, J Geophys Res Planets. 115 (2010).

[6] K.E. Scanlon, J.W. Head, L. Wilson, D.R. Marchant, Volcano-ice interactions in the Arsia Mons tropical mountain glacier deposits, Icarus. 237 (2014) 315–339. https://doi.org/10.1016/j.icarus.2014.04.024.

[7] C.R. Cousins, I.A. Crawford, Volcano-ice interaction as a microbial habitat on Earth and Mars, Astrobiology. 11 (2011) 695–710. https://doi.org/10.1089/ast.2010.0550.

[8] G.J. Ghatan, J.W. Head, Candidate subglacial volcanoes in the South polar region of Mars: Morphology, morphometry, and eruption conditions, Journal of Geophysical Research E: Planets. 107 (2002) 2–1. https://doi.org/10.1029/2001je001519.

[9] A. Grau Galofre, A.M. Jellinek, G.R. Osinski, Valley formation on early Mars by subglacial and fluvial erosion, Nat Geosci. 13 (2020) 663–668. https://doi.org/10.1038/s41561-020-0618-x.

[10] S. Ackiss, B. Horgan, F. Seelos, W. Farrand, J. Wray, Mineralogic evidence for subglacial volcanism in the Sisyphi Montes region of Mars, Icarus. 311 (2018) 357–370. https://doi.org/10.1016/j.icarus.2018.03.026.

[11] M.G. Chapman, C.C. Allen, M.T. Gudmundsson, V.C. Gulick, S.P. Jakobsson, B.K. Lucchitta, I.P. Skilling, R.B. Waitt, Volcanism and ice interactions on Earth and Mars, in: Environmental Effects on Volcanic Eruptions, Springer, 2000: pp. 39–73.

[12] J.L. Smellie, B.R. Edwards, Glaciovolcanism on Earth and Mars, Cambridge University Press, 2016.

[13] L. Wilson, J.W. Head III, Heat transfer and melting in subglacial basaltic volcanic eruptions: implications for volcanic deposit morphology and meltwater volumes, Geological Society, London, Special Publications. 202 (2002) 5–26.

[14] A. Grau Galofre, K.X. Whipple, P.R. Christensen, S.J. Conway, Valley Networks and the Record of Glaciation on Ancient Mars, Geophys Res Lett. 49 (2022) 1–10. https://doi.org/10.1029/2022GL097974.

[15] C.I. Fassett, J.W. Head III, Valley formation on martian volcanoes in the Hesperian: Evidence for melting of summit snowpack, caldera lake formation, drainage and erosion on Ceraunius Tholus, Icarus. 189 (2007) 118–135.

[16] K.E. Scanlon, J.W. Head, D.R. Marchant, Volcanism-induced, local wet-based glacial conditions recorded in the Late Amazonian Arsia Mons tropical mountain glacier deposits, Icarus. 250 (2015) 18–31. https://doi.org/10.1016/j.icarus.2014.11.016.

[17] P.J. Boston, M. V. Ivanov, C.P. McKay, On the Possibility of Chemosynthetic Ecosystems in Subsurface Habitats on Mars, Icarus. 95 (1992) 300–308.

[18] V.C. Gulick, Magmatic intrusions and a hydrothermal origin for fluvial valleys on Mars, J Geophys Res Planets. 103 (1998) 19365–19387.

[19] C.S. Cockell, E. Bagshaw, M. Balme, P. Doran, C.P. Mckay, K. Miljkovic, D. Pearce, M.J. Siegert, M. Tranter, M. Voytek, J. Wadham, Subglacial Environments and the Search for Life Beyond the Earth, Antarctic Subglacial Aquatic Environments. (2011) 129–148. https://doi.org/10.1002/9781118670354.ch8.

[20] J.L. Wadham, M. Tranter, M. Skidmore, A.J. Hodson, J. Priscu, W.B. Lyons, M. Sharp, P. Wynn, M. Jackson, Biogeochemical weathering under ice: Size matters, Global Biogeochem Cycles. 24 (2010). https://doi.org/10.1029/2009GB003688.

[21] M. Skidmore, Microbial communities in Antarctic subglacial aquatic environments, Antarctic Subglacial Aquatic Environments. 192 (2011) 61–81.

[22] J. Telling, E.S. Boyd, N. Bone, E.L. Jones, M. Tranter, J.W. MacFarlane, P.G. Martin, J.L. Wadham, G. Lamarche-Gagnon, M.L. Skidmore, Rock comminution as a source of hydrogen for subglacial ecosystems, Nat Geosci. 8 (2015) 851–855.

[23] C.A. Maggs, R. Castilho, D. Foltz, C. Henzler, M.T. Jolly, J. Kelly, J. Olsen, K.E. Perez, W. Stam, R. Väinölä, Evaluating signatures of glacial refugia for North Atlantic benthic marine taxa, Ecology. 89 (2008) S108–S122.

[24] J.R. Stewart, A.M. Lister, I. Barnes, L. Dalén, Refugia revisited: individualistic responses of species in space and time, Proceedings of the Royal Society B: Biological Sciences. 277 (2010) 661–671.

[25] J.R. Stewart, A.M. Lister, Cryptic northern refugia and the origins of the modern biota, Trends Ecol Evol. 16 (2001) 608–613.

[26] C.I. Fraser, A. Terauds, J. Smellie, P. Convey, S.L. Chown, Geothermal activity helps life survive glacial cycles, Proc Natl Acad Sci U S A. 111 (2014) 5634–5639. https://doi.org/10.1073/pnas.1321437111.

[27] J. Provan, K.D. Bennett, Phylogeographic insights into cryptic glacial refugia, Trends Ecol Evol. 23 (2008) 564–571.

[28] E. Kornobis, S. PÁlsson, B.K. KristjÁnsson, J. Svavarsson, Molecular evidence of the survival of subterranean amphipods (Arthropoda) during Ice Age underneath glaciers in Iceland, Mol Ecol. 19 (2010) 2516–2530. https://doi.org/10.1111/j.1365-294X.2010.04663.x.

[29] J. Xu, M. Perez-Losada, C.G. Jara, K.A. Crandall, Pleistocene glaciation leaves deep signature on the freshwater crab Aegla alacalufi in Chilean Patagonia, Mol Ecol. 18 (2009) 904–918.

[30] P. Convey, R.I. Lewis Smith, Geothermal bryophyte habitats in the South Sandwich Islands, maritime Antarctic, Journal of Vegetation Science. 17 (2006) 529. https://doi.org/10.1658/1100-9233(2006)17[529:gbhits]2.0.co;2.

[31] D.P. Schrag, P.F. Hoffman, Life, geology and snowball Earth, Nature. 409 (2001) 306.

[32] F.E.G. Butcher, M.R. Balme, C. Gallagher, N.S. Arnold, S.J. Conway, A. Hagermann, S.R. Lewis, Recent Basal Melting of a Mid-Latitude Glacier on Mars, J Geophys Res Planets. 122 (2017) 2445–2468. https://doi.org/10.1002/2017JE005434.

[33] S.Z. Woodley, F.E.G. Butcher, P. Fawdon, C.D. Clark, F.S.L. Ng, J.M. Davis, C. Gallagher, Multiple sites of recent wet-based glaciation identified from eskers in western Tempe Terra, Mars, Icarus. 386 (2022) 115147. https://doi.org/10.1016/j.icarus.2022.115147.

[34] F.E. Butcher, M.R. Balme, C. Gallagher, N.S. Arnold, S.J. Conway, A. Hagermann, S.R. Lewis, Recent Basal Melting of a Mid-Latitude Glacier on Mars, J Geophys Res Planets. 122 (2017) 2445–2468.

[35] F.E.G. Butcher, M.R. Balme, S.J. Conway, C. Gallagher, N.S. Arnold, R.D. Storrar, S.R. Lewis, A. Hagermann, J.M. Davis, Sinuous ridges in Chukhung crater, Tempe Terra, Mars: Implications for fluvial, glacial, and glaciofluvial activity, Icarus. 357 (2021) 114131. https://doi.org/10.1016/j.icarus.2020.114131.

[36] C.R. Cousins, M. Fogel, R. Bowden, I. Crawford, A. Boyce, C. Cockell, M. Gunn, Biogeochemical probing of microbial communities in a basalt-hosted hot spring at Kverkfjöll volcano, Iceland, Geobiology. 16 (2018) 507–521. https://doi.org/10.1111/gbi.12291.

[37] V.T. Marteinsson, Á. Rúnarsson, A. Stefánsson, T. Thorsteinsson, T. Jóhannesson, S.H. Magnússon, E. Reynisson, B. Einarsson, N. Wade, H.G. Morrison, E. Gaidos, Microbial communities in the subglacial waters of the Vatnajökull ice cap, Iceland, ISME Journal. 7 (2013) 427–437. https://doi.org/10.1038/ismej.2012.97.

[38] C.D. Georgiou, D.W. Deamer, Lipids as universal biomarkers of extraterrestrial life, Astrobiology. 14 (2014) 541–549. https://doi.org/10.1089/ast.2013.1134.

[39] J.J. Brocks, R.E. Summons, W. Schlesinger, Sedimentary hydrocarbons, biomarkers for early life, Treatise on Geochemistry. 8 (2005) 63–115.

[40] G. Vinnichenko, A.J.M. Jarrett, J.M. Hope, J.J. Brocks, Discovery of the oldest known biomarkers provides evidence for phototrophic bacteria in the 1.73 Ga Wollogorang Formation, Australia, Geobiology. 18 (2020) 544–559. https://doi.org/10.1111/gbi.12390.

[41] A.J.M. Jarrett, G.M. Cox, J.J. Brocks, E. Grosjean, C.J. Boreham, D.S. Edwards, Microbial assemblage and palaeoenvironmental reconstruction of the 1.38 Ga Velkerri Formation, McArthur Basin, northern Australia, Geobiology. 17 (2019) 360–380. https://doi.org/10.1111/gbi.12331.

[42] E. Ranta, S.A. Halldórsson, P.H. Barry, S. Ono, J.G. Robin, B.I. Kleine, A. Ricci, J. Fiebig, Á.E. Sveinbjörnsdóttir, A. Stefánsson, Deep magma degassing and volatile fluxes through volcanic hydrothermal systems: Insights from the Askja and Kverkfjöll volcanoes, Iceland, Journal of Volcanology and Geothermal Research. 436 (2023) 107776. https://doi.org/10.1016/j.jvolgeores.2023.107776.

[43] M. Olafsson, H. Torfason, K. Gronvold, Surface exploration and monitoring of geothermal activity in the kverkfjöll geothermal area, central iceland, World Geothermal Congres 2000. (2000) 1539–1545.

[44] G.E. Sigvaldason, S. Steinthorsson, N. Oskarsson, Compositional variation in recent Icelandic tholeiites and the K verkfjoll hot spot, 251 (1974).

[45] B.A. Óladóttir, O. Sigmarsson, G. Larsen, J.L. Devidal, Provenance of basaltic tephra from vatnajökull subglacial volcanoes, iceland, as determined by major- and trace-element analyses, Holocene. 21 (2011) 1037–1048. https://doi.org/10.1177/0959683611400456.

[46] M.T. Gudmundsson, Þ. Högnadóttir, Jökullón í Vestari Kverkfjöllum, þróun og jökulhlaupahætta, Skýrsla Til Rannsóknasjóðs Vegagerðarinnar. (2009).

[47] C. Montanaro, B. Scheu, M.T. Gudmundsson, K. Vogfjörd, H.I. Reynolds, T. Dürig, K. Strehlow, S. Rott, T. Reuschlé, D.B. Dingwell, Multidisciplinary constraints of hydrothermal explosions based on the 2013 Gengissig lake events, Kverkfjöll volcano, Iceland, Earth Planet Sci Lett. 434 (2016) 308–319. https://doi.org/10.1016/j.epsl.2015.11.043.

[48] A. Moreras-Marti, M. Fox-Powell, A.L. Zerkle, E. Stueeken, F. Gazquez, H.E.A. Brand, T. Galloway, L. Purkamo, C.R. Cousins, Volcanic controls on the microbial habitability of analogue hydrothermal environments, Geobiology. (2021) 1–21. https://doi.org/10.1111/gbi.12459.

[49] S.R. Taylor, S. McLennan, Mars: crustal composition and evolution, 2009. https://doi.org/10.1017/cbo9780511575358.008.

[50] W.F. McDonough, S.-S. Sun, The composition of the Earth, Chem Geol. 120 (1995) 223–253.

[51] S.S. Hughes, C.W. Haberle, S.E. Kobs Nawotniak, A. Sehlke, W.B. Garry, R.C. Elphic, S.J. Payler, A.H. Stevens, C.S. Cockell, A.L. Brady, J.L. Heldmann, D.S.S. Lim, Basaltic Terrains in Idaho and Hawai'i as Planetary Analogs for Mars Geology and Astrobiology, Astrobiology. 19 (2019) 260–283. https://doi.org/10.1089/ast.2018.1847.

[52] K. Lalonde, A. Mucci, A. Ouellet, Y. Gélinas, Preservation of organic matter in sediments promoted by iron, Nature. 483 (2012) 198–200.

[53] M.N. Parenteau, L.L. Jahnke, J.D. Farmer, S.L. Cady, Production and early preservation of lipid biomarkers in iron hot springs, Astrobiology. 14 (2014) 502–521. https://doi.org/10.1089/ast.2013.1122.

[54] F. Westall, D. Loizeau, F. Foucher, N. Bost, M. Betrand, J. Vago, G. Kminek, Habitability on mars from a microbial point of view, Astrobiology. 13 (2013) 887–897. https://doi.org/10.1089/ast.2013.1000.

[55] F. Westall, K. Hickman-Lewis, B. Cavalazzi, Biosignatures in deep time, Advances in Astrobiology and Biogeophysics. (2019) 145–164. https://doi.org/10.1007/978-3-319-96175-0_7.

[56] F. Westall, F. Foucher, N. Bost, M. Bertrand, D. Loizeau, J.L. Vago, G. Kminek, F. Gaboyer, K.A. Campbell, J.-G. Bréhéret, P. Gautret, C.S. Cockell, Biosignatures on Mars: What, Where, and How? Implications for the Search for Martian Life, Astrobiology. 15 (2015) 998–1029. https://doi.org/10.1089/ast.2015.1374.

[57] R.E. Summons, J.P. Amend, D. Bish, R. Buick, G.D. Cody, D.J. Des Marais, G. Dromart, J.L. Eigenbrode, A.H. Knoll, D.Y. Sumner, Preservation of Martian organic and environmental

records: Final report of the Mars biosignature working group, Astrobiology. 11 (2011) 157–181. https://doi.org/10.1089/ast.2010.0506.

[58] P.L. Finkel, D. Carrizo, V. Parro, L. Sa, An Overview of Lipid Biomarkers in Terrestrial Extreme Environments with Relevance for Mars Exploration, Astrobiology. 23 (2023). https://doi.org/10.1089/ast.2022.0083.

[59] G. Zhang, J.T. Germaine, R.T. Martin, A.J. Whittle, A simple sample-mounting method for random powder X-ray diffraction, Clays Clay Miner. 51 (2003) 218–225. https://doi.org/10.1346/CCMN.2003.0510212.

[60] E.G. Bligh, W.J. Dyer, A rapid method of total lipid extraction and purification, Can J Biochem Physiol. 37 (1959) 911–917.

[61] J. Fang, O. Chan, R.M. Joeckel, Y. Huang, Y. Wang, D.A. Bazylinski, T.B. Moorman, B.J. Ang Clement, Biomarker analysis of microbial diversity in sediments of a saline groundwater seep of Salt Basin, Nebraska, Org Geochem. 37 (2006) 912–931. https://doi.org/10.1016/j.orggeochem.2006.04.007.

[62] M. Derrien, L. Yang, J. Hur, Lipid biomarkers and spectroscopic indices for identifying organic matter sources in aquatic environments: A review, Water Res. 112 (2017) 58–71. https://doi.org/10.1016/j.watres.2017.01.023.

[63] M.P. Zakaria, C.W. Bong, V. Vaezzadeh, Fingerprinting of Petroleum Hydrocarbons in Malaysia Using Environmental Forensic Techniques: A 20-Year Field Data Review, Elsevier Inc., 2017. https://doi.org/10.1016/B978-0-12-804434-6.00016-1.

[64] L. Sánchez-García, D. Carrizo, A. Molina, V. Muñoz-Iglesias, M.Á. Lezcano, M. Fernández-Sampedro, V. Parro, O. Prieto-Ballesteros, Fingerprinting molecular and isotopic biosignatures on different hydrothermal scenarios of Iceland, an acidic and sulfur-rich Mars analog, Sci Rep. 10 (2020) 1–13. https://doi.org/10.1038/s41598-020-78240-2.

[65] D. Carrizo, Sánchez-García, F. Gómez, Lipid Biomarker and Carbon Stable Isotope Survey on the Dallol Hydrothermal System in Ethiopia, Astrobiology. 19 (2019). https://doi.org/10.1089/ast.2018.1963.

[66] R. Marzi, B.E. Torkelson, R.K. Olson, A revised carbon preference index, Org Geochem. 20 (1993) 1303–1306.

[67] A. V. Herrera-Herrera, L. Leierer, M. Jambrina-Enríquez, R. Connolly, C. Mallol, Evaluating different methods for calculating the Carbon Preference Index (CPI): Implications for palaeoecological and archaeological research, Org Geochem. 146 (2020). https://doi.org/10.1016/j.orggeochem.2020.104056.

[68] D.M. Moore, R.C. Reynolds Jr, X-Ray Diffraction and the Identification and Analysis of Clay Minerals, 2nd ed., Oxford University Press Inc., New York, 1997.

[69] D. Carroll, Clay Minerals: A Guide to Their X-ray Identification, The Geological Society of America. (1970).

[70] J. Shiea, S.C. Brassell, D.M. Ward, Mid-chain branched mono- and dimethyl alkanes in hot spring cyanobacterial mats: A direct biogenic source for branched alkanes in ancient sediments?, Org Geochem. 15 (1990) 223–231. https://doi.org/10.1016/0146-6380(90)90001-G.

[71] F. Joos, S.C. Doney, F.A. Mclaughlin, E.C. Carmack, S. Nishino, K. Shimada, K. Olsson, M. Chierici, J.T. Mathis, G.L. Van Dijken, S. Pabi, C.L. Parkinson, R. Gersten, L. Stock, J.E. Overland, T. Takizawa, L.G. Anderson, M. Chierici, Y. Nojiri, Z. Gao, C.N. Flagg, J.H. Swift, R.N. Glud, M.K. Sejr, J. Bendtsen, P.B. Christensen, G.L. Van Dijken, K.R. Arrigo, M. Levasseur, P.A. Wheeler, R.A. Horner, B.C. Booth, S.E. Moore, J.E. Overland, K.E. Frey, R. Gradinger, F.A. Mclaughlin, C. Lovejoy, E.C. Carmack, D.C. Chapman, J.W. Deming, R.W. Macdonald, D. Kadko, N.R. Bates, P. Yager, H. Li, Microbial Biosynthesis of Alkanes, (2010).

[72] R.C. Coates, S. Podell, A. Korobeynikov, A. Lapidus, P. Pevzner, D.H. Sherman, E.E. Allen, L. Gerwick, W.H. Gerwick, Characterization of cyanobacterial hydrocarbon composition and distribution of biosynthetic pathways, PLoS One. 9 (2014). https://doi.org/10.1371/journal.pone.0085140.

[73] H. Parveen, S.S. Yazdani, Insights into cyanobacterial alkane biosynthesis, J Ind Microbiol Biotechnol. 49 (2022) kuab075.

[74] J. Han, M. Calvin, Hydrocarbon distribution of algae and bacteria, and microbiological activity in sediments., Proc Natl Acad Sci U S A. 64 (1969) 436–443. https://doi.org/10.1073/pnas.64.2.436.

[75] J. Köster, J.K. Volkman, J. Rullkötter, B.M. Scholz-Böttcher, J. Rethmeier, U. Fischer, Mono-, di- and trimethyl-branched alkanes in cultures of the filamentous cyanobacterium Calothrix scopulorum, Org Geochem. 30 (1999) 1367–1379. https://doi.org/10.1016/S0146-6380(99)00110-2.

[76] T. Bauersachs, H.M. Talbot, F. Sidgwick, K. Sivonen, L. Schwark, Lipid biomarker signatures as tracers for harmful cyanobacterial blooms in the Baltic Sea, PLoS One. 12 (2017) 1–25. https://doi.org/10.1371/journal.pone.0186360.

[77] N. Robinson, G. Eglinton, Lipid chemistry of Icelandic hot spring microbial mats, Org Geochem. 15 (1990) 291–298. https://doi.org/10.1016/0146-6380(90)90007-M.

[78] D. Deamer, The role of lipid membranes in life's origin, Life. 7 (2017) 5.

[79] F.G. Botes, L.P. Dancuart, H.G. Nel, A.P. Steynberg, A.P. Vogel, B.B. Breman, J.H.M. Font Freide, Middle distillate fuel production from synthesis gas via the Fischer-Tropsch process, Woodhead Publishing Limited, 2011. https://doi.org/10.1533/9780857093783.4.329.

[80] H. Mißbach, B.C. Schmidt, J.P. Duda, N.K. Lünsdorf, W. Goetz, V. Thiel, Assessing the diversity of lipids formed via Fischer-Tropsch-type reactions, Org Geochem. 119 (2018) 110–121. https://doi.org/10.1016/j.orggeochem.2018.02.012.

[81] J.G. Jones, Studies on lipids of soil micro-organisms with particular reference to hydrocarbons., J Gen Microbiol. 59 (1969) 145–152. https://doi.org/10.1099/00221287-59-2-145.

[82] D.H. Welte, G. Ebhardt, Distribution of long chain n-paraffins and n-fatty acids in sediments from the Persian Gulf, Geochim Cosmochim Acta. 32 (1968) 465–466. https://doi.org/10.1016/0016-7037(68)90080-X.

[83] B.R.T. Simoneit, Diterpenoid compounds and other lipids in deep-sea sediments and their geochemical significance, Geochim Cosmochim Acta. 41 (1977) 463–476. https://doi.org/10.1016/0016-7037(77)90285-X.

[84] J.B. Davis, Paraffinic hydrocarbons in the sulfate-reducing bacterium Desulfovibrio desulfuricans, Chem Geol. 3.2 (1967) 155–160.

[85] J. Grimalt, J. Albaigés, Sources and occurrence of C12 C22 n-alkane distributions with even carbon-number preference in sedimentary environments, Geochim Cosmochim Acta. 51 (1987) 1379–1384. https://doi.org/10.1016/0016-7037(87)90322-X.

[86] M. Nishimura, E. Baker, Possible origin of n-alkanes with a remarkable even-to-odd predominance in recent marine sediments, Geochemica et Cosmochemica Acta. 50 (1986) 299–305.

[87] L. Moodley, H.T.S. Boschker, J.J. Middelburg, R. Pel, P.M.J. Herman, E. De Deckere, C.H.R. Heip, Ecological significance of benthic foraminifera: 13C Labelling experiments, Mar Ecol Prog Ser. 202 (2000) 289–295. https://doi.org/10.3354/meps202289.

[88] N.A. Dijkman, J.C. Kromkamp, Phospholipid-derived fatty acids as chemotaxonomic markers for phytoplankton: Application for inferring phytoplankton composition, Mar Ecol Prog Ser. 324 (2006) 113–125. https://doi.org/10.3354/meps324113.

[89] J. Han, E.D. McCarthy, W. Van Hoeven, M. Calvin, W.H. Bradley, Organic Geochemical Studies, II: a Preliminary Report on the Distribution of Aliphatic Hydrocarbons in Algae, in Bacteria, and in a Recent Lake Sediment, Proceedings of the National Academy of Sciences. 59 (1968) 29–33. https://doi.org/10.1073/pnas.59.1.29.

[90] J.D. Walker, Aliphatic hydrocarbons of Cladosporium resinae cultured on glucose, glutamic acid, and hydrocarbons, Appl Microbiol. 26 (1973) 705–708.

[91] E. Gelpi, J. Oro, H.J. Schneider, E.O. Bennett, Olefins of high molecular weight in two microscopic algae, Science (1979). 161 (1968) 700–702.

[92] A. Saliot, Natural Hydrocarbons in Sea Water Alain Saliot, Elsevier Oceanography Series. 31 (1981) 327–374. https://doi.org/10.1016/S0422-9894(08)70333-7.

[93] W.W. Youngblood, M. Blumer, R.L. Guillard, F. Fiore, Saturated and unsaturated hydrocarbons in marine benthic algae, Mar Biol. 8 (1971) 190–201. https://doi.org/10.1007/BF00355215.

[94] B. Ekpo, O.E. Oyo-Ita, D.R. Oros, B.R.T. Simoneit, Sources of Organic Contaminants in Solvents and Implications for Geochemistry and Environmental Forensics: An Example from Local Vendors in Nigeria, Environ Forensics. 13 (2012) 1–6. https://doi.org/10.1080/15275922.2011.643339.

[95] O. Ekpo, O. Oyo-ita, B. Wehner, Even-n-alkane / alkene predominances in surface sediments from the Calabar River , SE Niger Delta , Nigeria, Naturwissenschaften. 92 (2005) 341–346. https://doi.org/10.1007/s00114-005-0639-8.

[96] E.P. Fubara, B.O. Ekpo, O.D. Ekpa, H.L. Marynowski, Predominances and source implications of even n-alkenes in surface sediments from coastal areas of Niger Delta , Nigeria, International Journal of Basic and Applied Science. 12 (2012) 68–79.

[97] F. Aloulou, M. Kallel, M. Dammak, B. Elleuch, A. Saliot, Even-numbered n -alkanes / n -alkenes predominance in surface sediments of Gabes Gulf in Tunisia, Environ Earth Sci. 61 (2009) 1–10. https://doi.org/10.1007/s12665-009-0315-y.

[98] Y. Lu, P.A. Meyers, Sediment lipid biomarkers as recorders of the contamination and cultural eutrophication of Lake Erie, 1909-2003, Org Geochem. 40 (2009) 912–921. https://doi.org/10.1016/j.orggeochem.2009.04.012.

[99] J.M. Peters, K.E., Walters, C.C. and Moldowan, The biomarker guide: Volume 1, Biomarkers and isotopes in the environment and human history., Second, Cambridge University Press, Cambridge, 2005. https://doi.org/10.1016/0146-6380(93)90028-a.

[100] B.R.T. Simoneit, J.O. Grimalt, J.M. Hayes, H. Hartman, Low temperature hydrothermal maturation of organic matter in sediments from the Atlantis II Deep, Red Sea, Geochim Cosmochim Acta. 51 (1987) 879–894. https://doi.org/10.1016/0016-7037(87)90101-3.

[101] B.R.T. Simoneit, W.D. Goodfellow, J.M. Franklin, Hydrothermal petroleum at the seafloor and organic matter alteration in sediments of Middle Valley, Northern Juan de Fuca Ridge, Applied Geochemistry. 7 (1992) 257–264. https://doi.org/10.1016/0883-2927(92)90041-Z.

[102] J.O. Grimalt, E. Torras, J. Albaigés, Bacterial reworking of sedimentary lipids during sample storage, Org Geochem. 13 (1988) 741–746. https://doi.org/10.1016/0146-6380(88)90096-4.

[103] M.I. Venkatesan, I.R. Kaplan, Distribution and transport of hydrocarbons in surface sediments of the alaskan outer continental shelf, Geochim Cosmochim Acta. 46 (1982) 2135–2149. https://doi.org/10.1016/0016-7037(82)90190-9.

[104] B.R.T. Simoneit, Organic Geochemistry of Terrigenous Muds and Various Shales from the Black Sea, DSDP Leg 42B, Initial Reports of the Deep Sea Drilling Project, 42 Pt. 2. (1978) 749–753. https://doi.org/10.2973/dsdp.proc.42-2.136.1978.

[105] P.G. Hatcher, B.R.T. Simoneit, F.T. Mackenzie, A.C. Neumann, D.C. Thorstenson, S.M. Gerchakov, Organic geochemistry and pore water chemistry of sediments from Mangrove Lake, Bermuda, Org Geochem. 4 (1982) 93–112. https://doi.org/10.1016/0146-6380(82)90012-2.

[106] M.M. Pawlowska, N.J. Butterfield, J.J. Brocks, Lipid taphonomy in the Proterozoic and the effect of microbial mats on biomarker preservation, Geology. 41 (2013) 103–106.

[107] J.L. Eigenbrode, Fossil lipids for life-detection: A case study from the early Earth record, Space Sci Rev. 135 (2008) 161–185. https://doi.org/10.1007/s11214-007-9252-9.

[108] H. Xiao, M. Li, T. Wang, B. You, X. Lu, X. Wang, Organic molecular evidence in the∼ 1.40 Ga Xiamaling Formation black shales in North China Craton for biological diversity and paleoenvironment of mid-Proterozoic ocean, Precambrian Res. 381 (2022) 106848.

[109] V. Grossi, C. Cravo-Laureau, J.-F. Rontani, M. Cros, A. Hirschler-Réa, Anaerobic oxidation of n-alkenes by sulphate-reducing bacteria from the genus Desulfatiferula: n-ketones as potential metabolites, Res Microbiol. 162 (2011) 915–922.

[110] R. De Mesmay, V. Grossi, D. Williamson, S. Kajula, S. Derenne, Novel mono-, di-and tri-unsaturated very long chain (C37–C43) n-alkenes in alkenone-free lacustrine sediments (Lake Masoko, Tanzania), Org Geochem. 38 (2007) 323–333.

[111] T.S. Arnarson, R.G. Keil, Organic-mineral interactions in marine sediments studied using density fractionation and X-ray photoelectron spectroscopy, Org Geochem. 32 (2001) 1401–1415. https://doi.org/10.1016/S0146-6380(01)00114-0.

[112] R.G. Keil, L.M. Mayer, Mineral Matrices and Organic Matter, 2nd ed., Elsevier Ltd., 2014. https://doi.org/10.1016/B978-0-08-095975-7.01024-X.

[113] E.J.W. Wattel-Koekkoek, P. Buurman, J. Van Der Plicht, E. Wattel, N. Van Breemen, Mean residence time of soil organic matter associated with kaolinite and smectite, Eur J Soil Sci. 54 (2003) 269–278. https://doi.org/10.1046/j.1365-2389.2003.00512.x.

[114] E.B. Rampe, B.H.N. Horgan, R.J. Smith, N.A. Scudder, E.R. Bamber, A.M. Rutledge, R. Christoffersen, A mineralogical study of glacial flour from Three Sisters, Oregon: An analog for a cold and icy early Mars, Earth Planet Sci Lett. 584 (2022) 117471.

[115] P. Fulignati, Clay minerals in hydrothermal systems, Minerals. 10 (2020) 1–17. https://doi.org/10.3390/min10100919.

[116] S.J. Ralston, T.S. Peretyazhko, B. Sutter, D.W. Ming, R. V Morris, A. Garcia, A. Ostwald, Phyllosilicate formation on early Mars via open-system acid alteration of basaltic glass, Earth Planet Sci Lett. 603 (2023) 117987.

[117] A.P. Broz, Organic matter preservation in ancient soils of Earth and Mars, Life. 10 (2020) 113.

[118] S.R. McNally, M.H. Beare, D. Curtin, E.D. Meenken, F.M. Kelliher, R. Calvelo Pereira, Q. Shen, J. Baldock, Soil carbon sequestration potential of permanent pasture and continuous cropping soils in New Zealand, Glob Chang Biol. 23 (2017) 4544–4555.

[119] J. Hassink, The capacity of soils to preserve organic C and N by their association with clay and silt particles, Plant Soil. 191 (1997) 77–87.

[120] M.J. Kennedy, D.R. Pevear, R.J. Hill, Mineral Surface Control of Organic Carbon in Black Shale, Science (1979). 295 (2002) 657–660.

[121] R.G. Keil, D.B. Montluçon, F.G. Prahl, J.I. Hedges, Sorptive preservation of labile organic matter in marine sediments, Nature. 370 (1994) 549.

[122] M.J. Kennedy, T. Wagner, Clay mineral continental amplifier for marine carbon sequestration in a greenhouse ocean, Proc Natl Acad Sci U S A. 108 (2011) 9776–9781. https://doi.org/10.1073/pnas.1018670108.

[123] M.J. Kennedy, S.C. Löhr, S.A. Fraser, E.T. Baruch, Direct evidence for organic carbon preservation as clay-organic nanocomposites in a Devonian black shale; from deposition to diagenesis, Earth Planet Sci Lett. 388 (2014) 59–70. https://doi.org/10.1016/j.epsl.2013.11.044.

[124] B. Ransom, D. Kim, M. Kastner, S. Wainwright, Organic matter preservation on continental slopes: importance of mineralogy and surface area, Geochim Cosmochim Acta. 62 (1998) 1329–1345. https://doi.org/10.1016/S0016-7037(98)00050-7.

[125] B. Ransom, In situ Occurrence of Organic Matter in Marine Sediments: Processes and Preservation, Mineral Mag. 62A (1998) 1235–1236. https://doi.org/10.1180/minmag.1998.62a.2.311.

[126] D. Singh, R.K. Sinha, P. Singh, N. Roy, S. Mukherjee, Astrobiological Potential of Fe/Mg Smectites with Special Emphasis on Jezero Crater, Mars 2020 Landing Site, Astrobiology. 22 (2022) 579–597.

[127] M. Millan, A.J. Williams, A.C. McAdam, J.L. Eigenbrode, A. Steele, C. Freissinet, D.P. Glavin, C. Szopa, A. Buch, R.E. Summons, J.M.T. Lewis, G.M. Wong, C.H. House, B. Sutter, O. McIntosh, A.B. Bryk, H.B. Franz, C. Pozarycki, J.C. Stern, R. Navarro-Gonzalez, D.P. Archer, V. Fox, K. Bennett, S. Teinturier, C. Malespin, S.S. Johnson, P.R. Mahaffy, Sedimentary Organics in Glen Torridon, Gale Crater, Mars: Results From the SAM Instrument Suite and Supporting Laboratory Analyses, J Geophys Res Planets. 127 (2022). https://doi.org/10.1029/2021JE007107.

[128] J.L. Eigenbrode, R.E. Summons, A. Steele, C. Freissinet, M. Millan, R. Navarro-González, B. Sutter, A.C. McAdam, H.B. Franz, D.P. Glavin, P.D. Archer, P.R. Mahaffy, P.G. Conrad, J.A. Hurowitz, J.P. Grotzinger, S. Gupta, D.W. Ming, D.Y. Sumner, C. Szopa, C. Malespin, A. Buch, P. Coll, Organic matter preserved in 3-billion-year-old mudstones at Gale crater, Mars, Science (1979). 360 (2018). https://doi.org/10.1126/science.aas9185.

[129] M. Vandenbroucke, C. Largeau, Kerogen origin, evolution and structure, Org Geochem. 38 (2007) 719–833.

[130] B. Durand, Kerogen: Insoluble organic matter from sedimentary rocks, Editions technip, 1980.

[131] D.J. Burdige, Preservation of organic matter in marine sediments: Controls, mechanisms, and an imbalance in sediment organic carbon budgets?, Chem Rev. 107 (2007) 467–485. https://doi.org/10.1021/cr050347q.

[132] C. Hallmann, A.E. Kelly, S.N. Gupta, R.E. Summons, Reconstructing deep-time biology with molecular fossils, Quantifying the Evolution of Early Life: Numerical Approaches to the Evaluation of Fossils and Ancient Ecosystems. (2011) 355–401.

[133] J.J. Brocks, G.D. Love, C.E. Snape, G.A. Logan, R.E. Summons, R. Buick, Release of bound aromatic hydrocarbons from late Archean and Mesoproterozoic kerogens via hydropyrolysis, Geochim Cosmochim Acta. 67 (2003) 1521–1530.

[134] M. Reinhardt, W. Goetz, J.-P. Duda, C. Heim, J. Reitner, V. Thiel, Organic signatures in Pleistocene cherts from Lake Magadi (Kenya)–implications for early Earth hydrothermal deposits, Biogeosciences. 16 (2019) 2443–2465.

[135] A. Steele, F.M. McCubbin, M. Fries, L. Kater, N.Z. Boctor, M.L. Fogel, P.G. Conrad, M. Glamoclija, M. Spencer, A.L. Morrow, A reduced organic carbon component in martian basalts, Science (1979). 337 (2012) 212–215.

[136] M.R. Raven, D.A. Fike, M.L. Gomes, S.M. Webb, A.S. Bradley, H.-L.O. McClelland, Organic carbon burial during OAE2 driven by changes in the locus of organic matter sulfurization, Nat Commun. 9 (2018) 3409.

[137] J.S.S. Damst'e, J.W. De Leeuw, Analysis, structure and geochemical significance of organically-bound sulphur in the geosphere: state of the art and future research, Org Geochem. 16 (1990) 1077–1101.

[138] J.S.S. Damst'e, W.I.C. Rijpstra, A.C. Kock-van Dalen, J.W. De Leeuw, P.A. Schenck, Quenching of labile functionalised lipids by inorganic sulphur species: evidence for the formation of sedimentary organic sulphur compounds at the early stages of diagenesis, Geochim Cosmochim Acta. 53 (1989) 1343–1355.

[139] C.R. Cousins, I.A. Crawford, J.L. Carrivick, M. Gunn, J. Harris, T.P. Kee, M. Karlsson, L. Carmody, C. Cockell, B. Herschy, K.H. Joy, Glaciovolcanic hydrothermal environments in Iceland and implications for their detection on Mars, Journal of Volcanology and Geothermal Research. 256 (2013) 61–77. https://doi.org/10.1016/j.jvolgeores.2013.02.009.

[140] P. Van Thienen, N.J. Vlaar, A.P. Van den Berg, Plate tectonics on the terrestrial planets, Physics of the Earth and Planetary Interiors. 142 (2004) 61–74.

[141] N. Ladygina, E.G. Dedyukhina, M.B. Vainshtein, A review on microbial synthesis of hydrocarbons, Process Biochemistry. 41 (2006) 1001–1014. https://doi.org/10.1016/j.procbio.2005.12.007.

[142] S. Klähn, D. Baumgartner, U. Pfreundt, K. Voigt, V. Schön, C. Steglich, W.R. Hess, Alkane biosynthesis genes in cyanobacteria and their transcriptional organization, Front Bioeng Biotechnol. 2 (2014) 24.

[143] J.L. Vago, F. Westall, B. Cavalazzi, E.S.W. Team, Searching for signs of life on other planets: Mars a case study, Biosignatures for Astrobiology. (2019) 283–300.

[144] J.L. Vago, A.J. Coates, R. Jaumann, O. Korablev, V. Ciarletti, I. Mitrofanov, J.-L. Josset, F. Westall, M.C. De Sanctis, J.-P. Bibring, Searching for traces of life with the ExoMars rover, in: From Habitability to Life on Mars, Elsevier, 2018: pp. 309–347.

[145] R.E. Summons, S.A. Lincoln, Biomarkers: Informative molecules for studies in geobiology, Fundamentals of Geobiology. (2012) 269–296.

[146] S.-V. Albers, J. van de Vossenberg, A. Driessen, W. Konings, Adaptations of the archaeal cell membrane to heat stress, Frontiers in Bioscience. 5 (2000) 813–820.

[147] G. Kaur, B.W. Mountain, M.B. Stott, E.C. Hopmans, R.D. Pancost, Temperature and pH control on lipid composition of silica sinters from diverse hot springs in the Taupo Volcanic Zone, New Zealand, Extremophiles. 9 (2015) 327–344. https://doi.org/10.1007/s00792-014-0719-9.

[148] J.B. Guckert, M.A. Hood, D.C. White, Phospholipid ester-linked fatty acid profile changes during nutrient deprivation of Vibrio cholerae: Increases in the trans/cis ratio and proportions of cyclopropyl fatty acids, Appl Environ Microbiol. 52 (1986) 794–801. https://doi.org/10.1128/aem.52.4.794-801.1986.

[149] T. Kaneda, Iso-and anteiso-fatty acids in bacteria: biosynthesis, function, and taxonomic significance, Microbiol Rev. 55 (1991) 288–302.

[150] D. Sousa, H. Smidt, M. Alves, A. Stams, Ecophysiologyof syntrophic communities that degrade saturated andunsaturated long-chain fatty acids, Federation of European Microbiological Societies Microbial Ecology. 68 (2009) 257–272. https://doi.org/10.1111/j.1574-6941.2009.00680.x.

[151] H.R. Harvey, R.D. Fallon, J.S. Patton, The effect of organic matter and oxygen on the degradation of bacterial membrane lipids in marine sediments., Geochim Cosmochim Acta. 50 (1986) 795–804. https://doi.org/10.1016/0016-7037(86)90355-8.

[152] J.C. Stern, C.A. Malespin, J.L. Eigenbrode, C.R. Webster, G. Flesch, H.B. Franz, H.V. Graham, C.H. House, B. Sutter, P.D. Archer Jr, A.E. Hofmann, Organic carbon concentrations in 3.5-billion-year-old lacustrine mudstones of Mars, Proceedings of the National Academy of Sciences. 119 (2022). https://doi.org/https://doi.org/10.1073/pnas.2201139119.

[153] B. Fuentes, A. Choque, F. Gómez, J. Alarcón, E. Castro-Nallar, F. Arenas, D. Contreras, R. Mörchen, W. Amelung, C. Knief, Influence of physical-chemical soil parameters on microbiota composition and diversity in a deep hyperarid core of the Atacama Desert, Front Microbiol. 12 (2022) 794743.

[154] M. Fabiano, R. Danovaro, Enzymatic activity, bacterial distribution, and organic matter composition in sediments of the Ross Sea (Antarctica), Appl Environ Microbiol. 64 (1998) 3838–3845.

[155] A. Patel, D. Karageorgou, E. Rova, P. Katapodis, U. Rova, P. Christakopoulos, L. Matsakas, An overview of potential oleaginous microorganisms and their role in biodiesel and omega-3 fatty acid-based industries, Microorganisms. 8 (2020) 434.

[156] G. Breuer, P.P. Lamers, D.E. Martens, R.B. Draaisma, R.H. Wijffels, The impact of nitrogen starvation on the dynamics of triacylglycerol accumulation in nine microalgae strains, Bioresour Technol. 124 (2012) 217–226.

[157] Q. Hu, M. Sommerfeld, E. Jarvis, M. Ghirardi, M. Posewitz, M. Seibert, A. Darzins, Microalgal triacylglycerols as feedstocks for biofuel production: perspectives and advances, The Plant Journal. 54 (2008) 621–639.

[158] L.J. Rothschild, The evolution of photosynthesis… again?, Philosophical Transactions of the Royal Society B: Biological Sciences. 363 (2008) 2787–2801.

[159] N.H. Sleep, D.K. Bird, Niches of the pre-photosynthetic biosphere and geologic preservation of Earth's earliest ecology, Geobiology. 5 (2007) 101–117. https://doi.org/10.1111/j.1472-4669.2007.00105.x.

[160] G.F. Slater, R.K. Nelson, B.M. Kile, C.M. Reddy, Intrinsic bacterial biodegradation of petroleum contamination demonstrated in situ using natural abundance, molecular-level 14C analysis, Org Geochem. 37 (2006) 981–989. https://doi.org/10.1016/j.orggeochem.2006.06.014.

[161] D.A. Los, K.S. Mironov, Modes of fatty acid desaturation in cyanobacteria: an update, Life. 5 (2015) 554–567.

[162] Y. Meng, M. Zhang, Z. Yang, X. Shi, Y. Yu, L. Shi, Seasonal shifts in the morphological traits of bloom-forming cyanobacteria in lake Chaohu, China, Diversity (Basel). 14 (2022) 435.

[163] T. Song, L. Mårtensson, T. Eriksson, W. Zheng, U. Rasmussen, Biodiversity and seasonal variation of the cyanobacterial assemblage in a rice paddy field in Fujian, China, FEMS Microbiol Ecol. 54 (2005) 131–140.

[164] K. Kaštovská, M. Stibal, M. Šabacká, B. Černá, H. Šantrůčková, J. Elster, Microbial community structure and ecology of subglacial sediments in two polythermal Svalbard glaciers characterized by epifluorescence microscopy and PLFA, Polar Biol. 30 (2007) 277–287. https://doi.org/10.1007/s00300-006-0181-y.

[165] E.S. Boyd, K.M. Fecteau, J.R. Havig, E.L. Shock, J.W. Peters, Modeling the habitat range of phototrophs in Yellowstone National Park: toward the development of a comprehensive fitness landscape, Front Microbiol. 3 (2012) 221.

[166] V. Galy, B. Peucker-ehrenbrink, T. Eglinton, Global carbon export from the terrestrial biosphere controlled by erosion, Nature. 521 (2015) 204–207. https://doi.org/10.1038/nature14400.

[167] N. Mangold, G. Dromart, V. Ansan, F. Salese, M.G. Kleinhans, M. Massé, C. Quantin-Nataf, K.M. Stack, Fluvial regimes, morphometry, and age of Jezero crater paleolake inlet valleys and their exobiological significance for the 2020 Rover Mission Landing Site, Astrobiology. 20 (2020) 994–1013.

[168] C. Quantin-Nataf, J. Carter, L. Mandon, P. Thollot, M. Balme, M. Volat, L. Pan, D. Loizeau, C. Millot, S. Breton, Oxia Planum: The landing site for the ExoMars “Rosalind Franklin” rover mission: Geological context and prelanding interpretation, Astrobiology. 21 (2021) 345–366.

[169] A. Stefánsson, N.S. Keller, J.G. Robin, H. Kaasalainen, S. Björnsdóttir, S. Pétursdóttir, H. Jóhannesson, G.Ó. Hreggvidsson, Quantifying mixing, boiling, degassing, oxidation and

reactivity of thermal waters at Vonarskard, Iceland, Journal of Volcanology and Geothermal Research. 309 (2016) 53–62. https://doi.org/10.1016/j.jvolgeores.2015.10.014.

[170] V. V Evtimova, I. Donohue, Quantifying ecological responses to amplified water level fluctuations in standing waters: an experimental approach, Journal of Applied Ecology. 51 (2014) 1282–1291.

[171] L.E. Hays, H. V. Graham, D.J. Des Marais, E.M. Hausrath, B. Horgan, T.M. McCollom, M.N. Parenteau, S.L. Potter-McIntyre, A.J. Williams, K.L. Lynch, Biosignature Preservation and Detection in Mars Analog Environments, Astrobiology. 17 (2017) 363–400. https://doi.org/10.1089/ast.2016.1627.

[172] C.R. Cousins, Volcano-ice interaction: a haven for life on Mars?, Astronomy & Geophysics. 52 (2011) 1.36-1.38. https://doi.org/10.1111/j.1468-4004.2011.52136.x.

[173] M. Singh, B. Sarkar, S. Sarkar, J. Churchman, N. Bolan, S. Mandal, M. Menon, T.J. Purakayastha, D.J. Beerling, Stabilization of Soil Organic Carbon as Influenced by Clay Mineralogy, 1st ed., Elsevier Inc., 2018. https://doi.org/10.1016/bs.agron.2017.11.001.

[174] N.H. Warner, J.D. Farmer, Subglacial hydrothermal alteration minerals in Jökulhlaup deposits of Southern Iceland, with implications for detecting past or present habitable environments on mars, Astrobiology. 10 (2010) 523–547. https://doi.org/10.1089/ast.2009.0425.

[175] T.M. Hoehler, An energy balance concept for habitability, Astrobiology. 7 (2007) 824–838.

# PREFACE TO CHAPTER 4

Informed by the findings from earlier chapters on glaciovolcanic habitability and taphonomy, as well as a thorough review of related literature, my dissertation shifts its emphasis towards devising data-driven techniques that refine the performance of instruments on active Mars rovers. The overarching goal is to improve the caliber of data retrieved from Mars, bolstering our *in situ* capabilities to search for life.

Specifically, Chapter 4 presents a pilot study on using low-level data fusion of complementary spectral datasets for better clay mineral classification. The study is geared towards assessing the feasibility of the method and optimizing the analytical protocol, thereby laying the foundation for subsequent development and eventual deployment on Mars rovers. The motivation for developing this tool was informed by an in-depth review of existing literature and the needs of the astrobiological community, further reinforced by the findings presented in Chapter 3.

The preceding Chapter discussed the significance of identifying expandable 2:1 clay minerals, particularly smectites, in the glaciovolcanic system. This emphasis stems from the unique physicochemical characteristics of smectites, which afford them distinct advantages in stabilizing and preserving organic biosignatures. Among all phyllosilicates, smectites boast the highest specific surface area and cation exchange capacity (CEC) [1]. These attributes amplify the number and activity of the clay mineral's reactive sites, facilitating the creation of abundant and highly stable organo-mineral complexes. Once complexed to the smectite mineral surface, organic compounds have been found to be extremely resistant to desorption [2], allowing them to be retained for long periods of time with minimal degradation [3,4]. Studies have successfully demonstrated that this unique ability to sorb and preserve organic molecules persists under simulated Martian environmental conditions [5], making smectites a high priority astrobiological target for biosignature *preservation*.

More broadly, clay minerals are also useful in assessing habitability and establishing the geologic context of potential biosignatures. This is because the characteristics and speciation of clays in a stratigraphic profile depend on factors like the nature of the protolith, the physiochemistry of the alteration fluid, the climate of the source area, transportation, depositional environments, and the subsequent diagenetic processes [6,7]. This makes clays useful proxies for reconstructing the

dynamics of past geological processes, and, by extension, assessing past habitability [8–10]. As highlighted in Chapter 1, potential biosignatures are most robustly interpreted in the context of their formation environment and establishing whether the local/regional conditions were conducive to the generation and deposition of biosignatures is critical for arriving at a consensus interpretation of life.

In light of the above, it is clear that studying the precise identity and spatial arrangement of clays on Mars can empower exploration teams to concentrate their efforts in the most promising astrobiological areas and better contextualize potential biosignatures. However, analytical difficulties associated with the ultrafine grain size, defect-rich structures, preferred crystal orientation, mineral fluorescence, et cetera can complicate the characterization of clay minerals using single analytical techniques (e.g., [11,12]). It is for this reason that the following Chapter introduces an innovative approach for discriminating between different types of clay minerals using instruments that are already available on the *Perseverance* Mars rover. In brief, the chapter describes the development of a learning algorithm capable of accurately identifying clay minerals using spectroscopic data from two complementary instruments—a laser-induced breakdown spectrometer (LIBS) and a Raman spectrometer—combined using a data fusion methodology.

The execution of this pilot study has already contributed significantly to the scientific community. First and foremost, our data-driven approach was successful in enhancing clay mineral identifications. This proof of concept can then be built upon to develop more refined algorithms ready for deployment on the *Perseverance* rover with immediate relevance to exploration. Further, the rationale and methodology presented in Chapter 4 are generalizable. The publication of this method in *Spectrochimica Acta Part B: Atomic Spectroscopy* in 2020 has been cited more than 25 times across various domains (e.g., geology, food science, hazardous material management), which underscores the wide-reaching impact and relevance of demystifying data fusion strategies for material identification. Notably, colleagues and I worked to adapt the methodology to enhance the identification of various astrobiologically-relevant carbonate minerals, with the aim of even further improving *Perseverance's* capabilities (See: Veneranda et al. 2023 [13]).

**REFERENCES**


[1] A.P. Broz, Organic matter preservation in ancient soils of Earth and Mars, Life. 10 (2020) 113.

[2] R.G. Keil, D.B. Montluçon, F.G. Prahl, J.I. Hedges, Sorptive preservation of labile organic matter in marine sediments, Nature. 370 (1994) 549.

[3] E.J.W. Wattel-Koekkoek, P. Buurman, J. Van Der Plicht, E. Wattel, N. Van Breemen, Mean residence time of soil organic matter associated with kaolinite and smectite, Eur J Soil Sci. 54 (2003) 269–278. https://doi.org/10.1046/j.1365-2389.2003.00512.x.

[4] R.G. Keil, L.M. Mayer, Mineral Matrices and Organic Matter, 2nd ed., Elsevier Ltd., 2014. https://doi.org/10.1016/B978-0-08-095975-7.01024-X.

[5] R. dos Santos, M. Patel, J. Cuadros, Z. Martins, Influence of mineralogy on the preservation of amino acids under simulated Mars conditions, Icarus. 277 (2016) 342–353. https://doi.org/10.1016/j.icarus.2016.05.029.

[6] E. Galán, Genesis of clay minerals, Dev Clay Sci. 1 (2006) 1129–1162.

[7] J. Srodon, Use of clay minerals in reconstructing geological processes; recent advances and some perspectives, Clay Miner. 34 (1999) 27–37.

[8] R. Bonaccorsi, C.P. McKay, B. Chen, Biomass and habitability potential of clay minerals-and iron-rich environments: testing novel analogs for Mars Science Laboratory landing sites candidates, Philosophical Magazine. 90 (2010) 2309–2327.

[9] S.J. Ralston, T.S. Peretyazhko, B. Sutter, D.W. Ming, R. V Morris, A. Garcia, A. Ostwald, Phyllosilicate formation on early Mars via open-system acid alteration of basaltic glass, Earth Planet Sci Lett. 603 (2023) 117987.

[10] D. Singh, R.K. Sinha, P. Singh, N. Roy, S. Mukherjee, Astrobiological Potential of Fe/Mg Smectites with Special Emphasis on Jezero Crater, Mars 2020 Landing Site, Astrobiology. 22 (2022) 579–597.

[11] A. Wang, J.J. Freeman, B.L. Jolliff, Understanding the Raman spectral features of phyllosilicates, Journal of Raman Spectroscopy. 46 (2015) 829–845. https://doi.org/10.1002/jrs.4680.

[12] M. Ritz, L. Vaculíková, J. Kupková, E. Plevová, L. Barto, Vibrational Spectroscopy Different level of fluorescence in Raman spectra of montmorillonites, Vib Spectrosc. 84 (2016) 7–15. https://doi.org/10.1016/j.vibspec.2016.02.007.

[13] M. Veneranda, J.A. Manrique, G. Lopez-Reyes, S. Julve-Gonzalez, F. Rull, C. Alvarez Llamas, T. Delgado Pérez, E. Gibbons, E. Clavé, E. Cloutis, Developing tailored data combination strategies to optimize the SuperCam classification of carbonate phases on Mars, Earth and Space Science. 10 (2023) e2023EA002829.

# CHAPTER 4

# Data Fusion of Laser-Induced Breakdown and Raman Spectroscopies: Enhancing Clay Mineral Identification

Erin Gibbons[a*], Richard Léveillé[a1], and Kim Berlo[a1]

[a]Department of Earth and Planetary Sciences, McGill University, 3450 University Street, Montreal, Quebec, Canada, H3A 0E8

[1]These authors contributed equally to this work.

*Corresponding author: *erin.gibbons@mail.mcgill.ca*

Published & citable as:

Gibbons, E., Léveillé, R., & Berlo, K. (2020). Data fusion of laser-induced breakdown and Raman spectroscopies: Enhancing clay mineral identification. *Spectrochimica Acta Part B: Atomic Spectroscopy*, 170, 105905.

## ABSTRACT

A straight-forward, data-driven approach for the reliable identification of clay minerals based on spectroscopy and multivariate analyses is presented here. No other group of inorganic materials has so many species, exhibit such a range of physicochemical properties, or enjoy a greater diversity of practical applications as the clay minerals. The emerging role of clays in a variety of pioneering disciplines, such as the pharmaceutical and astrobiological sciences, highlights their broad-ranging significance in natural science and engineering efforts. However, the highly variable chemical compositions and defect-rich structures of the clay minerals pose difficulties in their classification and identification. We introduce a new methodological approach which uses Raman

and laser-induced breakdown spectroscopies (LIBS) to discriminate geological specimens based on their dominant clay mineralogy. Raman and LIBS provide complementary information about the molecular structure and elemental composition of an interrogated target, and, when considered simultaneously, contribute to a more comprehensive characterization of the system under study. What distinguishes this work from previous spectral investigations of clay mineralogy is the way in which the spectra are pre-processed and combined before analysis. Raman and LIBS data were collected from various clay-rich specimens and subsequently concatenated into a single data matrix to serve as a unique identifier of specimen composition – an approach known as low-level data fusion. Multivariate statistical analyses were used to identify mineralogical groups and to discriminate specimens based on their compositional similarities and differences. We evaluated the discrimination achieved by the fused data sets compared to that obtained by standalone use of Raman and LIBS data. Our results show that the use of data fusion strategies improved the discrimination model and allowed correct classification of all the samples based on their dominant clay mineralogy.

## 4.1 INTRODUCTION

Clay minerals belong to the phyllosilicate family of minerals, which are characterized by their parallel sheets of linked silica tetrahedra. As the primary product of chemical weathering and one of the more abundant components of sediments and soils, research into clay minerals has long been focused on the geological, geotechnical, and mineralogical characteristics of clays [1]. Indeed, the occurrence of clay minerals has been widely used to support geological surveys, stratigraphic correlations, and paleoenvironmental reconstructions in both terrestrial [1] and extra-terrestrial contexts [2,3]. It is only relatively recently that clay minerals have emerged as cross-disciplinary materials of interest with diverse practical applications. Today, clay minerals represent one of the most important commodities used for manufacturing [4] and recent literature indicates pioneering applications in the biological, medical, and pharmaceutical sciences as well as a growing role in environmental engineering for carbon sequestration and hazardous waste management [1]. The main features that evoke such broad interest in clays are their natural prevalence, low-cost, and their unique structural and chemical properties (*e.g.*, swelling behaviour, adsorption capacity, colloidal properties, surface reactivity, and nanometer-scale layer structure) [1]. These properties guarantee the continued use and innovation of clay mineral applications in the future, as has been the trend in the past.

Pronounced and ongoing advances in instrumentation and computational methods have continued to enable the development of fast, cost-efficient, and non-destructive techniques for the investigation of geomaterials, and in particular, clays. Given that optical spectroscopic techniques, particularly the laser-based spectroscopies, facilitate minimally destructive and highly sensitive analyses, these approaches are of rising importance for modern clay investigations. For instance, reflectance spectroscopy in the visible and infrared ranges, Raman spectroscopy, and laser-induced breakdown spectroscopy (LIBS), have all emerged as powerful tools for investigating clay minerals and clay-bearing assemblages [5,6] (and references therein). However, the characterization of clay minerals remains difficult relative to that of other minerals [5,7]. Clay mineral compositions are more complex than their chemical formulas indicate and may be heterogeneous within them due to isomorphous substitutions of elements [1]. Analytical difficulties associated with the ultrafine grain size, defect-rich structures, preferred crystal orientation, and mineral fluorescence serve to further complicate the interpretation of direct mineralogical techniques or mineralogical inferences from elemental techniques [8–10]. As such, a single analysis rarely provides a complete understanding of a clay-bearing assemblage, and it is common to collect multiple data sets using complementary acquisition methods to obtain a more comprehensive picture [11].

Amongst the surface laser spectroscopy approaches, the coupling of LIBS and Raman spectroscopy represents a fortuitous combination for clay mineral investigations by adding complementary information that each measurement alone would not detect. LIBS and Raman are sensitive to different physicochemical phenomena and respond uniquely to a given sample: LIBS records the elemental composition, from which researchers can determine the geochemistry and infer the mineralogy, whereas Raman spectroscopy records the molecular structure, from which researchers can determine the mineralogy and infer the elemental composition [12]. Moreover, LIBS and Raman may be applied to a very wide range of materials without sample preparation, making them versatile tools suitable for both *in situ* and *ex situ* analyses [13]. Although work by Sharma et al. [14] demonstrated that a combination of both techniques in a single instrument can effectively provide complementary physicochemical information of phyllosilicate specimens, the authors considered the spectral data sets separately. Our contribution is built upon the hypothesis that the analytical benefits and capabilities of combining LIBS and Raman spectroscopy have not been fully realized in the study of clay minerals and go beyond comparing atomic and structural

parameters to generate a mineral assignment that is consistent with the outputs of both technologies. We hypothesize that spectral fusion at the data level (*i.e.*, spectral concatenation) offers a simple means of increasing the scientific output of these technologies. Indeed, although the efficacy of LIBS and Raman data fusion for the discrimination and categorization of geological materials has only begun to be investigated, initial reports are promising (*e.g.,* [15–18]). Such reports generally indicate that data fusion strategies outperform individual spectroscopy approaches for mineral and rock classification because the uncertain identity of an unknown specimen that arises from its multi-elemental spectral data may be clarified by its vibrational counterpart, and vice versa. However, despite the evident potential benefit, the knowledge of how to actually exploit the added diversity that multiple data sets offer is in preliminary stages. Furthermore, data fusion strategies have yet to be applied systematically to specimens from the clay mineral group.

With this pilot study, we want to expand upon the limited existing studies of LIBS and Raman spectroscopy data fusion relevant for geological exploration. We contribute to this growing body of literature by concatenating the complete LIBS and Raman spectral responses into a new, combined data matrix, a process referred to as *low-level fusion* [19], which is then treated by multivariate statistical analyses. We assess the capability of this fusion architecture to enhance the rate of correct classifications relative to that which is achieved by either analytical technique individually for a suite of impure geological reference materials with a high clay content. The objective is to discriminate the specimens by their predominant clay mineralogy. We employ principal component analysis (PCA) for visualization, data reduction, and to determine the spectral features that are important for successful identification of the clay minerals. This is followed by the development of linear discriminant models for classification. We present separate multivariate models built separately on either LIBS *or* Raman data and compare the results with models built on their concatenated (low-level fusion) spectra. Consistent with previous studies, our results demonstrate that the discriminating potential is increased through the application of data fusion strategies, allowing for an improved classification of specimens. The approach to clay mineral discrimination presented here is intended as an illustration of the general applicability of data fusion to complex mixture analysis where two or more independent spectroscopic (or other multivariate analytical measurement) data sets are available for any sample cohort. Indeed, the benefits afforded by data fusion are derived from the inclusion of

complementary information to generate a more complete characterization of the physicochemical properties of a specimen and may be reasonably extended to other contexts and experimental parameters not explicitly included in this study. For instance, although bench-top instruments and pelletized mineral powders were considered here, portable systems for both LIBS and Raman spectroscopy have been developed for *in situ* analyses and would be amenable to the benefits of data fusion.

## 4.2 MATERIALS AND METHODS

### 4.2.1 Samples

We selected a suite of materials that allows us to test the ability of each data set to discriminate between compositionally similar samples as well as compositionally diverse samples. Fourteen mineral reference materials were obtained from the Clay Mineral Society (CMS), the American Petroleum Institute (API), and the Centre de Recherches Pétrographiques et Géochimiques (CRPG). Some of the reference materials are powders, others are rock chips; the rock chips were gently crushed by hand in a mortar and pestle until the grains could pass through a 250-μm mesh. The resulting powders were homogenized by careful stirring. Each powder was pressed into a pellet at an estimated pressure of $2\times10^6$ Pa (uncorrected for friction) for two minutes. Approximately 0.6 g of each sample was used to create a pellet 1 cm in diameter by 2 mm thick. A summary of specimens and preparation steps is provided in Table 4.1; chemical compositions (expressed as mass fraction %) are provided in Table 4.2. With the exception of SynH-1 (synthetic hectorite), the reference materials considered here are naturally occurring geological specimens. Although the dominant mineral component is the specified clay mineral, most of the specimens are known to contain variable amounts of mineral impurities, which are summarized in Table 4.3. No grain size fractionation or other purification steps were undertaken to isolate the clay mineral fraction. Purification was omitted in order to provide a realistic representation of naturally occurring, mixed geological specimens and to test the feasibility of developing a procedure that can discriminate clay-rich geological materials by their dominant mineralogy, with minimal specimen preparation. Moreover, analyses by [20] of some of the CMS reference materials considered here indicate that processing to obtain the clay-sized fraction does little to alter the mineralogy of the specimens or remove impurities.

| Group | Layer Type | Layer Charge | Octahedral Character | Subgroup | # | Mineral Species | Specimen ID | Source | Preparation Notes |
|---|---|---|---|---|---|---|---|---|---|
| **Kaolinite-Serpentine** | 1:1 | ~0 | Dioctahedral | Kaolinite | 1 | Low-defect Kaolinite | KGa-1 | CMS | Pressed as shipped |
| | | | | | 2 | High-defect Kaolinite | KGa-2 | CMS | Pressed as shipped |
| | | | | | 3 | Kaolinite | No. 4 | API | Ground by mortar and pestle, homogenized by stirring, pressed |
| **Mica Clay Minerals** | 2:1 | ~1 (true mica) | Dioctahedral | True Mica | 4 | Illite | IMt-1 | CMS | Ground by mortar and pestle, homogenized by stirring, pressed |
| | | | Trioctahedral | True Mica | 5 | Zinnwaldite* | ZW-C | CRPG | Pressed as shipped |
| | | | | | 6 | Fe-Biotite | Mica-Fe | CRPG | Pressed as shipped |
| | | | | | 7 | Phlogopite | Mica-Mg | CRPG | Pressed as shipped |
| **Smectite** | 2:1 | 0.2-0.6 | Dioctahedral | Nontronite | 8 | Nontronite | NAu-1 | CMS | Ground by mortar and pestle, homogenized by stirring, pressed |
| | | | | | 9 | Nontronite | NAu-2 | CMS | Dried at 35˚C for 24 hours**, ground by mortar and pestle, homogenized by stirring, pressed |
| | | | | Montmorillonite | 10 | Ca-, Na-Montmorillonite | SWy-1 | CMS | Pressed as shipped |
| | | | | | 11 | Ca-Montmorillonite | SAz-1 | CMS | Pressed as shipped |
| | | | | | 12 | Montmorillonite | STx-1 | CMS | Pressed as shipped |
| | | | Trioctahedral | Hectorite | 13 | Hectorite | SHCa-1 | CMS | Pressed as shipped |
| | | | | | 14 | Synthetic Hectorite | SYnH-1 | CMS | Pressed as shipped |

*Table 4.1: List of clay reference materials used in this study.*
*Table includes relevant classification attributes, sample identifiers, source information, and description of sample preparation steps.*
**Zinnwaldite was the descriptive name of the standard. Zinnwaldite is no longer a species, instead it is recognized as a series of trioctahedral micas on, or close to, the siderophyllite-polylithionite join [21].*
*** The NAu-2 material was damp and prone to aggregating. Gentle drying was necessary to facilitate manual grinding.*

| Groups | Kaolinite-Serpentine | | | Mica Clay Minerals | | | | Smectite | | | | | | |
|---|---|---|---|---|---|---|---|---|---|---|---|---|---|---|
| Subgroups | Kaolinite | | | True Mica | | | | Nontronite | | Montmorillonite | | | Hectorite | |
| # | 1 | 2 | 3 | 4 | 5 | 6 | 7 | 8 | 9 | 10 | 11 | 12 | 13 | 14 |
| ID | KGa-1 | KGa-2 | No. 4 | IMt-1 | ZW-C | Mica-Fe | Mica-Mg | NAu-1 * | NAu-2 * | SWy-1 | SAz-1 | STx-1 | SHCa-1 | SYnH-1 * |
| $SiO_2$ | 44.2 | 43.9 | 44.8 | 49.3 | 54.0 | 34.4 | 38.3 | 53.3 | 57.0 | 62.9 | 60.4 | 70.1 | 34.7 | 49.7 |
| $Al_2O_3$ | 39.7 | 38.5 | 37.2 | 24.3 | 18.5 | 19.5 | 15.2 | 10.2 | 3.4 | 19.6 | 17.6 | 16.0 | 0.7 | 38.2 |
| MgO | 0.0 | 0.0 | 0.3 | 2.6 | 0.2 | 4.6 | 20.4 | 0.3 | 0.3 | 3.1 | 6.5 | 3.7 | 15.3 | 0.0 |
| $Na_2O$ | 0.0 | 0.0 | 0.4 | 0.0 | 0.3 | 0.3 | 0.1 | 0.1 | 0.1 | 1.5 | 0.1 | 0.3 | 1.3 | 0.3 |
| CaO | n.d. | n.d. | 0.6 | 0.4 | 0.4 | 0.4 | 0.1 | 3.5 | 2.7 | 1.7 | 2.8 | 1.6 | 23.4 | n.r. |
| $Fe_2O_3$ | 0.1 | 1.0 | 0.4 | 7.3 | 1.3 | 4.6 | 2.0 | 34.2 | 37.4 | 3.4 | 1.4 | 0.7 | 0.0 | 0.0 |
| FeO | 0.1 | 0.2 | 0.1 | 0.6 | 7.3 | 18.9 | 6.7 | n.r. | n.r. | 0.3 | 0.1 | 0.2 | 0.3 | n.r. |
| $TiO_2$ | 1.4 | 2.1 | 1.3 | 0.6 | 0.1 | 2.5 | 1.6 | n.r. | n.r. | 0.1 | 0.2 | 0.2 | 0.0 | 0.0 |
| $K_2O$ | 0.1 | 0.1 | 0.4 | 7.8 | 7.7 | 8.8 | 10.0 | 0.0 | 0.0 | 0.5 | 0.2 | 0.1 | 0.1 | 0.0 |
| $P_2O_5$ | 0.0 | 0.0 | n.r. | n.r. | 0.0 | 0.5 | 0.1 | n.r. | n.r. | 0.0 | 0.0 | 0.0 | 0.0 | 0.0 |
| F | 0.0 | n.r. | n.r. | n.r. | 5.5 | 1.6 | 2.9 | n.r. | n.r. | 0.1 | 0.3 | n.r. | 2.6 | 0.8 |
| $Li_2O$ | n.r. | n.r. | n.r. | n.r. | 2.4 | 0.1 | 0.0 | n.r. | n.r. | n.r. | n.r. | n.r. | 2.2 | 0.3 |
| Loss on Ignition | 13.8 | 13.8 | 14.7 | 8.0 | 4.2 | 5.3 | 4.2 | n.r. | n.r. | 6.1 | 9.9 | 6.5 | 21.8 | 11.2 |
| Total | 99.4 | 99.5 | 100.1 | 100.8 | 93.9 | 99.8 | 98.7 | 101.6 | 101.0 | 99.2 | 99.2 | 99.3 | 97.6 | 99.4 |
| Reference | [22] | [22] | [23] | [22] | [24] | [25] | [25] | [26] | [26] | [22] | [22] | [22] | [22] | [22] |

*Table 4.2: Summary of chemical composition of the reference materials as reported by the supplier or by baseline studies.*
*Values are in weight percentage. n.r. = not reported by the reference.*
**Special clays from the Clay Mineral Society; their elemental data is unofficial and meant to be used as guideline and not an analytical certification.*

| # | ID | Mineralogy | Ref |
|---|---|---|---|
| **1** | KGa-1 | ~96% kaolinite and trace dickite, 3% anatase, 1% crandallite + quartz(?) | [20] |
| **2** | KGa-2 | ~96% kaolinite and trace dickite, 3% anatase, 1% crandallite + mica and/or illite | [20] |
| **3** | No. 4 | ~88-92% kaolinite, 2-3% quartz, 2-3% sericite, 2-3% titanite, 1-2% orthoclase, 1-2% albite, traces of limonite, carbonate, pyrite, anatase, and ferro-magnesian minerals | [23,27] |
| **4** | IMt-1 | ~90% illite, 8% quartz, 2% microcline, 0.3% kaolinite, traces of chlorite, traces of rutile and anatase | [28,29] |
| **5** | ZW-C | ~77% zinnwaldite, 22% quartz, 0.9% topaz, 0.2% fluorite, 0.1% sulfides, 0.1% cassiterite | [24] |
| **6** | Mica-Fe | 100% biotite | [30] |
| **7** | Mica-Mg | 100% phlogopite | [30] |
| **8** | NAu-1 | ~90% smectite, 4% kaolin, 2% quartz, <1% biotite, 3% goethite | [26] |
| **9** | NAu-2 | ~95% smectite, 5% plagioclase, <1% quartz | [26] |
| **10** | SWy-1 | ~75% smectite, 8% quartz, 16% feldspar, 1% gypsum + mica and/or illite + kaolinite(?) and/or chlorite(?) | [20] |
| **11** | SAz-1 | ~98% smectite, 1% quartz, 1% other | [20] |
| **12** | STx-1 | ~67% smectite, 30% opal-CT, 3% quartz + feldspar + kaolinite + talc(?) | [20] |
| **13** | SHCa-1 | ~50% smectite, 43% calcite, 3% dolomite, 3% quartz, 1% other | [20] |
| **14** | SYnH-1 | ~95% smectite, ~5% boehmite | [20] |

*Table 4.3: Mineralogy of the clay-bearing reference materials used in this study.*

### 4.2.2 Experimental Methods

#### *4.2.2.1 Raman Spectroscopy*

Raman spectra were collected at McGill University using an inVia™ Qontor® confocal Raman microscope with a 532 nm laser, adjustable up to 50 mW at 100% power. The laser radiation was focused on the sample using a 50× DM2700 M Leica microscope objective. All spectra were recorded under similar conditions: 25 accumulated exposures, exposure time of 0.5 s, 2400 L/mm grating system, and laser power adjusted to 12.5% (laser power needed to be reduced to 2.5% for the analysis of the three kaolinite specimens to avoid photodegradation). In the present study, we considered only the spectral region ranging from 120 – 1200 $cm^{-1}$, where the characteristic lattice vibrational modes of clay minerals are observed [8]. Frequencies in the 3000 – 3800 $cm^{-1}$ region relevant to the study of the $H_2O$/OH vibrations were not taken into account because the water content of the specimens could not be reliably controlled during analysis. An

internal Si reference sample was used to calibrate the Raman shift to the known position of the crystalline Si Raman band (520.7 $cm^{-1}$).

To partially offset the effects of sample heterogeneity and ensure adequate representation of the composition of the specimen, surface rastering and spectral averaging were employed. Specifically, the Raman spectra were acquired from 250 different positions on the surface of each specimen using a grid pattern to capture a realistic average mineral composition. A motorized stage was used to translate the specimen and expose a fresh surface for each subsequent recording. After data collection, the distribution of the 250 data points were visualized using principal component analysis (not shown); the individual spectra were randomly distributed within the data cloud, indicating that the surface rastering procedure adequately captured the specimen's compositional variance on the scale of the sampling area. Twenty-five recordings were averaged together to provide a composite spectral fingerprint representative of bulk mineralogy. This measurement strategy produced 10 averaged spectral signatures for each specimen, resulting in a total of 140 Raman spectroscopy samples (14 specimens × 10 signatures).

#### *4.2.2.2 LIBS*

The McGill University LIBS system consists of a J200 instrument (Applied Spectra) equipped with a high power, Q-switched, Nd:YAG laser and a 6 channel CCD-based broadband spectrometer. The laser operates at 213 nm with a 10 Hz repetition rate. The spectral window ranges from 190 to 1040 nm. Following the methods of [31], operating parameters such as laser fluence and detector gate delay were systematically varied and their effects on the quality and repeatability of the characteristic Si emission line at 288.2 nm were compared. The Si emission line was selected because it is a common element amongst all the studied specimens. A spot size of 100 μm, laser energy of 3.82 mJ/pulse, and a gate delay of 0.25 μs provided the best signal-to-noise ratio and repeatability of the Si line and were therefore used to record the LIBS spectra of all the specimens. The gate width is fixed at 1.05 μs. Samples were run in air.

As with the Raman analyses, to offset the effects of sample heterogeneity and ensure adequate representation of the composition of the specimen, the LIBS was operated in scanning mode and spectra were acquired from 250 different positions across the specimen surface. Homogeneity at the scale of the sampling area was checked via principal component analysis of the individual spectra (not shown) and twenty-five individual LIBS spectra were averaged together to produce

10 composite LIBS fingerprints for each specimen, resulting in a total of 140 LIBS samples (14 specimens × 10 signatures).

### 4.2.3 Data Treatment

#### *4.2.3.1 Spectral Pre-processing*

Pre-processing is generally required before chemometric modeling to increase the signal-to-noise ratio and improve the multivariate analysis [32]. Since the Raman and LIBS data were collected using different spectrometers, the dynamic range of their output spectra are non-identical, meaning that the intensity values observed by each instrument span different ranges in magnitude. Normalization to a metric that accurately reflects the total spectral intensity change overcomes these issues and permits spectral comparisons between specimens and between instruments [33]. Here, the data obtained from both techniques were imported into the Unscrambler X software (Camo Analytics, Version 10.4) and separately treated by the *unit vector normalization*. The *unit vector normalization* first computes the square root of the sum of the squared values of all the measured intensities (the spectral 'norm'). Each measured intensity is divided by the 'norm' to obtain the normalized value, *x'*:

$$x_i{}' = \frac{x_i}{|(x_1^2 + x_2^2 + x_3^2 + \cdots x_n^2)^{1/2}|}\ , \qquad i = 1, 2, 3, \ldots n$$

where *x* is the intensity value corresponding to either a LIBS wavelength or a Raman shift and *n* is the number of variables (spectral bands). This procedure converts each spectral vector to unit-vector length (*i.e*., gives it a magnitude of 1) which facilitates their direct comparison between individual spectra and between instruments and allows the data from both instruments to be fused without one data set unduly dominating the other due to differences in recorded energy. Unit vector normalization is ideal for qualitative pattern recognition efforts and has successfully been applied as a pre-treatment step in other investigations of LIBS+Raman data fusion [34,35]. The spectra were then smoothed by the Savitzky-Golay algorithm (2$^{nd}$ order polynomial, five-point smoothing window) to remove high-frequency noise.

Prior to normalization and smoothing, the Raman spectra were treated by the Renishaw factory-supplied WiRE™ software: cosmic ray interference was eliminated using the automated nearest neighbor option and the sloped fluorescence baseline was subtracted using a 12$^{th}$ order polynomial via the Intelligent Polynomial algorithm (Renishaw, WiRE™). Additionally, the

spectral regions corresponding to the laser wavelength (first order response at 212 – 213 nm and second order response at 425 – 426 nm) were discarded from the LIBS spectra.

#### *4.2.3.2 Data Fusion*

After individual pre-processing, the LIBS and Raman spectra were fused by low-level data fusion. The complete data arrays from each technique were concatenated into a new, unified matrix and treated as though they were a single spectral fingerprint of a given specimen. Given that multiple spectra were averaged over an area, each of the 10 averaged spectral fingerprints are taken to represent the bulk specimen composition. No effort was made to match the sampling areas between the Raman spectroscopy and LIBS analyses during concatenation; similar approaches are described by [34,35]. This procedure resulted in three separate data packages which were then evaluated by multivariate analyses, namely PCA and linear discriminant analysis (LDA) (see Section 4.2.3.1):

1) The LIBS data set;
2) The Raman spectroscopy data set;
3) The low-level fusion data set.

Initially, spectral data from LIBS and Raman were evaluated separately, then the results were compared with the results obtained by evaluating the fused data set.

#### *4.2.3.3 Statistical Analysis*

PCA is an unsupervised data reduction technique commonly used by spectroscopists to explore data sets of high dimensionalities. PCA defines new variables, called principal components (PCs), from linear combinations of the original variables [36]. The PCs are defined such that they are orthogonal to each other, thereby capturing complementary information and eliminating data redundancies by removing highly correlated variables [36]. The original data set is typically described satisfactorily in just a few PCs, which reduces the data volume with minimal loss of information and enables visualization within a lower-dimensional, more tractable space. The PCA models were built using the Unscrambler X software on mean centered data, calibrated using the non-linear iterative partial least squares (NIPALS) algorithm, and checked for multivariate outliers. Details about the implementation of PCA in the Unscrambler X may be found in Esbensen and Swarbrick [32] and a more nuanced description of PCA in general is available in several statistical texts, for example, [36].

LDA is one of the most commonly used approaches for studying the association between a set of predictors and a categorical response. It was applied here to evaluate whether the clay-bearing specimens could be discriminated on the basis of their dominant clay mineralogy, as described by LIBS and Raman signatures. We explored discrimination at the structural group and subgroup levels, according to the classification schemes described by Bergaya and Lagaly [1] and outlined in Table 4.1. Unlike PCA, LDA is a supervised technique in which the categorical (class) membership of each specimen is known *a priori* (in this case, the group-level and subgroup-level mineral designation is known). This information is used to construct a set of linear functions that maximizes the between-class variance (*i.e.*, the distance between class centroids) and simultaneously minimizes the within-class variance (*i.e.,* the distance of an object to its class centroid) [37]. In other words, LDA facilitates discrimination of objects by providing the most distinguishable classes.

However, LDA cannot be applied if the number of variables (spectral responses) is greater than the number of samples, as is the case with high-dimensional spectral data [38]. The large number of dimensions allows too much scope for discrimination to be achieved by chance, in directions that mainly represent noise [39]. A remedy for this is to use PCA to obtain a lower-dimensional feature set and then build the LDA classifier based on this reduced set of features [32]. By retaining only the most relevant, low-order PCs, the noise-part of the data set is effectively omitted and class discrimination may be defined upon a meaningful foundation [32]. The number of PCs included in the LDA were chosen based on the Cattell scree test [40] (not shown), a graphical technique that is widely used to define the cut-off point of non-informative PCs [36] and has been successfully applied to optimally reduce high-dimensional spectral data sets [41]. Moving forward, this approach will be referred to as principal component-linear discriminant analysis (PC-LDA). The PC-LDA models were built using NCSS Statistical Software (Version 20.1; NCSS, LLC. Kaysville, Utah, http://ncss.com/software/ncss).

Practically, the PC-LDA discriminant functions may be used to predict class membership of unknown objects based on probability [42]. The density of observations at a particular distance from a class centroid is a direct estimator of the probability that an object at this distance belongs to the class. Thus, a case with unknown classification is submitted to the discriminant functions to determine its distance from each class centroid and it is allocated to the class with which it has the greatest probability of membership; details of the algorithm used by NCSS to estimate the

classification probabilities are described in [42]. To simulate the practical use of our models on future data, the data were divided into a training set of specimens, in which the group/subgroup specifications were known, and a test set of specimens, which were treated as unknowns. Of the 140 spectra acquired from the clay-bearing reference materials, 112 (80%) were used as a training set and 28 (20%) as a test set for the validation step. To guarantee the representativeness of both the test set and the training set, the DUPLEX algorithm was used to split the data [43]. When applying DUPLEX, the two objects (spectra) which are farthest apart in terms of their Euclidean distance (*i.e.*, most dissimilar) are assigned to the training set. The next pair of points that are farthest apart in the remaining data set are assigned to the test data set. This process is repeated until both the training and the testing data sets are filled. Such a procedure leads to the formation of two balanced sets, consisting of objects uniformly distributed within the descriptors space. To ensure that each clay reference material was adequately represented in both the training and test data sets, the DUPLEX algorithm was separately applied to each set of averaged spectral samples from a given specimen. Since computational complexity impedes the use of the DUPLEX algorithm for large, high-dimensional data sets, the algorithm was applied to a matrix built by concatenating the significant PCs extracted separately from the LIBS and Raman data arrays. Given that the majority of the variance within the data set is contained within these low-order PCs, this approach ensures that the same training/test split may be used for the investigation of the single-spectroscopy data sets, as well as the fused matrix; this approach was successfully applied by [44]. The DUPLEX algorithm was applied in MATLAB (The Mathworks, Natick, MA) using a script modified from [45]. A graphical representation of the structure of the data splitting and discrimination scheme is displayed in Figure 4.1. To compare the performance of single- and fused-spectroscopy for the discrimination of clay-bearing specimens by their dominant mineralogy, PC-LDA models were built on each of the three data packages: LIBS, Raman, and low-level fusion of LIBS+Raman. The percentage of the specimens that were allocated to the correct class were compared.

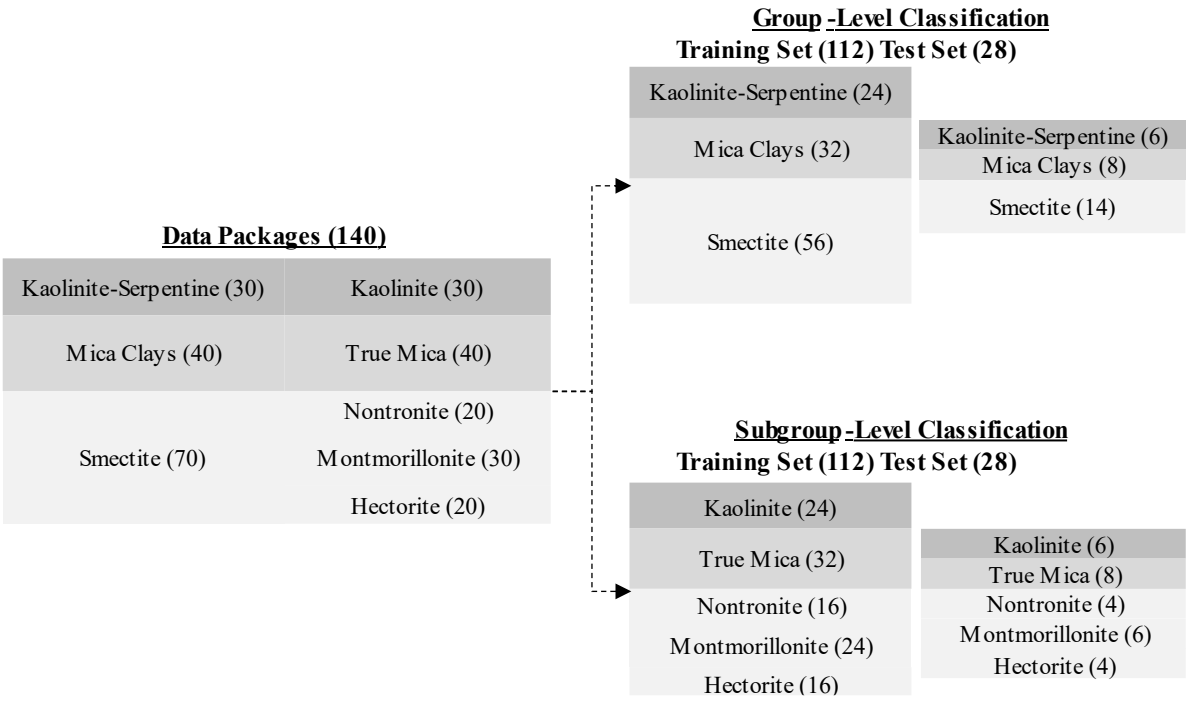


*Figure 4.1: Graphical representation of the sample set and validation scheme.*
*Eighty-percent of the measured spectra were used to train the PC-LDA models ("Training Set"), the remaining twenty-percent were set aside and treated as unknowns to simulate the practical use of the models in predicting future data ("Test Set"). The DUPLEX data splitting method was used to allocate each spectrum into either the Training or Test set. The number of samples included in each category is given in parentheses.*

## 4.3 RESULTS AND DISCUSSION

### 4.3.1 Spectral Feature Analysis

#### *4.3.1.1 LIBS*

Representative examples of the LIBS spectra obtained for each of the 14 specimens are given in Figure 4.2. Minimal variability was observed between the 10 spectral samples created by averaging consecutive measurements from the specimen surface, indicating that averaging measurements over an area successfully captured the range of compositions. Peak labels were assigned according to the National Institute of Standards (NIST) LIBS database [46].

LIBS spectra tend to be structurally complex, containing multiple emission lines for most of the elements corresponding to both the primary mineral and other minerals present in the specimen. Indeed, chemical signals associated with the known impurities (Table 4.3) were resolved. For instance, the Ti lines in the three kaolinite specimens are likely derived from the minor anatase components, a $TiO_2$ mineral. The prominent Ca lines in the SHCa-1 fingerprint are partially associated with the calcite ($CaCO_3$) impurity of the specimen; the influence of this impurity is especially apparent when comparing the SHCa-1 spectrum to the synthetic hectorite (SYnH-1),

which exhibits only a weak Ca signal. However, the peaks that dominate each of the measured spectra are those of the most abundant divalent and trivalent cations that fit into the layer and interlayer sites of the primary clay mineral phase (*i.e.*, Mg, Al, Fe, K, Ca, Na). The LIBS technique is more sensitive for detecting major cations and this observation is consistent with previous reports that mineralogical LIBS spectra are dominated by the emission of the cationic components of a specimen [14,16]. These peaks are observed in the spectral fingerprints from each specimen with relative intensity patterns that reflect the main chemical differences between the clay mineral groups. When tetrahedral and octahedral molecular sheets are joined to form a layer, the resulting structure can be classified based on the ratio of tetrahedral layers to octahedral layers (1:1 or 2:1), charge on the layers, and the type of material occurring between the layers (Table 4.1). The layers may either be electrically neutral or negatively charged. A negative layer charge arises from either isomorphic substitution of $Al^{3+}$ for $Si^{4+}$ in the tetrahedral layer or substitution of $Al^{3+}$ for $Mg^{2+}$ in octahedral sites [1]. The negative charge is balanced by cations intercalated between the structural layers (the interlayer). In the kaolinite-serpentine class, the layer charge is near 0 and no ionic species occupy the interlayer. The 2:1 layers in the true micas have a negative charge of $\simeq 1$ that is balanced by large univalent cations, usually $K^{+}$. The 2:1 layers of the smectite class have a smaller negative charge (0.2-0.6) that is typically balanced by a mixture of alkaline earth ions, $Ca^{2+}$ and $Mg^{2+}$, or the alkaline metal $Na^{+}$ [1]. These interlayer cationic trends are clearly reflected in the LIBS spectra. For example, the relatively K-rich nature of the true mica interlayer is reflected by the dominance of the K peak, as is the relatively K-poor nature of the kaolinite-serpentine and smectite groups. Although Si and O are both major chemical components of the clay mineral structure, they are known to be weakly resolved by the LIBS technique [47]; this is consistent with the low-intensity values recorded for these elements here. Minor elements associated with the dominant clay mineralogy were resolved in the LIBS signal as well. For instance, Li lines were ubiquitous amongst the samples, but most prominent in the spectra of the hectorites (SHCa-1 and SynH-1) and the Li-mica "zinnwaldite" (ZW-C), both of which have been recognized as commercial lithium minerals [48,49]. The Li is largely incorporated via the isomorphous substitution of $Li^{+}$ for $Mg^{2+}$ in hectorite and $Li^{+}$ for $Fe^{2+}$ in zinnwaldite [50,51].

The high degree of spectral similarity and complexity of the spectra prevent simple visually based classification of the specimens and highlight the need for multivariate statistical analysis

techniques to determine whether the LIBS spectra contain sufficient information to discriminate between the predominant clay minerals.

#### *4.3.1.2 Raman Spectroscopy*

Representative examples of the Raman spectra obtained for each of the 14 specimens are given in Figure 4.2. Minimal variability was observed between the 10 spectral samples created by averaging consecutive measurements from the specimen surface, indicating that averaging measurements over an area successfully captured the bulk mineralogy. Peak labels were assigned using the Renishaw WiRE™ software Peak Pick function and are presented in Table 4.4. We used the following commonly accepted peak assignments for phyllosilicates: peaks in the 800 – 1100 $cm^{-1}$ range arise from the stretching of the Si-$O_{nb}$ bond in the $SiO_4$ tetrahedra, where $O_{nb}$ refers to the non-bridging Oxygen atom; peaks in the 600 – 800 $cm^{-1}$ region are contributed by the vibrational modes of the Si-$O_b$-Si bonds, where $O_b$ refers to the bridging Oxygen atoms that connect the $SiO_4$ tetrahedra; peaks in the <600 $cm^{-1}$ region arise from lattice vibrational modes [8]. Spectral matching with the RRUFF™ Database [52] and the factory-supplied Renishaw Mineral and Inorganic Materials Database were used to cross-check that the observed peaks matched the primary mineralogy in question and to identify peaks contributed by mineral impurities. A discussion of the peaks observed within each specimen, organized by sub-group, follows.

The spectra measured from the three kaolinite specimens (KGa-1, KGa-2, No.4) are consistent with anatase-bearing kaolinites. Kaolinite is a very weak Raman scatterer characterized by a low intensity signal with its strongest band at ~130 $cm^{-1}$, corresponding to the lattice vibration of the $AlO_6$ complex [53]. In contrast, anatase is extremely Raman active due to the high degree of symmetry of the O-Ti-O vibration [53]. Thus, although anatase is present only as a minor impurity (Table 4.3), all three of the kaolinite-rich specimens studied here are dominated by Raman bands for anatase, which include the very intense 144 $cm^{-1}$ band as well as lower intensity bands at 198, 396 – 398, 514 – 516, and 635 $cm^{-1}$ [54,55]. The appearance of a shoulder at about 130 $cm^{-1}$ on the flank of the main anatase band (144 $cm^{-1}$) indicates the presence of kaolinite. Several of the low frequency Raman bands that Wang et al. [31] and Frost et al. [56] reported as characteristic of kaolinite are also resolved here, within a few wavenumbers, but are very weak in intensity: ~245, 272, 336, 425, and 464 $cm^{-1}$.

The true micas measured here (IMt-1, ZW-C, Mica-Fe, Mica-Mg) exhibited considerable between-specimen variability, which we attribute both to the peak shifts associated with di- and tri-octahedral phyllosilicates and the influence of various accessory phase impurities. The IMt-1 specimen is known to contain trace quantities of anatase and its spectrum is dominated by a very strong band near 146 $cm^{-1}$ associated with the symmetric stretching vibration of O-Ti-O; lower intensity bands at 197, 394, 514, and 635 $cm^{-1}$ support the attribution of this peak to anatase [53]. The peaks at 262 and 700 $cm^{-1}$ are consistent with the signature of dioctahedral mica and are attributed to the primary illite phase [57]. The ZW-C, Mica-Fe, and Mica-Mg specimens each exhibit their strongest peaks in the 677 – 772 $cm^{-1}$ region, along with a sharp peak in the 188 – 199 $cm^{-1}$ region, which is consistent with the vibrational modes of trioctahedral phyllosilicates [57]. In addition to the mica fingerprint bands, the ZW-C signature features prominent peaks at 239, 266, and 286 $cm^{-1}$ that correspond to the characteristic peaks of topaz, and a sharp band at 463 $cm^{-1}$ associated with quartz [52], both of which are known impurities. Quartz and topaz are both moderate Raman scatterers and the intensity of their peaks is on roughly the same order of intensity as the characteristic phyllosilicate bands in ZW-C.

The two nontronite specimens (NAu-1, NAu-2) produce similar Raman signatures. Both specimens exhibit prominent peaks associated with Si-O-Fe vibrations near ~240 and 286 $cm^{-1}$ [58], as well as lower frequency peaks associated with Al-O-Al interactions near ~166 and 189 $cm^{-1}$ [59]. Both specimens also contributed less intense peaks near ~421 – 429, 512, 606, 684, and 870 – 885 $cm^{-1}$. This pattern of peaks and their relative intensities match well with published Raman spectra of nontronite [8,58,59]. Notable differences between the two specimens include the relative intensity of the peak near 606 $cm^{-1}$, which is substantially more intense in the NAu-2 signature, and the peak position of the 870 $cm^{-1}$ band in NAu-2, which is observed at 885 $cm^{-1}$ in NAu-1.

The three montmorillonite specimens studied here (SWy-1, SAz-1, STx-1) exhibit similar spectral fingerprints. Each of the specimens exhibit a strong, sharp peak just above 700 $cm^{-1}$ which is characteristic of the symmetric vibration of the Si-$O_b$-Si bonds in dioctahedral phyllosilicates [8]. Sharp peaks near 290 and 202 $cm^{-1}$, as well as a broad band near 430 $cm^{-1}$, are also common amongst the specimens and match the signature of montmorillonite reported by Wang et al. [8]. These authors suggested that some of the prominent bands should shift between montmorillonite types due to different replacement of the central cation in the octahedral layer.

However, no notable shifts associated with octahedral cationic composition were reported by more recent investigations of montmorillonites [9,59] and only minor shifts were observed here. The SWy-1 specimen uniquely featured an additional sharp peak at 464 $cm^{-1}$, a characteristic response of quartz [52].

The two hectorite (SHCa-1, SYnH-1) specimens exhibited characteristic peaks associated with trioctahedral phyllosilicates and are consistent with those reported by [57]: prominent bands near 184 and 685 $cm^{-1}$ indicate vibrations of the $MO_6$ groups (both Mg and Li cations could contribute to this complex) and the symmetric vibrations of the trioctahedral Si-$O_b$-Si bonds, respectively. The spectra of SHCa-1 shows four additional prominent bands at 154, 281, 712, and 1085 $cm^{-1}$ that correspond to the four principal vibrations of calcite [60], as well as a signal at 464 $cm^{-1}$ that corresponds to the signature of quartz, both of which are known impurities of the SHCa-1 specimen. The symmetric stretching of the carbonate ion in the calcite molecule is very Raman active and is known to exhibit an intense peak in the 1084 – 1089 $cm^{-1}$ range [61]. This peak dominates the SHCa-1 spectrum and masks the asymmetric Si-$O_{nb}$ vibration contributed by the hectorite minerals (visible at 1087 $cm^{-1}$ in the synthetic hectorite, SYnH-1); indeed all of the characteristic phyllosilicate peaks are less-intense than the peaks contributed by calcite in the SHCa-1 specimen.

In summary, all the reference specimens studied here exhibited patterns characteristic of the specified clay mineral, although the relative intensities of these bands varied a great deal between the specimens. Clay minerals are known to be intrinsically very weak Raman scatterers. Wang et al. [8] attributed the weakness of the Raman signal strength, in part, to the aggregation of the ultrafine clay grains. The grain surface and grain boundaries of the aggregates scatter the laser photons as well as the Raman photons, resulting in a weak signal. We found that even minor amounts of impurities with highly symmetrical (and thereby highly Raman active) structures, such as the carbonate ion of calcite and Ti-O bonds of anatase, can overwhelm the Raman signal of the clay minerals. Indeed, the four anatase-bearing specimens (KGa-1, KGa-2, No.4, and IMT-1) yield remarkably similar spectra, even where the primary mineralogy is different (*i.e.*, in the case of the kaolinites vs. the illite specimen).

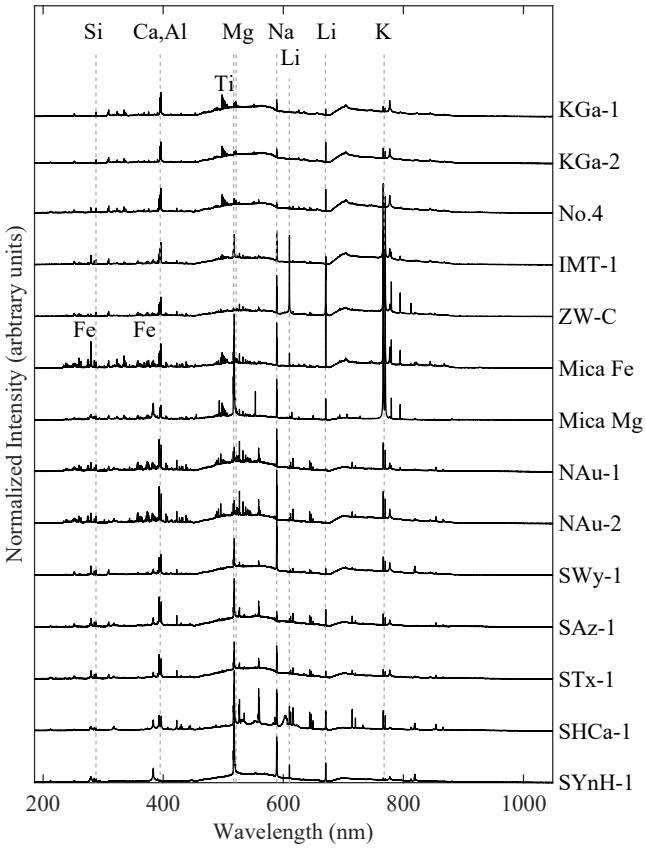
Si
Ca,Al
Mg
Na
Li
Li
K
Ti
Fe
Fe
KGa-1
KGa-2
No.4
IMT-1
ZW-C
Mica Fe
Mica Mg
NAu-1
NAu-2
SWy-1
SAz-1
STx-1
SHCa-1
SYnH-1
Normalized Intensity (arbtrary units)
200
400
600
800
1000
Wavelength (nm)

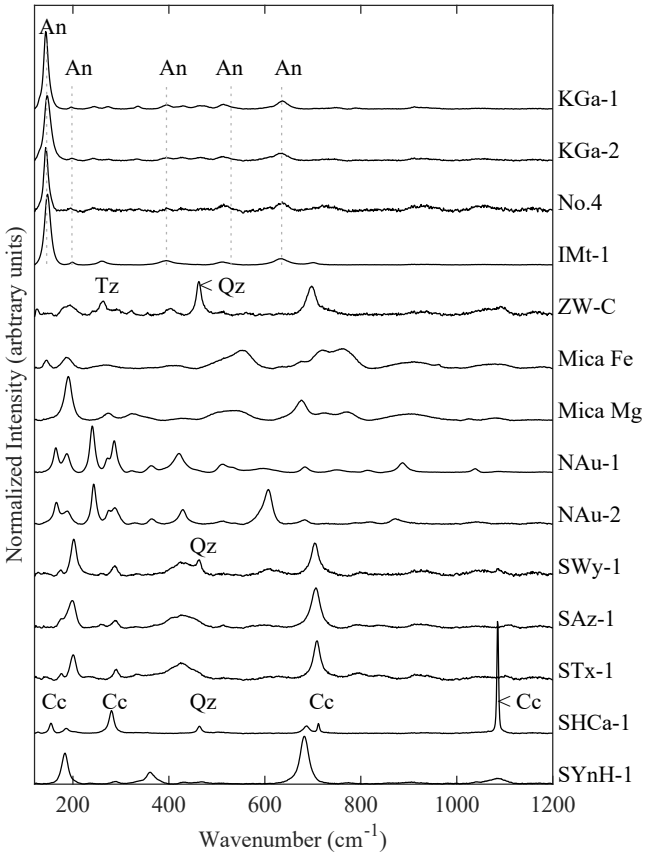
An
An
An
An
An
Tz
Qz
Qz
Cc
Cc
Qz
Cc
Cc
KGa-1
KGa-2
No.4
IMt-1
ZW-C
Mica Fe
Mica Mg
NAu-1
NAu-2
SWy-1
SAz-1
STx-1
SHCa-1
SYnH-1
Normalized Intensity (arbtrary units)
200
400
600
800
1000
1200
Wavenumber (cm-1)

*Figure 4.2: (previous page) Processed spectra from each of the 14 clay-bearing specimens.*
*Each spectrum is an average of 25 measurements from a different position on the specimen surface to capture bulk specimen composition.* ***Top:*** *LIBS spectra with relevant emission lines marked and labelled.* ***Bottom****: Raman spectra with impurities marked (Qz = Quartz, Cc = Calcite, Ae = Anatase, Tp = Topaz), see text for details of other spectral features.*

### 4.3.2 PCA

PCA models were built on data collected from each instrument, as well as the matrix of their concatenated information. The PCA scores plot depicts the distribution of the specimens in the new dimensions described by the PCs and the associated loadings plot expresses the extent to which the calculated PCs correlate with the original variables (Figure 4.3). The PCA models were used for preliminary visualization of the inherent data structures (*e.g.,* clusters, clines) in the specimen cohort. Although these latent structures were not explicitly quantified, we use visual inspection of the score plots to discuss the discrimination of the specimens according to the *a priori* knowledge of the group and the subgroup designations. Inspection of the loadings plots reveals the spectral features that are most influential in manifesting the observed structures and how they are correlated. For simplicity, biplots of only the first three PCs are shown.

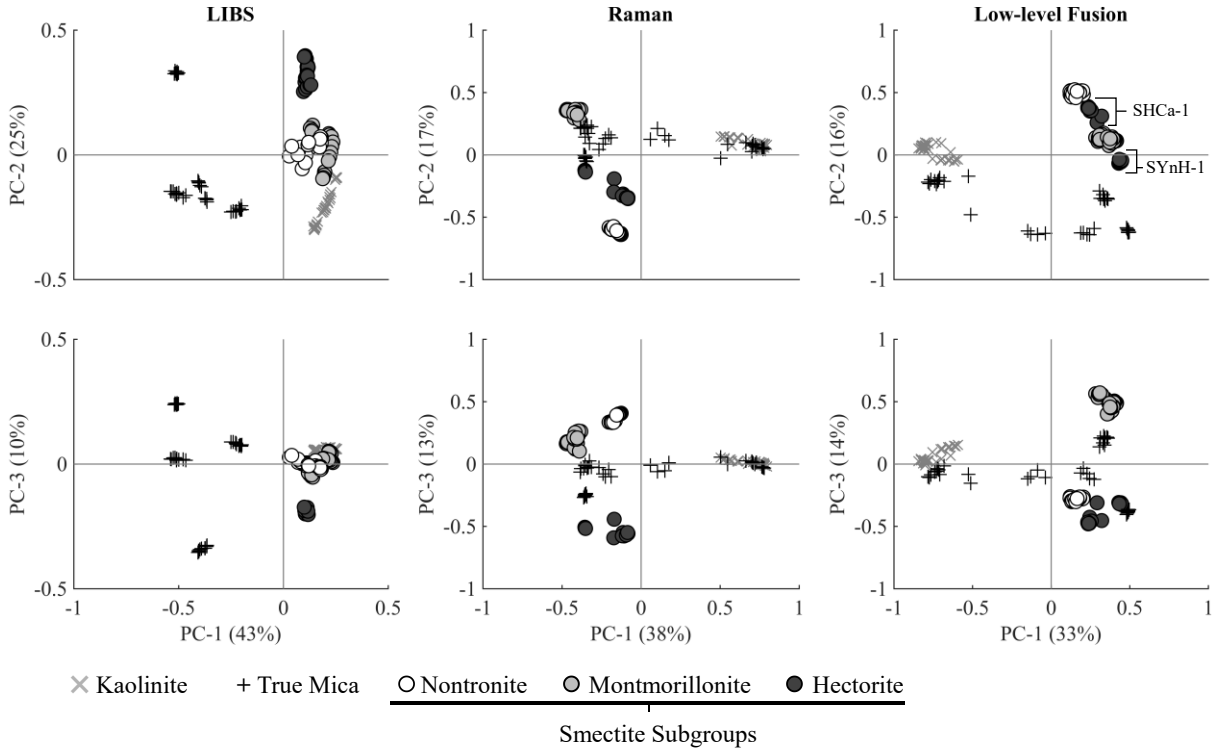


*Figure 4.3: Scatter plots of PC-1/PC-2 and PC-1/PC-3 scores distribution.*
*Each data point corresponds to a full pre-processed spectrum (or fused spectrum) in the original space.*

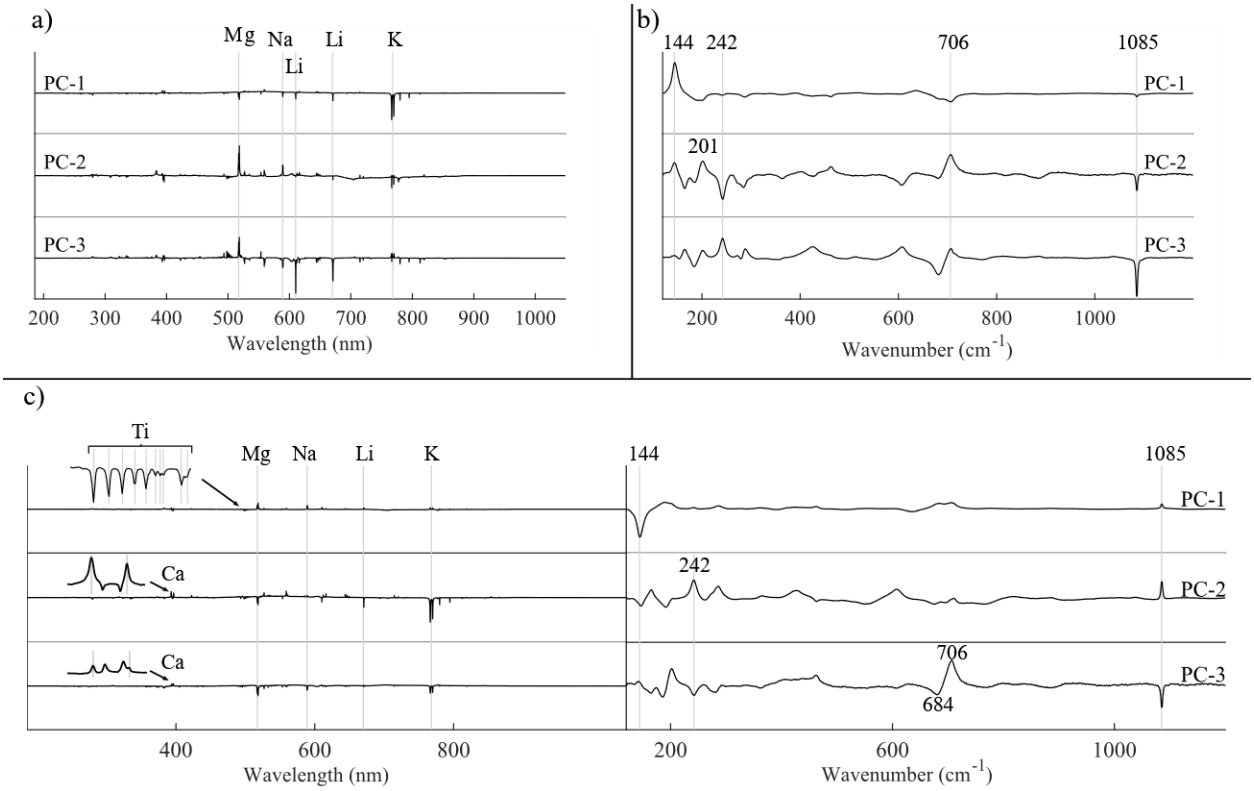


*Figure 4.4: Principal component loadings plots for the PCA models.*
*A) Model built on LIBS data, b) Model built on the Raman spectroscopy data, and c) Model built on the fused data. Each plot illustrates how each spectral feature influences a principal component. The relative magnitude of a loading indicates its degree of influence and the sign of a loading indicates whether a variable and a principal component are positively or negatively correlated.*

#### *4.3.2.1 LIBS*

The PCA model built on the LIBS spectral signatures reveals that the specimens form clusters consistent with the group-level classification of their dominant clay mineralogy along the first and second PCs (Figure 4.3). The most influential variables (*i.e*., the emission lines with the strongest loadings) are reflective of the composition of the interlayer (Figure 4.4a) and reflects the LIBS technique's unique sensitivity towards cations. The mica clay interlayer cation is usually $K^+$, and the true mica specimens all plot on the left-hand side of the PC-1/PC-2 biplot which is influenced by the strong negative loadings of K emission lines (766.5 and 769.9 nm) of PC-1 (Figure 4.4a), which itself captures 43% of the total variance of the complete LIBS data set. Smectitic clays usually accommodate interlayer cations of $Ca^{2+}$, $Mg^{2+}$, or $Na^+$, and are clustered primarily in the upper, right-hand quadrant of the PC-1/PC-2 biplot; this position is

influenced by a relative deficiency of K (PC-1) and positive PC-2 loadings of Mg (517.3 and 518.4 nm) and Na (589.0 and 589.6 nm) (Figure 4.4a). The kaolinite-serpentine group has no interlayer space and the specimens plot in the lower, right-hand quadrant due to their relatively low K, Mg, and Na contents; they are especially well-separated from the K-rich mica clays. The kaolinite-serpentine and smectite specimens plot proximally on the PC-1/PC-2 biplot, likely due to the fact that some montmorillonite specimens (namely, STx-1) have a low K content, similar to that of some of the kaolinite specimens (namely, KGa-1 and KGa-2). Judging by visual inspection of the smectite group specimens, there is overlap amongst the nontronite and montmorillonite specimens on both the PC-1/PC-2 and PC-1/PC-3 biplots. This is consistent with the compositions expressed in Table 4.2 and is reflective of the fact that the smectite interlayer can accommodate a variety of cations in various proportions. The interlayer cations of a smectite clay are uniquely exchangeable, resulting in a great deal of chemical variability within a single mineral species. For instance, the three montmorillonites studied here exhibit different proportions of Mg, Ca, and Na, primarily due to the composition of the interlayer (Table 4.2). LIBS is a high sensitivity elemental analysis technique and captures the chemical variability amongst the montmorillonites, which precluded pattern recognition amongst the chemically diverse smectites. Exceptionally, the Li-bearing hectorite specimens are distinct from the montmorillonite and nontronite clusters, especially along PC-3, which is influenced largely by the Li emission lines at 670.4 and 610.3 nm.

#### *4.3.2.2 Raman Spectroscopy*

The PCA model relying solely on the Raman spectra fails to cluster the specimens according to their dominant clay mineralogy at the group level. Figure 4.3 shows no clear clustering of the kaolinite-serpentine, mica clay, or smectite groups on the PC-1/PC-2 or PC-1/PC-3 biplots. Inspection of higher order PCs (not shown) did not yield clusters that were consistent with the predominant clay mineralogy at the group level.

Figure 4.4b reveals that the most influential loading along PC-1 is attributable to the characteristic vibration of anatase near 144 $cm^{-1}$. Thus, the primary source of variance within the Raman data set is attributable to the minor anatase impurity with its highly Raman-active vibrations that dominate the spectra of specimens KGa-1, KGa-2, No.4, and IMT-1, yielding clusters that are unrelated to the primary clay mineralogy. Indeed, the mica clay group is not well-clustered, in part because of the unique anatase contamination of IMt-1. This impurity

interferes with the characteristic clay bands and produces a signature similar to the anatase-bearing kaolinite specimens, resulting in notable overlap amongst the kaolinite specimens and IMt-1 specimen, despite their different modal mineralogy (Figure 4.3). Since the Raman spectra of these specimens are so dominated by the anatase bands, their spectral variance is mostly captured by the first component, and they plot near 0 along the higher order PC axes which capture some of the characteristic phyllosilicate vibrational modes.

PCs 2 and 3 contribute to clustering patterns that allow the smectite specimens to be discriminated by their subgroup designation (Figure 4.3). The montmorillonite specimens plot in the scores space defined by the positive PC-2 axis and the positive PC-3 axis. These axes are influenced positively by the peaks near 201 and 706 $cm^{-1}$, which are consistent with characteristic dioctahedral clay vibrations (Figure 4.4b) (the dioctahedral Si-$O_b$-Si vibration, which typically manifests at wavenumbers >700 $cm^{-1}$, is absent from the Raman spectra of nontronites, despite their dioctahedral character [62]). The nontronite specimens lie along negative PC-2 and positive PC-3. This is consistent with the expression of the Si-O-Fe band at 242 $cm^{-1}$ on the PC-2 and PC-3 loadings plot (Figure 4.4b). The hectorite specimens are isolated from the other smectites most notably along negative PC-3 due to a combination of the influence of the 1085 $cm^{-1}$ band associated with the calcite impurity of SHCa-1 and, to a lesser degree, the 684 $cm^{-1}$ band associated with the expression of the Si-$O_b$-Si vibration of trioctahedral clays, which typically manifests at wavenumbers <700 $cm^{-1}$. In brief, the inherently weak Raman signatures of the clay minerals are masked in the presence of highly symmetric impurities, even at trace quantities, which impedes the clustering of these specimens by their predominant clay mineralogy. However, the smectite specimens, which were minimally influenced by impurities, were effectively clustered according to their subgroup mineralogy due to band shifts in the vibrations of the Si-$O_b$-Si bonds in di- vs tri-octahedral clays and vibrational modes in the lattice region. This may be attributed to the nature of the Raman technique, which provides excellent molecular specificity because it probes fundamental vibrational states. Thus, despite the chemical differences amongst the specimens of each smectite subgroup, the Raman technique captured the commonalities amongst their molecular structures and permitted discrimination of the subgroups.

#### *4.3.2.3 Low-level Fusion*

PCA on the data set generated by low-level fusion showed that the separation of clay mineral groups and subgroups could be improved by spectral concatenation. In the PC-1/PC-2 biplot of the fused data set, which encapsulates the two primary directions of variance, the predominant clay mineral groups may be separated (Figure 4.3). The Raman band at 144 $cm^{-1}$ stands out as being particularly important in describing the specimen distribution along PC-1 (Figure 4.4c), indicating that this first component describes mainly the contribution of the titanium-oxide anatase impurity. Consequently, the anatase-bearing kaolinite-serpentine group specimens (KGa-1, KGa-2, and No.4) and the illite specimen (IMt-1) lie in one end of the PC-1 dimension and the anatase-free specimens (all of the smectite group specimens and the remaining specimens of the mica group) in the other. As in the Raman model, the anatase component of IMt-1 causes this specimen to plot *near* the anatase-bearing kaolinite-serpentine grouping. However, in the fused model, these clay mineral groups may be distinguished along PC-2; the true mica specimens plot on the negative axis while the kaolinite specimens lie near 0, indicating that they are not well described by the variance contained within this PC. The strong influence of the K emission line to PC-2 demonstrates that the K-bearing nature of the true mica interlayer allows these specimens to be distinguished from the other relatively K-poor clay mineral groups studied here (Table 4.2) by the LIBS technique, reinforcing the influence of major cation composition in the discrimination of clay mineral groups.

Visual inspection of the PC-1/PC-3 biplot reveals that the third component allows the smectite group specimens to be discriminated according to their known subgroup designations (nontronite, montmorillonite, and hectorite). PC-3 is influenced predominantly by the Raman spectra with only weak loadings of the LIBS spectra (Figure 4.4c). Positive loadings near 700 $cm^{-1}$ and negative loadings near 684$cm^{-1}$ correspond to the characteristic band positions of the symmetric stretching modes of the $SiO_4$ tetrahedra occurring in di-octahedral and tri-octahedral phyllosilicates, respectively, and contribute to the separation of the di-octahedral montmorillonite and tri-octahedral hectorite subgroups. The negative loadings of the bands near 187 and 242 $cm^{-1}$ that correspond to Si-O-Fe lattice vibrations contribute to the clustering of the nontronite specimens along negative PC-3.

Comparing the PCA results between the individual spectroscopies and the data fusion approach, we find that the LIBS and Raman spectroscopies contribute complementary information. In the

loadings of PC-1, the anatase 144 $cm^{-1}$ band measured by Raman spectroscopy and the Ti emission lines measured by LIBS bear the same sign, indicating that they are positively correlated variables (Figure 4.4c). Although intuitive, this correlation between the detection of a molecular O-Ti-O bond vibration and the atomic emission of Ti explicitly highlights the utility of the data fusion strategy: assembling Raman and LIBS responses in a single data set provides two independent, agreeable measures of the same physical phenomena detected via different sensors, thereby improving the reliability of identifying the phenomena. A similar observation may be highlighted with respect to the hectorite specimens (SHCa-1 and SYnH-1). In the positive PC-1 dimension and, to a much greater degree, the positive PC-2 dimension, the loadings of the 1085 $cm^{-1}$ band and the atomic emission of Ca are correlated parameters. This correlation is consistent with the detection of calcite ($CaCO_3$) and contributes to the positive loading of the calcite-bearing hectorite specimens (SHCa-1) on the PC-2 scores axis, whereas the synthetic, calcite-free hectorite specimens (SYnH-1) lie near the origin on PC-2. In PC-3 the Ca emission lines are smaller in magnitude and are anticorrelated with the vibrational signal near 1085 $cm^{-1}$. This pattern suggests that the variance associated with the calcite impurity has been accounted for within PCs 1 and 2. We suggest that the remaining variance described by the loading of the peak near 1085 $cm^{-1}$ corresponds to the Si-$O_{nb}$ stretch of the hectorite lattice, which is detectable in the spectrum of SYnH-1 at ~1087 (Figure 4.2, Table 4.4), but masked in the spectrum of SHCa-1 by the nearby calcite band. This is reflected in the associated PC-1/PC-3 biplot (Figure 4.3), in which both the SHCa-1 and SYnH-1 specimens plot more proximally, indicating compositional similarity in this scores space.

We have demonstrated the complementarity of the LIBS and Raman data sets in the geological context. The fused model incorporated both the high sensitivity of LIBS to capture the chemical differences imposed by the differing layer charges of each clay group, as well as the high specificity of Raman spectroscopy to capture the distinct molecular structure of each of the smectite species. Thus, where the individual models failed, the fused model succeeded in grouping the specimens in a way that is consistent with *both* the group and subgroup level classifications of their constituent clay mineralogy. Further, the two techniques delivered information about the same sample properties sensed under different measurement contexts.

### 4.3.3 PC-LDA

Results of the PC-LDA built on each data package are listed in Table 4.5, along with the number of PCs taken into consideration and their associated cumulative explained variance. In all cases, the cumulative explained variance was greater than or equal to 90%, indicating that each of the models successfully captured most of the variability in the data. Comparing just the individual spectroscopies, LIBS achieved better correct classification rates than Raman spectroscopy at both the group and subgroup level. This result contributes to the growing body of literature demonstrating the power of LIBS as a geo-analytical tool for mineral discrimination [6,63–68]. The best overall classification results were achieved by the low-level fusion model, which attained perfect classification at the group and subgroup level.

Multivariate models may be misused by overfitting [69]. Mathematically, PCs represent sources of successively maximized variance in the data, and it should be borne in mind, therefore, that better estimates of the data set are obtained as the number of PCs used to describe the data increases. However, retaining too many PCs poses the risk of overfitting, in which the model describes noise in addition to the structured variation in the data. Overfitted models often show data clustering where none exists and can produce overly optimistic models whose results are actually meaningless and misleading [69]. Although, efforts were made here to judiciously select the optimal number of PCs using Cattell's scree test, we acknowledge that there are several accepted methods used to select how many PCs to retain for modelling with no consensus in the literature regarding the best approach [36,70]. Thus, to ensure that the improvement in discrimination and classification performance realized by the low-level fusion model was not a consequence of merely retaining a greater number of PCs during model development (seven PCs for the low-level fusion model vs. five and six PCs for the LIBS and Raman models, respectively), the PC-LDA analyses were repeated, but with an identical number of PCs retained in each model (Table 4.6). The number of PCs were fixed at five to correspond to the most parsimonious model. Even in this conservative case, the low-level fusion model still achieved the highest rate of correct classification of the clay-bearing specimens at the group and subgroup level, with 100% correct classification of the test set spectra.

| | Groups | Kaolinite-Serpentine | | | Mica Clay Minerals | | | | Smectite | | | | | | |
|---|---|---|---|---|---|---|---|---|---|---|---|---|---|---|---|
| | Sub-groups | Kaolinite | | | True Mica | | | | Nontronite | | Montmorillonite | | | Hectorite | |
| | # | 1 | 2 | 3 | 4 | 5 | 6 | 7 | 8 | 9 | 10 | 11 | 12 | 13 | 14 |
| | ID | KGa-1 | KGa-2 | No. 4 | IMt-1 | ZW-C | Mica-Fe | Mica-Mg | NAu-1 | NAu-2 | SWy-1 | SAz-1 | STx-1 | SHCa-1 | SYnH-1 |
| Phyllosilicate Bands | $Si\text{-}O_{nb}$ | | | | | | 1080 | 1080 | 1037 | 1045 | 1085 | 1084 | | | 1087 |
| | | | | | | | | | 885 | 870 | | | | | |
| | $Si\text{-}O_{b}\text{-}Si$ | | | | | | | | | | | | 792 | | |
| | | | | | 700 | **698** | **677-775** | **677-772** | 683 | 684 | 705 | 704 | **708** | 688 | **682** |
| | | | | | | | | | 606 | **607** | | | | | |
| | Lattice Modes | 467 | 466 | | | | **550** | 541 | 512 | 512 | | | | | |
| | | 429 | 425 | | | | | | 421 | 429 | 431 | 430 | 427 | | |
| | | 336 | 335 | | | | | 330 | 363 | 364 | | | | | 361 |
| | | 272 | | | 262 | | | 275 | 286 | 286 | 286 | 287 | 290 | | |
| | | 247 | 245 | 241 | | | 255 | | **241** | **243** | | | | | |
| | | | | | | 199 | 188 | **191** | 187 | 190 | 202 | 198 | 200 | 187 | **183** |
| | | 130 | 130 | 130 | | | 145 | 147 | 165 | 166 | 174 | | 176 | | |
| Impurities | Anatase | *637* | *637* | *638* | *635* | | | | | | | | | | |
| | | *512* | *512* | *514* | *514* | | | | | | | | | | |
| | | *396* | *395* | *396* | *394* | | | | | | | | | | |
| | | *199* | *198* | *194* | *197* | | | | | | | | | | |
| | | ***144*** | ***144*** | ***144*** | ***146*** | | | | | | | | | | |
| | Quartz | | | | | ***463*** | | | | | *464* | | | *464* | |
| | Calcite | | | | | | | | | | | | | ***1085*** | |
| | | | | | | | | | | | | | | *281* | |
| | | | | | | | | | | | | | | *154* | |
| | Topaz | | | | | *286* | | | | | | | | | |
| | | | | | | *266* | | | | | | | | | |
| | | | | | | *239* | | | | | | | | | |

*Table 4.4: Major Raman peak positions reported as band centers in $cm^{-1}$.*
*We used the commonly accepted peak assignments for the major phyllosilicate peaks according to [8]. Bolded text indicates the most intense bands in the spectrum. Italicized text indicates bands associated with known impurities, see text for details.*

| Data Package | Number of PCs Used | Cumulative Proportion of Explained Variance (%) | Correct Classification at the Group Level (%) | | Correct Classification at the Sub-group Level (%) | |
|---|---|---|---|---|---|---|
| | | | Training | Test | Training | Test |
| **LIBS** | 5 | 91 | 98.2 | 96.4 | 96.4 | 96.4 |
| **Raman** | 6 | 90 | 92.0 | 92.9 | 92.9 | 92.9 |
| **Low-level fusion** | 7 | 91 | 100.0 | 100.0 | 100.0 | 100.0 |

*Table 4.5: Results of the PC-LDA.*
*Results of the PC-LDA applied to the data obtained individually by LIBS and Raman, as well data obtained from low-level fusion, in which the number of PCs used to build each model was selected based on Cattell's scree test.*

| Data Package | Number of PCs Used | Cumulative Proportion of Explained Variance (%) | Correct Classification at the Group Level (%) | | Correct Classification at the Sub-group Level (%) | |
|---|---|---|---|---|---|---|
| | | | Training | Test | Training | Test |
| **LIBS** | 5 | 91 | 98.2 | 96.4 | 96.4 | 96.4 |
| **Raman** | 5 | 86 | 84.8 | 85.7 | 92.9 | 89.3 |
| **Low-level fusion** | 5 | 82 | 99.1 | 100.0 | 99.1 | 100.0 |

*Table 4.6: Results of the PC-LDA.*
*Results of the PC-LDA applied to the data obtained individually by LIBS and Raman, as well data obtained from low-level fusion, in which the number of PCs used to build each model was fixed at 5.*

## 4.4 CONCLUDING REMARKS

The benefits afforded by spectroscopic data fusion for the identification and characterization of materials are well-documented in other disciplines but are still being explored in the context of the geological sciences. In this contribution, we presented the first investigation of low-level data fusion strategies for the discrimination and classification of mixed geological specimens by their dominant clay mineralogy. The advantage of using concatenated, rather than separate, LIBS+Raman data was demonstrated by a step-wise multivariate analysis approach. PCA produced a compact, low-dimensional visualization that provided insight into the structure of data clusters and allowed important discriminatory spectral regions to be identified. Subsequent application of PC-LDA demonstrated that the data fusion strategy improved the rate of correct classifications relative to that which was achieved by either analytical technique individually, permitting correct classification of all the specimens reserved for validation by matching the unknowns with a short database of fused spectra of the minerals of interest. This result was preserved even in the conservative case of restricted PC retention. The classification model built on fused spectra effectively incorporated both the high sensitivity of LIBS and high specificity of

Raman to converge of the correct classification of the predominant clay mineral phase in each specimen.

In brief, this pilot study presented a straight-forward data management strategy that improved the discrimination of clay minerals using spectroscopy and multivariate analysis tools. It is prudent to note that spectral concatenation at the data level is not the only data fusion strategy available to a spectral analyst (the reader is directed to [19] for details on other data fusion approaches). This work is intended to be a preliminary demonstration of the advantages afforded by data fusion to correctly discriminate geological specimens and stimulate future research into the development of spectral data fusion for the rapid, remote, and non-destructive identification of minerals. Considering that the benefits of data fusion are derived from the inclusion of complementary information that offers a more comprehensive description of the studied target, not the explicit experimental parameters themselves, our promising initial results may reasonably be extended to other contexts and/or conditions not directly investigated in this study. For instance, spectral data fusion strategies could enhance mineralogical analyses outside of the laboratory wherever two or more independent portable spectroscopic instruments are available. Indeed, compact LIBS and Raman spectroscopy instruments will both be available on NASA's Mars 2020 Perseverance rover [71]. Our results indicate that the synergistic use of their data may permit more reliable identification of clay minerals and clay-bearing assemblages, both of which have been proposed as high priority targets for the search for Martian life [72]. Further work should be dedicated to developing a database of concatenated LIBS and Raman spectra of minerals expected to be encountered on Mars which could then be used to equip the rover with a centralized, comprehensive library from which to interpret mission data. Lastly, it is important to acknowledge that there are numerous other combinations of analytical probes that are amenable to data fusion and could enhance clay mineral identification. For example, integrating reflectance spectroscopy data from the visible and infrared ranges could add complementary structural information to the LIBS and Raman pairing. Research into this topic is underway.

## 4.5 ACKNOWLEDGMENTS

We gratefully acknowledge the support of the Natural Sciences and Engineering Research Council of Canada (NSERC) as well as the Canadian Space Agency's support of the Mars Science Laboratory Participating Scientists Program. The LIBS instrument at McGill was purchased through a JELF grant from the Canada Foundation for Innovation. We also extend our

sincere thanks to the staff of the Morningside College Library and Alberta Innovates for helping us access literature during the library closures associated with the Coronavirus disease (COVID-19) outbreak situation, their selfless dedication to knowledge sharing was greatly appreciated. Lastly, we thank the input of three anonymous reviewers whose comments greatly improved the quality and clarity of this manuscript.

### 4.6 COMPETING INTERESTS

The authors have no competing interests to declare.

### 4.7 ROLE OF FUNDING SOURCES

The funding sources for this work had no role in the design or execution of the study and did not influence the interpretation of the data or decision to submit results.

### 4.8 DATA AVAILABILITY

Supporting data not printed in the text are available upon request.

### 4.9 REFERENCES

[1] F. Bergaya, G. Lagaly, eds., Handbook of clay science, 2nd ed., Elsevier Ltd., Amsterdam, 2013.

[2] B.L. Ehlmann, J.F. Mustard, S.L. Murchie, J.-P. Bibring, A. Meunier, A.A. Fraeman, Y. Langevin, Subsurface water and clay mineral formation during the early history of Mars, Nature. 479 (2011) 53–60. https://doi.org/10.1038/nature10582.

[3] T.F. Bristow, E.B. Rampe, C.N. Achilles, D.F. Blake, S.J. Chipera, P. Craig, J.A. Crisp, D.J. Des Marais, R.T. Downs, R. Gellert, J.P. Grotzinger, S. Gupta, R.M. Hazen, B. Horgan, J. V. Hogancamp, N. Mangold, P.R. Mahaffy, A.C. McAdam, D.W. Ming, J.M. Morookian, R. V. Morris, S.M. Morrison, A.H. Treiman, D.T. Vaniman, A.R. Vasavada, A.S. Yen, Clay mineral diversity and abundance in sedimentary rocks of Gale crater, Mars, Sci Adv. 4 (2018). https://doi.org/10.1126/sciadv.aar3330.

[4] U.S. Geological Survey, Clays - Data Sheet - Mineral Commodity Summaries 2020, 2020. https://doi.org/10.1017/CBO9781107415324.004.

[5] W. Gates, J.T. Kloprogge, J. Madejova, F. Bergaya, eds., Infrared and Raman spectroscopies of clay minerals, 1st ed., Elsevier, Amsterdam, 2017.

[6] R.S. Harmon, R.E. Russo, R.R. Hark, Applications of laser-induced breakdown spectroscopy for geochemical and environmental analysis: A comprehensive review, Spectrochimica Acta Part B. 87 (2013) 11–26.

[7] X. Zhou, D. Liu, H. Bu, L. Deng, H. Liu, P. Yuan, P. Du, H. Song, XRD-based quantitative analysis of clay minerals using reference intensity ratios, mineral intensity factors, Rietveld, and full pattern summation methods: A critical review, Solid Earth Sciences. 3 (2018) 16–29. https://doi.org/10.1016/j.sesci.2017.12.002.

[8] A. Wang, J.J. Freeman, B.L. Jolliff, Understanding the Raman spectral features of phyllosilicates, Journal of Raman Spectroscopy. 46 (2015) 829–845. https://doi.org/10.1002/jrs.4680.

[9] M. Ritz, L. Vaculíková, J. Kupková, E. Plevová, L. Barto, Vibrational Spectroscopy Different level of fluorescence in Raman spectra of montmorillonites, Vib Spectrosc. 84 (2016) 7–15. https://doi.org/10.1016/j.vibspec.2016.02.007.

[10] J. Madejová, W.P. Gates, S. Petit, IR spectra of clay minerals, in: W. Gates, J.T. Kloprogge, J. Madejova, F. Bergaya (Eds.), Infrared and Raman Spectroscopies of Clay Minerals., 2017: pp. 107–149. https://doi.org/10.1016/B978-0-08-100355-8.00005-9.

[11] V.C. Khang, M. V. Korovkin, L.G. Ananyeva, Identification of clay minerals in reservoir rocks by FTIR spectroscopy, in: IOP Conf Ser Earth Environ Sci, 2016. https://doi.org/10.1088/1755-1315/43/1/012004.

[12] S.M. Clegg, R. Wiens, A.K. Misra, S.K. Sharma, J. Lambert, S. Bender, R. Newell, K. Nowak-lovato, S. Smrekar, M.D. Dyar, S. Maurice, Planetary geochemical investigations using Raman and laser-induced breakdown spectroscopy, Appl Spectrosc. 68 (2014) 925–936. https://doi.org/10.1366/13-07386.

[13] G.E. Schweitzer, Countering terrorism: Biological agents, transportation networks, and energy systems: Summary of a US-Russian workshop, National Academies Press, 2009.

[14] S.K. Sharma, A.K. Misra, P.G. Lucey, R.C.F. Lentz, A combined remote Raman and LIBS instrument for characterizing minerals with 532 nm laser excitation, Spectrochim Acta A Mol Biomol Spectrosc. 73 (2009) 468–476. https://doi.org/10.1016/j.saa.2008.08.005.

[15] K. Rammelkamp, Investigation of LIBS and Raman data analysis methods in the context of in-situ planetary exploration, Humboldt-Universität zu Berlin, 2019.

[16] J. Moros, M.M. Elfaham, J.J. Laserna, Dual-spectroscopy platform for the surveillance of Mars mineralogy using a decisions fusion architecture on simultaneous LIBS-Raman data, Anal Chem. 90 (2018) 2079–2087. https://doi.org/10.1021/acs.analchem.7b04124.

[17] Y. Bi, M. Yan, X. Dong, Z. Li, Y. Zhang, Y. Li, Recognition of 25 natural geological samples using a modified correlation analysis method and laser-induced breakdown spectroscopic data, Optik (Stuttg). 158 (2018) 1058–1062. https://doi.org/10.1016/j.ijleo.2017.12.167.

[18] N. Khajehzadeh, O. Haavisto, L. Koresaar, On-stream mineral identification of tailing slurries of an iron ore concentrator using data fusion of LIBS, reflectance spectroscopy and XRF measurement techniques, Miner Eng. 113 (2017) 83–94. https://doi.org/10.1016/j.mineng.2017.08.007.

[19] M. Cocchi, ed., Data fusion methodology and applications, Volume 31: Data handling in science and technology, 1st ed., Elsevier, Amsterdam, 2019.

[20] S.J. Chipera, D.L. Bish, Baseline studies of the clay minerals society source clays: Powder X-ray diffraction analyses, Clays Clay Miner. 49 (2001) 398–409. https://doi.org/10.1346/CCMN.2001.0490507.

[21] M. Rieder, G. Cavazzini, Y.S. D'yakonov, V.A. Frank-Kamenetskii, G. Gottardi, S. Guggenheim, P.W. Koval, G. Mueller, A.M.R. Neiva, E.W. Radoslovich, Nomenclature of the micas, Clays Clay Miner. 46 (1998) 586–595.

[22] H. van Olphen, J.J. Fripiat, Data handbook for clay materials and other non-metallic minerals, (1979).

[23] American Petroleum Institute, Reference clay minerals American Petroleum Institute research project 49. Preliminary reports no. 1-8., Columbia University, New York, 1951.

[24] K. Govindaraju, I. Rubeska, T. Paukert, 1994 Report on Zinnwaldite ZW-C analysed by ninety-two GIT-IWG member-laboratories, Geostandards Newsletter. 18 (1994) 1–42.

[25] K. Govindaraju, Compilation Report (1966-1987) on Trace Elements in Five CRPG Geochemical Reference Samples: Basalt BR; Granites , GA and GH; Micas, Biotite Mica-Fe and Phlogopite Mica-Mg, Vandœuvre-lès-Nancy, 1988.

[26] J.L. Keeling, M.D. Raven, W.P. Gates, Geology and characterization of two hydrothermal nontronites from weathered metamorphic rocks at the Uley graphite mine, South Australia, Clays Clay Miner. 48 (2000) 537–548.

[27] R.A. Baker, M.D. Luh, Pyridine sorption from aqueous solution by montmorillonite and kaolinite, Water Res. 5 (1971) 839–848. https://doi.org/10.1016/0043-1354(71)90020-0.

[28] H.M. Köster, Mineralogical and chemical heterogeneity of three standard clay mineral samples, Clay Miner. 31 (1996) 417–422.

[29] H. Gailhanou, J.C. Van Miltenburg, J. Rogez, J. Olives, M. Amouric, E.C. Gaucher, P. Blanc, Thermodynamic properties of anhydrous smectite MX-80, illite IMt-2 and mixed-layer illite–smectite ISCz-1 as determined by calorimetric methods. Part I: Heat capacities, heat contents and entropies, Geochim Cosmochim Acta. 71 (2007) 5463–5473.

[30] H. de la Roche, K. Govindaraju, Tables of recommended or proposed values (major, minor or trace elements) for the ten geochemical standards of the Centre de Recherches Pétrographiques et Géochimiques and of the Association Nationale de la Recherche Technique, Methodes Physiques d'analyse : Revue Du Groupement Pour l'Avancement Des Methodes d'Analyse Spectographique, GAMS. 7 (1951) 314–322. https://doi.org/10.1017/CBO9781107415324.004.

[31] X. Wang, L. Zhang, J. Fan, Y. Li, Y. Gong, L. Dong, W. Ma, W. Yin, S. Jia, Parameters optimization of laser-induced breakdown spectroscopy experimental setup for the case with beam expander, Plasma Science and Technology. 17 (2015) 914–918. https://doi.org/10.1088/1009-0630/17/11/04.

[32] K.H. Esbensen, B. Swarbrick, F. Westad, P. Whitcombe, M.J. Anderson, Multivariate data analysis: An introduction to multivariate analysis, process analytical technology and quality by design, CAMO, 2018.

[33] J. Moros, J. Laserna, New Raman-laser-induced breakdown spectroscopy identity sensing platform, Anal Chem. 83 (2011) 6275–6285. https://doi.org/10.1021/ac2009433.

[34] M. Hoehse, A. Paul, I. Gornushkin, U. Panne, Multivariate classification of pigments and inks using combined Raman spectroscopy and LIBS, Anal Bioanal Chem. 402 (2012) 1443–1450. https://doi.org/10.1007/s00216-011-5287-6.

[35] D. Prochazka, M. Mazura, O. Samek, K. Rebro, P. Po, J. Klus, P. Prochazková, J. Novotný, Combination of laser-induced breakdown spectroscopy and Raman spectroscopy for multivariate classification of bacteria, Spectrochimica Acta Part B. 139 (2018) 6–12. https://doi.org/10.1016/j.sab.2017.11.004.

[36] I. Jolliffe, Principal components analysis, 2nd ed., Springer, 2002. https://doi.org/10.1016/B978-0-08-044894-7.01358-0.

[37] A. Webb, K. Copsey, Linear discriminant analysis, in: Statistical Pattern Recognition, 3rd ed., John Wiley & Sons, Ltd, 2011: pp. 221–273.

[38] K. Fukunaga, Introduction to Statistical Pattern Recognition, 2nd ed., Academic Press Professional, Inc., 1990.

[39] T. Fearn, Discriminant Analysis, Handbook of Vibrational Spectroscopy. (2001). https://doi.org/doi:10.1002/0470027320.s4302.

[40] R.B. Cattell, The scree test for the number of factors, Multivariate Behav Res. 1 (1966) 245–276.

[41] E. Vors, K. Tchepidjian, J.B. Sirven, Evaluation and optimization of the robustness of a multivariate analysis methodology for identification of alloys by laser induced breakdown spectroscopy, Spectrochim Acta Part B At Spectrosc. 117 (2016) 16–22. https://doi.org/10.1016/j.sab.2015.12.004.

[42] M. James, Classification Algorithms, Collins, 1985.

[43] R.D. Snee, Validation of regression models: methods and examples, Technometrics. 19 (1977) 415–428.

[44] A. Biancolillo, R. Bucci, A.L. Magrì, A.D. Magrì, F. Marini, Data-fusion for multiplatform characterization of an italian craft beer aimed at its authentication, Anal Chim Acta. 820 (2014) 23–31. https://doi.org/10.1016/j.aca.2014.02.024.

[45] M. Daszykowski, B. Walczak, D.L. Massart, Representative subset selection, Anal Chim Acta. 468 (2002) 91–103.

[46] A. Kramida, Yu. Ralchenko, J. Reader, NIST ASD team, NIST Atomic Spectra Database (Version 5.6.1), National Institute of Standards and Technology. (2018). https://doi.org/https://doi.org/10.18434/T4W30F.

[47] R.S. Harmon, J. Remus, N.J. McMillan, C. McManus, L. Collins, J.L. Gottfried Jr, F.C. DeLucia, A.W. Miziolek, LIBS analysis of geomaterials: Geochemical fingerprinting for the rapid analysis and discrimination of minerals, Applied Geochemistry. 24 (2009) 1125–1141. https://doi.org/10.1016/j.apgeochem.2009.02.009.

[48] L. Kavanagh, J. Keohane, G. Garcia Cabellos, A. Lloyd, J. Cleary, Global lithium sources—industrial use and future in the electric vehicle industry: a review, Resources. 7 (2018) 57.

[49] H. Vu, J. Bernardi, J. Jandová, L. Vaculíková, V. Goliáš, Lithium and rubidium extraction from zinnwaldite by alkali digestion process: Sintering mechanism and leaching kinetics, Int J Miner Process. 123 (2013) 9–17.

[50] M.J. Wilson, Rock-forming minerals, in: Geological Society of London, 1978.

[51] M.D. Foster, Interpretation of the composition of lithium micas, Geological Survey Professional Paper. 354 (1960) 38.

[52] B. Lafuente, R.T. Downs, H. Yang, N. Stone, The power of databases: The RRUFF project, 2016. https://doi.org/10.1515/9783110417104-003.

[53] S. Shoval, G. Panczer, M. Boudeulle, Study of the occurrence of titanium in kaolinites by micro-Raman spectroscopy, Opt Mater (Amst). 30 (2008) 1699–1705.

[54] S. Shoval, M. Boudeulle, G. Panczer, S. Yariv, G. Baer, A. Heimann, Physics and Chemistry of Dykes, Balkema, Rotterdam. (1995) 325.

[55] H.E. Bennett, L.L. Chase, A.H. Guenther, B.E. Newnam, M.J. Soileau, Laser-Induced Damage in Optical Materials: 1990, US Department of Commerce, National Institute of Standards and Technology, 1991.

[56] R.L. Frost, T.H. Tran, J. Kristof, FT-Raman spectroscopy of the lattice region of kaolinite and its intercalates, Vib Spectrosc. 13 (1997) 175–186.

[57] C. Rinaudo, M. Roz, V. Boero, M. Franchini-Angela, FT-Raman spectroscopy on several di- and tri-octahedral T-O-T phyllosilicates, Neues Jahrbuch Fur Mineralogie, Monatshefte. (2004) 537–554. https://doi.org/10.1127/0028-3649/2004/2004-0537.

[58] R.L. Frost, J.T. Kloprogge, Vibrational spectroscopy of ferruginous smectite and nontronite, Spectrochimica Acta Part A. 56 (2000) 2177–2189.

[59] D. Hamilton, Biosignature detection in Mars analogue aqueous alteration minerals using Raman spectroscopy, York University, 2016.

[60] D. Krishnamurti, The Raman spectrum of calcite and its interpretation, in: Proceedings of the Indian Academy of Sciences-Section A, Springer, 1957: pp. 183–202.

[61] Z. Tomić, P. Makreski, B. Gajić, Identification and spectra–structure determination of soil minerals: Raman study supported by IR spectroscopy and X-ray powder diffraction, Journal of Raman Spectroscopy. 41 (2010) 582–586.

[62] A. Wang, J. Freeman, K.E. Kuebler, Raman Spectroscopic Characterization of Phyllosilicates, Lunar and Planetary Science XXXIII. (2002) 1–2.

[63] N.L. Lanza, R.C. Wiens, S.M. Clegg, A.M. Ollila, S.D. Humphries, H.E. Newsom, J.E. Barefield, C. Team, Calibrating the ChemCam laser-induced breakdown spectroscopy instrument for carbonate minerals on Mars, Appl Opt. 49 (2010) 211–217.

[64] S.M. Clegg, E. Sklute, M.D. Dyar, J.E. Barefield, R.C. Wiens, Multivariate analysis of remote laser-induced breakdown spectroscopy spectra using partial least squares, principal component analysis, and related techniques, Spectrochim Acta Part B At Spectrosc. 64 (2009) 79–88. https://doi.org/10.1016/j.sab.2008.10.045.

[65] N.J. McMillan, R.S. Harmon, F.C. De Lucia, A.M. Miziolek, Laser-induced breakdown spectroscopy analysis of minerals: Carbonates and silicates, Spectrochim Acta Part B At Spectrosc. 62 (2007) 1528–1536. https://doi.org/10.1016/j.sab.2007.10.037.

[66] R.R. Hark, R.S. Harmon, Geochemical Fingerprinting Using LIBS, 2014. https://doi.org/10.1007/978-3-642-45085-3.

[67] K. Léveillé, R.J., Bridges, J., Wiens, R.C., Mangold, N., Cousin, A., Lanza, N., Forni, O., Ollila, A., Grotzinger, J., Clegg, S. and Siebach, Chemistry of fracture-filling raised ridges in

Yellowknife Bay, Gale Crater: Window into past aqueous activity and habitability on Mars, J Geophys Res Planets. 1191 (2014) 2398–2415. https://doi.org/10.1002/2015JE004932.Received.

[68] G.S. Senesi, Laser-Induced Breakdown Spectroscopy (LIBS) applied to terrestrial and extraterrestrial analogue geomaterials with emphasis to minerals and rocks, Earth Sci Rev. 139 (2014) 231–267. https://doi.org/10.1016/j.earscirev.2014.09.008.

[69] M. Defernez, E.K. Kemsley, The use and misuse of chemometrics for treating classification problems, Trends in Analytical Chemistry. 16 (1997) 216–221. https://doi.org/10.1016/S0165-9936(97)00015-0.

[70] L. Ferré, Selection of components in principal component analysis: A comparison of methods, Comput Stat Data Anal. 19 (1995) 669–682. https://doi.org/10.1016/0167-9473(94)00020-J.

[71] T. Fouchet, R. Wiens, S. Maurice, J.R. Johnson, S. Clegg, S. Sharma, F. Rull, F. Montmessin, R. Anderson, O. Beyssac, The superCam remote sensing suite for MARS 2020: nested and co-aligned LIBS, Raman, and VISIR spectroscopies, and color micro-imaging, in: AAS/Division for Planetary Sciences Meeting Abstracts# 48, 2016.

[72] B.L. Ehlmann, J.F. Mustard, C.I. Fassett, S.C. Schon, J.W. Head, D.J. Des Marais, J.A. Grant, S.L. Murchie, Clay minerals in delta deposits and organic preservation potential on Mars, Nat Geosci. 1 (2008) 355–358. https://doi.org/10.1038/ngeo207.

# PREFACE TO CHAPTER 5

The preceding Chapter emphasized the practicality and significance of data-centric strategies, demonstrating their potential to immediately improve the scientific insights derived from Mars rovers without the need for new instrumentation. Building on this foundation, Chapter 5 presents a baseline study of strategies for accurately quantifying nitrogen (N) sequestered in Mars' crust using instrumentation already available on Mars. As with the previous chapter, the motivation for this work was based upon the ecological trends reported in Chapters 2 and 3, as well as a thorough review of existing literature and acknowledgment of the needs of the (Mars-focused) astrobiological community.

Specifically, Chapter 2 demonstrated that biomass and total sedimentary N were strongly linearly correlated. We interpreted this as evidence that the indigenous microbial community was, in part, regulated by the availability of N in the sediments. This interpretation is in line with previous research in terrestrial ecosystems showing that N is often a limiting nutrient that imposes restrictions on both biomass and biodiversity (see Chapters 2 and 5 for further explanation and references). Therefore, we hypothesized that the sedimentary N content on Mars could be used as a viable proxy for the potential vitality and diversity of life possible in a given environment—a roadmap for identifying high priority astrobiological targets. This hypothesis was the foundation for our successful Canadian Space Agency grant application entitled "Seeking Signs of Life: Using Nitrogen as a Mineral Tracer for Habitable Environments on Mars" (Grant number: [21EXPCOI1]).

Moreover, a review of recent literature revealed that quantifying the N content of Mars crustal materials could have broader implications for understanding habitability through time on a *planetary scale*. Planetary models predict the widespread presence of N-bearing minerals (e.g., nitrate or nitrite salts, ammonium-bearing clay minerals) and these models are validated (in part) by positive detection of nitrate ($NO_3^-$) in both Martian meteorites and surface materials [1–3]. However, the true quantity and distribution of N phases in Mars' crust remain unknown. This could pose a severe limitation on the overall habitability of Mars given that N is a key component of life's most basic building blocks (e.g., amino acids and nucleotides). Therefore, to

refine our search for life on Mars, it is imperative to discern whether sufficient bioavailable N was/is present. Indeed, Mars' uncertain N budget has been identified as one of the most important outstanding questions of Mars' habitability [4,5].

To date, *in situ* detections of sedimentary N have been achieved solely by the Sample Analysis at Mars (SAM) instrument on the *Mars Science Laboratory* (MSL) *Curiosity* rover. This instrument, optimized for analyzing organics and gases from various samples, detected low levels of NO during the pyrolysis of certain sedimentary rock and regolith samples. The NO was interpreted as a byproduct of $NO_3^-$ decomposition [3]. These findings corroborate planetary models that predict $NO_3^-$ deposition [1] and confirm that a feedstock of bioavailable N exists within Mars' surface materials.

However, the use of SAM to detect sequestered N presents some challenges that complicate our understanding of the stratigraphic trends associated with N distribution and its geologic context, making it difficult to develop robust predictions about the abundance and distribution of the buried N [6]. For instance, SAM analyses are performed on drilled or scooped samples, which means they are confined to a relatively small region and are also limited in frequency due to the time and energy cost of each analysis. This results in a somewhat sparse dataset of sequestered N. Further, a significant portion of stratigraphy, ~188 vertical meters, remained unexamined during *Curiosity's* traverse because of a drilling malfunction [6]. In addition, a high degree of variability in NO content has been observed, both between different samples from the same stratigraphic position and within repeated measurements of a single sample [3]. This led Navarro-Gonzolez et al. (2019) to speculate that issues in sample homogenization combined with natural variability in the extent of leaching might account for these inconsistencies [6]. Thus, while SAM has provided the first direct, *in situ* evidence of $NO_3^-$ on Mars, the patchy stratigraphic record and multiple sources of variance introduces uncertainty about the relationship between N sequestration and its geological environment, as well as its wider planetary distribution [6].

Motivated by this gap in knowledge, Chapter 5 explores the nature of N emission by laser-induced breakdown spectroscopy (LIBS). LIBS can be used to rapidly detect and quantify elements from standoff distance (~2-12 m on Mars) and is available on at least two Mars rovers

currently exploring different depositional settings, however, very little has been published regarding the detection of N with LIBS. This scarcity of information is likely attributable to a couple of factors: firstly, N possesses inherently weak emission within the typical LIBS observational range, making detection a complex endeavor; secondly, Earth's N-rich atmosphere restricts the practicality of advancing this technology for terrestrial applications. Consequently, this Chapter aims to establish a baseline understanding of the LIBS N spectrum in Mars-relevant matrices, determine the best emissions lines for detection and quantification, elucidate strategies to maximize quantification accuracy, and then discuss how these results may be best translated to current and future Mars rovers. A logical and pressing next step of this work will be to refine the proposed methodology to align with the specific instrument configurations of active planetary LIBS instruments. This will enable the frequent and expansive stratigraphic surveys of N that are required to understand the evolution of Mars N budget through space and time.

**REFERENCES**


[1] C. V. Manning, K.J. Zahnle, C.P. McKay, Impact processing of nitrogen on early Mars, Icarus. 199 (2009) 273–285. https://doi.org/10.1016/j.icarus.2008.10.015.

[2] S.P. Kounaves, B.L. Carrier, G.D. O'Neil, S.T. Stroble, M.W. Claire, Evidence of martian perchlorate, chlorate, and nitrate in Mars meteorite EETA79001: Implications for oxidants and organics, Icarus. 229 (2014) 206–213. https://doi.org/10.1016/j.icarus.2013.11.012.

[3] J.C. Stern, B. Sutter, C. Freissinet, R. Navarro-González, C.P. McKay, P.D. Archer Jr, A. Buch, A.E. Brunner, P. Coll, J.L. Eigenbrode, Evidence for indigenous nitrogen in sedimentary and aeolian deposits from the Curiosity rover investigations at Gale crater, Mars, Proceedings of the National Academy of Sciences. 112 (2015) 4245–4250.

[4] C.S. Cockell, Trajectories of martian habitability, Astrobiology. 14 (2014) 182–203. https://doi.org/10.1089/ast.2013.1106.

[5] R.L. Mancinelli, A. Banin, Where is the nitrogen on Mars?, Int J Astrobiol. 2 (2003) 217–225. https://doi.org/10.1017/S1473550403001599.

[6] R. Navarro-González, K.F. Navarro, P. Coll, C.P. McKay, J.C. Stern, B. Sutter, P.D. Archer, A. Buch, M. Cabane, P.G. Conrad, J.L. Eigenbrode, H.B. Franz, C. Freissinet, D.P. Glavin, J. V. Hogancamp, A.C. McAdam, C.A. Malespin, F.J. Martín-Torres, D.W. Ming, R. V. Morris, B. Prats, F. Raulin, J.A. Rodríguez-Manfredi, C. Szopa, M.P. Zorzano-Mier, P.R. Mahaffy, S. Atreya, M.G. Trainer, A.R. Vasavada, Abiotic Input of Fixed Nitrogen by Bolide Impacts to Gale Crater During the Hesperian: Insights From the Mars Science Laboratory, J Geophys Res Planets. 124 (2019) 94–113. https://doi.org/10.1029/2018JE005852.

# CHAPTER 5

# Assessing the Feasibility of Laser Induced Breakdown Spectroscopy for Detecting Nitrogen in Martian Surface Sediments

Erin Gibbons[a*], Richard Léveillé[a1], and Kim Berlo[a1]

[a] Geotop, Department of Earth and Planetary Sciences, McGill University, 3450 University Street, Montreal, Quebec, Canada, H3A 0E8

[1]These authors contributed equally to this work.

*Corresponding author*: erin.gibbons@mail.mcgill.ca*

Submitted to *Spectrochimica Acta Part B: Atomic Spectroscopy*

**ABSTRACT**

Despite the detection of fixed nitrogen in meteorites and directly on Mars' surface, the abundance and distribution of nitrogen sequestered in the Martian crust remains unknown. Given that nitrogen is a bioessential element that is required for the synthesis of amino acids, nucleic acids, and other organic molecules vital for life, this gap in knowledge is one of the most important challenges in constraining Martian habitability. Laser-induced breakdown spectroscopy (LIBS) has the capability to detect N in natural rock samples and is available as a stand-off survey instrument on multiple currently active Mars rovers, creating an immediate opportunity to map the stratigraphic distribution of N withing diverse depositional settings. However, little has been published regarding the detection of N with LIBS.

To lay a foundation for N detection on Mars using LIBS, we synthesized a comprehensive suite of samples with variable amounts of nitrogen (as nitrate or ammonium) in either a Mars regolith

simulant or a clay matrix. We present baseline spectra of N emission in Mars-relevant matrices and identify spectral interferences. Our results indicate that 17 diagnostic N emission lines are reliably detectable from mineral-bound N against a basaltic background, but only four lines exhibit sufficient sensitivity to be detected across a range of N concentrations and within all tested matrices. To elucidate optimized strategies for quantification, we present an iterative series of PLS models. We find that prediction accuracy is improved by restricting the compositional range of the training set, normalizing the data, subtracting baseline continuum emission, and simultaneously modeling the emission behaviour of multiple diagnostic N lines at once. We observe that the prediction uncertainty increases (worsens) from 8.4% to 29.9% if models are used to predict N in samples with a dissimilar matrix than those used during training, suggesting poor generalizability outside the training range. Consequently, future work should focus on developing a larger, more diverse training set that encompasses the range of N concentrations and phases expected to be encountered on Mars, which may be used to train generalizable models. Overall, this work demonstrates that LIBS is a promising tool for determining the abundance of N sequestered in Martian surface materials and lays a foundation for future development.

## 5.1 INTRODUCTION

The search for evidence of habitable conditions and signs of life—whether extinct or extant—on Mars is now a primary objective for space agencies [1–3]. While data from previous missions have illustrated that Mars satisfied many of the prerequisites for life throughout its history, at least episodically [1,4,5], Mars' nitrogen (N) budget remains poorly constrained [6,7]. Nitrogen is one of the fundamental elements used by life to construct complex biomolecules and polymers with a range of shapes, properties, and uses [8], leading multiple authors to argue that it is difficult to imagine a functional biochemistry that does not make use of N [9–11]. Indeed, in terrestrial ecosystems, N is often a limiting nutrient that exerts a principal control on biomass and biodiversity [12–14]. Therefore, determining the amount and distribution of bioavailable N sequestered in Mars' crust, past and present, has been recognized as one of the most important outstanding challenges in constraining Martian habitability [4,7].

### 5.1.1 Background

Data collected from the Viking lander and Mars Science Laboratory (MSL) indicate that dinitrogen ($N_{2\,(g)}$) comprises ~2.6% of the Martian atmosphere, which is equivalent to ~0.15-0.2 mbar [15–17]. However, Mars' primordial $N_{2\,(g)}$ inventory is projected to have been much larger

[18–21], with the most recent estimates suggesting that the partial pressure of $N_{2\,(g)}$ was 60–740 mbar 3.8 billion years ago (median value of 310 mbar) [22]. While the exact processes leading to the depletion of $N_{2\,(g)}$ through time are not fully understood, two primary types of loss mechanism have been hypothesized: (1) losses to space (e.g., via solar wind 'sputtering' or impact erosion), or (2) burial within the lithosphere as nitrate/nitrite salts or as ammonium sorbed/fixed in clay minerals [7,23,24]. The extent to which each of these mechanisms has played a role remains an area of ongoing investigation and debate.

Understanding the overall loss of $N_{2\,(g)}$ from Mars' atmosphere holds critical significance for assessing the planet's habitability. On the one hand, previous one-dimensional radiative-convective climate models have demonstrated that the estimated primordial $N_{2\,(g)}$ concentrations could have enhanced Mars' early greenhouse effect via pressure broadening of $CO_2$ absorption bands, contributing up to 13 K of surface warming [25]. This degree of warming could have sustained nearly continuous habitable conditions on the surface in certain regions [22,25]. Consequently, the loss of $N_{2\,(g)}$ partial pressure, by any mechanism, may have been an important driver of the degradation of surface habitability through time.

On the other hand, a fraction of the $N_{2\,(g)}$ lost from the atmosphere is predicted to have become sequestered in the lithosphere. Indeed, several natural mechanisms, such as thermal shock processes (e.g., induced by lightning, volcanism, or impact events) or photolysis, have been proposed to initiate N fixation on Mars, breaking the strong $N_2$ triple bond and forming oxidized or reduced N ions [26–29]. Some of the fixed N intermediates are expected to undergo dry or wet deposition onto the surface, subsequently accumulating in the regolith [7,19,20,26]. Nitrate ions ($NO_3^-$) are predicted to be the most significant end product of Martian N fixation and could become buried in the regolith by forming thermodynamically stable nitrate salts with the major cations in the regolith [7]; Manning et al. [20] calculated an impact-generated nitrate reservoir of $\sim 5\times10^{18}$ mole on Mars. Ammonium ions ($NH_4^+$) are also likely to form through reactions with iron minerals [7,28] and could subsequently become fixed/sorbed within phyllosilicates [30]. Importantly, these stable end products represent bioavailable forms of N, demonstrating that the redistribution of N from Mars' atmosphere to its lithosphere could have generated a critical reservoir of essential N for life.

Therefore, understanding the balance between the depletion of $N_{2\,(g)}$ in the atmosphere, potentially contributing to surface warming through greenhouse effects, and the sequestration of bioavailable N is essential for unraveling the complex history and conditions that have shaped Mars as a potentially habitable world. Directly assessing Mars' lithospheric N deposits could help elucidate this interplay by offering a tangible record of atmosphere-lithosphere interactions. However, although fixed N has been detected in meteorites [31] and directly on the surface of Mars [32], we do not have sufficient data to understand the distribution and form of fixed N in the Martian crust. Indeed, the only successful in situ detection of Martian N has been achieved by the Sample Analysis at Mars (SAM) instrument on the *Mars Science Laboratory* [32]. Unfortunately, SAM analyses are confined to a relatively small area and are energy-expensive, which has limited the spatial extent of N surveys to date. Efforts to detect fixed N compounds from orbit have been unsuccessful thus far, either because their concentrations fall below the detection limit of current orbiters or due to interference from dust [19,33]. Consequently, there is a need for rapid and frequent in situ N measurements to advance our understanding of the stratigraphic distribution of sequestered N phases.

### 5.1.2 Objectives

We explore the capacity for laser-induced breakdown spectroscopy (LIBS) to meet this need. At the time of writing, LIBS technology has been included on the payloads of the three most recent Mars rovers, including NASA's *Curiosity* and *Perseverance* rovers, and the China National Space Administration's *Zhùróng* rover. The two NASA instruments (ChemCam and SuperCam) are used frequently as chemical surveyors and have proven effective in generating a near-continuous record of geochemical trends throughout the rovers' traverses [34–38]. By enabling accurate N detection and quantification with LIBS, we could immediately begin a high-resolution characterization of the N buried within distinct Martian depositional environments.

There are, however, three significant challenges to detecting N with LIBS. First, N has a high ionization potential (first ionization energy = 14.5 eV), resulting in generally weak emission lines in a LIBS spectrum [39]. This becomes problematic when N coexists with elements that have lower ionization energies–such as alkalis, alkaline Earth elements, and transition metals–which produce more intense emission lines due to a higher number of atoms excited by a given input of energy. Second, the strongest N emission lines are found in the vacuum ultraviolet region (30-200 nm) [39], which most spectrometers, including those on the Mars rovers, cannot

register. Thus, LIBS N detection is limited to the relatively less intense emission lines in the ultraviolet, visible, and infrared regions [40–43]. Lastly, the use of LIBS for routine N analyses on Earth is challenged by interference from our $N_2$-rich atmosphere (>78%), which has impeded the depth and breadth of research on LIBS N emission characteristics [44]. In addition, it is important to clarify that while some previous work has investigated LIBS N emission from organic compounds [45,46], these studies did not concentrate on a systematic characterization of emission features. Moreover, research on inorganic nitrogen sources using LIBS has been limited, further emphasizing the need for more extensive investigation in this area.

Considering these challenges and the dearth of systematic studies for optimizing N detection with LIBS, we undertook a focused investigation designed to:

1. Establish a baseline understanding of the LIBS N spectrum, with consideration of potentially interfering emission lines from other rock-forming elements expected to coexist in natural N-bearing materials on Mars.
2. Elucidate the optimal strategies for reliable detections and quantification.

The ultimate goal of this work is to lay the foundation for the use of remote LIBS for N analyses in planetary exploration so that astrobiologically important N stores may be discovered, explored, and possibly prioritized for sample return.

## 5.2 METHODS AND RATIONALE

### 5.2.1 Sample Synthesis

On Mars, abiotic $N_{2\,(g)}$ fixation is expected to result in two primary N sinks: nitrate salts and ammoniated phyllosilicates [7]. We synthesized two distinct sample suites to simulate both possible outcomes.

#### *5.2.1.1 Nitrate Salt Sample Suite*

To investigate the potential for LIBS to identify $NO_3^-$-derived N in Mars' sedimentary deposits, we created a series of mixtures containing decreasing proportions of various nitrate salts dispersed in a basaltic matrix. For the salt phases, we purchased high-purity nitrate salts complexed to cations known to be abundant on the Martian surface: $NaNO_3$, $KNO_3$, $Mg(NO_3)_2$, $Ca(NO_3)_2$, and $Fe(NO_3)_3$. For the matrix, we use the Mars Global Simulant (MGS-1) from the Exolith Lab [35], a high-fidelity basalt soil standard developed based on quantitative mineralogy from the Mars Science Laboratory (MSL) *Curiosity* rover [47]. The product details of the

purchased salts and the bulk chemical and mineralogical properties of MGS-1 are summarized in Appendix C, Tables S1-S3.

To facilitate homogenous mixing and enable pellet pressing without the use of a binding agent, the particle sizes of the salts and MGS-1 powder were reduced as follows. An aliquot of each salt was first placed in a vacuum desiccator for 24 hours to reduce clumping and gently crushed using an agate mortar and pestle; the MGS-1 powder was ground in a planetary ball mill to <1 μm. Predetermined amounts of each salt were then weighed on a four-decimal-point scale and separately mixed with MGS-1, creating a sample series with increasing proportions of each salt. Mixture ratios were calculated to produce samples with 0.5, 5, 10, 15, 25, and 30 wt.% of the $NO_3^-$ ion. We specifically calculated the mixing ratios according to the quantity of the $NO_3^-$ ion to ensure that the molecular fraction of N was identical across each series, regardless of the stoichiometric content of N in each salt. The lowest concentration of 0.5 wt.% $NO_3^-$ is commensurate with the quantity of $NO_3^-$ identified in the Mars meteorite EETA79001 [31], while the higher concentrations reflect the range of $NO_3^-$ observed in the Atacama Desert [48,49], a high-fidelity terrestrial analogue site for investigating Mars' nitrate deposits [7,50]. We followed the mixing procedure described by Chen et al. (2019) [51] for the preparation of homogenously spiked soils.

Finally, the mixed samples were pressed into 13 mm diameter pellets using an estimated pressure of $2 \times 10^6$ Pa (uncorrected for friction) for two minutes (a procedure previously validated in our lab to produce robust pellets for LIBS analysis without binding agents [52]). A portion of MGS-1 powder, and an aliquot of each pure salt powder, were also pressed into pellets using the same procedure to represent the end-members of each dilution series.

Table 5.1 summarizes the full nitrate salt sample suite. The total N content of the end-member samples and a subset of the mixture samples (5 and 30 wt.% mixtures) was verified externally by Activation Laboratories Ltd. using a Leco CNS-2000 Analyzer. The measured N values match the concentrations based on the relative weights with a mean percentage error of 5.2% (details provided in Appendix C).

| Nitrate Salt | Doping Condition of $NO_3^-$ ion | Corresponding N wt.% |
|---|---|---|
| $Fe(NO_3)_3$ | 0.5 | 0.11 |
| | 5 | 1.13 |
| | 10 | 2.26 |
| | 15 | 3.39 |
| | 25 | 5.65 |
| | 30 | 6.78 |
| | 100 (pure salt) | 10.40 |
| $Ca(NO_3)_2$ | 0.5 | 0.11 |
| | 5 | 1.13 |
| | 10 | 2.26 |
| | 15 | 3.39 |
| | 25 | 5.65 |
| | 30 | 6.78 |
| | 100 (pure salt) | 11.86 |
| $Mg(NO_3)_2$ | 0.5 | 0.11 |
| | 5 | 1.13 |
| | 10 | 2.26 |
| | 15 | 3.39 |
| | 25 | 5.65 |
| | 30 | 6.78 |
| | 100 (pure salt) | 10.93 |
| $NaNO_3$ | 0.5 | 0.11 |
| | 5 | 1.13 |
| | 10 | 2.27 |
| | 15 | 3.39 |
| | 25 | 5.65 |
| | 30 | 6.78 |
| | 100 (pure salt) | 16.48 |
| $KNO_3$ | 0.5 | 0.11 |
| | 5 | 1.13 |
| | 10 | 2.26 |
| | 15 | 3.39 |
| | 25 | 5.65 |
| | 30 | 6.78 |
| | 100 (pure salt) | 13.85 |

*Table 5.1: Summary of nitrate sample suite.*

*Predetermined amounts of each salt were weighed and separately mixed with MGS-1 to yield 5 salt dilution series, each containing samples with 0.5, 5, 10, 15, 25, and 30 wt.% of the $NO_3^-$ ion. The corresponding wt.% of N, based on the weighing procedure is listed.*

#### *5.2.1.2 Ammoniated Clay Sample Suite*

To investigate the potential for LIBS to identify $NH_4^+$-derived N, we considered the possible modes of $NH_4^+$ sequestration. On Mars, otherwise labile $NH_4^+$ ions could be stabilized by phyllosilicate minerals via adsorption to the mineral surface or by penetrating into the interlayer of 2:1 minerals as an exchangeable cation and subsequently becoming chemically bound [7,30]. To assess both these pathways, we saturated various Mars-relevant clays with a solution of $NH_4^+$, then leached them to remove all but the chemically bound $NH_4^+$ ions.

We chose to focus our investigation on 2:1 clay minerals, as these are the most effective phyllosilicates for storing $NH_4^+$ ions [53]. The most commonly identified 2:1 clay minerals on Mars are Fe/Mg-smectites (e.g., nontronites) and Al-smectites (e.g., montmorillonites) [54] and are therefore the subject of our investigation. We purchased two nontronite samples, NAu-1 and NAu-2, and two montmorillonite samples, SAz-1 and SWy-3, from the Clay Mineral Society. The bulk chemical and mineralogical properties of these samples are summarized in Appendix C Table S2 and S3, respectively. The clays were gently crushed in an agate mortar and pestle to permit better pellet cohesion.

To ammoniate the clays, separate aliquots of each sample were suspended in 1 M $NH_4$-acetate solution at a ratio of 10 parts solution to 1 part mineral powder (vol./wt.) (an excess solution volume is required to accommodate for the swelling of the clay mineral). The mixture was agitated on a shaker table at 500 rpm for 1.5 hours to ensure complete saturation and then allowed to settle for 72 hours at room temperature. After settling, the majority of the $NH_4$-acetate supernatant was removed via pipetting. Half of slurry was removed, dried at 40° C for 24 h, and lightly disaggregated in a mortar and pestle. This aliquot was designated the “saturated” condition and represents clays with both surface-adsorbed and interlayer $NH_4^+$ ions. The other half of the slurry was leached according to the methods described by Bishop et al. [30]. In brief, these slurries were suspended in excess de-ionized water (10:1 vol./wt.), shaken to dissolve the surficially adsorbed salts, and centrifuged at 9000 rpm for 25 minutes to concentrate the clay particles. The liquid supernatant was removed by pipetting and the leaching treatment was repeated twice more. Finally, the leached slurries were dried and lightly disaggregated. These samples were designated as the “leached” condition and represent clays with primarily the interlayer $NH_4^+$ ions remaining.

Powders from the “saturated” and “leached” treatments were pressed into pellets using the same protocol described for the nitrate samples. The ammoniated clay sample suite is summarized in Table 5.2. As above, the total N content of each sample was measured externally by Activation Laboratories Ltd. using a Leco CNS-2000 Analyzer.

| Clay Matrix | Saturation Condition | N wt.% |
|---|---|---|
| Nau-1 | Leached | 1.34 |
| | Saturated | 1.99 |
| Nau-2 | Leached | 1.01 |
| | Saturated | 1.59 |
| SAz-1 | Leached | 1.61 |
| | Saturated | 2.26 |
| SWy-3 | Leached | 0.95 |
| | Saturated | 1.83 |

*Table 5.2: Summary of ammoniated clay sample suite.*

*The $NH_4^+$ ion was introduced to four Mars-relevant clays using 1 M $NH_4$-acetate solution. N content was verified by Activation Laboratories Ltd. (see text for details).*

### 5.2.2 LIBS Measurements

LIBS spectra were collected at McGill University using a J200 instrument (Applied Spectra, Fremont, CA, USA) controlled by the Axiom 2.0 software. This system consists of a 213 nm nanosecond Nd:YAG laser with a pulse width of <5 ns, a repetition rate of 10 Hz, and a maximum power output of 100 mJ. The six-channel spectrometer is fitted with gated CCD arrays for instant whole spectrum registration in the 186–1042 nm range at a resolution of ~0.07 nm. The sealed ablation chamber features an *xyz* translational stage, a full-colour camera for focus and targeting, and the option to supply gases during the course of the experiment.

To remove interference from atmospheric $N_{2\,(g)}$, the sample chamber was purged of air before each analysis and flushed with Helium (He) for 4.5 minutes. Samples were allowed to sit in the He atmosphere for at least 30 minutes prior to analysis.

Before beginning data collection, the adjustable instrument parameters were systematically varied to optimize the peak-to-base ratio of the N(I) line at 746.8 nm. The 746.8 nm line was used as an initial reference because it has a high relative intensity (compared to other N emission lines) [55], has only a small number of potential spectral interferences, and has previously been reported as a reliable emission feature from inorganic N sources [39]. Optimal parameters were:

a laser power of 1.5 mJ/pulse, a spot size of 25 μm, and a delay time of 0.15 μs (the gate width is fixed at 1.05 μs).

Using these parameters, 100 consecutive laser pulses were fired in a line pattern on each sample surface; their data were accumulated into a single spectrum. A linear scan was used to expose a new portion of the sample surface for each acquisition, ensuring that the final accumulated spectrum represented an average bulk chemical fingerprint and accounted for any small heterogeneities that may have persisted through the sample synthesis process. This acquisition procedure was repeated for a total of five (non-overlapping) line scans per sample, producing five accumulated spectra per sample. For the calibration exercises described in section 5.4.1.1, the five spectra from each pellet were averaged to provide one representative spectrum for each sample with which to model.

### 5.2.3 Spectral Identification

Visualization of the LIBS spectra and line identification was carried out using version 18.0.1.34 of the built-in Clarity Software (Applied Spectra) of the LIBS instrument. Emission features that are diagnostic of the presence of N were initially identified within the samples by regressing the known quantity of N in each sample against the 12,288 channels (186 - 1042 nm) in the recorded spectra. Wavelengths with an $R^2$ (coefficient of determination) greater than 0.7, suggesting a high degree of correlation with N content, were marked as candidate N lines. To avoid confusion with other elements that may have also been correlated with the N content (e.g., O in the $NO_3^-$ ion), the flagged emission features were also required to meet the following selection criteria:

1) The wavelength should coincide with a reference wavelength for N emission listed in the NIST database [55].
2) The wavelength region should be featureless in the blank sample (Mars Global Simulant) in order to avoid false attribution of N to an emission feature associated with the matrix material.
3) The peak height must rise sufficiently above the level of the background emission such that it may be reliably distinguished from noise. Specifically, we only considered a candidate emission peak to be ‘detected’ as N if the peak height was greater than 3x the standard deviation of the random noise on the baseline measured from a featureless portion of the spectrum before or after the signal peak.

Emission features with a strong correlation with N content and met these additional criteria were considered as robust and diagnostic signatures of N, suitable for *detection* in Mars-like matrices.

## 5.3 RESULTS: LIBS SPECTRA AND GENERAL CHARACTERISTICS

Exemplary spectra from each sample suite are shown in Figure 5.1. As expected, the N lines exhibit a very weak intensity relative to the emission of other elements in the matrices, especially elements of the alkali metal, alkaline-Earth metal, and transition metal groups, which dominate each spectral fingerprint.

We did not observe any N lines in the lowest doping condition (0.5 wt.% $NO_3^-$), suggesting that this is below the limit of detection achievable by our setup. Twenty spectroscopic lines were highly correlated with the known N content in the remaining samples and satisfied the three criteria described in Section 5.2.3 as being diagnostic N emission features. The observed N lines all lie in the visible and near-infrared portion of the electromagnetic spectrum (~400-1100 nm) and are ascribed to electronic transitions from neutral N. Table 5.3 provides a list of these lines along with comments regarding their emission behaviour, potential spectral interferences, the minimum level at which they could be reliably detected in the nitrate samples set (limit of detection), and a record of whether the lines were also observed in the spectra from the ammoniated clay sample suite.

Several characteristic N lines reported in previous publications were not detected here, despite being within the spectral range of our detector. In most cases, such discrepancies may be attributed to investigating different N phases or spectral interference from the Mars-relevant matrix material used in our samples (see discussion in section 5.5.1). This highlights the importance of identifying suitable emission features within samples that closely mimic the expected target materials. Consequently, the lines listed in Table 5.3 provide a catalogue of diagnostic N lines that have been validated to be detectable amid the medley of co-occurring emission lines likely to be encountered on Mars during N surveys, making them the most robust signatures for N *detection* during in situ analyses.

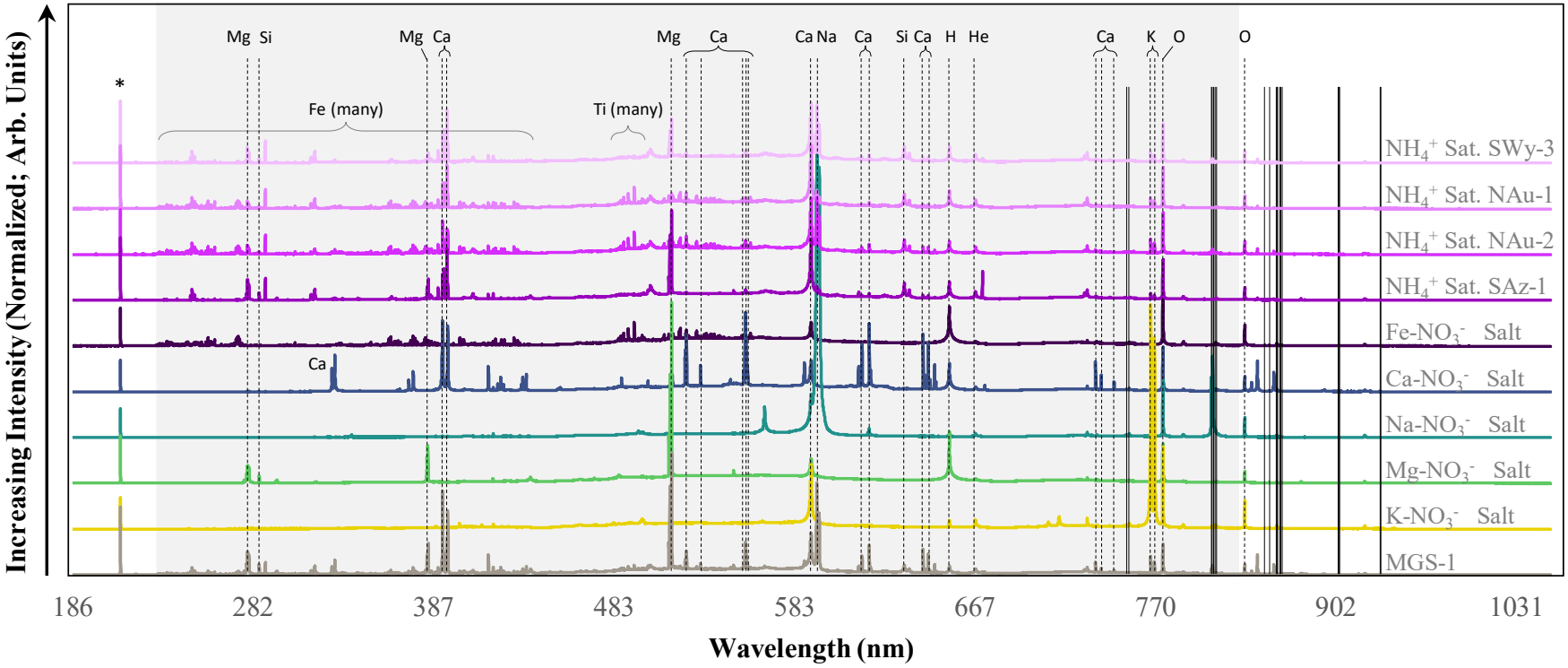


*Figure 5.1: Representative LIBS spectra from samples used in this study.*

*The position of the N emission lines identified in this study (listed in Table 5.3) are marked with solid black lines. Co-occurring emission from elements of the matrix and atmosphere are marked with dashed lines and labels; identification of co-occurring elements is not exhaustive in this figure for simplicity. The grey shading marks the spectral range used by the LIBS instruments onboard the three Mars rovers active at the time of writing. The asterisks marks the 213 nm emission feature from the laser.*

| Emission Wavelength (nm) | Comments | Lowest Concentration Peak is Observed in Nitrate Dilution Series | Observed in Ammoniated Clays |
|---|---|---|---|
| 744.2 | Some interference from weak Fe peak at 744.6 nm in high-Fe samples | 5 wt.% | NAu-1, SAz-1, SWy-1 |
| 746.8 | Strong, slight interference from unresolved grouping of O peaks at 747.6-748.6 nm | 5 wt.% | NAu-1, NAu-2, SAz-1, SWy-1 |
| 818.5 | Interference from Na at 818.3 nm | Pure salts only; not detected in samples with MGS-1 | None |
| 818.8 | Interference from Na at 818.3 nm | 15 wt.% | None |
| 820.2 | Weak; Interference from Na at 819.5 nm | Pure salts only; not detected in samples with MGS-1 | None |
| 821.6 | Strong; Superimposed on Na shoulder (819.5 nm) in high-Na samples | 5 wt.% | NAu-1, SAz-1, SWy-1 |
| 822.3 | Weak; Superimposed on Na shoulder (819.5 nm) in high-Na samples | Pure salts only; not detected in samples with MGS-1 | None |
| *859.4* | *Weak* | *25 wt.%* | *None* |
| *862.9* | *Moderate* | *10 wt.%* | *None* |
| *868.0* | *Strong, part of a triplet emission pattern with N peaks at 868.3 and 868.6* | *5 wt.%* | *NAu-1, NAu-2, SAz-1, SWy-1* |
| *868.3* | *Moderate, part of a triplet emission pattern with N peaks at 868.0 and 868.6* | *10 wt.%* | *None* |
| *868.6* | *Moderate, part of a triplet emission pattern with N peaks at 868.0 and 868.3* | *10 wt.%* | *None* |
| *870.3* | *Moderate* | *10 wt.%* | *None* |
| *871.2* | *Moderate* | *10 wt.%* | *None* |
| *871.9* | *Moderate* | *10 wt.%* | *None* |
| *904.6* | *Weak* | *15 wt.%* | *None* |
| *905.0* | *Weak* | *15 wt.%* | *None* |
| *906.0* | *Weak* | *25 wt.%* | *None* |
| *938.7* | *Weak* | *10 wt.%* | *None* |
| *939.3* | *Weak* | *10 wt.%* | *None* |

*Table 5.3: Diagnostic N lines.*

*These lines exhibit a high correlation with the N content of the sample and satisfy the initial three criteria listed in section 5.2.3. Column 3 lists the lowest concentration that the given peak could be observed within the nitrate sample series – the limit of detection. Column 4 provides a record of which lines could be observed in which of the $NH_4^+$-bearing clay samples. Italicized rows are beyond the spectral range of the LIBS instruments currently operational on Mars.*

## 5.4 DATA PROCESSING: TOWARDS AN OPTIMAL FRAMEWORK FOR QUANTIFYING N

Whereas Table 5.3 lists the spectroscopic N lines determined to be effective for the *qualitative* detection of N in plausible Mars matrices, the remainder of this paper is focused on processing the spectra to achieve optimal *quantification* of N.

Section 5.4.1 describes the development of a suite of quantitative models, each testing distinct preprocessing strategies or modeling architectures. Section 5.4.2 critically evaluates the performance of this suite of models, with the goal of identifying which approach yields the most accurate N predictions. Section 5.4.3 describes the generalizability of the optimized model and Section 5.5 synthesizes the entire effort to discuss the implications of applying the lessons learned to Mars.

### 5.4.1 Steps Towards Quantification

#### *5.4.1.1 Preprocessing*

##### *5.4.1.1.1 Normalization*

There is no universally suitable normalization procedure to compensate for parameter variations in a LIBS plasma. Instead, different methods need to be experimentally tested to understand their impact on the observed spectral behavior of the analyte of interest [44]. Three normalization techniques were tested here for their influence on N emission behaviour. Each technique emulates a normalization procedure routinely applied to actual LIBS data returned from the ChemCam and SuperCam instruments currently operating on Mars:

1) *Normalized to He* involves dividing each data point by the signal intensity of the He (I) emission line at 667.8 nm [55], derived from the He buffer gas in the sample analysis chamber. This procedure is meant to simulate the practice of normalizing LIBS spectra collected on Mars to a component of the Martian atmosphere (C or O derived from gaseous $CO_2$) to standardize for fluctuations in laser/solid coupling efficiency [56,57].
2) *Normalized to Total* involves dividing each data point by the total emission intensity integrated across the complete spectral range. This procedure is akin to the "Norm 1" technique described by Clegg et al. [58] when testing calibration schemes for ChemCam.
3) *Normalized to Detector* involves dividing each data point by the total emission intensity integrated across the wavelength range of the detector to which the data point corresponds. This procedure is akin to "Norm 3" described in Clegg et al. [58].

A comparison of these normalization methods and their effect on the N emission signal is integrated in the next subsection.

*5.4.1.1.2 Spectral Feature Extraction – Selecting the Most Sensitive N Lines*

To identify which N lines may be most effective for *quantification* across a range of concentrations, we defined three additional criteria to down-select only the most robust, stable N lines from our spectra. First, from the lines presented in Table 5.3, we filtered out any lines resulting from electronic transitions involving the ground state. These emission lines are the most severely affected by self-absorption phenomena, which alters the spectral line profiles and hinders quantitative determination of element abundance [59]. Second, we filtered out N lines that could not be detected across a range of concentrations. This criterion removes N lines that are unsuitable for constructing multi-point calibration curves to evaluate the reliability of the relationship between the measured signal and the N content. Priority was given to N lines that were detected across the *widest* range of concentrations, as well as those that could be resolved regardless of the host matrix (*i.e.*, detectable in both the nitrate sample suite and the ammoniated clay sample suite).

Only four of the N emission lines listed in Table 5.3, namely 744.2 nm, 746.8 nm, 821.2 nm, and 868.6 nm, satisfied these initial two criteria. As indicated previously, we did not observe N lines in the lowest doping condition, 0.5 wt.% and only these four emission lines were detectable in samples carrying the next lowest doping condition, 5 wt.% $NO_3^-$ (Table 5.3). These lines are thus detectable across the greatest range of concentrations tested. These same four lines were the only N lines detectable in the clays treated with ammonium, which retained N at levels comparable to the 5 wt.% $NO_3^-$ condition (Table 5.2). It is important to note that the emission line centered at 744.2 nm was not consistently detectable at the 5 wt.% $NO_3^-$ condition – it only surpassed our detection threshold in ~60% of the spectral replicates of each sample in the nitrate suite – however, because it was resolved in over half of these replicates *and* was resolvable in the ammoniated clay suite, we have chosen to include it in our assessment moving forward.

As a third and final criterion for extracting N emission features that may be useful for quantitative modeling, we required that the intensity of the candidate emission features increase proportionally with increasing N abundance in the sample suite. This is a crucial criterion. For an emission feature to be useful for quantitation, it must respond to the analyte in a predictable

manner and therefore increase monotonically with increasing concentration. The simplest way to evaluate this requirement is to draw a calibration curve where the measured signal is plotted against the analyte's known concentration across a series of samples [60].

In this paper, peak areas were used to quantify the "measured signal", rather than the height of the peak centroid. This was done because the intensity of a LIBS emission line is typically broadened over multiple spectral channels and this method accommodates for minor imprecisions in the resolution of the spectrometer. The use of peak areas is common practice for quantitative LIBS studies of geological samples [61,62]. To compute the peak areas, the Aspen Unscrambler™ software package (Aspen Technology Inc., Version 11.0) was first used to define and subtract a local linear baseline from a small range around each selected peak. The local region to be subtracted was generally selected to include any nearby N peaks or any peaks that interfered with the peaks of interest. The only exception was for the 821.6 nm peak, which lies on the shoulder of a high-intensity Na peak; the baseline subtraction area was defined tightly around the peak to minimize the influence of Na. After baseline correction, the area of the N peak was obtained by summing the intensity values between the local minima on either side of the N peak centroid (the specific position of the minima were selected after reviewing the N peak shapes in all our spectra and replicates). Figure 5.2 offers a graphical depiction of the wavelength ranges used for local baseline correction as well as the wavelength range used for peak area summation (a numerical summary is provided in Appendix C, Table S4).

To draw the calibration curve, the peak areas were then plotted against the molecular fraction of N in each sample (known precisely from the doping procedure or from stoichiometry in the case of the pure salt end-members). We plot against molecular fraction because the strength of LIBS emission lines depends on the number of atoms producing emission rather than the mass of these atoms (wt.%). For this initial assessment of N line response, calibration curves were only generated for the spectra acquired from the nitrate sample suite. The nitrate samples are ideal for evaluating whether a candidate N line is suitable for quantification because: (i) each sample in the suite contains a precisely controlled concentration of N, whereas the clay samples contain random abundances governed by the sorption characteristics of the clay, (ii) the nitrate sample suite was designed to cover a large range of concentrations and facilitates assessment at high and low concentrations, and (iii) the sample suite provides N sourced from five distinct nitrate minerals, allowing us to investigate the influence of chemical diversity on N response.

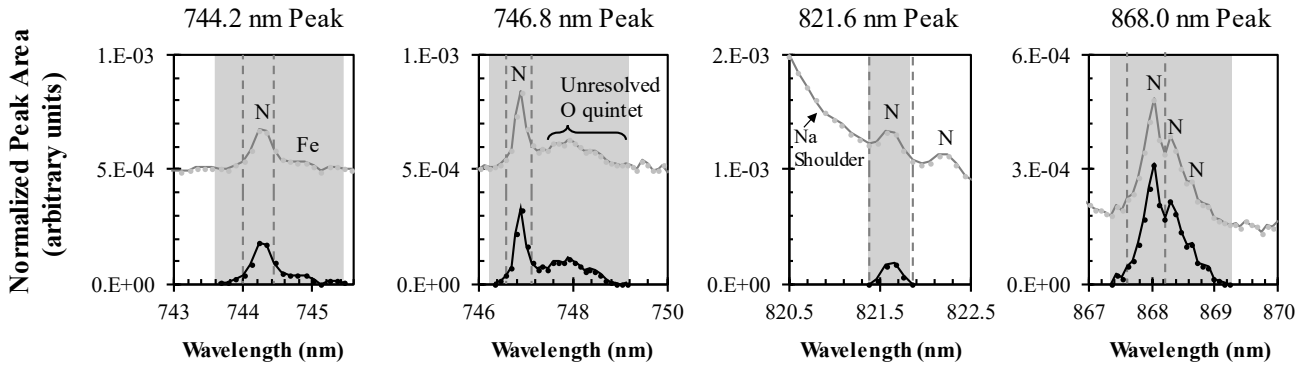


*Figure 5.2: Representative pre-processing of the four N emission features identified as potentially useful for quantification.*

*The uncorrected spectra are depicted as a grey line. The grey shading shows the channel range used for baseline correction. Linear baseline subtraction produced spectra with 0 vertical offset, shown by the black line. To channel range used for peak area integration, following baseline subtraction, is designated by the vertical dashed lines. The position of the peak envelope was chosen to capture the apex of the peak and minimize interference from neighboring peaks; the specific position was based on a thorough review of our entire spectral dataset.*

Figure 5.3 depicts representative examples of the calibration curve exercise; additional plots are provided in Appendix C, Figure S2 and S3. Overall, the calibration curves revealed three important results. First, regarding the unnormalized data, we found that the N peak area increased proportionally with the N content in the samples (Figure 5.3, top panel). This held true for each of the four N lines considered and each of the cationic mixtures. However, the *magnitude* of change in the N peak area with increasing N concentration was not uniform between cationic mixtures, resulting in different slopes for each salt series. For instance, the samples doped with $KNO_3$ consistently yielded the brightest N emission peaks for each doping condition, resulting in the steepest calibration curve, whereas the samples doped with $Mg(NO_3)_2$ yielded the weakest peaks and shallowest slope (Figure 5.3, top panel). Given that the doping procedure was designed specifically to produce samples with identical quantities of the $NO_3^-$ ion, *regardless* of the salt type used during the doping, this observation indicates that the emission behaviour of the unnormalized N emission peaks are significantly influenced by factors other than N content.

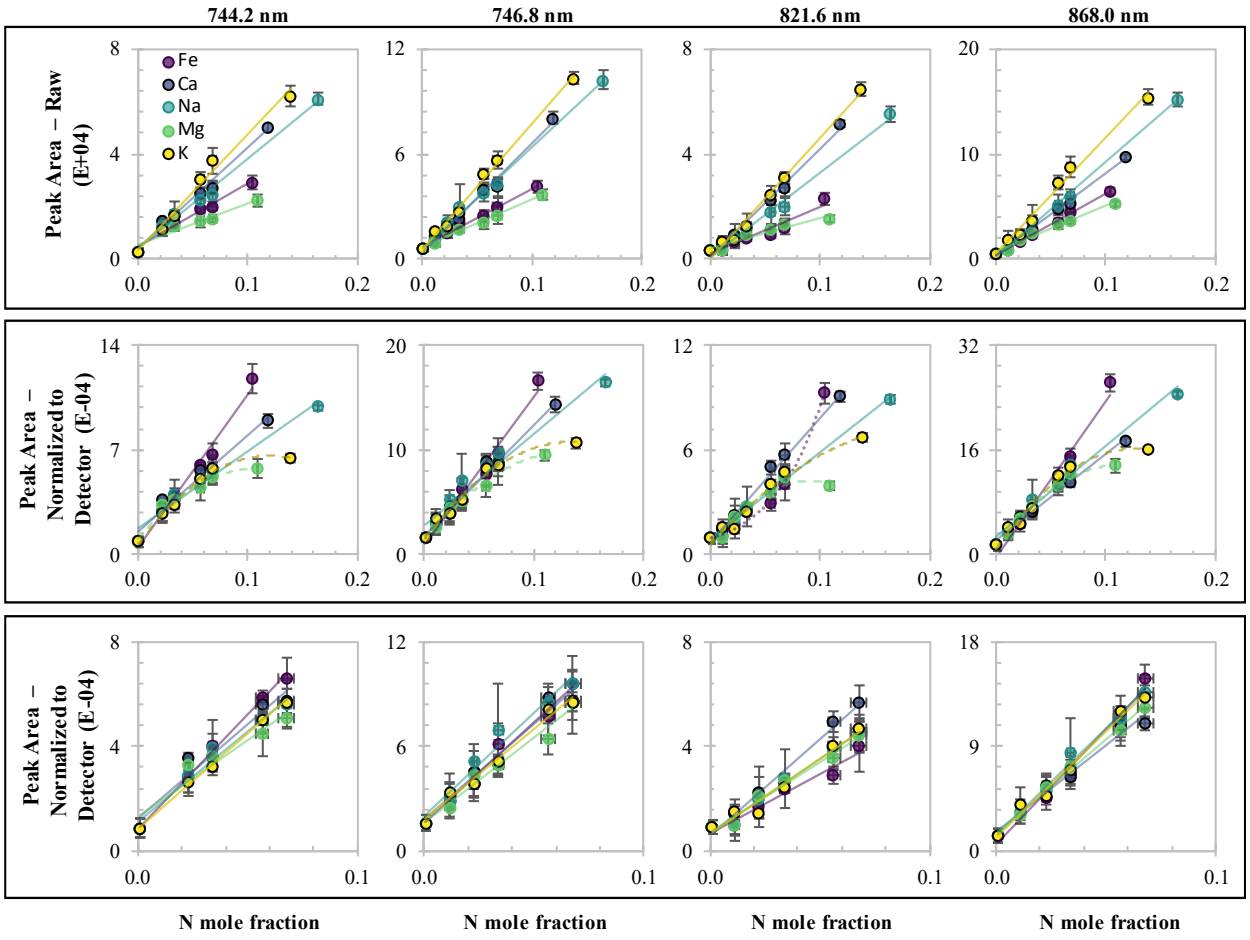


*Figure 5.3: Select calibration curves showing the measured N peak area versus the molar fraction of N.*

*The four vertical columns correspond to the four emission lines tested (to facilitate a comparison of the usefulness of each line for tracing N concentration) and the three horizontal panels depict selected pre-processing conditions. The top panel presents the unnormalized data, showcasing the monotonic increase in measured N peak area with respect to the molecular fraction of N in the samples. The middle panel depicts the same data, but this time normalized to the total emission of the detector; additional calibration curves depicting the other tested normalization conditions are included in Figure S2&3. Note the introduction of non-linear, and in some cases non-monotonic, behaviour into the relationship between the N peak area and the known N content. The bottom panel depicts the same normalized data, but with the salt endmember samples removed from the calibration curve (right-most data points). Different colours represent the different salt series, where the legend identifies the cationic composition of the salt used in the doping procedure. Each point is an average of the five replicate scans measured from each sample; vertical error bars represent the standard deviation across the five replicates. Horizontal error bars represent the average error between the calculated and validate N contents. Solid best-fit lines represent linear functions. Where a linear function lay outside 70% of the vertical error bars, an additional curve fitting algorithm was attempted: second order polynomial fits are represented by dashed lines and exponential fits are indicated by dotted lines.*

The second key observation was that all three of the normalization procedures introduced non-linear, and in some cases non-monotonic, behaviour into the relationship between the N peak area and the known N content (Figure 5.3, middle panel; Appendix C Figure S2). This non-linear behaviour was absent in the unnormalized data. Although a non-linear relationship between LIBS emission intensity and the analyte concentration may indicate that spectral self-absorption or detector saturation are at play [63], we reject these explanations here because: (i) our suite of selected N emission lines were filtered to avoid electronic transitions that are particularly susceptible to self-absorption, (ii) the N lines are far weaker than co-occurring cation emission lines, which themselves did not saturate the detector, (iii) we do not observe evidence of self-absorbance or saturation, such as a the characteristic distorted flat-topped peak or a peak shape with a narrow dip in the center where the strongest absorption occurs [64], and (iv) the non-linear behaviour is only apparent *after* normalizing the spectra. Furthermore, we observed that it is only the pure salt end-member samples that do not lie on the ideal linear trendline traced by the series of mixed samples (MGS-1 + salts dopant). Indeed, upon re-plotting the emission peak areas, but with the data from the pure salt end-member samples removed, the calibration curves all adopted an ideal monotonic and linearly increasing trend (Figure 5.3, bottom panel; Appendix C Figure S3). Together, these observations indicate that the non-linearity observed in our calibration curves is an artefact of normalizing spectra from samples with sufficiently different matrices: pure salts and salts mixed with basalt regolith.

Consider for example, the concentration series made with $KNO_3$ salt, normalized to the total emission intensity. Potassium has a low first ionization energy (4.3 eV) and produces very bright emission lines. The pure $KNO_3$ salt spectrum is thus scaled according to a few very bright K lines, and a few relatively weak N and O lines. In samples mixed with MGS-1, the K content is diluted and the presence of other elements (from MGS-1) means that the scaling will be different. As a result, N peaks in the spectrum of pure $KNO_3$ salt will be artificially suppressed because of the strong emission intensity of K (large normalization denominator) and will not be aligned with that of the rest of the samples in the series. These findings indicate that the selected N lines respond predictably to N content in samples of similar matrices, where laser-sample interactions remain relatively constant. This suggests that normalized spectra may provide accurate calibration only within a restricted range of compositions that exhibit similar emission

behaviour but may perform poorly if extrapolated to different samples. This possibility is further evaluated in section 5.4.3.

The third notable result is that the *Normalization to Detector* condition equalized the calibration slopes amongst the different salt types to the greatest degree. This suggests that normalizing to the range of the detector most effectively corrected for the influence of the matrix on the N emission, producing a N signal that is consistently proportional to the N content, regardless of the salt type.

*5.4.1.1.3 Line Stability*

Once the characteristic lines were filtered to only those that are consistently sensitive to N content across a range of concentrations, we assessed the stability/repeatability of each line. We calculated the relative standard deviation (%RSD) of the peak areas measured across the five replicate line scans of each sample. Where,

$$\text{RSD} = \frac{\sigma}{\mu} \text{ x } 100\%$$

and $\sigma$ and $\mu$ are the standard deviation and the mean of the peak areas computed from each of the five accumulated spectra from each pellet, respectively. Higher %RSD values indicate a greater degree of spot-to-spot signal fluctuation (instability), and vice versa.

Table 5.4 lists the %RSD values for each of the four lines, averaged from all samples in the nitrate suite (excluding the end-member samples). Values for both normalized and unnormalized data are provided. The values range from 12.0 - 23.9 % which is within the range of %RSD values previously reported from LIBS measurements of minor elements [65,66]. A Mann–Whitney U test reveals no significant difference ($p > 0.05$) in the emission stability of N between the normalized and unnormalized spectra. This holds true for all three tested normalization approaches and all four tested emission lines.

| | 744.2 | 746.8 | 821.6 | 868.0 | Average |
|---|---|---|---|---|---|
| Unnormalized Data | 12.5 | 18.8 | 23.4 | 14.6 | 17.3 |
| Normalized to He | 12.0 | 19.2 | 23.9 | 17.2 | 18.1 |
| Normalized to Total | 13.5 | 18.7 | 23.4 | 18.5 | 18.5 |
| Normalized to Detector | 12.0 | 17.9 | 22.5 | 14.7 | 16.8 |
| Average | 12.5 | 18.6 | 23.3 | 16.2 | |

*Table 5.4: %RSD of selected peaks, separated by normalization treatment.*

*Values are an average of all the %RSDs compiled for the complete nitrate suite (excluding the salt end-members), thereby representing the emission variability of these lines across a range of nitrate salt sources.*

#### *5.4.1.2 Developing Quantitative Models*

Several calibration approaches have been investigated to translate LIBS spectra into quantitative element abundances, which can broadly be categorized as univariate and multivariate approaches (e.g., [58,67–70]). Using the largest suite of LIBS rock spectra ever assembled, Dyar et al. (2016) [71], conclusively demonstrated that multivariate algorithms almost universally outperform univariate analyses for geological applications. Our work therefore seeks to optimize key multivariate modeling parameters for accurate N quantification.

Of the multivariate algorithms described in the literature, partial least squares (PLS) regression models are, by far, the most common technique applied to spectra of geological samples [71] and are the focus of this investigation. Briefly, a PLS regression model is a mathematical equation that describes the fundamental relations between two matrices (X and Y) and therefore allows a user to predict a response, Y, for a given matrix of predictors, X [72]. In the LIBS application, the X matrix is comprised of the measured LIBS data and the Y matrix is populated with reference elemental compositions.

For our work, initial PLS development was conducted only on the spectra acquired from the nitrate sample suite, for the same reasons described in section 5.4.1.1.2. These initial models were designed to optimize the input parameters for predicting N across a range of concentrations and with variable cations in the nitrate/regolith matrix. As a final, additional step to assess the capacity for extrapolation, the best performing model calibrated on the nitrate sample suite was used to predict the N content of the leached and saturated $NH_4^+$-bearing clay samples, which were treated as “unknowns” (see section 5.4.3).

We trialed three PLS permutations with different input parameters:

1) Full Spectrum Model: X matrix consisted of the entire spectral range (186–1042 nm).
2) Single-Line Models: X matrix consists of the spectral data from only one N peak. Here, a spectral range was defined around each peak (the summation window in Figure 5.2) and linear baseline subtraction was applied. Then, the X matrix was populated with the individual intensity values measured across the spectral range. Separate Single-Line Models were built using spectral ranges from each peak meeting the cumulative criteria for quantification (Section 5.4.1.1.2).
3) Multi-Line Models: X matrix consists of the spectral data from multiple N peaks. This model uses the same intensity values used in model permutation 2, but the spectral ranges of each peak are concatenated into a single X matrix.

All models were developed using Aspen Unscrambler™ with the kernel PLS algorithm. Data from the complete nitrate sample suite were included in each model (*i.e.*, models were not made separately for each salt type). This allowed us to assess whether the models were robust to cationic variations in salt composition and likely to be generalizable to nitrate salts not included in the study.

*5.4.1.2.1 Validation*

Models were validated using K-fold cross validation. With K-fold cross validation, the same samples are used both for model estimation and testing. A selection of samples (a "fold") were withheld and the model is calibrated on the remaining data points. The values of the held-out samples are then predicted using the working model and the prediction errors (residuals) are computed. The process is repeated, this time with a different fold of samples held out, and repeated again until every fold has been held out and predicted once. The prediction residuals from each iteration are then combined to compute the overall error, classically expressed as the square root of the average sum of squared errors – called the Root Mean Square Error (RMSE) of cross validation.

Here, we applied a *categorical* K-fold cross validation in which each fold contained the complete mixture series of a given salt (five folds for five different types of salts: Ca-, Na-, Fe-, Mg-, and K-nitrate). In other words, the model was trained to recognize N emission from four types of salt, variably mixed with regolith, and then used to predict the N content in the samples containing

the remaining ('unknown') salt type. By iteratively training and testing the model on the different salt series, the resultant RMSE provides an estimate of how robust the model is to predicting N from nitrate salt types that are not included in this study. It may be difficult to predict the cationic composition of a Martian nitrate salt *a priori*, thus a calibration algorithm should by optimized such that it minimizes the prediction error across various salt types.

*5.4.1.2.2 Figures of Merit*

Two figures of merit are used here to compare the performance of the tested model permutations. $R^2$ is a statistic that describes how well the data are fit by the regression model, where a perfect prediction would have an $R^2$ of 1. It does not, however, indicate the accuracy of the regression model. Thus, to evaluate accuracy, we consider the RMSE. The lower the RMSE, the lower the error on the predictions achieved by the model. The RMSE has the benefit of being reported in the same units as the dependent variable. In this project, we normalize the RMSE by dividing it by the mean concentration of N in our samples, multiplied by 100. This converts the RMSE to a percentage error which facilitates comparisons between datasets or models with different scales, allowing our work to be compared with future studies that make use of different sample sets.

### 5.4.2 Evaluating the Performance of the PLS Models: Insights into an Optimal Quantitative N Protocol

The Full Spectrum Model (model permutation 1) was built to establish a baseline. This model is the simplest case for quantification as it requires no spectral feature selection. However, it was also expected to have the highest error and be the least robust due to influence from the many other peaks in the spectra, most of which are dramatically more intense than N. Models were built separately on unnormalized spectra, and spectra pre-treated with the *Normalized to Total* and *Normalized to He* conditions (we did not use the spectra treated with the *Normalized to Detector* condition as this is not a full-spectrum normalization approach).

All these models were unsuccessful. A review of the PLS regression coefficients and variable loadings (not shown) demonstrated that the most influential variables driving the PLS predictions corresponded to emission lines from the matrix material, such as Si, Al, Mg, Ca, Na, and K. These findings highlight the deficiency of the Full Spectrum Models in providing the necessary specificity for N quantification.

To force the models to focus on the emission trends encoded in the subtly varying N lines, permutations #2 and #3 adopt a targeted approach, exclusively using the wavelength positions

validated to be sensitive to N. These permutations explore single- and multi-line calibration strategies, respectively. We repeated each Single- and Multi-Line Model on every normalized dataset, including the unnormalized data as a control, to investigate the influence of various normalizations on prediction accuracy. In addition, for each strategy, two sets of models were developed: one using the full nitrate sample suite, and the other using the restricted sample set that excluded the pure salt end-members. The rationale behind this dual construction lies in of distinct behavior in the normalized spectra of pure end-member samples compared to those mixed with MGS-1, attributed to matrix dissimilarity (Figure 5.3). Hence, a comprehensive investigation into the influence of training with limited versus broad compositional ranges was undertaken to assess its impact on the model's performance and predictive capabilities.

The exclusion of pure end-member samples yielded improvement in both prediction accuracy and regression fit for every repeated model permutation, regardless of the tested normalization (Appendix C, Figure S4). This finding aligns with the observations reported by Anderson et al. (2017) [73], who established that regression models trained across very different geological matrices are often inaccurate because the LIBS emission intensity of an element is influenced not only by the abundance of that element, but also by the nature of the matrix and co-existing elements. These authors demonstrated that regression models trained on a restricted range of compositions with comparable emission line behavior can significantly improve performance within the training range. Consequently, we focused our subsequent parameter optimization investigation on the suite of models using the restricted compositional range. The performance outcomes of these models compared graphically in Figure 5.4, permitting several insights to be drawn.

Firstly, we observe that normalization exerts a strong control on overall model quality. The normalized models universally exhibit superior figures of merit relative to their unnormalized counterparts. The greatest degree of improvement overall is observed in the series of models utilizing data preprocessed with the *Normalization to Detector* condition, corroborating our previous observation that this approach most effectively standardized the magnitude of the N peak areas between the sample series. Interestingly, none of the normalization methods resulted in a statistically significant change in the emission stability (%RSD) of any of the four N lines we tested (at a 95% confidence interval), indicating that normalization does not grant significant advantages in terms of the emission repeatability. The performance improvement associated with

normalization is thus taken to reflect each method's capacity to standardize the N emission behaviour in different matrices (salt types), thereby producing a N signal that is consistently proportional to the N content. As above, we focus our exploration of additional parameter optimization on this subset of models normalized to the range of the detector.

Secondly, by comparing the figures of merit for each Single-Line Model within this optimal normalization framework, we can evaluate the relative efficacy of each tested N line for quantification. We find that the figures of merit are primarily influenced by the extent of spectral interference experienced by the respective N lines. For instance, the 821.6 nm N line suffers substantial interference from a bright Na peak at 819.5 nm (Figure 5.2), resulting in the poorest relative figures of merit (NRMSE = 13.7% and $R^2$ = 0.93) among the tested Single-Line Models (Figure 5.4). This poor modeling outcome persisted despite the fact that the N peak was consistently detectable above the tail of the interfering Na peak and despite the tight linear baseline subtraction envelope designed to minimize Na influence (Figure 5.2). In comparison, the 868.0 nm N line suffers the least interference from other emissions features in the spectrum (Figure 5.2) yielding the best figures of merit (NRMSE = 9.0% and $R^2$ = 0.97) among the tested Single-Line Models. Notably, the 868.0 nm line does not exhibit the most stable emission behaviour of the four N lines tested here, suggesting that the performance of the Single-Line Models is more significantly influenced by the absence of spectral interference than the stability of the emission lines.

Thirdly, Figure 5.4 illustrates that the best overall performance is achieved by the Multi-Line Model (implemented in the *Normalization to Detector* condition), which yielded the lowest NRMSE (8.4%) and highest $R^2$ (0.98). The regression coefficients and loadings of this model reveal that emission in the 868.0 nm range played the most influential role as regressors. This is consistent with the relative performance of the associated Single-Line Models. However, the superior performance of the Multi-Line Model highlights the synergistic effect of combining discrete spectral ranges, resulting in an input object with predictive power that surpasses the sum of its individual parts.

As a final evaluation of PLS model optimization, we re-ran this optimal Multi-Line Model using the same spectral ranges, but without prior baseline correction for the LIBS peaks. The objective for this test was to assess the impact of baseline correction on prediction accuracy and determine

if this pre-processing step was necessary. This model iteration (not shown) performed dramatically worse than the Multi-Line Model with the baseline correction applied, producing an increase in NMRSE from 8.4% to 20.2% and a decrease of $R^2$ from 0.98 to 0.87. We suspect that this decline in performance is due to the introduction of irrelevant latent chemical information about the matrix that is encoded into the magnitude of the baseline and is uncorrelated to N content. Indeed, previous research has indicated that the LIBS baseline signal is influenced by the bulk composition of the target material, with certain elements (e.g., Mg) contributing disproportionately to the baseline shape [74,75]. The magnitude of the increase in NRMSE by simply not removing the baseline demonstrates how critical this pre-processing step is in accurately modeling subtle N variations.

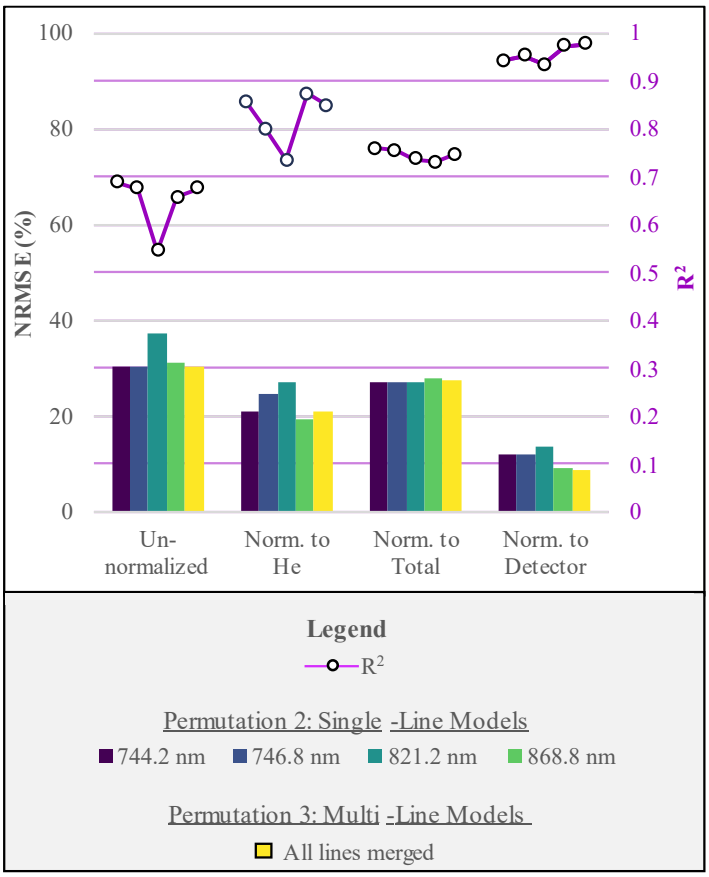


*Figure 5.4: Figures of merit for Single-Line and Multi-Line PLS models.*

*Figure depicts data from the restricted nitrate suite after the exclusion of end-member salt samples (See text for details; a comparison with the full nitrate sample suite is available in the SI file). Bars are shaded according to the model permutation (Single-Line versus Multi-Line). Each model permutation was repeated for each normalized ("Norm.") dataset, including the unnormalized data as a control, permitting an evaluation of the relative influence of normalization on model performance. Note that the normalized datasets universally achieve lower prediction error (NRMSE) and improved model fit ($R^2$), with* Normalization to Detector *achieving the best overall figures of merit.*

### 5.4.3 Evaluating the Predictive Accuracy in Samples with a Dissimilar Matrix: N in Ammoniated Clays

The last step in our quantification exercise was to extrapolate the best performing model, trained on the nitrate suite, to predict the N content in the ammoniated clay samples (saturated and leached conditions). Figure 5.5 illustrates the result of this exercise by plotting the N content predicted by the model against the true N content, as validated by Activation Laboratories Ltd.

The predicted values consistently plot below the regression line of the calibrated model and the identity line. This suggests that our best performing nitrate-N model is biased towards

consistently underestimating the ammonium-N in the clay matrices. The resulting NRMSE value of 29.9% signifies a substantial increase in uncertainty compared to the cross-validated results obtained from the nitrate samples (8.4%). Furthermore, the linear best-fit line of the predicted samples exhibits a distinct slope (m = 0.67) that deviates from the regression line of the calibration model (m = 0.97). This discrepancy in slope highlights that the under-prediction is not solely attributed to a linear offset and underscores the inadequate fit of the regression model to the predicted data. These findings emphasize the challenges and limitations associated with extending the applicability of the nitrate-N model to ammoniated clay samples.

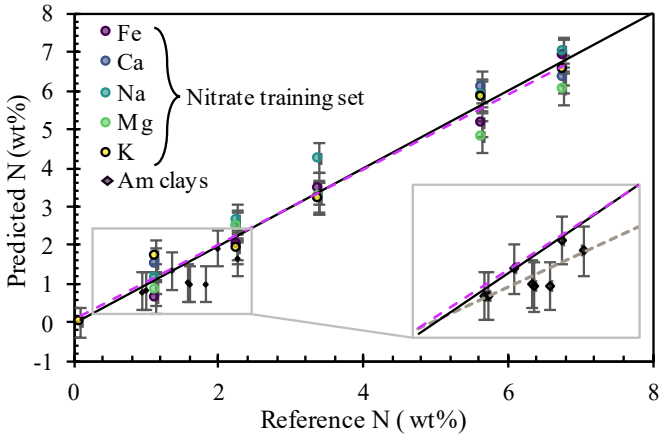


*Figure 5.5: PLS prediction model: reference N versus predicted N.*

*The calibration model is optimized nitrate-N Multi-Line PLS model normalized to the range of the detector. Calibration data are depicted in coloured dots (the model ingested data from all the nitrate salt types simultaneously, however they are shaded distinctly in the plot to highlight that the model does not consistently over- or under-predict N based on the cationic constituent, suggesting that the model is robust to variable nitrate salt types). The calibration regression line is depicted as a purple dashed line, with the identity line in black. Grey diamonds depict the predicted N content of the ammoniated clay samples. The inset highlights the predicted N content of the ammoniated-clay samples and the regression line of the predictions (grey dotted line). Vertical error bars are the NRMSE.*

## 5.5 DISCUSSION: STRATEGIES FOR N DETECTION AND QUANTIFICATION ON MARS

Enabling the detection of N with LIBS on Mars is the ultimate goal of this work. However, developing quantitative calibration curves for use on Mars is beyond the scope of this project as it requires further investigation of laboratory-to-Mars instrument differences, the impact of sample distance, and the influence of the Martian atmosphere on the nature of LIBS N emission.

Our focus here is instead on elucidating the *strategies* that improve the identification and quantification of N in Mars-relevant materials, thereby laying the foundation for these next steps. Many of our findings are independent of the acquisition conditions and may be reasonably extrapolated beyond our terrestrial laboratory study to planetary LIBS investigations.

### 5.5.1 LIBS is a Promising Technique for N Detection in Mars-relevant Matrices

The novelty of our works lies in the explicit investigation of inorganic LIBS N emission from high-fidelity Mars-analogue geologic samples. The 20 spectroscopic lines reported in Table 5.3 represent the subset of theoretical N emission lines that are consistently detectable across a range of nitrate salts – the primary inorganic N phase expected to be sequestered on Mars [7]. When mixed with Mars Global Simulant (MGS-1), the spectra become much more complicated, posing challenges for the detection of N emission lines, and increasing the likelihood of non-detection due to spectral interference. Nevertheless, 17 characteristic N lines could clearly be detected in the samples that incorporated the MGS-1 simulant at 30 wt.% $NO_3^-$, with certain emission lines providing detection limits down to the 5 wt.% level.

It is important here to note the differences between our observations and previous investigations of LIBS N emission for Mars applications. We do not detect any of the fifteen N emission lines reported in the *Laser Induced Breakdown Spectroscopy Library for the Martian Environment* [76] (later incorporated into the *ChemCam Quick Element Search Tool* (C-QuEST)). These N signals were acquired through the ablation of pure metal targets (e.g., sheets of titanium, iron, or manganese with >99.98% purity), whereby the N emission originated from the breakdown of the $N_2$ present in the buffer gas of the sample chamber [76]. Consequently, the N lines reported in the *Laser Induced Breakdown Spectroscopy Library for the Martian Environment* were obtained from a gaseous source, rather than mineral-bound N, and were not subject to the myriad spectral interferences encountered in heterogenous geologic samples. Hence, they are less representative of the emission environment that will be encountered during in situ LIBS surveys on Mars.

We also do not detect the theoretical N (II) line at 500.5 nm reported by Dequaire et al. (2017) [46] during the study of N-bearing organic molecules within lab-synthesized nontronite. Although the nontronite matrix synthesized by Dequaire et al. [46] is an appropriate mineralogical analogue for Mars, it is a pure phase. The absence of accessory minerals that commonly co-occur with Martian clay minerals and the lack of mineral impurities in the synthetic product limited the assessment of possible spectral interferences associated with the N

emission. Most notably, titanium (Ti) produces a cluster of emission lines between ~498–504 nm that interfere with the N (II) line at 500.5 nm [39]. Previous work by Harris et al. [39] demonstrated that it is not possible to construct an accurate N calibration curve in this spectral region when Ti is present due to the overlapping emission features. Considering that $TiO_2$ is a ubiquitous component of the bulk Martian crust [77] and is distributed globally within Mars' ubiquitous eolian dust [78], this interference will likely pose a problem during in situ LIBS analyses on Mars. Furthermore, the emission line at 500.5 nm was not detected even in samples of pure nitrate salt, indicating that it is not a strong emission line in our samples. Based on these findings, we recommend against using the 500.5 nm N line for in situ surveys on Mars.

Lastly, although the theoretical N (I) emission feature at 742.4 nm is regularly reported by other workers as a reliable indicator of N [39,79–83] (especially because it forms an easily recognizable triplet pattern with the 744.2 and 746.8 nm peaks), we found that emission from silicon (Si) at 742.5 nm interferes with this N line. Given the resolution of our spectrometer, it was not possible to fully distinguish these two peaks in samples containing Si (present in both MGS-1 and the clay matrices) and we could not generate a linear N calibration curve using the peak observed at 742.4 nm. As with the Ti scenario described above, spectral interference with Si is expected to be problematic during in situ analyses on Mars because $SiO_2$ is a major component of the Martian crust [77]. Importantly, the spectral resolution of the planetary LIBS spectrometers currently operational on Mars are also insufficient to resolve these two lines (0.45 nm spectral resolution for MarSCoDe [84], 0.65 nm resolution for these wavelengths on ChemCam and SuperCam [43,85]). We therefore do not consider the 742.4 nm N line to be suitable for N detection in siliceous matrices and do not list it in Table 5.3.

In summary, our study demonstrates that clear detection of N against a basaltic background is possible with LIBS and provides critical insights into potential spectral interferences and/or limitations of certain emission lines. Table 5.3 may therefore be considered as a fundamental resource for the successful implementation of LIBS for mineral-bound N detection during ongoing and future planetary exploration missions.

### 5.5.2 Feasibility of N Quantification

Although multivariate algorithms that use information contained in the entire LIBS spectrum have been shown to perform well for major element quantification [58,73], we find that they are insufficient in discerning the subtle variation of weak N lines in Mars-like geological samples.

This necessitates spectral feature extraction during the preprocessing phase. Our assessment revealed that four characteristic N lines exhibit high sensitivity to N concentration within Mars-relevant materials (744.2, 746.8, 821.6, and 868.0 nm) and we recommend these as candidate lines for constructing Martian models.

We note that our minimum detection limit (5 wt.% $NO_3^-$) exceeds the quantity of $NO_3^-$ detected in Martian materials to date (0.48 ± 0.006 wt.% $NO_3^-$ measured in Mars meteorite EETA79001 [31]). However, it has previously been reported that the reduced pressure condition of Mars facilitates much brighter LIBS plasmas, with more intense emission and correspondingly stronger signals than those observed under terrestrial conditions [63,86,87]. Our study should therefore be considered as a conservative demonstration of LIBS N detectability. Lower N concentrations may yield a resolvable signal under Mars conditions and this possibility deserves further investigation. Of course, the lower pressure conditions of Mars will also intensify signals from co-occurring and potentially interfering elements from the matrix. However, with the exception of the N emission peak at 821.6 nm which lies on the shoulder of a bright Na peak, the N lines discussed here are relatively free of interfering spectral features and are expected to remain as robust markers of N under Mars conditions.

The peak centered at 868.0 nm was the most effective regressor for N predictions (in both Single-Line and Multi-Line Models) because it suffered the least spectral interference from other elements. Unfortunately, the 868.0 nm line is beyond the range of the planetary LIBS instruments currently operational on Mars, which only acquire LIBS emission up to 850 nm. The peak centered at 746.8 nm offered the next best performance (in the Single-Line Model suite) and is within the observational range of current rovers. This therefore represents an immediately relevant emission feature with which to search for N on Mars using currently available technology. Nevertheless, we recommend that future Mars exploration missions consider an expanded LIBS range that encompasses the 868.0 nm region to optimize N detectability and quantification.

We also recommend that baseline correction and normalization be included in any future N quantification pipeline. Our findings unequivocally demonstrate that both of these techniques significantly enhanced the model's performance, making them crucial for accurate and reliable N content predictions. However, we acknowledge that the operational conditions and hardware of

planetary LIBS instruments will differ from those tested here. Consequently, although we suspect that the advantages of baseline subtraction are generalizable, we refrain from asserting the objective superiority of any specific normalization scheme. Our experiments show that normalization to the range of the detector worked best for our setup, but different conditions may yield different results. Instead, our results should be taken as a demonstration that the thoughtful selection of a normalization procedure, after experimentation, can enhance the accuracy and reliability of N quantification in LIBS analyses. We encourage analysts to thoroughly compare different normalization methods when operating under different conditions and emphasize that both calibration curves and PLS figures of merit can be used to rigorously determine the optimal normalization approach.

Regarding the generalization of the model, we observed that our best performing nitrate-trained model did not perform well when extrapolated to predict ammonium-derived N content in the clay sample suite. While our optimized model excelled with distinctive nitrate salts, its generalizability to all N-bearing geological samples remains limited. Our methodology does not allow us to distinguish the relative impact of the dissimilar matrices (basaltic regolith versus clay minerals) from the impact of dissimilar N sources ($NO_3^-$ versus $NH_4^+$), but our findings are consistent with previous reports that prediction accuracy declines when a regression model is extrapolated beyond the compositional range of its calibration set [88].

Future work should therefore focus on developing a diverse training set of N-bearing samples, encompassing the ranges and phases expected to be encountered on Mars. Given the limited number of N sequestration mechanisms predicted for Mars (*i.e.*, the stabilization of $NO_3^-$ and/or $NO_2^-$ by regolith cations, the binding of $NH_4^+$ on/in clays, and/or the burial of nitrogenous organic matter [7]), it is reasonable to envision the creation of a compositionally comprehensive N calibration set for Mars applications. However, both our own findings, and those of Anderson et al. [73], suggest that improved accuracy is achieved when PLS models are trained on samples with a restricted compositional range, and whose spectral line intensities respond similarly to changes in composition. Therefore, we recommend that a larger calibration set be used to develop *sub-models* optimized for specific N occurrences (e.g., nitrates dispersed in sedimentary rocks or ammoniated clays), rather than one comprehensive and generalizable model. During rover operations, contextual information from cameras (e.g., grain size), as well as chemical and mineralogical information from complementary instruments could help select the most

appropriate sub-model. For instance, sedimentary rock/regolith compositions, and even specific clay minerals, may be identified by CheMin on the *Curiosity* rover [89] or by SuperCam on the *Perseverance* rover [52,90], or may be inferred through appropriate weathering proxies [91]. In addition, Hurowitz et al. (2017) [92] demonstrated that a combination of in situ mineralogy, geochemistry, textural properties, and stratigraphic relationships can be used to elucidate paleo-redox conditions, which could be helpful in predicting whether nitrogenous phases will be oxidized or reduced and selecting an appropriate sub-model.

## 5.6 CONCLUSIONS

We investigated the nature of inorganic LIBS N emission from high-fidelity Mars-analogue samples. Our work revealed 20 characteristic N emission lines that are reliably detectable in pure nitrate salt phases, including 17 lines that are detectable when salts are dispersed within a basaltic matrix. For accurate quantification of N in geological materials, we found that multivariate calibration algorithms generated from the entire LIBS spectrum lack the necessary specificity to capture N emission amidst the multitude of high-intensity lines from major rock-forming elements. Consequently, we recommend employing spectral feature extraction to focus the model on stable N emission features and enhance accuracy. Specifically, four emission lines (744.2, 746.8, 821.6, and 868.0 nm) demonstrated sufficiently high sensitivity to N concentration to produce robust calibration models. The simultaneous use of all four lines exhibited the best performance.

We also find that quantification accuracy is optimized by implementing baseline correction, experimentally validated normalization techniques, and restricting the calibration range to samples whose N line intensities respond similarly to changes in composition. This latter optimization yields improved performance within the restricted training range, but poor generalizability. Future work should be dedicated to developing a more comprehensive training set to encompass the range of N concentrations and phases expected to be encountered on Mars and facilitate the generation of suitably targeted sub-models.

In summary, our investigation demonstrates that LIBS holds promise as a tool for mapping astrobiologically important N in Martian surface materials, despite its weak emission characteristics. The rapid survey capabilities of LIBS provide it with the capacity to significantly

advance our understanding of N distribution on Mars and our quest to decipher the planet's geological, and potentially biological, past.

## 5.7 CONFLICT OF INTEREST

We have no conflicts of interest to disclose.

## 5.8 ACKNOWLEDGEMENTS

We acknowledge the support of the Canadian Space Agency (CSA) [21EXPCOI1] and the Natural Sciences and Engineering Research Council of Canada (NSERC).

E.F.G thanks the SuperCam team for thoughtful comments, discussion, and ideas during the conceptualization and modeling stages, with special thanks to Dr. David Vogt, Dr. Sam Clegg, Dr. Roger Wiens, and Dr. Ann Ollila. E.F.G also thanks the staff at Applied Spectra Inc. and Aspen Unscrambler for their exceptional customer support and personalized software troubleshooting.

## 5.9 REFERENCES


[1] J.L. Vago, F. Westall, A.J. Coates, R. Jaumann, O. Korablev, V. Ciarletti, I. Mitrofanov, J.L. Josset, M.C. De Sanctis, J.P. Bibring, F. Rull, F. Goesmann, H. Steininger, W. Goetz, W. Brinckerhoff, C. Szopa, F. Raulin, H.G.M. Edwards, L.G. Whyte, A.G. Fairén, J. Bridges, E. Hauber, G.G. Ori, S. Werner, D. Loizeau, R.O. Kuzmin, R.M.E. Williams, J. Flahaut, F. Forget, D. Rodionov, H. Svedhem, E. Sefton-Nash, G. Kminek, L. Lorenzoni, L. Joudrier, V. Mikhailov, A. Zashchirinskiy, S. Alexashkin, F. Calantropio, A. Merlo, P. Poulakis, O. Witasse, O. Bayle, S. Bayón, U. Meierhenrich, J. Carter, J.M. García-Ruiz, P. Baglioni, A. Haldemann, A.J. Ball, A. Debus, R. Lindner, F. Haessig, D. Monteiro, R. Trautner, C. Voland, P. Rebeyre, D. Goulty, F. Didot, S. Durrant, E. Zekri, D. Koschny, A. Toni, G. Visentin, M. Zwick, M. Van Winnendael, M. Azkarate, C. Carreau, Habitability on Early Mars and the Search for Biosignatures with the ExoMars Rover, Astrobiology. 17 (2017) 471–510. https://doi.org/10.1089/ast.2016.1533.

[2] J.P. Grotzinger, J. Crisp, A.R. Vasavada, R.C. Anderson, C.J. Baker, R. Barry, D.F. Blake, P. Conrad, K.S. Edgett, B. Ferdowski, Mars Science Laboratory mission and science investigation, Space Sci Rev. 170 (2012) 5–56.

[3] K.A. Farley, K.H. Williford, K.M. Stack, R. Bhartia, A. Chen, M. de la Torre, K. Hand, Y. Goreva, C.D.K. Herd, R. Hueso, Mars 2020 mission overview, Space Sci Rev. 216 (2020) 1–41.

[4] C.S. Cockell, Trajectories of martian habitability, Astrobiology. 14 (2014) 182–203. https://doi.org/10.1089/ast.2013.1106.

[5] F. Westall, D. Loizeau, F. Foucher, N. Bost, M. Betrand, J. Vago, G. Kminek, Habitability on mars from a microbial point of view, Astrobiology. 13 (2013) 887–897. https://doi.org/10.1089/ast.2013.1000.

[6] Space Studies Board and National Research Council, An Astrobiology Strategy for the Exploration of Mars, National Academies Press, Washington, DC, 2007.

[7] R.L. Mancinelli, A. Banin, Where is the nitrogen on Mars?, Int J Astrobiol. 2 (2003) 217–225. https://doi.org/10.1017/S1473550403001599.

[8] C. Nelson, Lehninger's principles of biochemistry, 2013.

[9] D.G. Capone, R. Popa, B. Flood, K.H. Nealson, Follow the nitrogen, Science (1979). 312 (2006) 708–709. https://doi.org/10.1126/science.1111863.

[10] T. Hoehler, W. Bains, A. Davila, M. Parenteau, A. Pohorille, Life's requirements, habitability, and biological potential, Planet. Astrobiol. 13 (2020) 37.

[11] D.P. Summers, The Prebiotic Chemistry of Nitrogen and the Origin of Life, in: J. Seckbach (Ed.), Genesis - In The Beginning | Precursors of Life, Chemical Models and Early Biological Evolution, Springer, Dordrecht, 2012: pp. 201–216. https://doi.org/10.1007/978-94-007-2941-4.

[12] R.W. Howarth, R. Marino, Nitrogen as the limiting nutrient for eutrophication in coastal marine ecosystems: evolving views over three decades, Limnol Oceanogr. 51 (2006) 364–376.

[13] A.J. Bloom, Nitrogen as a Limiting Factor: Crop Acquisition of Ammonium and Nitrate, Ecology in Agriculture. 145 (1997).

[14] S.W. Nixon, C.A. Oviatt, J. Frithsen, B. Sullivan, Nutrients and the productivity of estuarine and coastal marine ecosystems, Journal of the Limnological Society of Southern Africa. 12 (1986) 43–71.

[15] M.G. Trainer, M.H. Wong, T.H. McConnochie, H.B. Franz, S.K. Atreya, P.G. Conrad, F. Lefèvre, P.R. Mahaffy, C.A. Malespin, H.L.K. Manning, Seasonal variations in atmospheric composition as measured in Gale Crater, Mars, J Geophys Res Planets. 124 (2019) 3000–3024.

[16] P.R. Mahaffy, C.R. Webster, S.K. Atreya, H. Franz, M. Wong, P.G. Conrad, D. Harpold, J.J. Jones, L.A. Leshin, H. Manning, Abundance and isotopic composition of gases in the Martian atmosphere from the Curiosity rover, Science (1979). 341 (2013) 263–266.

[17] T. Owen, K. Biemann, D.R. Rushneck, J.E. Biller, D.W. Howarth, A.L. Lafleur, The composition of the atmosphere at the surface of Mars, J Geophys Res. 82 (1977) 4635–4639.

[18] C.P. McKay, C.R. Stoker, The early environment and its evolution on Mars: Implications for life, Reviews of Geophysics. 27 (1989) 189–214. https://doi.org/10.1029/RG027i002p00189.

[19] C. V. Manning, C.P. McKay, K.J. Zahnle, The nitrogen cycle on Mars: Impact decomposition of near-surface nitrates as a source for a nitrogen steady state, Icarus. 197 (2008) 60–64. https://doi.org/10.1016/j.icarus.2008.04.015.

[20] C. V. Manning, K.J. Zahnle, C.P. McKay, Impact processing of nitrogen on early Mars, Icarus. 199 (2009) 273–285. https://doi.org/10.1016/j.icarus.2008.10.015.

[21] M.L. Smith, M.W. Claire, D.C. Catling, K.J. Zahnle, The formation of sulfate, nitrate and perchlorate salts in the martian atmosphere, Icarus. 231 (2014) 51–64. https://doi.org/10.1016/j.icarus.2013.11.031.

[22] R. Hu, T.B. Thomas, A nitrogen-rich atmosphere on ancient Mars consistent with isotopic evolution models, Nat Geosci. 15 (2022) 106–111. https://doi.org/10.1038/s41561-021-00886-y.

[23] B.M. Jakosky, R.O. Pepin, R.E. Johnson, J.L. Fox, Mars atmospheric loss and isotopic fractionation by solar-wind-induced sputtering and photochemical escape, Icarus. 111 (1994) 271–288.

[24] H.J. Melosh, A.M. Vickery, Impact erosion of the primordial atmosphere of Mars, Nature. 338 (1989) 487–489.

[25] P. Von Paris, J.L. Grenfell, H. Rauer, J.W. Stock, N2-associated surface warming on early Mars, Planet Space Sci. 82–83 (2013) 149–154. https://doi.org/10.1016/j.pss.2013.04.009.

[26] D.P. Summers, B. Khare, Nitrogen fixation on early Mars and other terrestrial planets: Experimental demonstration of abiotic fixation reactions to nitrite and nitrate, Astrobiology. 7 (2007) 333–341. https://doi.org/10.1089/ast.2006.0032.

[27] A. Segura, R. Navarro-González, Nitrogen fixation on early Mars by volcanic lightning and other sources, Geophys Res Lett. 32 (2005) 1–4. https://doi.org/10.1029/2004GL021910.

[28] D.P. Summers, R.C.B. Basa, B. Khare, D. Rodoni, Abiotic nitrogen fixation on terrestrial planets: Reduction of NO to ammonia by FeS, Astrobiology. 12 (2012) 107–114. https://doi.org/10.1089/ast.2011.0646.

[29] R. Navarro-González, K.F. Navarro, P. Coll, C.P. McKay, J.C. Stern, B. Sutter, P.D. Archer, A. Buch, M. Cabane, P.G. Conrad, J.L. Eigenbrode, H.B. Franz, C. Freissinet, D.P. Glavin, J. V. Hogancamp, A.C. McAdam, C.A. Malespin, F.J. Martín-Torres, D.W. Ming, R. V. Morris, B. Prats, F. Raulin, J.A. Rodríguez-Manfredi, C. Szopa, M.P. Zorzano-Mier, P.R. Mahaffy, S. Atreya, M.G. Trainer, A.R. Vasavada, Abiotic Input of Fixed Nitrogen by Bolide Impacts to Gale Crater During the Hesperian: Insights From the Mars Science Laboratory, J Geophys Res Planets. 124 (2019) 94–113. https://doi.org/10.1029/2018JE005852.

[30] J.L. Bishop, A. Banin, R.L. Mancinelli, M.R. Klovstad, Detection of soluble and fixed NH4+ in clay minerals by DTA and IR reflectance spectroscopy: A potential tool for planetary surface exploration, Planet Space Sci. 50 (2002) 11–19. https://doi.org/10.1016/S0032-0633(01)00077-0.

[31] S.P. Kounaves, B.L. Carrier, G.D. O'Neil, S.T. Stroble, M.W. Claire, Evidence of martian perchlorate, chlorate, and nitrate in Mars meteorite EETA79001: Implications for oxidants and organics, Icarus. 229 (2014) 206–213. https://doi.org/10.1016/j.icarus.2013.11.012.

[32] J.C. Stern, B. Sutter, R. Navarro-González, C.P. Mckay, P.D.A. Jr, A. Buch, A.E. Brunner, J.L. Eigenbrode, A.G. Fairen, H.B. Franz, D.P. Glavin, S. Kashyap, A.C. Mcadam, W. Douglas, A. Steele, C. Szopa, J.J. Wray, F. Javier, M. Zorzano, P.G. Conrad, R. Paul, J.C. Stern, B. Sutter, C. Freissinet, R. Navarro-González, C.P. Mckay, Evidence for indigenous nitrogen in sedimentary and aeolian deposits from the Curiosity rover investigations at Gale crater, Mars, Proc Natl Acad Sci U S A. 112 (2015) E3085. https://doi.org/10.1073/pnas.1507795112.

[33] B. Sutter, J.B. Dalton, S.A. Ewing, R. Amundson, C.P. McKay, Terrestrial analogs for interpretation of infrared spectra from the Martian surface and subsurface: Sulfate, nitrate, carbonate, and phyllosilicate-bearing atacama desert soils, J Geophys Res Biogeosci. 112 (2007) 1–19. https://doi.org/10.1029/2006JG000313.

[34] R.C. Wiens, S. Maurice, ChemCam: Chemostratigraphy by the first mars microprobe, Elements. 11 (2015) 33–38. https://doi.org/10.2113/gselements.11.1.33.

[35] C.C. Bedford, J.C. Bridges, S.P. Schwenzer, R.C. Wiens, E.B. Rampe, J. Frydenvang, P.J. Gasda, Alteration trends and geochemical source region characteristics preserved in the fluviolacustrine sedimentary record of Gale crater , Mars, Geochim Cosmochim Acta. 246 (2019) 234–266. https://doi.org/10.1016/j.gca.2018.11.031.

[36] P.J. Gasda, E.B. Haldeman, R.C. Wiens, W. Rapin, T.F. Bristow, J.C. Bridges, S.P. Schwenzer, B. Clark, K. Herkenhoff, J. Frydenvang, N.L. Lanza, S. Maurice, S. Clegg, D.M. Delapp, V.L. Sanford, M.R. Bodine, R. McInroy, In situ detection of boron by ChemCam on Mars, Geophys Res Lett. 44 (2017) 8739–8748. https://doi.org/10.1002/2017GL074480.

[37] N. Mangold, E. Dehouck, C. Fedo, O. Forni, C. Achilles, T. Bristow, R.T. Downs, J. Frydenvang, O. Gasnault, J. L'Haridon, L. le Deit, S. Maurice, S.M. McLennan, P.Y. Meslin, S. Morrison, H.E. Newsom, E. Rampe, W. Rapin, F. Rivera-Hernandez, M. Salvatore, Chemical

alteration of fine-grained sedimentary rocks at Gale crater, Icarus. 321 (2019) 619–631. https://doi.org/10.1016/j.icarus.2018.11.004.

[38] J. L'Haridon, L. Mangold, N., Meslin, P.Y., Johnson, J.R., Rapin, W., Forni, O., Cousin, A., Payré, V., Dehouck, E., Nachon, M. and Le Deit, Chemical variability in mineralized veins observed by ChemCam on the lower slopes of Mount Sharp in Gale crater Mars, Icarus. 311 (2018) 69–86.

[39] R.D. Harris, D.A. Cremers, M.H. Ebinger, B.K. Bluhm, Determination of nitrogen in sand using laser-induced breakdown spectroscopy, Appl Spectrosc. 58 (2004) 770–775. https://doi.org/10.1366/0003702041389201.

[40] R.C. Wiens, S. Maurice, F.R. Perez, The SuperCam remote sensing instrument suite for the mars 2020 rover: A preview, Spectroscopy (Santa Monica). 32 (2017) 50–55.

[41] X. Wan, C. Li, H. Wang, W. Xu, J. Jia, Y. Xin, Design, Function, and Implementation of China's First LIBS Instrument (MarSCoDe) on the Zhurong Mars Rover, At Spectrosc. 42 (2021). https://doi.org/10.46770/AS.2021.608.

[42] S. Maurice, R.C. Wiens, M. Saccoccio, B. Barraclough, O. Gasnault, O. Forni, N. Mangold, D. Baratoux, S. Bender, G. Berger, J. Bernardin, M. Berthé, N. Bridges, D. Blaney, M. Bouyé, P. Caïs, B. Clark, S. Clegg, A. Cousin, D. Cremers, A. Cros, L. Deflores, C. Derycke, B. Dingler, G. Dromart, B. Dubois, M. Dupieux, E. Durand, L. D'Uston, C. Fabre, B. Faure, A. Gaboriaud, T. Gharsa, K. Herkenhoff, E. Kan, L. Kirkland, D. Kouach, J.L. Lacour, Y. Langevin, J. Lasue, S. le Mouélic, M. Lescure, E. Lewin, D. Limonadi, G. Manhès, P. Mauchien, C. McKay, P.Y. Meslin, Y. Michel, E. Miller, H.E. Newsom, G. Orttner, A. Paillet, L. Parès, Y. Parot, R. Pérez, P. Pinet, F. Poitrasson, B. Quertier, B. Sallé, C. Sotin, V. Sautter, H. Séran, J.J. Simmonds, J.B. Sirven, R. Stiglich, N. Striebig, J.J. Thocaven, M.J. Toplis, D. Vaniman, The ChemCam instrument suite on the Mars Science Laboratory (MSL) rover: Science objectives and mast unit description, Space Sci Rev. 170 (2012) 95–166. https://doi.org/10.1007/s11214-012-9912-2.

[43] R.C. Wiens, S. Maurice, B. Barraclough, M. Saccoccio, W.C. Barkley, J.F. Bell, S. Bender, J. Bernardin, D. Blaney, J. Blank, M. Bouyé, N. Bridges, N. Bultman, P. Caïs, R.C. Clanton, B. Clark, S. Clegg, A. Cousin, D. Cremers, A. Cros, L. Deflores, D. Delapp, R. Dingler, C. D'Uston, M. Darby Dyar, T. Elliott, D. Enemark, C. Fabre, M. Flores, O. Forni, O. Gasnault, T.

Hale, C. Hays, K. Herkenhoff, E. Kan, L. Kirkland, D. Kouach, D. Landis, Y. Langevin, N. Lanza, F. Larocca, J. Lasue, J. Latino, D. Limonadi, C. Lindensmith, C. Little, N. Mangold, G. Manhes, P. Mauchien, C. McKay, E. Miller, J. Mooney, R. v. Morris, L. Morrison, T. Nelson, H. Newsom, A. Ollila, M. Ott, L. Pares, R. Perez, F. Poitrasson, C. Provost, J.W. Reiter, T. Roberts, F. Romero, V. Sautter, S. Salazar, J.J. Simmonds, R. Stiglich, S. Storms, N. Striebig, J.J. Thocaven, T. Trujillo, M. Ulibarri, D. Vaniman, N. Warner, R. Waterbury, R. Whitaker, J. Witt, B. Wong-Swanson, The ChemCam instrument suite on the Mars Science Laboratory (MSL) rover: Body unit and combined system tests, Space Sci Rev. 170 (2012) 167–227. https://doi.org/10.1007/s11214-012-9902-4.

[44] D.W. Hahn, N. Omenetto, Laser-induced breakdown spectroscopy (LIBS), part II: Review of instrumental and methodological approaches to material analysis and applications to different fields, Appl Spectrosc. 66 (2012) 347–419. https://doi.org/10.1366/11-06574.

[45] T. Delgado, L. García-Gómez, L.M. Cabalín, J.J. Laserna, Detectability and discrimination of biomarker organic precursors in a low pressure CO2 atmosphere by LIBS, J Anal At Spectrom. 35 (2020) 1947–1955. https://doi.org/10.1039/d0ja00167h.

[46] T. Dequaire, P.Y. Meslin, P. Beck, M. Jaber, A. Cousin, W. Rapin, J. Lasne, O. Gasnault, S. Maurice, A. Buch, C. Szopa, P. Coll, Analysis of carbon and nitrogen signatures with laser-induced breakdown spectroscopy; the quest for organics under Mars-like conditions, Spectrochim Acta Part B At Spectrosc. 131 (2017) 8–17. https://doi.org/10.1016/j.sab.2017.02.015.

[47] K.M. Cannon, D.T. Britt, T.M. Smith, R.F. Fritsche, D. Batcheldor, Mars global simulant MGS-1: A Rocknest-based open standard for basaltic martian regolith simulants, Icarus. 317 (2019) 470–478. https://doi.org/10.1016/j.icarus.2018.08.019.

[48] G.E. Ericksen, The Chilean nitrate deposits, Am Sci. 71 (1983) 366–374.

[49] I. Bowman, R.A.F. Penrose, The Nitrate Deposits of Chile, Bulletin of the American Geographical Society. 42 (1910) 532. https://doi.org/10.2307/199542.

[50] F. Wang, B.B. Bowen, J.-H. Seo, G. Michalski, Laboratory and field characterization of visible to near-infrared spectral reflectance of nitrate minerals from the Atacama Desert, Chile, and implications for Mars, American Mineralogist. 103 (2018) 197–206.

[51] L. Chen, S.L. Larson, J.H. Ballard, Y. Ma, Q. Zhang, J. Li, L. Wu, Z. Arslan, F.X. Han, Laboratory spiking process of soil with various uranium and other heavy metals, MethodsX. 6 (2019) 734–739.

[52] E. Gibbons, R. Léveillé, K. Berlo, Data fusion of laser-induced breakdown and Raman spectroscopies: Enhancing clay mineral identification, Spectrochim Acta Part B At Spectrosc. 170 (2020) 105905. https://doi.org/10.1016/j.sab.2020.105905.

[53] R. Nieder, D.K. Benbi, H.W. Scherer, Fixation and defixation of ammonium in soils: A review, Biol Fertil Soils. 47 (2011) 1–14. https://doi.org/10.1007/s00374-010-0506-4.

[54] B.L. Ehlmann, J.F. Mustard, S.L. Murchie, J.-P. Bibring, A. Meunier, A.A. Fraeman, Y. Langevin, Subsurface water and clay mineral formation during the early history of Mars, Nature. 479 (2011) 53–60. https://doi.org/10.1038/nature10582.

[55] A. Kramida, Yu. Ralchenko, J. Reader, NIST ASD team, NIST Atomic Spectra Database (Version 5.6.1), National Institute of Standards and Technology. (2018). https://doi.org/https://doi.org/10.18434/T4W30F.

[56] N.H. Thomas, B.L. Ehlmann, D.E. Anderson, S.M. Clegg, O. Forni, S. Schröder, W. Rapin, P.Y. Meslin, J. Lasue, D.M. Delapp, M.D. Dyar, O. Gasnault, R.C. Wiens, S. Maurice, Characterization of Hydrogen in Basaltic Materials With Laser-Induced Breakdown Spectroscopy (LIBS) for Application to MSL ChemCam Data, J Geophys Res Planets. 123 (2018) 1996–2021. https://doi.org/10.1029/2017JE005467.

[57] W. Rapin, P. Meslin, S. Maurice, R.C. Wiens, D. Laporte, B. Chauviré, O. Gasnault, S. Schröder, P. Beck, S. Bender, O. Beyssac, A. Cousin, E. Dehouck, C. Drouet, O. Forni, M. Nachon, N. Melikechi, B. Rondeau, N. Mangold, N.H. Thomas, Quantification of water content by laser induced breakdown spectroscopy on Mars, Spectrochim Acta Part B At Spectrosc. 130 (2017) 82–100. https://doi.org/10.1016/j.sab.2017.02.007.

[58] S.M. Clegg, R.C. Wiens, R. Anderson, O. Forni, J. Frydenvang, J. Lasue, A. Cousin, V. Payré, T. Boucher, M.D. Dyar, S.M. Mclennan, R. V Morris, T.G. Graff, S.A. Mertzman, B.L. Ehlmann, I. Belgacem, H. Newsom, B.C. Clark, N. Melikechi, A. Mezzacappa, R.E. Mcinroy, R. Martinez, P. Gasda, O. Gasnault, S. Maurice, Recalibration of the Mars Science Laboratory

ChemCam instrument with an expanded geochemical database, Spectrochim Acta Part B At Spectrosc. 129 (2017) 64–85. https://doi.org/10.1016/j.sab.2016.12.003.

[59] R. Gaudiuso, M. Dell'Aglio, O. de Pascale, G.S. Senesi, A. de Giacomo, Laser induced breakdown spectroscopy for elemental analysis in environmental, cultural heritage and space applications: A review of methods and results, Sensors. 10 (2010) 7434–7468. https://doi.org/10.3390/s100807434.

[60] J. el Haddad, L. Canioni, B. Bousquet, Good practices in LIBS analysis: Review and advices, Spectrochim Acta Part B At Spectrosc. 101 (2014) 171–182. https://doi.org/10.1016/j.sab.2014.08.039.

[61] W. Rapin, B. Bousquet, J. Lasue, P. Meslin, J. Lacour, C. Fabre, R.C. Wiens, J. Frydenvang, Roughness effects on the hydrogen signal in laser-induced breakdown spectroscopy, Spectrochim Acta Part B At Spectrosc. 137 (2017) 13–22. https://doi.org/10.1016/j.sab.2017.09.003.

[62] C.R. Ytsma, M.D. Dyar, Accuracies of lithium, boron, carbon, and sulfur quantification in geological samples with laser-induced breakdown spectroscopy in Mars, Earth, and vacuum conditions, Spectrochim Acta Part B At Spectrosc. 162 (2019) 105715. https://doi.org/10.1016/j.sab.2019.105715.

[63] D. Cremers, L. Radziemski, Handbook of Laser-Induced Breakdown Spectroscopy, 2nd ed., John Wiley & Sons, Ltd, Tucson, 2013.

[64] S.M. Aberkane, A. Safi, A. Botto, B. Campanella, S. Legnaioli, F. Poggialini, S. Raneri, F. Rezaei, V. Palleschi, Laser-induced breakdown spectroscopy for determination of spectral fundamental parameters, Applied Sciences (Switzerland). 10 (2020). https://doi.org/10.3390/app10144973.

[65] C. Fabre, A. Cousin, R.C. Wiens, A. Ollila, O. Gasnault, S. Maurice, V. Sautter, O. Forni, J. Lasue, R. Tokar, D. Vaniman, N. Melikechi, In situ calibration using univariate analyses based on the onboard ChemCam targets: First prediction of Martian rock and soil compositions, Spectrochim Acta Part B At Spectrosc. 99 (2014) 34–51. https://doi.org/10.1016/j.sab.2014.03.014.

[66] N. Aras, Ş. Yalçın, Development and validation of a laser-induced breakdown spectroscopic method for ultra-trace determination of Cu, Mn, Cd and Pb metals in aqueous droplets after drying, Talanta. 149 (2016) 53–61.

[67] O. Forni, S. Maurice, O. Gasnault, R.C. Wiens, A. Cousin, S.M. Clegg, J.B. Sirven, J. Lasue, Independent component analysis classification of laser induced breakdown spectroscopy spectra, Spectrochim Acta Part B At Spectrosc. 86 (2013) 31–41. https://doi.org/10.1016/j.sab.2013.05.003.

[68] J.B. Sirven, B. Sallé, P. Mauchien, J.L. Lacour, S. Maurice, G. Manhès, Feasibility study of rock identification at the surface of Mars by remote laser-induced breakdown spectroscopy and three chemometric methods, J Anal At Spectrom. 22 (2007) 1471–1480. https://doi.org/10.1039/b704868h.

[69] A.M. Ollila, H.E. Newsom, B. Clark, R.C. Wiens, A. Cousin, J.G. Blank, N. Mangold, V. Sautter, S. Maurice, S.M. Clegg, O. Gasnault, O. Forni, R. Tokar, E. Lewin, M.D. Dyar, J. Lasue, R. Anderson, S.M. McLennan, J. Bridges, D. Vaniman, N. Lanza, C. Fabre, N. Melikechi, G.M. Perrett, J.L. Campbell, P.L. King, B. Barraclough, D. Delapp, S. Johnstone, P.Y. Meslin, A. Rosen-Gooding, J. Williams, Trace element geochemistry (Li, Ba, Sr, and Rb) using Curiosity's ChemCam: Early results for Gale crater from Bradbury Landing Site to Rocknest, Journal of Geophysical Research E: Planets. 119 (2014) 255–285. https://doi.org/10.1002/2013JE004517.

[70] R.B. Anderson, O. Forni, A. Cousin, R.C. Wiens, S.M. Clegg, J. Frydenvang, T.S.J. Gabriel, A. Ollila, S. Schröder, O. Beyssac, E. Gibbons, D.S. Vogt, E. Clavé, J.A. Manrique, C. Legett, P. Pilleri, R.T. Newell, J. Sarrao, S. Maurice, G. Arana, K. Benzerara, P. Bernardi, S. Bernard, B. Bousquet, A.J. Brown, C. Alvarez-Llamas, B. Chide, E. Cloutis, J. Comellas, S. Connell, E. Dehouck, D.M. Delapp, A. Essunfeld, C. Fabre, T. Fouchet, C. Garcia-Florentino, L. García-Gómez, P. Gasda, O. Gasnault, E.M. Hausrath, N.L. Lanza, J. Laserna, J. Lasue, G. Lopez, J.M. Madariaga, L. Mandon, N. Mangold, P.Y. Meslin, A.E. Nelson, H. Newsom, A.L. Reyes-Newell, S. Robinson, F. Rull, S. Sharma, J.I. Simon, P. Sobron, I.T. Fernandez, A. Udry, D. Venhaus, S.M. McLennan, R. v. Morris, B. Ehlmann, Post-landing major element quantification using SuperCam laser induced breakdown spectroscopy, Spectrochim Acta Part B At Spectrosc. 188 (2022). https://doi.org/10.1016/j.sab.2021.106347.

[71] M.D. Dyar, C.I. Fassett, S. Giguere, K. Lepore, S. Byrne, T. Boucher, C.J. Carey, S. Mahadevan, Comparison of univariate and multivariate models for prediction of major and minor elements from laser-induced breakdown spectra with and without masking, Spectrochim Acta Part B At Spectrosc. 123 (2016) 93–104. https://doi.org/10.1016/j.sab.2016.07.010.

[72] S. Wold, M. Sjöström, L. Eriksson, PLS-regression: A basic tool of chemometrics, Chemometrics and Intelligent Laboratory Systems. 58 (2001) 109–130. https://doi.org/10.1016/S0169-7439(01)00155-1.

[73] R.B. Anderson, S.M. Clegg, J. Frydenvang, R.C. Wiens, S. McLennan, R. V. Morris, B. Ehlmann, M.D. Dyar, Improved accuracy in quantitative laser-induced breakdown spectroscopy using sub-models, Spectrochim Acta Part B At Spectrosc. 129 (2017) 49–57. https://doi.org/10.1016/j.sab.2016.12.002.

[74] J.M. Tucker, M.D. Dyar, M.W. Schaefer, S.M. Clegg, R.C. Wiens, Optimization of laser-induced breakdown spectroscopy for rapid geochemical analysis, Chem Geol. 277 (2010) 137–148. https://doi.org/10.1016/j.chemgeo.2010.07.016.

[75] M.D. Dyar, S. Giguere, C.J. Carey, T. Boucher, Comparison of baseline removal methods for laser-induced breakdown spectroscopy of geological samples, Spectrochim Acta Part B At Spectrosc. 126 (2016) 53–64. https://doi.org/10.1016/j.sab.2016.10.018.

[76] A. Cousin, O. Forni, S. Maurice, O. Gasnault, C. Fabre, V. Sautter, R.C. Wiens, J. Mazoyer, Laser induced breakdown spectroscopy library for the Martian environment, Spectrochim Acta Part B At Spectrosc. 66 (2011) 805–814. https://doi.org/10.1016/j.sab.2011.10.004.

[77] S.R. Taylor, S. McLennan, Planetary crusts: their composition, origin and evolution, Cambridge University Press, 2009.

[78] J. Lasue, A. Cousin, P.Y. Meslin, N. Mangold, R.C. Wiens, G. Berger, E. Dehouck, O. Forni, W. Goetz, O. Gasnault, W. Rapin, S. Schroeder, A. Ollila, J. Johnson, S. le Mouélic, S. Maurice, R. Anderson, D. Blaney, B. Clark, S.M. Clegg, C. d'Uston, C. Fabre, N. Lanza, M.B. Madsen, J. Martin-Torres, N. Melikechi, H. Newsom, V. Sautter, M.P. Zorzano, Martian Eolian Dust Probed by ChemCam, Geophys Res Lett. 45 (2018) 10,968-10,977. https://doi.org/10.1029/2018GL079210.

[79] A.R. Angkat, K.B. Seminar, M. Rahmat, A. Sutandi, Estimation of Soil Nitrate (NO 3) Level Using Laser-Induced Breakdown Spectroscopy (LIBS), Earth and Environmental. 41 (2018) 1–6.

[80] F.C. de Lucia, J.L. Gottfried, Characterization of a series of nitrogen-Rich molecules using laser induced breakdown spectroscopy, Propellants, Explosives, Pyrotechnics. 35 (2010) 268–277. https://doi.org/10.1002/prep.201000009.

[81] L.M. Cabalín, T. Delgado, J.J. Laserna, Considerations on formation mechanisms of emitting species of organic and C-containing inorganic compounds in CO2 atmosphere using laser-induced breakdown spectroscopy as a strategy for detection of molecular solids, Spectrochimica Acta Part B. 169 (2020) 105869. https://doi.org/10.1016/j.sab.2020.105869.

[82] J. Moros, J. Laserna, Laser-Induced Breakdown Spectroscopy (LIBS) of Organic Compounds: A Review, Appl Spectrosc. 73 (2019) 963–1011. https://doi.org/10.1177/0003702819853252.

[83] P.R. Villas-Boas, M.A. Franco, L. Martin-Neto, H.T. Gollany, D.M. Milori, Applications of laser-induced breakdown spectroscopy for soil characterization, part II : Review of elemental analysis and soil classification, Eur J Soil Sci. 71 (2020) 805–818. https://doi.org/10.1111/ejss.12889.

[84] W. Xu, X. Liu, Z. Yan, L. Li, Z. Zhang, Y. Kuang, H. Jiang, H. Yu, F. Yang, C. Liu, T. Wang, C. Li, Y. Jin, J. Shen, B. Wang, W. Wan, J. Chen, S. Ni, Y. Ruan, R. Xu, C. Zhang, Z. Yuan, X. Wan, Y. Yang, Z. Li, Y. Shen, D. Liu, B. Wang, R. Yuan, T. Bao, R. Shu, The MarSCoDe Instrument Suite on the Mars Rover of China's Tianwen-1 Mission, The Author(s), under exclusive licence to Springer Nature B.V., 2021. https://doi.org/10.1007/s11214-021-00836-5.

[85] R.C. Wiens, S. Maurice, S.H. Robinson, A.E. Nelson, P. Cais, P. Bernardi, R.T. Newell, S. Clegg, S.K. Sharma, S. Storms, J. Deming, D. Beckman, A.M. Ollila, O. Gasnault, R.B. Anderson, Y. André, S. Michael Angel, G. Arana, E. Auden, P. Beck, J. Becker, K. Benzerara, S. Bernard, O. Beyssac, L. Borges, B. Bousquet, K. Boyd, M. Caffrey, J. Carlson, K. Castro, J. Celis, B. Chide, K. Clark, E. Cloutis, E.C. Cordoba, A. Cousin, M. Dale, L. Deflores, D. Delapp, M. Deleuze, M. Dirmyer, C. Donny, G. Dromart, M. George Duran, M. Egan, J. Ervin, C. Fabre, A. Fau, W. Fischer, O. Forni, T. Fouchet, R. Fresquez, J. Frydenvang, D. Gasway, I. Gontijo, J. Grotzinger, X. Jacob, S. Jacquinod, J.R. Johnson, R.A. Klisiewicz, J. Lake, N. Lanza, J. Laserna, J. Lasue, S. le Mouélic, C. Legett, R. Leveille, E. Lewin, G. Lopez-Reyes, R. Lorenz, E.

Lorigny, S.P. Love, B. Lucero, J.M. Madariaga, M. Madsen, S. Madsen, N. Mangold, J.A. Manrique, J.P. Martinez, J. Martinez-Frias, K.P. McCabe, T.H. McConnochie, J.M. McGlown, S.M. McLennan, N. Melikechi, P.Y. Meslin, J.M. Michel, D. Mimoun, A. Misra, G. Montagnac, F. Montmessin, V. Mousset, N. Murdoch, H. Newsom, L.A. Ott, Z.R. Ousnamer, L. Pares, Y. Parot, R. Pawluczyk, C. Glen Peterson, P. Pilleri, P. Pinet, G. Pont, F. Poulet, C. Provost, B. Quertier, H. Quinn, W. Rapin, J.M. Reess, A.H. Regan, A.L. Reyes-Newell, P.J. Romano, C. Royer, F. Rull, B. Sandoval, J.H. Sarrao, V. Sautter, M.J. Schoppers, S. Schröder, D. Seitz, T. Shepherd, P. Sobron, B. Dubois, V. Sridhar, M.J. Toplis, I. Torre-Fdez, I.A. Trettel, M. Underwood, A. Valdez, J. Valdez, D. Venhaus, P. Willis, The SuperCam Instrument Suite on the NASA Mars 2020 Rover: Body Unit and Combined System Tests, The Author(s), 2021. https://doi.org/10.1007/s11214-020-00777-5.

[86] R. Brennetot, J.L. Lacour, E. Vors, A. Rivoallan, D. Vailhen, S. Maurice, Mars Analysis by Laser-Induced breakdown Spectroscopy (MALIS): Influence of mars atmosphere on plasma emission and study of factors influencing plasma emission with the use of Doehlert designs, Appl Spectrosc. 57 (2003) 744–752. https://doi.org/10.1366/000370203322102816.

[87] A.K. Knight, N.L. Scherbarth, D.A. Cremers, M.J. Ferris, Characterization of laser-induced breakdown spectroscopy (LIBS) for application to space exploration, Appl Spectrosc. 54 (2000) 331–340. https://doi.org/10.1366/0003702001949591.

[88] K.H. Lepore, C.I. Fassett, E.A. Breves, S. Byrne, S. Giguere, T. Boucher, J.M. Rhodes, M. Vollinger, C.H. Anderson, R.W. Murray, M.D. Dyar, Matrix Effects in Quantitative Analysis of Laser-Induced Breakdown Spectroscopy (LIBS) of Rock Powders Doped with Cr, Mn, Ni, Zn, and Co, Appl Spectrosc. 71 (2017) 600–626. https://doi.org/10.1177/0003702816685095.

[89] M.T. Thorpe, T.F. Bristow, E.B. Rampe, N.J. Tosca, J.P. Grotzinger, K.A. Bennett, C.N. Achilles, D.F. Blake, S.J. Chipera, G. Downs, Mars Science Laboratory CheMin data from the Glen Torridon region and the significance of lake-groundwater interactions in interpreting mineralogy and sedimentary history, J Geophys Res Planets. 127 (2022) e2021JE007099.

[90] E. Dehouck, O. Forni, C. Quantin-Nataf, P. Beck, N. Mangold, C. Royer, E. Clavé, O. Beyssac, J.R. Johnson, L. Mandon, Overview of the Bedrock Geochemistry and Mineralogy Observed by Supercam During Perseverance's Delta Front Campaign, in: 54th Lunar and Planetary Science Conference, 2023: p. 2862.

[91] E. Dehouck, A. Cousin, N. Mangold, J. Frydenvang, O. Gasnault, O. Forni, W. Rapin, P.J. Gasda, G. Caravaca, G. David, Bedrock geochemistry and alteration history of the clay-bearing Glen Torridon region of Gale crater, Mars, J Geophys Res Planets. 127 (2022) e2021JE007103.

[92] J.A. Hurowitz, J.P. Grotzinger, W.W. Fischer, S.M. McLennan, R.E. Milliken, N. Stein, A.R. Vasavada, D.F. Blake, E. Dehouck, J.L. Eigenbrode, A.G. Fairén, J. Frydenvang, R. Gellert, J.A. Grant, S. Gupta, K.E. Herkenhoff, D.W. Ming, E.B. Rampe, M.E. Schmidt, K.L. Siebach, K. Stack-Morgan, D.Y. Sumner, R.C. Wiens, Redox stratification of an ancient lake in Gale crater, Mars, Science (1979). 356 (2017). https://doi.org/10.1126/science.aah6849.

# CHAPTER 6

# From Glaciovolcanic Sites to Martian Exploration: Interdisciplinary Insights into Optimizing the Search for Life on Mars

## 6.1 CONTEXT AND FOUNDATIONS OF THE WORK

Taken together, the Chapters of this thesis describe a multidisciplinary suite of strategies tailored to enhance the search for life on Mars. The approaches span from foundational studies of habitability and biomarker preservation potential in underexplored Mars-analogue environments, to purpose-driven development of procedures to augment the operational capacity of Mars rovers and the scientific return of Mars missions more broadly. This effort was pursued because the search for evidence of life beyond Earth stands as a pinnacle objective in planetary exploration, with Mars representing the nearest habitable world.

With the clock ticking to investigate Mars' potential habitats before human exploration irrevocably changes the environment [1–4], the necessity for optimizing the search parameters is more crucial than ever. Throughout this thesis I have highlighted the importance of Martian refugia—the isolated niches that potentially remained permanently or episodically hospitable even as Mars underwent global climate change. The last two decades of Mars exploration have focused on the early spatiotemporal range (environments >3 Ga), owing to Mars' more widely habitable conditions during this time, including the widespread presence of water-rich environments. However, a shift towards exploring Martian refugia holds distinct advantages. Their value lies not only in concentrating possible biomarkers but also in their potential to host the most recent, and therefore the least degraded, vestiges of Martian life [5,6]. This thesis aimed, in part, to empirically investigate the astrobiological potential of one such potential refuge: glaciovolcanic settings. Prior research has described potential habitats in glaciovolcanic areas, documented nutrient and energy sources, and revealed evidence of life through gene analysis. Yet, the distribution of biomass in these systems and the fidelity of the potential

biomarker record had not been investigated in detail. We sought to address these gaps and to develop tools to enhance Mars rover survey capabilities, both in glaciovolcanic areas and more broadly. This discussion first centers on a synthesis of the collective results and their implications for glaciovolcanic exploration (given the high astrobiological potential of these settings), before expanding to elucidate refined exploration strategies for Mars more broadly.

## 6.2 SYNTHESIS OF RESULTS AND THEIR SIGNIFICANCE

In Chapter 2, our detailed exploration of the physicochemical gradients in the active glaciovolcanic hydrothermal field at Kverkfjöll illustrated how the interplay between ascending volcanic heat and overlying glacial ice or snow can lead to pronounced environmental heterogeneity. Such heterogeneity has previously been identified as a critical driver for species diversity [7,8]. Aligned with this concept, we find that significant differences in the microbial biomass, total organic carbon, total nitrogen, and the community structure were each statistically linked to variations in the hydrothermal fluid physiochemistry. More specifically, we reported evidence that the microbial community was actively responding to gradients of temperature, salinity, dissolved oxygen, and likely pH, and that distinct microbial lipid assemblages had been produced within unique niche spaces. These findings reflect possible trends of divergent adaptation and niche differentiation within the system, highlighting that the diverse environments resulting from volcanic-ice interactions foster the emergence of varied communities (or at the very least, varied lipid profiles). This molecular diversity of lipids is an important consideration in the search for Martian life, independent of the lipid-derived biomass. Indeed, the production of a broad spectrum of lipids increases the likelihood that some of those lipids will be chemically stable enough to withstand harsh environmental conditions, offering a potentially more resilient and informative molecular fossil record, compared to a less diverse lipid pool. In sum, our findings underscore that the dynamic environment of Mars-like glaciovolcanic settings is favourable for fostering varied biological communities, further bolstering the case for the habitability of such environments.

Chapter 3 demonstrated that the indigenous microbial community also synthesizes a complex suite of refractory alkanes (straight and branched chain), alkenes, and an unresolved complex mixture. Crucially, multiple mutually consistent biogenic patterns were evident in the hydrocarbon profiles. This enhanced the credibility of our findings and also increases the

likelihood that evidence for biogenicity will be preserved in the geologic record. Furthermore, we revealed that the study site is dominated by volumetrically abundant dioctahedral smectites. While prior investigations had acknowledged the presence of smectites [9], our findings highlighted their widespread occurrence across the site, irrespective of the diversity of hydrothermal features and the broad spectrum of physicochemical conditions observed. This finding was important because, on Earth, smectites are the major reservoirs of organic carbon in subaqueous environments due to their high specific surface area and potent cation exchange capacity, which enable them to adsorb substantial volumes of organic compounds [10–13]. Once adsorbed, organic compounds benefit from increased stability and physical protection from natural degradative actions such as oxidation or predation [14]. Thus, the widespread presence of smectites across the study area suggests an enhanced potential for consistent and extensive preservation of organic materials. This pervasive occurrence not only increases the potential fidelity of the organic record but also the likelihood of capturing a diverse range of biological interactions and events over time. An additional advantage of smectites is their capacity to also adsorb essential macro- and micro-nutrients (e.g., $K^+$, $NH_4^+$, $Ca^{2+}$, $Mg^{2+}$, $Cu^{2+}$, and $Zn^{2+}$) in a bioavailable form on the cation exchange sites, further bolstering habitability [15]. In sum, we identified a combination of intrinsically refractory organic biomarkers and a mineralogical assemblage amenable to the initial capture and retention of molecular biomarkers. This combination presents a strong case for the potential longevity and fidelity of the organic record within our study system and bolsters the case for exploration. While our findings mark a substantial advancement in understanding biomarker preservation in Mars-like glaciovolcanic settings, future investigations should delve deeper into post-burial diagenetic processes that could further influence the integrity of the fossil record. Specifically, exploring the potential formation of macromolecular matrices, a process proposed to be important for biomarker preservation on the Martian surface [16], will be informative. This next phase of research will not only complement our current understanding but also enhance the overall impact and applicability of our findings in the context of astrobiology and the search for life on Mars.

In light of our collective findings, and the knowledge that evidence for glaciovolcanism is widespread throughout Mars history and across a range of latitudes [17], we strongly recommend these settings be prioritized for astrobiological investigation. However, a nuanced read of our results also reveals critical exploration challenges that need to be addressed. For instance, it is

important to consider that a nearby hydrothermal area at Kverkfjöll summit, ~2 kilometers away from our study region, featured kaolinite as the predominant mineral [18]. Kaolinite, which forms at the expense of smectite during advanced stages of hydrothermal alteration [19], has a reduced capacity for retaining organic compounds and bioavailable nutrients [20]. This underscores that that not all glaciovolcanic settings are equally promising for astrobiology and therefore necessitates thorough reconnaissance to accurately gauge the habitability and preservation potential of each distinct glaciovolcanic setting. In addition, our direct results reveal exploration challenges brought on by variability *within* the study site itself, such as:

1. *Biomarker Preservation Bias:* Our findings indicate a pronounced preservation bias for primary hydrocarbons. Notably, we found a conspicuous absence of hydrocarbon profiles resembling membrane phospholipid fatty acids. We interpret this as evidence that energy-dense lipids are quantitatively recycled as vital energy and nutrient sources in this carbon-poor environment. This preservation bias has several critical implications. First, it demonstrates that the biomarker record may not accurately represent the original community, compromising the fidelity of the preserved biological signature and potentially hindering biological reconstructions. Second, it diminishes the quantity of organic matter that has the potential to enter the geological record. Indeed, we find that primary hydrocarbons are produced in very low abundance by bacteria (much less than functionalized membrane-associated hydrocarbons). Thus, should Martian sediments exhibit a similar degradation bias towards functionalized lipids, the detectability of the biogenic lipid reservoir would be significantly challenged. Third, our understanding of the physiological role of primary hydrocarbons is lacking. This knowledge gap not only complicated our ability to accurately attribute the hydrocarbon source in our study, but also raises uncertainties about interpreting analogous findings in Martian environments.
2. *Uneven Distribution of Biomass and Associated Hydrocarbons*: Across the study area, both biomass and hydrocarbon abundances were generally low, yet exhibited significant local variability. Notably, biomass and hydrocarbon “hotspots” appeared to be localized in physicochemical zones that are conducive to the establishment of autotrophic communities. These zones could be relatively small in size and dissipate over centimeter-scale distances. The combination of low overall abundance and patchy distribution heightens the risk of

overlooking critical zones of biological activity, potentially leading to false negative results during exploration.

3. *Lack of Hydraulic Transport*: Following directly from (2), we had optimistically anticipated that the crater lake, Gengissig, could mitigate the risks of patchy initial organic distribution by consolidating residual compounds from the catchment, thus providing a more concentrated and representative record. However, our observations did not support this assumption. We find that the hydrocarbon biomarkers are not effectively transported and do not accumulate in the lake sediment, instead remaining highly localized.
4. *Mineralogical Homogeneity Within Site*: While the site displayed significant environmental heterogeneity that influenced biological distributions, this variability was not mirrored in the mineralogical composition. Indeed, the mineralogical assemblage was strikingly uniform. The observed mineralogical homogeneity could be attributed either to a consistent hydrothermal alteration influence or to sediment mixing and homogenization processes occurring in the subglacial environment or during periods of elevated lake stands. Regardless, it is apparent that the mineralogy does not serve as a reliable indicator for differing habitats or areas of pronounced chemical disequilibria, which could make pinpointing habitability "hotspots" more challenging.

These difficulties, while significant, are not insurmountable. They serve as guiding factors for how to optimize exploration strategies of glaciovolcanic environments. By drawing attention to the inherent variability of glaciovolcanic habitats, they underscore the need to focus biomarker detection efforts in areas where they are most likely to be concentrated and, thus, detectable. The following subsections will detail strategies to achieve this based on the patterns we observed at Kverkfjöll.

### 6.2.1 Recommendation 1: Prioritize Sampling Glaciovolcanic Source Areas

While the preceding list enumerates how glaciovolcanic interactions can present investigation challenges within the source environment, it is important to emphasize that the source environments are the crucial niches that might have extended Mars' habitable window. Thus, while distal glaciovolcanic deposits, like jökulhlaup flood plains, have been suggested as promising surrogate targets due to their vast size, orbital detectability, and potential for rapid organic burial [17,21,22], they would lack the environmental context required to interpret any

potential biological record. Furthermore, our novel investigation of the sediments in Lake Gengissig—a jökulhlaup source—cast doubts on the very legitimacy of this approach.

Our results demonstrate that Lake Gengissig harbours some of the lowest concentrations of total organic carbon and biomass across the system, highlighting the lake as a relatively unfavourable habitat for colonization. This is particularly evident from the markedly high starvation markers identified within the pelagic microbial community, underlining the pronounced nutrient deficiency. Moreover, as highlighted in *Problem #3* above, Gengissig does not act as a principal repository for organic biomarkers produced within its catchment, thereby challenging our preconceptions about its function as a biomarker sink. Consequently, any jökulhlaup emanating from Lake Gengissig would further dilute the already faint organic record. Relying on such outburst floods as an accessible window into the subglacial glaciovolcanic realm might be counterproductive, potentially obscuring rather than amplifying the evidence we seek.

Therefore, we posit that the source region is the most promising locale for accessing an authentic and concentrated repository of glaciovolcanic biomarkers. Recently presented evidence for glaciovolcanic hydrothermal systems on Mars provides viable exploration candidates. For instance, orbital topographic data of a fan-shaped deposit northwest of the giant Arsia Mons shield volcano revealed landforms reminiscent of classic terrestrial subglacial volcanic morphologies [23]. These include flat-topped mountains and ridges typical of subglacial eruptions (morphologically similar to terrestrial tuya and tindar), steep-sided elongate features interpreted as ice-confined lava flows, and low-relief, laterally extensive mounds typical of pillow lava effusions under high confining ice pressure [23]. Spatially associated landforms indicative of geologically recent (late Amazonian) wet-based glacial flow and accelerated basal erosion, despite globally freezing climes, reinforce the glaciovolcanic interpretation [23]. Subsequent thermodynamic modeling of the area suggest that massive volumes of meltwater would have been produced within and beneath the glacier, generating liquid englacial lakes that were potentially stable for hundreds of thousands of years [23].

An additional candidate site lies within the Sisyphi Montes region, situated at higher latitudes, and dated to the Noachian or early Hesperian Periods [24]. Here, landforms exhibit morphologies that are hallmarks for subglacial volcanism. Crucially, this region is relatively dust free, enabling the first detailed examination of mineralogy in a putative Martian glaciovolcanic

system. Ackiss et al. (2018) [24] reported an assemblage dominated by smectites, zeolites, iron oxides, and hydrated sulfates, collectively interpreted to reflect low temperature hydrothermal alteration at high water:rock ratios [24]. This region therefore provides the first mineralogical evidence for subglacial hydrothermalism on Mars. Notably, the assemblage presents similarities to the smectite- and zeolite-dominated profile at our field site on Kverkfjöll.

Both of these glaciovolcanic source regions present compelling targets for exploration. Indeed, the distinction in age between the ancient Sisyphi Montes volcanoes and the younger Arsia Mons area provides an exciting temporal framework for exploration. Investigating the Sisyphi Montes glaciovolcanic region would provide insight into the early development of glaciovolcanic hydrothermal systems and their potential role in shaping initial life-sustaining environments. On the other hand, the Arsia Mons deposits are some of the youngest potentially habitable terrains on Mars, exemplifying a potential refugium environment [23]. This site could potentially shed light on recent sources of liquid water on Mars' surface, provide a key assessment of the glaciovolcanic refugia hypothesis, and perhaps house relatively recent biomarkers. However, the mineralogy at Arsia Mons cannot be studied from orbit due to a thick mantle of dust [23], making it difficult to interpret the biomarker preservation potential (see Recommendation 2). A worthy avenue of future research would be an *in situ* investigation of the Arsia Mons deposits to clarify their biomarker preservation potential.

### 6.2.2 Recommendation 2: Prioritize Smectite-Bearing Source Regions

Glaciovolcanic interactions are highly conducive to the development of hydrothermal systems given the juxtaposition of upwelling geothermal heat and supply of meltwater [17]. Nevertheless, not all glaciovolcanic systems evolve into hydrothermal areas. Various factors, such as the proximity of magma, the regional heat flow through the crust, and the relative infiltration of water (meteoric or meltwater) can influence whether a glaciovolcanic site will develop a hydrothermal system [25]. Given that hydrothermal environments are often regarded as prime astrobiological candidates due to their nutrient-rich fluids and energy gradients [26,27], it would be effective to prioritize glaciovolcanic source areas that exhibit evidence for past hydrothermal activity. Phyllosilicates offer a key piece of evidence in this regard as they are important mineralogical products of hydrothermal alteration [19], but are not significant components of cold subglacial chemical weathering systems [28]. Notably, zones with smectite-dominated

hydrothermal alteration facies, which occur early in the paragenetic sequence [19], hold the highest promise for astrobiological exploration, as highlighted previously.

Thus, we recommend that astrobiological exploration of glaciovolcanic sites prioritize smectite-bearing zones. While mineralogical reconnaissance should begin with orbital data products where possible, glacial debris and Mars' extensive dust coverage have been known to limit the usefulness of orbital mineral mappers in putative glaciovolcanic areas, like Arsia Mons [23]. Hence, initial site selection may need to rely on the orbital identification of glaciovolcanic landforms, followed by comprehensive *in situ* mineralogical surveying to pinpoint the most auspicious areas for detailed examination (smectite-rich). Drawing parallels with Kverkfjöll, where the dominant hydrothermal alteration facies varied over kilometer-scale distances, it is clear that reconnoitering rovers must have the capacity to conduct phyllosilicate surveys over large areas, ideally at a rapid pace. In this context, the spectral data fusion approach delineated in Chapter 4 holds great promise. Chapter 4 illustrated that by combining the spectral outputs from LIBS and Raman spectrometers, Mars-relevant phyllosilicate groups and subgroups can be identified with greater accuracy compared to using either spectrometer on its own. Crucially, these instruments require only visual access to a specimen and can significantly enhance the pace and spatial coverage of reconnaissance relative to other mineralogical techniques that require direct sample contact.

A valuable exploration approach in heterogenous, but discrete, glaciovolcanic zones would therefore be the "walkabout" strategy [29]. This strategy begins with a reconnaissance traverse around the study area, capturing imaging and spectral data to identify and characterize lithologic variability. Once the features and chemical characteristics with the greatest astrobiological potential are identified, a targeted contact-science traverse homes in on these areas. In this case, equipping these missions with LIBS-Raman survey capabilities to map the occurrence of smectites rapidly and remotely would benefit the reconnaissance traverse, allowing the bulk of the mission resources to be focused on areas most likely to retain a biological record. Indeed, a walkabout-first strategy has been shown to be highly effective where narrow hypotheses are being tested and thus specific evidence is being searched for in a discrete area (this is contrasted with the "linear" approach commonly used by planetary rover missions, where the rover does not backtrack, but examines all sites in the order they are encountered) [29].

### 6.2.3 Recommendation 3: Prioritize Areas Conducive to Autotrophy

We found that the concentrations of both intact phospholipids and hydrocarbons were patchily distributed and concentrated in areas favourable for autotrophic communities. We argued that an organism's capacity to "self-feed" by fixing organic compounds from inorganic sources conferred a specific ecological advantage at Kverkfjöll given the absence of exogenous organic inputs, leading to biomass concentration in these areas. Moreover, without significant aqueous organic transport within the system, the initial biomass distribution significantly influenced the spatial distribution of lipid hydrocarbons. Therefore, to overcome the predominantly low organic content of glaciovolcanic sediments and the lack of hydraulic concentration mechanisms, it would be optimal to focus on areas amenable to autotrophy.

*Problem #4* (homogeneous mineralogy) underscores a challenge in *how* to identify areas amenable to autotrophy. Although physicochemical metrics recorded during sampling highlighted factors likely supporting autotrophy (e.g., moderate temperatures and circumneutral pH for phototrophy, and rich geochemistry for potential autotrophy), these properties were not comprehensively captured in the mineralogical record. Therefore, although mineralogy can help identify areas of enhanced preservation potential (see Recommendation 2), our results demonstrate that it is not clearly linked to areas of high biomass. Consequently, it is not an informative proxy for areas that might concentrate biomarkers and alternative proxies are required.

Morphological markers could be informative. For instance, we posited that the dehydration/ rehydration cycles of the Kverkfjöll mud pots locally amplify both inorganic and organic substrates, thereby enhancing geochemical disequilibria and potentially aiding chemoautotrophy. Indeed, fluctuating environments in the form of wet-dry cycles at elevated temperature ranges have long been considered to be possible sources of free energy that could drive life-sustaining reactions [30]. Hence, searching for morphological evidence of these cycles—such as mud cracks, mud curls, fluid escape structures, or evaporite minerals—might be a fruitful approach. Furthermore, the only example of active photoautotrophy in the Kverkfjöll system was identified within a short segment of the hot-spring overflow stream measuring ~30-44°C. This corresponds to the "mid" and "distal" classifications of hydrothermal spring facies [31,32] and is consistent with where phototrophs are dominant in other hydrothermal systems [33]. Thus, if morphological or mineralogical evidence of a vent/spring can be identified within a glaciovolcanic system,

prioritizing the surrounding apron, where temperatures were likely more moderate, would be a valuable strategy.

In addition, Chapters 2 and 3 revealed a strong, statistically significant correlation between biomass (and hydrocarbon abundance) and the levels of sedimentary organic C and N. This is not surprising given the critical importance of C and N to biomolecules, but it does highlight potential elemental metrics with which to identify where biomarkers are concentrated. As above, it would be preferable if future missions could survey these elements rapidly and remotely during a walkabout reconnaissance traverse, thus maximizing the exploration range and focusing consumable resources only on samples with the greatest astrobiological potential. The LIBS survey technique therefore represents an excellent tool in this regard, thanks to its sensitivity to lighter elements. Nevertheless, the high concentration of $CO_2$ in Mars' atmosphere (~95%) poses a challenge for delineating between sedimentary and atmospheric C in a LIBS plasma, although encouraging developments are being made in this area [34–37]. Mars' atmospheric $N_2$ content is comparatively much lower (~2.7%) and is not likely to interfere with sedimentary N detection [38], rendering N a potentially powerful marker for areas with a higher likelihood of biomarker concentration. In light of this, the baseline study on LIBS N emission detailed in Chapter 5 serves as a cornerstone for advancing biomarker surveying capabilities. While the focus of Chapter 5 was largely on *inorganic* N sources, aspects such as the positioning and intensity of N emission lines, spectral interferences with basaltic matrices, and data processing techniques for optimizing N response are all relevant for developing algorithms sensitive to *organic*-N emission. Consequently, Chapter 5 lays the groundwork for mapping astrobiologically significant N in glaciovolcanic settings and locating areas conducive to biomarker concentration.

### 6.2.4 General Glaciovolcanic Exploration Plan

The three preceding subsections progressed from a broad to a narrow scope and provide the elements necessary to begin formulating a comprehensive exploration plan. To summarize, glaciovolcanic source areas should be prioritized over distal deposits. Recent years have seen a notable increase in the glaciovolcanic landforms identified on Mars, including several examples from the late Amazonian Period [23,39–43]. This body of work, and future iterations will serve as the foundation of identifying ideal exploration sites. Where possible, orbital mineral data can help select exploration sites with evidence of hydrothermal activity; the well-characterized

assemblage at Sisyphi Planum can be used as a benchmark for identifying hydrothermal glaciovolcanism on Mars [24].

On the ground, a nested walkabout strategy will help overcome the inherent variability in the dynamic glaciovolcanic system. Initial reconnaissance should focus on rapidly characterizing the distribution of phyllosilicates as proxies for hydrothermal alteration extent [19]. Incorporating LIBS-Raman data fusion techniques will be particularly useful in this phase. By identifying zones richest in smectite, this preliminary survey will help focus subsequent work on areas where biomarkers could be preserved and also offer a geological framework essential for contextualizing any potential biomarkers within their larger ecological setting. Subsequently, a more focused walkabout should use LIBS to map sequestered N (and possibly C) as a proxy for habitability/organic matter concentration.

By streamlining our approach in this manner and leveraging modern tools, we can narrow the search to where biomarkers may be concentrated. Prior research offers insight into optimal sample collection practices in heterogeneous volcanic terrains, including guidance on sample size and frequency [44]. Collectively, these concepts offer a comprehensive exploration plan.

### 6.2.5 Broader Implications of Thesis Results and Areas of Future Research

Several insights presented throughout this thesis have broader implications for how we conceptualize the search for life on Mars and for refining our general exploration strategies, beyond glaciovolcanic regions. For instance, the distinctive value of the Kverkfjöll field site is that it fundamentally represents a remote basaltic environment with Mars-analogous geochemistry, uniquely isolated from the influences of complex life, and where phototrophy is not the dominant form of primary production. It offers a glimpse into a relatively simple indigenous biosphere, the biomarkers produced, and the potential of basaltic sediments to retain a record of low biological productivity. Observations made here are relevant far beyond the scope of the glaciovolcanic analogy; a few of these, with ripe opportunities for future research, merit special attention.

As one example, the selective preservation of “primary” hydrocarbons, as detailed in Chapter 3, offers insight into organic preservation in carbon-poor systems, on Mars and Earth. We argued that the scarcity of organic carbon in the environment promoted rapid, exhaustive, and preferential degradation of energy-dense membrane-lipids, precluding their conversion into

molecular fossils. This finding reveals a significant taphonomic filter that not only reduces the overall quantity of organic matter that may become preserved, but also significantly diminishes the fidelity of the ultimate molecular fossil record by removing information-rich membrane lipids at the earliest stage of diagenesis. This underscores a crucial knowledge gap, as much of the current discourse on lipid production, preservation, and interpretation in Martian environments focuses on data derived from membrane-based lipids (e.g., [45–47]). Comparatively little is understood about the physiological role of primary hydrocarbons [48]. Considering that the Mars Science Laboratory recently reported low organic carbon levels in the lacustrine mudstones of Gale Crater [49], it is prudent to consider that Mars' broader sedimentary environments might also be vulnerable to this preservation bias. As a consequence, our expectations of Mars' potential molecular fossil record may need to be recalibrated, recognizing that the organic record might be both sparser and less informative than previously anticipated. Therefore, continued research on the production and functional role of primary hydrocarbons holds promise for advancing astrobiological exploration as well as broadening our foundational grasp of biological systems.

Further, an open question in the realm of Mars astrobiology is: How would biomarkers be expressed if photosynthesis never evolved? [50]. Insight into this question has remained elusive because the ecology of modern Earth, and much of our geologic record, is so dominated by photosynthesis that it is difficult to find evidence of life that is not at least peripherally affected by the products of photosynthesis. While Kverkfjöll is not completely isolated from photosynthesis, we demonstrated that lake Gengissig neither contains evidence for viable phototrophs (Chapter 2) nor displays evidence of their hydrocarbon byproducts (Chapter 3). We therefore proposed that the hydrocarbon deposits in the depths of Lake Gengissig might provide insight to the aforementioned question. A worthy avenue of future research would be to subject these sediments to simulated Martian degradation conditions to fully understand how such a signal might be expressed on Mars today.

It is also important to highlight the broad applicability of the methodologies introduced in Chapters 4 and 5, which aim to enhance the operational efficacy of remote survey instruments on Mars rovers. As outlined in the preceding subsections, the development of both tools would benefit the search for life within glaciovolcanic terrains, offering tangible means to guide a rover

towards targets with the greatest potential for concentrating and preserving signs of life. Yet, their function extends beyond such specific terrains. These tools were tested and trained on relatively generic Mars-analogue samples and have practical relevance to myriad basalt-dominated environmental contexts. Their relevance is further bolstered by the fact that they are designed around spectroscopic techniques currently in use on Mars rovers, highlighting that the results can directly inform and elevate ongoing exploration efforts. Indeed, it is important to reiterate that both of the proposed tools performed well in the pilot studies, either by increasing the accuracy of identifying critically important clay minerals (Chapter 4), or by pioneering the remote detection of sequestered N, a feat yet unachieved in missions (Chapter 5). A logical extension of this work would involve subjecting these studies to conditions that closely mimic those on Mars so that the algorithms can be refined for integration onto the rovers themselves.

Developing these tools for use on Mars underlines the distinct value of developing improved data analysis strategies. Optimized data analysis protocols have the capacity to augment the results of space missions in real-time. They enable us to harness the full potential of current hardware, extracting maximum insights without waiting for the next generation of rovers. The tools outlined in Chapters 4 and 5 are exemplary demonstrations of the synergy between space exploration and data science, but they are only the beginning. Indeed, the procedures of Chapter 4 have already been adapted to build additional data processing protocols to enhance the identification of carbonate minerals [51]. Thus, while future missions will undoubtedly carry hardware innovations that will dramatically advance our capacity to explore Mars and search for signs of life, the immediate future of Martian exploration can be significantly elevated by further developing data-driven methodologies.

## 6.3 CONCLUDING REMARKS

Over the last two decades our view of Mars as a homogeneous “red planet” has given way to a nuanced understanding of a much more dynamic world. We now understand Mars once hosted a more Earth-like climate and a breadth of environments that could have been habitable. Although Mars’ surface today is an irradiated frozen desert, we continue to see evidence for ongoing landscape evolution and recent work has identified a variety of possible niches that could have remained habitable despite these challenges. Such niches could preserve critical records of recent inhabitation (viable during the Late Amazonian) or potentially host extant life.

The possibility of finding evidence for life on Mars, either extinct or extant, holds profound scientific and philosophical significance. There is much to be learned from a once-habitable planet that has either died out or on which life never got started. Knowledge from the former can be used as a cautionary tale, whereas knowledge from the latter brings us closer to understanding the true boundary conditions of life and how it begins in the first place. Recent advances in launch capabilities, precision landing techniques, orbital mapping, and biomarker detection technologies now position us, as never before, to conduct a rigorous search for this possible evidence of life. The research presented in this thesis was pursued with the goal of helping to optimize this search.

Chapters 2 and 3 present a complementary approach to understanding the astrobiological potential of glaciovolcanic settings, which had previously been identified as potential Martian refugia [17,43]. These chapters aimed to characterize, for the first time, the distribution of biomass and biological community structure in basalt-hosted glaciovolcanic areas, as well as their potential to retain an organic fossil record. In Chapter 2, we presented an analysis of phospholipid fatty acids, revealing a low biomass, but viable community of microorganisms adapted to local environmental extremes. We demonstrated that biomass appeared concentrated in areas conducive to the development of autotrophic metabolisms. In Chapter 3, we showed that the local sediments were dominated by smectite clay and retained a complex suite of intrinsically refractory biomarker hydrocarbon with a clear imprint of biological influence, both of which underscore the environment's potential to preserve a molecular fossil record. Yet, we also identified mineralogical heterogeneity on kilometer scales and an organic preservation bias, which have important implications for planning future missions—both in terms of exploration planning and instrument resolution requirements. Overall, our work generated a clearer picture of the astrobiological potential of these systems and uncovered important avenues of future work to optimize exploration.

The work presented in Chapter 4 aimed to improve the accuracy of clay mineral identification using instrumentation onboard the Mars 2020 Perseverance rover. We presented a proof-of-concept study on using low-level data fusion to simultaneously model spectral data from laser-induced breakdown spectroscopy and Raman spectroscopy during automated classification. This work achieved its stated objective by demonstrating a significant improvement in the

classification accuracy of clay mineral groups and subgroups when using the concatenated spectral data product, versus either spectral data product independently. The results imply that in multivariate data analysis, a high dimensional data product can be more than the sum of its parts. Further development of this architecture and its use on the Mars surface will have implications for more accurately interesting geologic context and for guiding rovers towards sites with the greatest potential for organic preservation. More broadly, this work highlights how data analysis tools can be used to augment the performance of existing Mars assets such that missions can be continuously improved throughout their operational lifetime.

Lastly, Chapter 5 was motivated by the realization that the amount of N sequestered in Mars' surface remains largely unknown—a significant gap in our understanding of potential habitability given the essential importance of N to life on Earth. This Chapter aimed to assess the feasibility of detecting N using the remote survey capabilities of LIBS, a technique available on multiple active Mars rovers. We successfully presented a baseline study on the nature of N emission from Mars-relevant substrates. Specifically, we identified three emission lines that are good candidates for immediate detection of N and presented data analysis strategies to optimize quantification accuracy. We also highlighted that for optimal N surveying, future planetary LIBS instruments should expand their spectral range to incorporate stronger N emission features at longer wavelengths. This pilot study lays the foundation for using LIBS to rapidly map astrobiologically relevant N on Mars.

Looking to the future, we strongly advocate that glaciovolcanic regions of Mars be considered as compelling astrobiological targets. This recommendation is bolstered by recent evidence indicating glaciovolcanic interactions have fostered habitable conditions as recently as 100-200 Myr; unambiguous molecular biomarkers have been retrieved from much older terrestrial environments. The insights and tools detailed in this thesis may be used to help refine the search strategies in these high priority areas and bring us closer to addressing the age-old question: Are we alone?

## 6.4 MASTER REFERENCE LIST

### 6.4.1 Chapter 1


[1] C. Nelson, Lehninger's principles of biochemistry, 2013.

[2] C.R. Woese, Bacterial evolution, Microbiol Rev. 51 (1987) 221–271.

[3] C.P. McKay, What is life—and how do we search for it in other worlds?, PLoS Biol. 2 (2004) e302.

[4] A.F. Davila, Life on Mars: Independent Genesis or Common Ancestor?, Astrobiology. 21 (2021) 802–812.

[5] B. Damer, D. Deamer, The hot spring hypothesis for an origin of life, Astrobiology. 20 (2020) 429–452.

[6] W. Martin, J. Baross, D. Kelley, M.J. Russell, Hydrothermal vents and the origin of life, Nat Rev Microbiol. 6 (2008) 805–814.

[7] N. Lane, J.F. Allen, W. Martin, How did LUCA make a living? Chemiosmosis in the origin of life, BioEssays. 32 (2010) 271–280.

[8] C.P. McKay, The search for a second genesis of life in our Solar System, in: First Steps in the Origin of Life in the Universe: Proceedings of the Sixth Trieste Conference on Chemical Evolution Trieste, Italy 18–22 September, 2000, Springer, 2001: pp. 269–277.

[9] N.H. Sleep, K. Zahnle, P.S. Neuhoff, Initiation of clement surface conditions on the earliest Earth, Proceedings of the National Academy of Sciences. 98 (2001) 3666–3672.

[10] V.R. Oberbeck, G. Fogleman, Estimates of the maximum time required to originate life, Origins of Life and Evolution of the Biosphere. 19 (1989) 549–560.

[11] M.T. Rosing, D.K. Bird, N.H. Sleep, W. Glassley, F. Albarede, The rise of continents—an essay on the geologic consequences of photosynthesis, Palaeogeogr Palaeoclimatol Palaeoecol. 232 (2006) 99–113.

[12] A.H. Knoll, The geological consequences of evolution, Geobiology. 1 (2003) 3–14.

[13] B.S. Lieberman, Geobiology and paleobiogeography: tracking the coevolution of the Earth and its biota, Palaeogeogr Palaeoclimatol Palaeoecol. 219 (2005) 23–33.

[14] C.S. Cockell, M. Balme, J.C. Bridges, A. Davila, S.P. Schwenzer, Uninhabited habitats on Mars, Icarus. 217 (2012) 184–193. https://doi.org/10.1016/j.icarus.2011.10.025.

[15] C.S. Cockell, T. Bush, C. Bryce, S. Direito, M. Fox-Powell, J.P. Harrison, H. Lammer, H. Landenmark, J. Martin-Torres, N. Nicholson, L. Noack, J. O'Malley-James, S.J. Payler, A. Rushby, T. Samuels, P. Schwendner, J. Wadsworth, M.P. Zorzano, Habitability: A Review, Astrobiology. 16 (2016) 89–117. https://doi.org/10.1089/ast.2015.1295.

[16] T. Hoehler, W. Bains, A. Davila, M. Parenteau, A. Pohorille, Life's requirements, habitability, and biological potential, Planet. Astrobiol. 13 (2020) 37.

[17] Space Studies Board and National Research Council, An Astrobiology Strategy for the Exploration of Mars, National Academies Press, Washington, DC, 2007.

[18] N. Lane, W.F. Martin, The origin of membrane bioenergetics, Cell. 151 (2012) 1406–1416.

[19] J.J.R.F. Da Silva, R.J.P. Williams, The biological chemistry of the elements: the inorganic chemistry of life, Oxford University Press, 2001.

[20] C.S. Cockell, Astrobiology: understanding life in the universe, John Wiley & Sons, 2020.

[21] J.J. Petkowski, W. Bains, S. Seager, On the potential of silicon as a building block for life, Life. 10 (2020) 1–47. https://doi.org/10.3390/life10060084.

[22] R. West, Chemistry of the Silicon-Silicon Double Bond, Angewandte Chemie International Edition in English. 26 (1987) 1201–1211. https://doi.org/10.1002/anie.198712013.

[23] A. Jacobs, ed., The effect of heteroatoms, in: Understanding Organic Reaction Mechanisms, Cambridge University Press, Cambridge, 1997: pp. 115–157. https://doi.org/DOI: 10.1017/CBO9781139170796.006.

[24] N.R. Pace, The universal nature of biochemistry, Proc Natl Acad Sci U S A. 98 (2001) 805–808. https://doi.org/10.1073/pnas.98.3.805.

[25] L.J. Rothschild, R.L. Mancinelli, Life in extreme environments, Nature. 409 (2001) 1092–1101.

[26] A. Pohorille, L.R. Pratt, Is Water the Universal Solvent for Life?, Origins of Life and Evolution of Biospheres. 42 (2012) 405–409. https://doi.org/10.1007/s11084-012-9301-6.

[27] C.S. Cockell, Trajectories of martian habitability, Astrobiology. 14 (2014) 182–203. https://doi.org/10.1089/ast.2013.1106.

[28] C.P. McKay, Requirements and limits for life in the context of exoplanets, Proc Natl Acad Sci U S A. 111 (2014) 12628–12633. https://doi.org/10.1073/pnas.1304212111.

[29] M.H. Carr, J.W. Head, Geologic history of Mars, Earth Planet Sci Lett. 294 (2010) 185–203. https://doi.org/10.1016/j.epsl.2009.06.042.

[30] I. Kanik, J.-P. Paul de Vera, Astrobiology of Mars, Europa, Titan and Enceladus-Most Likely Places for Alien Life, Frontiers in Astronomy and Space Sciences. 8 (2021) 643268.

[31] S.L. Nixon, C.R. Cousins, C.S. Cockell, Plausible microbial metabolisms on Mars, Astronomy and Geophysics. 54 (2013) 13–16. https://doi.org/10.1093/astrogeo/ats034.

[32] P.B. Price, T. Sowers, Temperature dependence of metabolic rates for microbial growth, maintenance, and survival, Proceedings of the National Academy of Sciences. 101 (2004) 4631–4636.

[33] R. Morita, Bacteria in Oligotrophic Environments: Starvation-Survival Lifestyle, Chapman & Hall, New York, 1997.

[34] G.J. Taylor, W. V. Boynton, J. Brückner, H. Wänke, G. Dreibus, K.E. Kerry, J.M. Keller, R.C. Reedy, L.G. Evans, R.D. Starr, S.W. Squyres, S. Karunatillake, O. Gasnault, S. Maurice, C. d'Uston, P. Englert, J.M. Dohm, V. Baker, D. Hamara, D.M. Janes, A.L. Sprague, K.J. Kim, D. Drake, Bulk composition and early differentiation of Mars, J Geophys Res Planets. 112 (2007). https://doi.org/10.1029/2005JE002645.

[35] C. Fitoussi, B. Bourdon, X. Wang, The building blocks of Earth and Mars: A close genetic link, Earth Planet Sci Lett. 434 (2016) 151–160.

[36] C. V. Manning, K.J. Zahnle, C.P. McKay, Impact processing of nitrogen on early Mars, Icarus. 199 (2009) 273–285. https://doi.org/10.1016/j.icarus.2008.10.015.

[37] C. V. Manning, C.P. McKay, K.J. Zahnle, The nitrogen cycle on Mars: Impact decomposition of near-surface nitrates as a source for a nitrogen steady state, Icarus. 197 (2008) 60–64. https://doi.org/10.1016/j.icarus.2008.04.015.

[38] R.L. Mancinelli, A. Banin, Where is the nitrogen on Mars?, Int J Astrobiol. 2 (2003) 217–225. https://doi.org/10.1017/S1473550403001599.

[39] R. Navarro-González, K.F. Navarro, P. Coll, C.P. McKay, J.C. Stern, B. Sutter, P.D. Archer, A. Buch, M. Cabane, P.G. Conrad, J.L. Eigenbrode, H.B. Franz, C. Freissinet, D.P. Glavin, J. V. Hogancamp, A.C. McAdam, C.A. Malespin, F.J. Martín-Torres, D.W. Ming, R. V. Morris, B. Prats, F. Raulin, J.A. Rodríguez-Manfredi, C. Szopa, M.P. Zorzano-Mier, P.R. Mahaffy, S. Atreya, M.G. Trainer, A.R. Vasavada, Abiotic Input of Fixed Nitrogen by Bolide Impacts to Gale Crater During the Hesperian: Insights From the Mars Science Laboratory, J Geophys Res Planets. 124 (2019) 94–113. https://doi.org/10.1029/2018JE005852.

[40] J.C. Stern, B. Sutter, R. Navarro-González, C.P. Mckay, P.D.A. Jr, A. Buch, A.E. Brunner, J.L. Eigenbrode, A.G. Fairen, H.B. Franz, D.P. Glavin, S. Kashyap, A.C. Mcadam, W. Douglas, A. Steele, C. Szopa, J.J. Wray, F. Javier, M. Zorzano, P.G. Conrad, R. Paul, J.C. Stern, B. Sutter, C. Freissinet, R. Navarro-González, C.P. Mckay, Evidence for indigenous nitrogen in sedimentary and aeolian deposits from the Curiosity rover investigations at Gale crater, Mars, Proc Natl Acad Sci U S A. 112 (2015) E3085. https://doi.org/10.1073/pnas.1507795112.

[41] W.F. McDonough, S.-S. Sun, The composition of the Earth, Chem Geol. 120 (1995) 223–253.

[42] S.R. Taylor, S. McLennan, Mars: crustal composition and evolution, 2009. https://doi.org/10.1017/cbo9780511575358.008.

[43] S.R. Taylor, S. McLennan, Planetary crusts: their composition, origin and evolution, Cambridge University Press, 2009.

[44] G.M. Martínez, C.N. Newman, A. De Vicente-Retortillo, E. Fischer, N.O. Renno, M.I. Richardson, A.G. Fairén, M. Genzer, S.D. Guzewich, R.M. Haberle, The modern near-

surface Martian climate: a review of in situ meteorological data from Viking to Curiosity, Space Sci Rev. 212 (2017) 295–338.

[45] W.H. Horne, R.P. Volpe, G. Korza, S. DePratti, I.H. Conze, I. Shuryak, T. Grebenc, V.Y. Matrosova, E.K. Gaidamakova, R. Tkavc, Effects of desiccation and freezing on microbial ionizing radiation survivability: considerations for mars sample return, Astrobiology. 22 (2022) 1337–1350.

[46] J.R. Michalski, T.C. Onstott, S.J. Mojzsis, J. Mustard, Q.H.S. Chan, P.B. Niles, S.S. Johnson, The Martian subsurface as a potential window into the origin of life, Nat Geosci. 11 (2018) 21–26. https://doi.org/10.1038/s41561-017-0015-2.

[47] C.I. Fassett, J.W.I. Head, The timing of martian valley network activity: Constraints from buffered crater counting, Icarus. 195 (2008) 61–89. https://doi.org/10.1016/j.icarus.2007.12.009.

[48] C.I. Fassett, J.W. Head III, Valley network-fed, open-basin lakes on Mars: Distribution and implications for Noachian surface and subsurface hydrology, Icarus. 198 (2008) 37–56.

[49] Y. Matsubara, A.D. Howard, J.P. Gochenour, Hydrology of early Mars: Valley network incision, J Geophys Res Planets. 118 (2013) 1365–1387.

[50] A. Grau Galofre, K.X. Whipple, P.R. Christensen, S.J. Conway, Valley Networks and the Record of Glaciation on Ancient Mars, Geophys Res Lett. 49 (2022) 1–10. https://doi.org/10.1029/2022GL097974.

[51] R.D. Wordsworth, The Climate of Early Mars, Annu Rev Earth Planet Sci. 44 (2016) 381–408. https://doi.org/10.1146/annurev-earth-060115-012355.

[52] A.D. Howard, J.M. Moore, R.P. Irwin III, An intense terminal epoch of widespread fluvial activity on early Mars: 1. Valley network incision and associated deposits, J Geophys Res Planets. 110 (2005).

[53] B.L. Ehlmann, J.F. Mustard, C.I. Fassett, S.C. Schon, J.W. Head, D.J. Des Marais, J.A. Grant, S.L. Murchie, Clay minerals in delta deposits and organic preservation potential on Mars, Nat Geosci. 1 (2008) 355–358. https://doi.org/10.1038/ngeo207.

[54] G. de Villiers, M.G. Kleinhans, G. Postma, Experimental delta formation in crater lakes and implications for interpretation of Martian deltas, J Geophys Res Planets. 118 (2013) 651–670.

[55] V.G. Rangarajan, R. Bharti, S. Dutta, An Investigation of Hydrated Minerals in Jezero Crater, 12 (2018) 5–6.

[56] B.L. Ehlmann, J.F. Mustard, S.L. Murchie, J.-P. Bibring, A. Meunier, A.A. Fraeman, Y. Langevin, Subsurface water and clay mineral formation during the early history of Mars, Nature. 479 (2011) 53–60. https://doi.org/10.1038/nature10582.

[57] F. Poulet, J.-P. Bibring, J.F. Mustard, A. Gendrin, N. Mangold, Y. Langevin, R.E. Arvidson, B. Gondet, C. Gomez, M. Berthé, J.-P. Bibring, Y. Langevin, S. Erard, O. Forni, A. Gendrin, B. Gondet, N. Manaud, F. Poulet, G. Poulleau, A. Soufflot, M. Combes, P. Drossart, T. Encrenaz, T. Fouchet, R. Melchiorri, G. Bellucci, F. Altieri, V. Formisano, S. Fonti, F. Capaccioni, P. Cerroni, A. Coradini, O. Korablev, V. Kottsov, N. Ignatiev, D. Titov, L. Zasova, N. Mangold, P. Pinet, B. Schmitt, C. Sotin, E. Hauber, H. Hoffmann, R. Jaumann, U. Keller, R. Arvidson, J. Mustard, F. Forget, Phyllosilicates on Mars and implications for early martian climate, Nature. 438 (2005) 623–627. https://doi.org/10.1038/nature04274.

[58] B.L. Ehlmann, J.F. Mustard, G.A. Swayze, R.N. Clark, J.L. Bishop, F. Poulet, D.J. Des Marais, L.H. Roach, R.E. Milliken, J.J. Wray, Identification of hydrated silicate minerals on Mars using MRO-CRISM: Geologic context near Nili Fossae and implications for aqueous alteration, J Geophys Res Planets. 114 (2009).

[59] A.P. Broz, J. Clark, B. Sutter, D.W. Ming, V. Tu, B. Horgan, L.C.R. Silva, Mineralogy and diagenesis of Mars-analog paleosols from eastern Oregon, USA, Icarus. 380 (2022) 114965.

[60] E. Leask, B. Ehlmann, Evidence for Deposition of Chloride on Mars From Small-Volume Surface Water Events Into the Late Hesperian-Early Amazonian, AGU Advances. 3 (2021). https://doi.org/https://doi.org/10.1029/2021AV000534.

[61] B.L. Ehlmann, C.S. Edwards, Mineralogy of the Martian surface, Annu Rev Earth Planet Sci. 42 (2014) 291–315.

[62] A. Gendrin, N. Mangold, J.-P. Bibring, Y. Langevin, B. Gondet, F. Poulet, G. Bonello, C. Quantin, J. Mustard, R. Arvidson, Sulfates in Martian layered terrains: the OMEGA/Mars Express view, Science (1979). 307 (2005) 1587–1591.

[63] A. Grau Galofre, A.M. Jellinek, G.R. Osinski, Valley formation on early Mars by subglacial and fluvial erosion, Nat Geosci. 13 (2020) 663–668. https://doi.org/10.1038/s41561-020-0618-x.

[64] A.P. Jones, A.S. McEwen, L.L. Tornabene, V.R. Baker, H.J. Melosh, D.C. Berman, A geomorphic analysis of Hale crater, Mars: The effects of impact into ice-rich crust, Icarus. 211 (2011) 259–272.

[65] N. Mangold, Fluvial landforms on fresh impact ejecta on Mars, Planet Space Sci. 62 (2012) 69–85.

[66] T.L. Segura, O.B. Toon, A. Colaprete, K. Zahnle, Environmental effects of large impacts on Mars, Science (1979). 298 (2002) 1977–1980.

[67] M.M. Marinova, O. Aharonson, E. Asphaug, Mega-impact formation of the Mars hemispheric dichotomy, Nature. 453 (2008) 1216–1219.

[68] C.I. Fassett, J.W. Head III, Valley formation on martian volcanoes in the Hesperian: Evidence for melting of summit snowpack, caldera lake formation, drainage and erosion on Ceraunius Tholus, Icarus. 189 (2007) 118–135.

[69] C.I. Fassett, J.W. Head III, Valleys on Hecates Tholus, Mars: Origin by basal melting of summit snowpack, Planet Space Sci. 54 (2006) 370–378.

[70] V.C. Gulick, Magmatic intrusions and a hydrothermal origin for fluvial valleys on Mars, J Geophys Res Planets. 103 (1998) 19365–19387.

[71] R.J. Phillips, M.T. Zuber, S.C. Solomon, M.P. Golombek, B.M. Jakosky, W.B. Banerdt, D.E. Smith, R.M.E. Williams, B.M. Hynek, O. Aharonson, Ancient geodynamics and global-scale hydrology on Mars, Science (1979). 291 (2001) 2587–2591.

[72] J.W. Head, D.R. Marchant, Cold-based mountain glaciers on Mars: western Arsia Mons, Geology. 31 (2003) 641–644.

[73] T.L. Segura, C.P. McKay, O.B. Toon, An impact-induced, stable, runaway climate on Mars, Icarus. 220 (2012) 144–148.

[74] G.D. Clow, Generation of liquid water on Mars through the melting of a dusty snowpack, Icarus. 72 (1987) 95–127.

[75] I. Halevy, J.W. Head III, Episodic warming of early Mars by punctuated volcanism, Nat Geosci. 7 (2014) 865–868.

[76] M.H. Carr, J.W. Head, Basal melting of snow on early Mars: A possible origin of some valley networks, Geophys Res Lett. 30 (2003) 1–4. https://doi.org/10.1029/2003GL018575.

[77] M.P. Golombek, J.A. Grant, L.S. Crumpler, R. Greeley, R.E. Arvidson, J.F. Bell III, C.M. Weitz, R. Sullivan, P.R. Christensen, L.A. Soderblom, Erosion rates at the Mars Exploration Rover landing sites and long-term climate change on Mars, J Geophys Res Planets. 111 (2006).

[78] N.E. Putzig, M.T. Mellon, K.A. Kretke, R.E. Arvidson, Global thermal inertia and surface properties of Mars from the MGS mapping mission, Icarus. 173 (2005) 325–341.

[79] P.R. Christensen, J.L. Bandfield, V.E. Hamilton, S.W. Ruff, H.H. Kieffer, T.N. Titus, M.C. Malin, R. V Morris, M.D. Lane, R.L. Clark, Mars Global Surveyor Thermal Emission Spectrometer experiment: investigation description and surface science results, J Geophys Res Planets. 106 (2001) 23823–23871.

[80] L.A. Haskin, A. Wang, B.L. Jolliff, H.Y. McSween, B.C. Clark, D.J. Des Marais, S.M. McLennan, N.J. Tosca, J.A. Hurowitz, J.D. Farmer, Water alteration of rocks and soils on Mars at the Spirit rover site in Gusev crater, Nature. 436 (2005) 66–69.

[81] J.-P. Bibring, Y. Langevin, J.F. Mustard, F. Poulet, R. Arvidson, A. Gendrin, B. Gondet, N. Mangold, P. Pinet, F. Forget, Global mineralogical and aqueous Mars history derived from OMEGA/Mars Express data, Science (1979). 312 (2006) 400–404.

[82] B.M. Hynek, T.M. McCollom, A Volcanic Environment for Bedrock Diagenesis at Meridiani Planum, Mars, in: AGU Fall Meeting Abstracts, 2005: pp. P12A-08.

[83] L.P. Knauth, D.M. Burt, K.H. Wohletz, Impact origin of sediments at the Opportunity landing site on Mars, Nature. 438 (2005) 1123–1128.

[84] K.L. Tanaka, J.A. Skinner, T.M. Hare, Geologic map of the northern plains of Mars, US Department of the Interior, US Geological Survey, 2005.

[85] H.J. Leask, L. Wilson, K.L. Mitchell, Formation of Mangala Valles outflow channel, Mars: Morphological development and water discharge and duration estimates, J Geophys Res Planets. 112 (2007).

[86] L. Wilson, G.J. Ghatan, J.W. Head Iii, K.L. Mitchell, Mars outflow channels: A reappraisal of the estimation of water flow velocities from water depths, regional slopes, and channel floor properties, J Geophys Res Planets. 109 (2004).

[87] J.C. Hanna, R.J. Phillips, Hydrological modeling of the Martian crust with application to the pressurization of aquifers, J Geophys Res Planets. 110 (2005).

[88] M.H. Carr, Formation of Martian flood features by release of water from confined aquifers, J Geophys Res Solid Earth. 84 (1979) 2995–3007.

[89] B.L. Ehlmann, F.S. Anderson, D.C. Catling, P.R. Christensen, B.A. Cohen, C.D. Dressing, C.S. Edwards, K.A. Farley, C.I. Fassett, W.W. Fischer, A.A. Fraeman, M.P. Golombek, V.E. Hamilton, A.G. Hayes, C.D.K. Herd, B. Horgan, R. Hu, B.M. Jakosky, J.R. Johnson, J.F. Kasting, L. Kerber, K.M. Kinch, E.S. Kite, H.A. Knutson, J.I. Lunine, P.R. Mahaffy, N. Mangold, F.M. Mccubbin, J.F. Mustard, P.B. Niles, M.S. Rice, K.M. Stack, D.J. Stevenson, S.T. Stewart, M.J. Toplis, T. Usui, B.P. Weiss, S.C. Werner, R.D. Wordsworth, J.J. Wray, R.A. Yingst, Y.L. Yung, K.J. Zahnle, The sustainability of habitability on terrestrial planets: Insights, questions, and needed measurements from Mars for understanding the evolution of Earth-like worlds, J Geophys Res Planets. 121 (2016) 1927–1961. https://doi.org/10.1002/2016JE005134.Received.

[90] J.H. Roberts, R.J. Lillis, M. Manga, Giant impacts on early Mars and the cessation of the Martian dynamo, J Geophys Res Planets. 114 (2009).

[91] J. Ruiz, The early heat loss evolution of Mars and their implications for internal and environmental history, Sci Rep. 4 (2014) 4338.

[92] B.M. Jakosky, R.O. Pepin, R.E. Johnson, J.L. Fox, Mars atmospheric loss and isotopic fractionation by solar-wind-induced sputtering and photochemical escape, Icarus. 111 (1994) 271–288.

[93] B.M. Jakosky, Atmospheric loss to space and the history of water on Mars, Annu Rev Earth Planet Sci. 49 (2021) 71–93.

[94] H.J. Melosh, A.M. Vickery, Impact erosion of the primordial atmosphere of Mars, Nature. 338 (1989) 487–489.

[95] R. Hu, T.B. Thomas, A nitrogen-rich atmosphere on ancient Mars consistent with isotopic evolution models, Nat Geosci. 15 (2022) 106–111. https://doi.org/10.1038/s41561-021-00886-y.

[96] I. Halevy, M.T. Zuber, D.P. Schrag, A sulfur dioxide climate feedback on early Mars, Science (1979). 318 (2007) 1903–1907.

[97] J. Head, L. Wilson, The Noachian-Hesperian Transition on Mars: Geological Evidence for a Punctuated Phase of Global Volcanism as a Key Driver in Climate and Atmospheric Evolution, in: 42nd Lunar and Planetary Science Conference, 2011.

[98] M.C. Malin, M.H. Carr, Groundwater formation of Martian valleys, Nature. 397 (1999) 589.

[99] R. Orosei, S.E. Lauro, E. Pettinelli, A. Cicchetti, M. Coradini, B. Cosciotti, F. Di Paolo, E. Flamini, E. Mattei, M. Pajola, Radar evidence of subglacial liquid water on Mars, Science (1979). 361 (2018) 490–493.

[100] I.B. Smith, D.E. Lalich, C. Rezza, B.H.N. Horgan, J.L. Whitten, S. Nerozzi, J.W. Holt, A solid interpretation of bright radar reflectors under the Mars south polar ice, Geophys Res Lett. 48 (2021) e2021GL093618.

[101] A.G. Fairén, A.F. Davila, D. Lim, N. Bramall, R. Bonaccorsi, J. Zavaleta, E.R. Uceda, C. Stoker, J. Wierzchos, J.M. Dohm, R. Amils, D. Andersen, C.P. McKay, Astrobiology

through the ages of Mars: The study of terrestrial analogues to understand the habitability of Mars, Astrobiology. 10 (2010) 821–843. https://doi.org/10.1089/ast.2009.0440.

[102] I-MIM MDT, Final Report of the International Mars Ice Mapper Reconnaissance/Science Measurement Definition Team, 2022. https://doi.org/10.1016/S0065-2113(08)60505-2.

[103] J.L. Dickson, A.M. Palumbo, J.W. Head, L. Kerber, C.I. Fassett, M.A. Kreslavsky, Gullies on Mars could have formed by melting of water ice during periods of high obliquity, Science (1979). 380 (2023) 1363–1367.

[104] M. Willmes, D. Reiss, H. Hiesinger, M. Zanetti, Surface age of the ice–dust mantle deposit in Malea Planum, Mars, Planet Space Sci. 60 (2012) 199–206.

[105] J.F. Mustard, C.D. Cooper, M.K. Rifkin, Evidence for recent climate change on Mars from the identification of youthful near-surface ground ice, Nature. 412 (2001) 411–414.

[106] S.J. Kadish, J.W. Head, R.L. Parsons, D.R. Marchant, The Ascraeus Mons fan-shaped deposit: Volcano–ice interactions and the climatic implications of cold-based tropical mountain glaciation, Icarus. 197 (2008) 84–109.

[107] K.E. Scanlon, J.W. Head, D.R. Marchant, Volcanism-induced, local wet-based glacial conditions recorded in the Late Amazonian Arsia Mons tropical mountain glacier deposits, Icarus. 250 (2015) 18–31. https://doi.org/10.1016/j.icarus.2014.11.016.

[108] K.E. Scanlon, J.W. Head, L. Wilson, D.R. Marchant, Volcano-ice interactions in the Arsia Mons tropical mountain glacier deposits, Icarus. 237 (2014) 315–339. https://doi.org/10.1016/j.icarus.2014.04.024.

[109] C. Gallagher, F.E.G. Butcher, M. Balme, I. Smith, N. Arnold, Landforms indicative of regional warm based glaciation, Phlegra Montes, Mars, Icarus. 355 (2021) 114173. https://doi.org/10.1016/j.icarus.2020.114173.

[110] S.Z. Woodley, F.E.G. Butcher, P. Fawdon, C.D. Clark, F.S.L. Ng, J.M. Davis, C. Gallagher, Multiple sites of recent wet-based glaciation identified from eskers in western Tempe Terra, Mars, Icarus. 386 (2022) 115147. https://doi.org/10.1016/j.icarus.2022.115147.

[111] F.E. Butcher, M.R. Balme, C. Gallagher, N.S. Arnold, S.J. Conway, A. Hagermann, S.R. Lewis, Recent Basal Melting of a Mid-Latitude Glacier on Mars, J Geophys Res Planets. 122 (2017) 2445–2468.

[112] F.E.G. Butcher, M.R. Balme, S.J. Conway, C. Gallagher, N.S. Arnold, R.D. Storrar, S.R. Lewis, A. Hagermann, J.M. Davis, Sinuous ridges in Chukhung crater, Tempe Terra, Mars: Implications for fluvial, glacial, and glaciofluvial activity, Icarus. 357 (2021) 114131. https://doi.org/10.1016/j.icarus.2020.114131.

[113] F. Westall, D. Loizeau, F. Foucher, N. Bost, M. Betrand, J. Vago, G. Kminek, Habitability on mars from a microbial point of view, Astrobiology. 13 (2013) 887–897. https://doi.org/10.1089/ast.2013.1000.

[114] F. Westall, F. Foucher, N. Bost, M. Bertrand, D. Loizeau, J.L. Vago, G. Kminek, F. Gaboyer, K.A. Campbell, J.-G. Bréhéret, P. Gautret, C.S. Cockell, Biosignatures on Mars: What, Where, and How? Implications for the Search for Martian Life, Astrobiology. 15 (2015) 998–1029. https://doi.org/10.1089/ast.2015.1374.

[115] J.L. Vago, F. Westall, A.J. Coates, R. Jaumann, O. Korablev, V. Ciarletti, I. Mitrofanov, J.L. Josset, M.C. De Sanctis, J.P. Bibring, F. Rull, F. Goesmann, H. Steininger, W. Goetz, W. Brinckerhoff, C. Szopa, F. Raulin, H.G.M. Edwards, L.G. Whyte, A.G. Fairén, J. Bridges, E. Hauber, G.G. Ori, S. Werner, D. Loizeau, R.O. Kuzmin, R.M.E. Williams, J. Flahaut, F. Forget, D. Rodionov, H. Svedhem, E. Sefton-Nash, G. Kminek, L. Lorenzoni, L. Joudrier, V. Mikhailov, A. Zashchirinskiy, S. Alexashkin, F. Calantropio, A. Merlo, P. Poulakis, O. Witasse, O. Bayle, S. Bayón, U. Meierhenrich, J. Carter, J.M. García-Ruiz, P. Baglioni, A. Haldemann, A.J. Ball, A. Debus, R. Lindner, F. Haessig, D. Monteiro, R. Trautner, C. Voland, P. Rebeyre, D. Goulty, F. Didot, S. Durrant, E. Zekri, D. Koschny, A. Toni, G. Visentin, M. Zwick, M. Van Winnendael, M. Azkarate, C. Carreau, Habitability on Early Mars and the Search for Biosignatures with the ExoMars Rover, Astrobiology. 17 (2017) 471–510. https://doi.org/10.1089/ast.2016.1533.

[116] J.R. Sedell, G.H. Reeves, F.R. Hauer, J.A. Stanford, C.P. Hawkins, Role of refugia in recovery from disturbances: modern fragmented and disconnected river systems, Environ Manage. 14 (1990) 711–724.

[117] C.I. Fraser, A. Terauds, J. Smellie, P. Convey, S.L. Chown, Geothermal activity helps life survive glacial cycles, Proc Natl Acad Sci U S A. 111 (2014) 5634–5639. https://doi.org/10.1073/pnas.1321437111.

[118] G.M. Hewitt, Genetic consequences of climatic oscillations in the Quaternary, Philosophical Transactions of the Royal Society B: Biological Sciences. 359 (2004) 183–195. https://doi.org/10.1098/rstb.2003.1388.

[119] B.L. Carrier, D.W. Beaty, M.A. Meyer, J.G. Blank, L. Chou, S. Dassarma, D.J. Des Marais, J.L. Eigenbrode, N. Grefenstette, N.L. Lanza, A.C. Schuerger, P. Schwendner, H.D. Smith, C.R. Stoker, J.D. Tarnas, K.D. Webster, C. Bakermans, B.K. Baxter, M.S. Bell, S.A. Benner, H.H. Bolivar Torres, P.J. Boston, R. Bruner, B.C. Clark, P. Dassarma, A.E. Engelhart, Z.E. Gallegos, Z.K. Garvin, P.J. Gasda, J.H. Green, R.L. Harris, M.E. Hoffman, T. Kieft, A.H.D. Koeppel, P.A. Lee, X. Li, K.L. Lynch, R. MacKelprang, P.R. Mahaffy, L.H. Matthies, M.A. Nellessen, H.E. Newsom, D.E. Northup, B.R.W. O'Connor, S.M. Perl, R.C. Quinn, L.A. Rowe, B. Sauterey, M.A. Schneegurt, D. Schulze-Makuch, L.A. Scuderi, M.N. Spilde, V. Stamenković, J.A. Torres Celis, D. Viola, B.D. Wade, C.J. Walker, R.C. Wiens, A.J. Williams, J.M. Williams, J. Xu, Mars Extant Life: What's Next? Conference Report, Astrobiology. 20 (2020) 785–814. https://doi.org/10.1089/ast.2020.2237.

[120] C.R. Cousins, I.A. Crawford, Volcano-ice interaction as a microbial habitat on Earth and Mars, Astrobiology. 11 (2011) 695–710. https://doi.org/10.1089/ast.2010.0550.

[121] M.S. Phillips, M. McInenly, M.H. Hofmann, N.W. Hinman, K. Warren-Rhodes, E.G. Rivera-Valentín, N.A. Cabrol, Salt Constructs in Paleo-Lake Basins as High-Priority Astrobiology Targets, Remote Sens (Basel). 15 (2023) 314.

[122] J.L. Smellie, The relative importance of supraglacial versus subglacial meltwater escape in basaltic subglacial tuya eruptions: An important unresolved conundrum, Earth Sci Rev. 74 (2006) 241–268. https://doi.org/10.1016/j.earscirev.2005.09.004.

[123] A.A. Agrawal, Phenotypic plasticity in the interactions and evolution of species, Science (1979). 294 (2001) 321–326.

[124] L.J. Rothschild, The evolution of photosynthesis… again?, Philosophical Transactions of the Royal Society B: Biological Sciences. 363 (2008) 2787–2801.

[125] N.H. Sleep, D.K. Bird, Niches of the pre-photosynthetic biosphere and geologic preservation of Earth's earliest ecology, Geobiology. 5 (2007) 101–117. https://doi.org/10.1111/j.1472-4669.2007.00105.x.

[126] D.J. Des Marais, L.J. Allamandola, S.A. Benner, A.P. Boss, D. Deamer, P.G. Falkowski, J.D. Farmer, S.B. Hedges, B.M. Jakosky, A.H. Knoll, The NASA astrobiology roadmap, Astrobiology. 3 (2003) 219–235.

[127] C.D. Georgiou, D.W. Deamer, Lipids as universal biomarkers of extraterrestrial life, Astrobiology. 14 (2014) 541–549. https://doi.org/10.1089/ast.2013.1134.

[128] M. Derrien, L. Yang, J. Hur, Lipid biomarkers and spectroscopic indices for identifying organic matter sources in aquatic environments: A review, Water Res. 112 (2017) 58–71. https://doi.org/10.1016/j.watres.2017.01.023.

[129] P.L. Finkel, D. Carrizo, V. Parro, L. Sa, An Overview of Lipid Biomarkers in Terrestrial Extreme Environments with Relevance for Mars Exploration, Astrobiology. 23 (2023). https://doi.org/10.1089/ast.2022.0083.

[130] Y.M. Zhang, C.O. Rock, Membrane lipid homeostasis in bacteria, Nat Rev Microbiol. 6 (2008) 222–233. https://doi.org/10.1038/nrmicro1839.

[131] J.J. Brocks, R.E. Summons, W. Schlesinger, Sedimentary hydrocarbons, biomarkers for early life, Treatise on Geochemistry. 8 (2005) 63–115.

[132] G. Vinnichenko, A.J.M. Jarrett, J.M. Hope, J.J. Brocks, Discovery of the oldest known biomarkers provides evidence for phototrophic bacteria in the 1.73 Ga Wollogorang Formation, Australia, Geobiology. 18 (2020) 544–559. https://doi.org/10.1111/gbi.12390.

[133] A.J.M. Jarrett, G.M. Cox, J.J. Brocks, E. Grosjean, C.J. Boreham, D.S. Edwards, Microbial assemblage and palaeoenvironmental reconstruction of the 1.38 Ga Velkerri Formation, McArthur Basin, northern Australia, Geobiology. 17 (2019) 360–380. https://doi.org/10.1111/gbi.12331.

[134] J.J. Wray, Gale crater: the Mars Science Laboratory/Curiosity rover landing site, Int J Astrobiol. 12 (2013) 25–38.

[135] N. Mangold, S. Gupta, O. Gasnault, G. Dromart, J.D. Tarnas, S.F. Sholes, B. Horgan, C. Quantin-Nataf, A.J. Brown, S. Le Mouélic, Perseverance rover reveals an ancient delta-lake system and flood deposits at Jezero crater, Mars, Science (1979). 374 (2021) 711–717.

[136] C. Quantin-Nataf, J. Carter, L. Mandon, P. Thollot, M. Balme, M. Volat, L. Pan, D. Loizeau, C. Millot, S. Breton, Oxia Planum: The landing site for the ExoMars "Rosalind Franklin" rover mission: Geological context and prelanding interpretation, Astrobiology. 21 (2021) 345–366.

[137] E. Kornobis, S. PÁlsson, B.K. KristjÁnsson, J. Svavarsson, Molecular evidence of the survival of subterranean amphipods (Arthropoda) during Ice Age underneath glaciers in Iceland, Mol Ecol. 19 (2010) 2516–2530. https://doi.org/10.1111/j.1365-294X.2010.04663.x.

[138] S.C. Brown, T.M.L. Wigley, B.L. Otto-Bliesner, C. Rahbek, D.A. Fordham, Persistent Quaternary climate refugia are hospices for biodiversity in the Anthropocene, Nat Clim Chang. 10 (2020) 244–248.

[139] F. Médail, K. Diadema, Glacial refugia influence plant diversity patterns in the Mediterranean Basin, J Biogeogr. 36 (2009) 1333–1345. https://doi.org/10.1111/j.1365-2699.2008.02051.x.

[140] C. Parisod, Plant speciation in the face of recurrent climate changes in the Alps, Alp Bot. 132 (2022) 21–28.

[141] L. Wilson, J.W. Head III, Heat transfer and melting in subglacial basaltic volcanic eruptions: implications for volcanic deposit morphology and meltwater volumes, Geological Society, London, Special Publications. 202 (2002) 5–26.

[142] F. Butcher, Wet-Based Glaciation on Mars, (2019). https://doi.org/10.21954/ou.ro.0000ed1f.

[143] H. Björnsson, Jökulhlaups in iceland: Sources, release and drainage, Megaflooding on Earth and Mars. (2009) 50–64. https://doi.org/10.1017/CBO9780511635632.004.

[144] I.D. Barr, C.M. Lynch, D. Mullan, L. De Siena, M. Spagnolo, Volcanic impacts on modern glaciers: A global synthesis, Earth Sci Rev. 182 (2018) 186–203.

[145] J.L. Wadham, M. Tranter, M. Skidmore, A.J. Hodson, J. Priscu, W.B. Lyons, M. Sharp, P. Wynn, M. Jackson, Biogeochemical weathering under ice: Size matters, Global Biogeochem Cycles. 24 (2010). https://doi.org/10.1029/2009GB003688.

[146] H. V. Pryer, J.R. Hawkings, J.L. Wadham, L.F. Robinson, K.R. Hendry, J.E. Hatton, A.M. Kellerman, S. Bertrand, B. Gill-Olivas, M.G. Marshall, R.A. Brooker, G. Daneri, V. Häussermann, The Influence of Glacial Cover on Riverine Silicon and Iron Exports in Chilean Patagonia, Global Biogeochem Cycles. 34 (2020). https://doi.org/10.1029/2020GB006611.

[147] T. Fegel, C.M. Boot, C.D. Broeckling, J.S. Baron, E.K. Hall, Assessing the chemistry and bioavailability of dissolved organic matter from glaciers and rock glaciers, J Geophys Res Biogeosci. 124 (2019) 1988–2004.

[148] C.S. Cockell, E. Bagshaw, M. Balme, P. Doran, C.P. Mckay, K. Miljkovic, D. Pearce, M.J. Siegert, M. Tranter, M. Voytek, J. Wadham, Subglacial Environments and the Search for Life Beyond the Earth, Antarctic Subglacial Aquatic Environments. (2011) 129–148. https://doi.org/10.1002/9781118670354.ch8.

[149] M. Skidmore, Microbial communities in Antarctic subglacial aquatic environments, Antarctic Subglacial Aquatic Environments. 192 (2011) 61–81.

[150] H.Y. McSween, G.J. Taylor, M.B. Wyatt, Elemental composition of the Martian crust, Science (1979). 324 (2009) 736–739.

[151] A.S. Yen, R. Gellert, C. Schröder, R. V Morris, J.F. Bell III, A.T. Knudson, B.C. Clark, D.W. Ming, J.A. Crisp, R.E. Arvidson, An integrated view of the chemistry and mineralogy of Martian soils, Nature. 436 (2005) 49–54.

[152] P.R. Christensen, H.Y. McSween Jr, J.L. Bandfield, S.W. Ruff, A.D. Rogers, V.E. Hamilton, N. Gorelick, M.B. Wyatt, B.M. Jakosky, H.H. Kieffer, Evidence for magmatic evolution and diversity on Mars from infrared observations, Nature. 436 (2005) 504–509.

[153] S.S. Hughes, C.W. Haberle, S.E. Kobs Nawotniak, A. Sehlke, W.B. Garry, R.C. Elphic, S.J. Payler, A.H. Stevens, C.S. Cockell, A.L. Brady, J.L. Heldmann, D.S.S. Lim, Basaltic Terrains in Idaho and Hawai'i as Planetary Analogs for Mars Geology and Astrobiology, Astrobiology. 19 (2019) 260–283. https://doi.org/10.1089/ast.2018.1847.

[154] L.C. Kelly, C.S. Cockell, Y.M. Piceno, G.L. Andersen, T. Thorsteinsson, V. Marteinsson, Bacterial Diversity of Weathered Terrestrial Icelandic Volcanic Glasses, Microb Ecol. 60 (2010) 740–752. https://doi.org/10.1007/s00248-010-9684-8.

[155] S. Bhattacharya, S. Mitra, S. Gupta, N. Jain, P. Chauhan, G. Parthasarathy, Ajai, Jarosite occurrence in the Deccan Volcanic Province of Kachchh, western India: Spectroscopic studies on a Martian analog locality, J Geophys Res Planets. 121 (2016) 402–431.

[156] J.J. Hagerty, H.E. Newsom, Hydrothermal alteration at the Lonar Lake impact structure, India: Implications for impact cratering on Mars, Meteorit Planet Sci. 38 (2003) 365–381.

[157] A.L. Brady, E. Gibbons, A. Sehlke, C.J. Renner, S.E. Kobs Nawotniak, D.S.S. Lim, G.F. Slater, Microbial community distribution in variously altered basalts: Insights into astrobiology sample site selection, Planet Space Sci. 194 (2020). https://doi.org/10.1016/j.pss.2020.105107.

[158] B.A. Óladóttir, O. Sigmarsson, G. Larsen, J.L. Devidal, Provenance of basaltic tephra from vatnajökull subglacial volcanoes, iceland, as determined by major- and trace-element analyses, Holocene. 21 (2011) 1037–1048. https://doi.org/10.1177/0959683611400456.

[159] S.P. Jakobsson, K. Jonasson, I.A. Sigurdsson, The three igneous rock series of Iceland, Jokull. 58 (2008) 117–138.

[160] M.T. Thorpe, J.A. Hurowitz, E. Dehouck, Sediment geochemistry and mineralogy from a glacial terrain river system in southwest Iceland, Geochim Cosmochim Acta. 263 (2019) 140–166. https://doi.org/10.1016/j.gca.2019.08.003.

[161] C.S. Cockell, S. McMahon, D.S.S. Lim, J. Rummel, A. Stevens, S.S. Hughes, S.E. Kobs Nawotniak, A.L. Brady, V. Marteinsson, J. Martin-Torres, M.P. Zorzano, J. Harrison, Sample Collection and Return from Mars: Optimising Sample Collection Based on the Microbial Ecology of Terrestrial Volcanic Environments, Space Sci Rev. 215 (2019). https://doi.org/10.1007/s11214-019-0609-7.

[162] H. Furnes, K. Muehlenbachs, T. Torsvik, I.H. Thorseth, O. Tumyr, Microbial fractionation of carbon isotopes in altered basaltic glass from the Atlantic Ocean, Lau Basin and Costa Rica Rift, Chem Geol. 173 (2001) 313–330. https://doi.org/10.1016/S0009-2541(00)00285-0.

[163] C.M. Santelli, B.N. Orcutt, E. Banning, W. Bach, C.L. Moyer, M.L. Sogin, H. Staudigel, K.J. Edwards, Abundance and diversity of microbial life in ocean crust, Nature. 453 (2008) 653–656.

[164] K. Lysnes, I.H. Thorseth, B.O. Steinsbu, L. Øvreås, T. Torsvik, R.B. Pedersen, Microbial community diversity in seafloor basalt from the Arctic spreading ridges, FEMS Microbiol Ecol. 50 (2004) 213–230.

[165] A. Yin, Structural analysis of the Valles Marineris fault zone: Possible evidence for large-scale strike-slip faulting on Mars, Lithosphere. 4 (2012) 286–330.

[166] R.C. Wiens, S. Maurice, F.R. Perez, The SuperCam remote sensing instrument suite for the mars 2020 rover: A preview, Spectroscopy (Santa Monica). 32 (2017) 50–55.

[167] R.C. Wiens, S. Maurice, ChemCam: Chemostratigraphy by the first mars microprobe, Elements. 11 (2015) 33–38. https://doi.org/10.2113/gselements.11.1.33.

[168] L.E. Hays, H. V. Graham, D.J. Des Marais, E.M. Hausrath, B. Horgan, T.M. McCollom, M.N. Parenteau, S.L. Potter-McIntyre, A.J. Williams, K.L. Lynch, Biosignature Preservation and Detection in Mars Analog Environments, Astrobiology. 17 (2017) 363–400. https://doi.org/10.1089/ast.2016.1627.

[169] M. Veneranda, J.A. Manrique, G. Lopez-Reyes, S. Julve-Gonzalez, F. Rull, C. Alvarez Llamas, T. Delgado Pérez, E. Gibbons, E. Clavé, E. Cloutis, Developing tailored data

combination strategies to optimize the SuperCam classification of carbonate phases on Mars, Earth and Space Science. 10 (2023) e2023EA002829.

[170] J.E. Chambers, G.W. Wetherill, Making the terrestrial planets: N-body integrations of planetary embryos in three dimensions, Icarus. 136 (1998) 304–327.

[171] C.W. Ormel, H.H. Klahr, The effect of gas drag on the growth of protoplanets-analytical expressions for the accretion of small bodies in laminar disks, Astron Astrophys. 520 (2010) A43.

[172] M.S. Clement, N.A. Kaib, S.N. Raymond, K.J. Walsh, Mars' growth stunted by an early giant planet instability, Icarus. 311 (2018) 340–356.

### 6.4.2 Chapter 6

[1] A.G. Fairén, V. Parro, D. Schulze-Makuch, L. Whyte, Searching for life on Mars before it is too late, Astrobiology. 17 (2017) 962–970.

[2] J.D. Rummel, D.W. Beaty, M.A. Jones, C. Bakermans, N.G. Barlow, P.J. Boston, V.F. Chevrier, B.C. Clark, J.-P.P. de Vera, R. V Gough, A new analysis of Mars "special regions": findings of the second MEPAG Special Regions Science Analysis Group (SR-SAG2), (2014).

[3] A.G. Fairen, D. Schulze-Makuch, L. Whyte, V. Parro, A. Pavlov, J. Gomez-Elvira, A. Azua-Bustos, W. Fink, V. Baker, Planetary protection and the astrobiological exploration of Mars: proactive steps in moving forward, Advances in Space Research. 63 (2019) 1491–1497.

[4] C.A. Conley, J.D. Rummel, Planetary protection for human exploration of Mars, Acta Astronaut. 66 (2010) 792–797.

[5] B.L. Carrier, D.W. Beaty, M.A. Meyer, J.G. Blank, L. Chou, S. Dassarma, D.J. Des Marais, J.L. Eigenbrode, N. Grefenstette, N.L. Lanza, A.C. Schuerger, P. Schwendner, H.D. Smith, C.R. Stoker, J.D. Tarnas, K.D. Webster, C. Bakermans, B.K. Baxter, M.S. Bell, S.A. Benner, H.H. Bolivar Torres, P.J. Boston, R. Bruner, B.C. Clark, P. Dassarma, A.E. Engelhart, Z.E. Gallegos, Z.K. Garvin, P.J. Gasda, J.H. Green, R.L. Harris, M.E. Hoffman, T. Kieft, A.H.D. Koeppel, P.A. Lee, X. Li, K.L. Lynch, R. MacKelprang, P.R.

Mahaffy, L.H. Matthies, M.A. Nellessen, H.E. Newsom, D.E. Northup, B.R.W. O'Connor, S.M. Perl, R.C. Quinn, L.A. Rowe, B. Sauterey, M.A. Schneegurt, D. Schulze-Makuch, L.A. Scuderi, M.N. Spilde, V. Stamenković, J.A. Torres Celis, D. Viola, B.D. Wade, C.J. Walker, R.C. Wiens, A.J. Williams, J.M. Williams, J. Xu, Mars Extant Life: What's Next? Conference Report, Astrobiology. 20 (2020) 785–814. https://doi.org/10.1089/ast.2020.2237.

[6] A. Williams, B. Muirhead, Mars Life Explorer: Mission Concept Study, in: Planetary Science and Astrobiology Decadal Survey, 2021.

[7] M.S. Thomsen, A.H. Altieri, C. Angelini, M.J. Bishop, F. Bulleri, R. Farhan, V.M.M. Frühling, P.E. Gribben, S.B. Harrison, Q. He, Heterogeneity within and among co-occurring foundation species increases biodiversity, Nat Commun. 13 (2022) 581.

[8] A. Stein, K. Gerstner, H. Kreft, Environmental heterogeneity as a universal driver of species richness across taxa, biomes and spatial scales, Ecol Lett. 17 (2014) 866–880.

[9] C.R. Cousins, M. Fogel, R. Bowden, I. Crawford, A. Boyce, C. Cockell, M. Gunn, Biogeochemical probing of microbial communities in a basalt-hosted hot spring at Kverkfjöll volcano, Iceland, Geobiology. 16 (2018) 507–521. https://doi.org/10.1111/gbi.12291.

[10] M.J. Kennedy, T. Wagner, Clay mineral continental amplifier for marine carbon sequestration in a greenhouse ocean, Proc Natl Acad Sci U S A. 108 (2011) 9776–9781. https://doi.org/10.1073/pnas.1018670108.

[11] M.J. Kennedy, D.R. Pevear, R.J. Hill, Mineral Surface Control of Organic Carbon in Black Shale, Science (1979). 295 (2002) 657–660.

[12] M.J. Kennedy, S.C. Löhr, S.A. Fraser, E.T. Baruch, Direct evidence for organic carbon preservation as clay-organic nanocomposites in a Devonian black shale; from deposition to diagenesis, Earth Planet Sci Lett. 388 (2014) 59–70. https://doi.org/10.1016/j.epsl.2013.11.044.

[13] B. Ransom, D. Kim, M. Kastner, S. Wainwright, Organic matter preservation on continental slopes: importance of mineralogy and surface area, Geochim Cosmochim Acta. 62 (1998) 1329–1345. https://doi.org/10.1016/S0016-7037(98)00050-7.

[14] R.G. Keil, D.B. Montluçon, F.G. Prahl, J.I. Hedges, Sorptive preservation of labile organic matter in marine sediments, Nature. 370 (1994) 549.

[15] D.A. Reid-Soukup, A.L. Ulery, Smectites, Soil Mineralogy with Environmental Applications. 7 (2002) 467–499.

[16] J.L. Eigenbrode, R.E. Summons, A. Steele, C. Freissinet, M. Millan, R. Navarro-González, B. Sutter, A.C. McAdam, H.B. Franz, D.P. Glavin, P.D. Archer, P.R. Mahaffy, P.G. Conrad, J.A. Hurowitz, J.P. Grotzinger, S. Gupta, D.W. Ming, D.Y. Sumner, C. Szopa, C. Malespin, A. Buch, P. Coll, Organic matter preserved in 3-billion-year-old mudstones at Gale crater, Mars, Science (1979). 360 (2018). https://doi.org/10.1126/science.aas9185.

[17] C.R. Cousins, I.A. Crawford, Volcano-ice interaction as a microbial habitat on Earth and Mars, Astrobiology. 11 (2011) 695–710. https://doi.org/10.1089/ast.2010.0550.

[18] A. Moreras-Marti, M. Fox-Powell, A.L. Zerkle, E. Stueeken, F. Gazquez, H.E.A. Brand, T. Galloway, L. Purkamo, C.R. Cousins, Volcanic controls on the microbial habitability of analogue hydrothermal environments, Geobiology. (2021) 1–21. https://doi.org/10.1111/gbi.12459.

[19] P. Fulignati, Clay minerals in hydrothermal systems, Minerals. 10 (2020) 1–17. https://doi.org/10.3390/min10100919.

[20] E.J.W. Wattel-Koekkoek, P. Buurman, J. Van Der Plicht, E. Wattel, N. Van Breemen, Mean residence time of soil organic matter associated with kaolinite and smectite, Eur J Soil Sci. 54 (2003) 269–278. https://doi.org/10.1046/j.1365-2389.2003.00512.x.

[21] N.H. Warner, J.D. Farmer, Subglacial hydrothermal alteration minerals in Jökulhlaup deposits of Southern Iceland, with implications for detecting past or present habitable environments on mars, Astrobiology. 10 (2010) 523–547. https://doi.org/10.1089/ast.2009.0425.

[22] C.R. Cousins, Volcano-ice interaction: a haven for life on Mars?, Astronomy & Geophysics. 52 (2011) 1.36-1.38. https://doi.org/10.1111/j.1468-4004.2011.52136.x.

[23] K.E. Scanlon, J.W. Head, D.R. Marchant, Volcanism-induced, local wet-based glacial conditions recorded in the Late Amazonian Arsia Mons tropical mountain glacier deposits, Icarus. 250 (2015) 18–31. https://doi.org/10.1016/j.icarus.2014.11.016.

[24] S. Ackiss, B. Horgan, F. Seelos, W. Farrand, J. Wray, Mineralogic evidence for subglacial volcanism in the Sisyphi Montes region of Mars, Icarus. 311 (2018) 357–370. https://doi.org/10.1016/j.icarus.2018.03.026.

[25] J.L. Smellie, B.R. Edwards, Glaciovolcanism on Earth and Mars: Products, Processes and Palaeoenvironmental Significance, 2016. https://doi.org/10.1017/CBO9781139764384.

[26] D. Schulze-Makuch, J.M. Dohm, C. Fan, A.G. Fairén, J.A.P. Rodriguez, V.R. Baker, W. Fink, Exploration of hydrothermal targets on Mars, Icarus. 189 (2007) 308–324. https://doi.org/10.1016/j.icarus.2007.02.007.

[27] E.S. Varnes, B.M. Jakosky, T.M. McCollom, Biological potential of Martian hydrothermal systems, Astrobiology. 3 (2003) 407–414.

[28] E.B. Rampe, B.H.N. Horgan, R.J. Smith, N.A. Scudder, E.R. Bamber, A.M. Rutledge, R. Christoffersen, A mineralogical study of glacial flour from Three Sisters, Oregon: An analog for a cold and icy early Mars, Earth Planet Sci Lett. 584 (2022) 117471.

[29] R.A. Yingst, J. Berger, B.A. Cohen, B. Hynek, M.E. Schmidt, Determining best practices in reconnoitering sites for habitability potential on Mars using a semi-autonomous rover: a GeoHeuristic Operational Strategies Test, Acta Astronaut. 132 (2017) 268–281.

[30] D. Deamer, The role of lipid membranes in life's origin, Life. 7 (2017) 5.

[31] A.J. Williams, K.L. Craft, S.S. Johnson, C.A. Knudson, M.J. Rivera, A.C. Mcadam, D. Tobler, J.R. Skok, Fatty Acid Preservation in Modern and Relict Hot-Spring Deposits Deposits in Iceland, with Implications for Organics Detection on Mars, Astrobiology. 21 (2021) 1–23. https://doi.org/10.1089/ast.2019.2115.

[32] P.L. Finkel, D. Carrizo, V. Parro, L. Sa, An Overview of Lipid Biomarkers in Terrestrial Extreme Environments with Relevance for Mars Exploration, Astrobiology. 23 (2023). https://doi.org/10.1089/ast.2022.0083.

[33] E.S. Boyd, K.M. Fecteau, J.R. Havig, E.L. Shock, J.W. Peters, Modeling the habitat range of phototrophs in Yellowstone National Park: toward the development of a comprehensive fitness landscape, Front Microbiol. 3 (2012) 221.

[34] E. Clavé, K. Benzerara, P. Meslin, O. Forni, C. Royer, L. Mandon, P. Beck, C. Quantin-Nataf, O. Beyssac, A. Cousin, Carbonate detection with SuperCam in igneous rocks on the floor of Jezero Crater, Mars, J Geophys Res Planets. 128 (2023) e2022JE007463.

[35] T. Delgado, L. García-Gómez, L.M. Cabalín, J.J. Laserna, Detectability and discrimination of biomarker organic precursors in a low pressure CO 2 atmosphere by LIBS, J Anal At Spectrom. 35 (2020) 1947–1955.

[36] A.M. Ollila, J.G. Blank, H.E. Newsom, P.L. King, D.A. Cremers, Detection of Biosignatures in a Mars-Like Environment Using LIBS, AGUFM. 2009 (2009) P43C-1452.

[37] A.M. Ollila, J.G. Blank, R.C. Wiens, J. Lasue, H.E. Newsom, S.M. Clegg, A. Cousin, S. Maurice, Preliminary Results on the Capabilities of the ChemCam Laser-Induced Breakdown Spectroscopy (LIBS) Instrument to Detect Carbon on Mars, 42nd Lunar and Planetary Science Conference. (2011) 2395. http://adsabs.harvard.edu/abs/2011LPI....42.2395O%0Ahttp://www.lpi.usra.edu/meetings/lpsc2011/pdf/2395.pdf.

[38] T. Dequaire, P.Y. Meslin, P. Beck, M. Jaber, A. Cousin, W. Rapin, J. Lasne, O. Gasnault, S. Maurice, A. Buch, C. Szopa, P. Coll, Analysis of carbon and nitrogen signatures with laser-induced breakdown spectroscopy; the quest for organics under Mars-like conditions, Spectrochim Acta Part B At Spectrosc. 131 (2017) 8–17. https://doi.org/10.1016/j.sab.2017.02.015.

[39] C. Gallagher, F.E.G. Butcher, M. Balme, I. Smith, N. Arnold, Landforms indicative of regional warm based glaciation, Phlegra Montes, Mars, Icarus. 355 (2021) 114173. https://doi.org/10.1016/j.icarus.2020.114173.

[40] F.E.G. Butcher, M.R. Balme, C. Gallagher, N.S. Arnold, S.J. Conway, A. Hagermann, S.R. Lewis, Recent Basal Melting of a Mid-Latitude Glacier on Mars, J Geophys Res Planets. 122 (2017) 2445–2468. https://doi.org/10.1002/2017JE005434.

[41] S.Z. Woodley, F.E.G. Butcher, P. Fawdon, C.D. Clark, F.S.L. Ng, J.M. Davis, C. Gallagher, Multiple sites of recent wet-based glaciation identified from eskers in western Tempe Terra, Mars, Icarus. 386 (2022) 115147. https://doi.org/10.1016/j.icarus.2022.115147.

[42] F.E.G. Butcher, M.R. Balme, S.J. Conway, C. Gallagher, N.S. Arnold, R.D. Storrar, S.R. Lewis, A. Hagermann, J.M. Davis, Sinuous ridges in Chukhung crater, Tempe Terra, Mars: Implications for fluvial, glacial, and glaciofluvial activity, Icarus. 357 (2021) 114131. https://doi.org/10.1016/j.icarus.2020.114131.

[43] K.E. Scanlon, J.W. Head, L. Wilson, D.R. Marchant, Volcano-ice interactions in the Arsia Mons tropical mountain glacier deposits, Icarus. 237 (2014) 315–339. https://doi.org/10.1016/j.icarus.2014.04.024.

[44] C.S. Cockell, S. McMahon, D.S.S. Lim, J. Rummel, A. Stevens, S.S. Hughes, S.E. Kobs Nawotniak, A.L. Brady, V. Marteinsson, J. Martin-Torres, M.P. Zorzano, J. Harrison, Sample Collection and Return from Mars: Optimising Sample Collection Based on the Microbial Ecology of Terrestrial Volcanic Environments, Space Sci Rev. 215 (2019). https://doi.org/10.1007/s11214-019-0609-7.

[45] A.J. Williams, J. Eigenbrode, M. Floyd, M.B. Wilhelm, S. O'Reilly, S.S. Johnson, K.L. Craft, C.A. Knudson, S. Andrejkovičová, J.M.T. Lewis, A. Buch, D.P. Glavin, C. Freissinet, R.H. Williams, C. Szopa, M. Millan, R.E. Summons, A. McAdam, K. Benison, R. Navarro-González, C. Malespin, P.R. Mahaffy, Recovery of Fatty Acids from Mineralogic Mars Analogs by TMAH Thermochemolysis for the Sample Analysis at Mars Wet Chemistry Experiment on the Curiosity Rover, Astrobiology. 19 (2019) 522–546. https://doi.org/10.1089/ast.2018.1819.

[46] J. Tan, J.M.T. Lewis, M.A. Sephton, The Fate of Lipid Biosignatures in a Mars-Analogue Sulfur Stream, Sci Rep. 8 (2018) 1–8. https://doi.org/10.1038/s41598-018-25752-7.

[47] J.L. Eigenbrode, Fossil lipids for life-detection: A case study from the early Earth record, Space Sci Rev. 135 (2008) 161–185. https://doi.org/10.1007/s11214-007-9252-9.

[48] N. Ladygina, E.G. Dedyukhina, M.B. Vainshtein, A review on microbial synthesis of hydrocarbons, Process Biochemistry. 41 (2006) 1001–1014. https://doi.org/10.1016/j.procbio.2005.12.007.

[49] J.C. Stern, C.A. Malespin, J.L. Eigenbrode, C.R. Webster, G. Flesch, H.B. Franz, H.V. Graham, C.H. House, B. Sutter, P.D. Archer Jr, A.E. Hofmann, Organic carbon concentrations in 3.5-billion-year-old lacustrine mudstones of Mars, Proceedings of the National Academy of Sciences. 119 (2022). https://doi.org/https://doi.org/10.1073/pnas.2201139119.

[50] L.E. Hays, H. V. Graham, D.J. Des Marais, E.M. Hausrath, B. Horgan, T.M. McCollom, M.N. Parenteau, S.L. Potter-McIntyre, A.J. Williams, K.L. Lynch, Biosignature Preservation and Detection in Mars Analog Environments, Astrobiology. 17 (2017) 363–400. https://doi.org/10.1089/ast.2016.1627.

[51] M. Veneranda, J.A. Manrique, G. Lopez-Reyes, S. Julve-Gonzalez, F. Rull, C. Alvarez Llamas, T. Delgado Pérez, E. Gibbons, E. Clavé, E. Cloutis, Developing tailored data combination strategies to optimize the SuperCam classification of carbonate phases on Mars, Earth and Space Science. 10 (2023) e2023EA002829.

# Appendix A:

# Supplementary Information for Chapter 2

Supplementary Information File for

Organic Biosignatures in Glaciovolcanic Terrains: Implications for Astrobiological Exploration on Mars

Gibbons E.F. [a]*, Leveille R.J. [a], Berlo K. [a], Slater G. [b]

[a] Department of Earth and Planetary Sciences, McGill University, 3450 University Street, Montreal, Quebec, Canada, H3A 0E8

[b] School of Earth, Environment & Society, McMaster University, 1280 Main Street West, Hamilton, Ontario, Canada, L8S 4K1

*Corresponding author: *erin.gibbons@mail.mcgill.ca*

## A.1 ADDITIONAL METHODOLOGICAL DETAILS

### A.1.1 Dissolved Ion Analyses

Dissolved cations (Si, Na, Mg, K, Ca, Fe, Al, Mn, Zn, Pb, Cr, As, Cu, Ni) of samples, field blanks, standard solutions, and solution blanks were analyzed at the Department of Earth and Planetary Sciences, McGill University, using a Thermo Scientific ICAP-6000 inductively coupled plasma-optical emissions spectrometer (ICP-OES). Where values were below detection by ICP-OES, measurements were repeated using Inductively Coupled Plasma Mass Spectrometry (ICP-MS) using a NewWave 213 nm Nd-YAG laser system coupled to a Thermo Finnigan iCAP-Qc quadrupole ICP-MS instrument.

Dissolved anions ($F^-$, $Cl^-$, $NO_3^-$, $NO_2^-$, $SO_4^{2-}$, $PO_4^{3-}$) of samples, field blanks, standard solutions, and solution blanks were analyzed at the Département des sciences de la Terre et de l'atmosphère, Université du Québec à Montréal, using ion chromatography using a Dionex LC20 chromatograph with ED40 electrochemical detector (Dionex Corp). We analyzed 5 mL of each replicate. The column was a Dionex IonPac™ AG22 and the eluant consisted of carbonate ions (4.5 mM Sodium Carbonate, 1.4 mM Sodium Bicarbonate) in ultrapure water (milli-Q). The dissolved cation analysis of the Mud Pot samples revealed high levels of alkaline earth and transition metals. Consequently, Thermo Scientific™ Dionex™ Guardcap™ H vial caps were used for these samples to prevent fouling.

The limit of detection (LOD) is specific to each element and technique. LOD was thus determined for each analyte using the following standard formula from the International Committee on Harmonization [8]: LOD = 3.3 $\sigma$ / m. Where $\sigma$ is the standard deviation of three replicate measurements of the solution blank and $m$ is the analytical sensitivity (slope) of the five-point calibration curve of the standard analyte.

| Analyte | Instrument | LOD (ppm) |
|---|---|---|
| **Si** | ICP-OES | 1.4E-05 |
| **Na** | ICP-OES | 4.3E-05 |
| **Mg** | ICP-OES | 1.4E-06 |
| **K** | ICP-OES | 5.5E-05 |
| **Ca** | ICP-OES | 1.6E-05 |
| **Fe** | ICP-OES | 2.8E-05 |
| **Al** | ICP-MS | 2.8E-02 |
| **Mn** | ICP-OES | 2.4E-07 |
| **Zn** | ICP-OES | 1.6E-02 |
| **Pb** | ICP-OES | 1.3E-03 |
| **Cr** | ICP-MS | 1.0E-02 |
| **As** | ICP-MS | 1.3E-02 |
| **Cu** | ICP-MS | 1.2E-02 |
| **Ni** | ICP-MS | 5.9E-03 |
| **$F^-$** | Ion Chromatography | 1.2E-02 |
| **$Cl^-$** | Ion Chromatography | 4.1E-03 |
| **$Br^-$** | Ion Chromatography | 4.9E-03 |
| **$NO_2^-$** | Ion Chromatography | 6.5E-03 |
| **$NO_3^-$** | Ion Chromatography | 1.2E-02 |
| **$PO_4^-$** | Ion Chromatography | 1.7E-02 |
| **$SO_4^-$** | Ion Chromatography | 1.5E-02 |

*Table S1: Methodological details for dissolved ion measurements, including the instrument technique and associated LOD.*

### A.1.2 Statistical Methods

A variety of statistical methods were applied to explore relationships amongst various datasets. The details of the application are provided here.

The physicochemical variability of the site was investigated using unsupervised hierarchical clustering (HC) and principal component analysis (PCA) with the R 2022.12.0 software (The R Foundation for Statistical Computing, Vienna, Austria). Input variables consisted of dissolved ion chemistry and environmental attributes measured at the time of sampling. For the paired samples *L_3m_Filter* + *L_3m_Sed.* and *L_60m_DeepFilter* + *L_60m_Sed*., environmental variables were averaged. Prior to analysis, the variables were scaled to unit variance to prevent any potential bias caused by differences in measurement scales or units. In cases where dissolved ions were below the detection limit, the missing values were replaced with very small numbers (half the value of the limit of detection). However, the following ions were omitted because they were not detected in most (or all) samples, resulting in variables with close to 0 variance: Cr, As, Cu, Ni, and Br. To perform HC, we utilized the *hclust*() function with the 'complete' linkage

method. The 'complete' linkage defines the cluster distance between two clusters to be the maximum distance between their individual components. In the context of the study, applying the ‘complete’ linkage method helps identify clusters with maximum dissimilarity, contributing to a comprehensive exploration of the physicochemical heterogeneity of the site and the relationships and patterns in the data. PCA was conducted using the *prcomp()* function and visualized with the *factoextra* package. Both HC and PCA revealed a separation of the hydrothermal fluids in the Mud Pot Area and the Sprin-Lake transect area, suggesting dissimilarity in the local fluids. The resulting clusters from HC and PCA were evaluated for statistical significance using permutational multivariate analysis of variance (PERMANOVA) with the *adonis2*() function in the *vegan* package, employing the Euclidean dissimilarity measure.

The same approach (HC, PCA, PERMANOVA) was applied to investigate the variability among PLFA profiles. The input data included the proportional abundances of each PLFA class (saturated, monounsaturated, polyunsaturated, mid-chain branched, terminally branched, and cyclopropyl-bearing, and hydroxy fatty acids) for each sediment and filter sample. For the PERMANOVA validation of apparent clusters, the Bray-Curtis distance metric was utilized in the PERMANOVA dissimilarity matrix due to the presence of closed proportional variables.

The Mann-Whitney U test, also known as the Wilcoxon rank sum test, was employed to determine if there were significant variations in organic proxies throughout the site. Pearson’s Correlation Coefficient was used to assess the nature of these relationships. Both tests were conducted in the Past 4.13 free software for scientific data analysis.

Lastly, previous research has established that external environmental conditions, such as temperature and pH, can have a complex influence on microbial community composition [9,10] and also induce biophysical changes in the membrane lipid composition [6,11–13]. However, these factors have not been systematically investigated in glaciovolcanic regions. Thus, we computed Spearman’s Correlation Coefficient (Past 4.13) for relationships between the measured environmental variables (T, pH, DO, TDS, salinity) and whole biomarker PLFA profiles. Spearman’s Correlation Coefficient was selected as it is more robust to outliers and a great deal of environmental variability was observed. Given that the YSI ProMeter is a subaqueous probe, contextual environmental data could not be comprehensively collected from the relict mud pot

samples (MP13-16). Consequently, we only included data from the Spring-Lake Transect in the correlation analysis. This transect represents an interconnected ecosystem with steep hydrothermal gradients and serves as a microcosm for the variability observed across the system at large.

## A.2 SUPPORTING RESULTS

### A.2.1 Dissolved Ion Chemistry

Table S2 provides a record of the dissolved ion chemistry measured and the limit of detection.

***Table S2:*** *Dissolved ion chemistry (mg/L) of fluids investigated in this study.*

*See main text for graphical depictions. Samples are named according to the numeric code provided in Table 2.1. n.d. = not detected / below detection limit.*
** measured by ICP-MS due to low response by ICP-OES*

| ID # | 1 | 2 | 3 | 4 & 5 | 6 | 7 | 8 | 9 & 10 | 11 | 12 | LOD |
|---|---|---|---|---|---|---|---|---|---|---|---|
| **Si** | 81.02 | 77.35 | 50.02 | 20.16 | 23.96 | n.m. | 22.65 | 23.07 | 99.26 | 98.85 | 1.4E-05 |
| **Na** | 65.22 | 62.65 | 41.07 | 13.81 | 12.53 | n.m. | 12.67 | 12.41 | 15.83 | 19.16 | 4.3E-05 |
| **Mg** | 0.78 | 0.90 | 0.58 | 4.96 | 6.52 | n.m. | 5.80 | 6.33 | 20.23 | 38.12 | 1.4E-06 |
| **K** | 13.63 | 12.90 | 8.49 | 2.95 | 2.17 | n.m. | 2.15 | 2.16 | 8.01 | 8.61 | 5.5E-05 |
| **Ca** | 12.54 | 12.66 | 8.68 | 37.76 | 46.85 | n.m. | 43.00 | 45.96 | 73.92 | 146.64 | 1.6E-05 |
| **Fe** | 0.24 | 0.04 | 4.70E-03 | n.d. | 0.48 | n.m. | 0.01 | 0.01 | 40.62 | 91.56 | 2.8E-05 |
| **Al*** | 0.26 | 0.15 | 0.12 | n.d. | 0.21 | n.m. | 0.03 | n.d. | 9.19 | 8.37 | 2.8E-02 |
| **Mn** | 0.01 | 2.55E-03 | 0.01 | 0.50 | 0.70 | n.m. | 0.65 | 0.69 | 1.79 | 5.89 | 2.4E-07 |
| **Zn** | 0.36 | n.d. | n.d. | 0.24 | n.d. | n.m. | 0.02 | n.d. | 0.14 | 0.25 | 1.6E-02 |
| **Pb** | 0.07 | 0.06 | 0.04 | 0.01 | 0.02 | n.m. | 0.02 | 0.02 | 0.08 | 0.08 | 1.3E-03 |
| **Cr*** | n.d. | n.d. | n.d. | n.d. | n.d. | n.m. | n.d. | n.d. | n.d. | n.d. | 1.0E-02 |
| **As*** | n.d. | n.d. | n.d. | n.d. | n.d. | n.m. | n.d. | n.d. | n.d. | n.d. | 1.3E-02 |
| **Cu*** | n.d. | n.d. | n.d. | n.d. | n.d. | n.m. | n.d. | n.d. | n.d. | 0.02 | 1.2E-02 |
| **Ni*** | n.d. | n.d. | n.d. | n.d. | n.d. | n.m. | n.d. | n.d. | n.d. | 0.01 | 5.9E-03 |
| **$F^-$** | 0.19 | 0.17 | 0.17 | 0.02 | n.d. | n.m. | n.d. | 0.02 | n.d. | 0.96 | 1.2E-02 |
| **$Cl^-$** | 1.76 | 1.50 | 1.43 | 0.28 | 0.40 | n.m. | 0.35 | 0.33 | 0.95 | 1.05 | 4.1E-03 |
| **$Br^-$** | n.d. | n.d. | n.d. | n.d. | n.d. | n.m. | n.d. | n.d. | n.d. | n.d. | 4.9E-03 |
| **$NO_2^-$** | 0.01 | 0.01 | 0.02 | n.d. | 0.01 | n.m. | n.d. | n.d. | n.d. | n.d. | 6.5E-03 |
| **$NO_3^-$** | n.d. | 0.37 | 0.05 | n.d. | 0.69 | n.m. | n.d. | n.d. | 1.60 | 1.40 | 1.2E-02 |
| **$PO_4^-$** | n.d. | 0.06 | 0.09 | 0.05 | n.d. | n.m. | n.d. | n.d. | n.d. | 1.43 | 1.7E-02 |
| **$SO_4^-$** | 69.13 | 64.47 | 64.76 | 76.54 | 76.21 | n.m. | 73.69 | 61.39 | 511.60 | 981.30 | 1.5E-02 |
| **NH3** | 0.60 | 0.40 | 0.40 | 0.40 | 0.30 | n.m. | 0.70 | 0.53 | 5.33 | 32.30 | |

## A.2.2 PLFA identified (Table extends for 3 pages)

***Table S3:*** *Complete list of phospholipid fatty acid compounds detected, reported in ug of PLFA per g or sediment extracted or per mL of water filtered (ug/g or ug/mL).*

*Samples are named according to the numeric code provided in Table 2.1. For unsaturated compounds where the position of the unsaturation is unknown, a generic alphabetic suffix is used to differentiate separate compounds. Compounds are listed in the order of elution. Retention times (RT) are approximate and taken as the average RT of each compound across all runs. Compounds are classified according to their molecular structure: Sat = saturated fatty acids, Mono = monounsaturated fatty acids, Poly = polyunsaturated fatty acids, Term = terminally branched fatty acids, Br = mid-chain branched fatty acids, Cyclo = cycloprpyl-bearing fatty acids. N.d. = not detected, where limits of detection were taken as the y-intercept of the calibration curve of the closest eluting standard*

| Fatty Acid | RT | Class | 1 | 2 | 3 | 5 | 7 | 10 | 4 | 6 | 8 | 9 | 11 | 13 | 14 | 15 | 16 |
|---|---|---|---|---|---|---|---|---|---|---|---|---|---|---|---|---|---|
| **12:0** | **11.33** | **Sat** | n.d. | 0.026 | 0.006 | 0.003 | n.d. | 0.006 | n.d. | n.d. | n.d. | n.d. | 0.063 | 1.534 | 0.010 | n.d. | 0.079 |
| **a-12:0** | **12.69** | **Term** | n.d. | 0.027 | 0.005 | 0.003 | n.d. | 0.007 | n.d. | n.d. | n.d. | n.d. | 0.062 | 1.542 | 0.010 | 1.590 | 0.078 |
| **br-12:0** | **12.71** | **Br** | n.d. | n.d. | n.d. | n.d. | n.d. | n.d. | n.d. | n.d. | n.d. | n.d. | n.d. | n.d. | n.d. | n.d. | n.d. |
| **i-12:0** | **12.84** | **Term** | n.d. | 0.026 | 0.005 | 0.003 | n.d. | 0.006 | n.d. | n.d. | n.d. | n.d. | 0.062 | 1.542 | 0.010 | 1.617 | 0.082 |
| **13:0** | **13.46** | **Sat** | n.d. | 0.022 | n.d. | n.d. | n.d. | n.d. | n.d. | n.d. | n.d. | n.d. | n.d. | n.d. | n.d. | n.d. | n.d. |
| **i-14:0** | **14.67** | **Term** | n.d. | 0.038 | 0.007 | 0.003 | 0.007 | 0.007 | n.d. | n.d. | n.d. | n.d. | n.d. | 2.246 | 0.017 | 2.752 | 0.138 |
| **14:1a** | **14.93** | **Mono** | n.d. | 0.028 | 0.006 | 0.003 | 0.007 | 0.008 | 0.001 | 0.001 | 0.001 | 0.001 | n.d. | n.d. | n.d. | n.d. | n.d. |
| **14:1 (n-5)** | **15.09** | **Mono** | 0.002 | 0.028 | 0.007 | 0.003 | 0.007 | 0.007 | n.d. | n.d. | n.d. | n.d. | n.d. | n.d. | n.d. | n.d. | n.d. |
| **14:0** | **15.32** | **Sat** | n.d. | 0.126 | 0.008 | 0.004 | 0.007 | 0.028 | 0.002 | 0.002 | 0.001 | 0.002 | 0.076 | 2.434 | 0.017 | 2.765 | 0.137 |
| **15:1a** | **15.96** | **Mono** | n.d. | 0.028 | 0.006 | 0.003 | 0.007 | 0.008 | n.d. | n.d. | n.d. | n.d. | n.d. | n.d. | n.d. | n.d. | n.d. |
| **15:1b** | **16.02** | **Mono** | n.d. | 0.035 | 0.007 | 0.003 | n.d. | 0.007 | n.d. | n.d. | n.d. | n.d. | n.d. | n.d. | n.d. | n.d. | n.d. |
| **15:1c** | **16.15** | **Mono** | n.d. | 0.030 | 0.007 | n.d. | n.d. | n.d. | n.d. | n.d. | n.d. | n.d. | n.d. | n.d. | n.d. | n.d. | n.d. |
| **i-15:0** | **16.38** | **Term** | 0.002 | 0.592 | 0.019 | 0.005 | 0.008 | 0.074 | 0.001 | 0.001 | 0.001 | 0.001 | 0.084 | 3.822 | 0.108 | 9.137 | 0.824 |
| **a-15:0** | **16.50** | **Term** | 0.002 | 0.204 | 0.011 | 0.004 | 0.007 | 0.026 | 0.001 | 0.001 | 0.001 | 0.001 | 0.077 | 3.622 | 0.062 | 7.231 | 0.456 |
| **15:1d** | **16.69** | **Mono** | n.d. | n.d. | 0.007 | 0.003 | n.d. | 0.008 | n.d. | n.d. | n.d. | n.d. | n.d. | n.d. | n.d. | n.d. | n.d. |
| **15:0** | **16.97** | **Sat** | n.d. | 0.059 | 0.007 | 0.003 | 0.007 | 0.007 | 0.001 | 0.001 | 0.001 | 0.001 | 0.075 | 2.245 | 0.015 | 2.460 | 0.121 |
| **16:1a** | **17.51** | **Mono** | n.d. | 0.033 | n.d. | n.d. | n.d. | n.d. | n.d. | n.d. | n.d. | n.d. | n.d. | n.d. | 0.017 | 2.688 | n.d. |
| **16:1b** | **17.59** | **Mono** | n.d. | 0.034 | 0.007 | 0.004 | n.d. | 0.008 | n.d. | n.d. | n.d. | n.d. | n.d. | 2.629 | 0.017 | 2.748 | 0.135 |
| **16:1c** | **17.65** | **Mono** | n.d. | 0.028 | 0.007 | 0.004 | n.d. | n.d. | n.d. | n.d. | n.d. | n.d. | n.d. | 2.622 | 0.017 | 2.706 | 0.132 |
| **i-16:0** | **17.91** | **Term** | 0.003 | 0.386 | 0.010 | 0.004 | 0.008 | 0.009 | 0.001 | 0.001 | 0.001 | 0.001 | 0.086 | 2.865 | 0.037 | 3.834 | 0.238 |

| | | | | | | | | | | | | | | | | | |
|---|---|---|---|---|---|---|---|---|---|---|---|---|---|---|---|---|---|
| **16:1c** | **18.05** | **Mono** | 0.003 | 4.910 | 0.009 | n.d. | 0.008 | n.d. | n.d. | n.d. | n.d. | n.d. | 0.087 | 2.988 | 0.019 | 3.650 | 0.173 |
| **Cis-16:1 (n-7)** | **18.12** | **Mono** | 0.003 | 0.862 | 0.069 | 0.054 | 0.013 | 0.250 | 0.012 | 0.017 | 0.011 | 0.024 | 0.086 | 5.372 | 0.044 | 11.088 | 0.622 |
| **16:1d** | **18.19** | **Mono** | 0.003 | n.d. | 0.019 | 0.011 | 0.008 | 0.044 | 0.002 | 0.003 | 0.002 | 0.003 | n.d. | 3.394 | 0.022 | 4.121 | 0.216 |
| **16:1e** | **18.26** | **Mono** | n.d. | 0.143 | 0.012 | 0.010 | 0.008 | 0.029 | 0.001 | 0.002 | 0.001 | 0.002 | n.d. | 2.849 | 0.019 | 3.558 | 0.168 |
| **16:0** | **18.43** | **Sat** | 0.003 | 10.468 | 0.127 | 0.057 | 0.012 | 0.105 | 0.006 | 0.007 | 0.005 | 0.008 | 0.150 | 32.805 | 0.147 | 38.390 | 2.044 |
| **17:1a** | **18.65** | **Mono** | n.d. | 0.037 | n.d. | n.d. | n.d. | n.d. | n.d. | n.d. | n.d. | n.d. | n.d. | n.d. | n.d. | n.d. | n.d. |
| **17:1b** | **18.73** | **Mono** | n.d. | 0.038 | n.d. | n.d. | n.d. | n.d. | n.d. | n.d. | n.d. | n.d. | n.d. | n.d. | n.d. | n.d. | n.d. |
| **17:1c** | **18.86** | **Mono** | n.d. | n.d. | 0.008 | 0.004 | 0.007 | 0.008 | 0.001 | 0.001 | 0.001 | n.d. | n.d. | n.d. | 0.018 | 2.826 | 0.142 |
| **17:1d** | **18.95** | **Mono** | n.d. | 0.056 | 0.008 | 0.004 | 0.008 | 0.009 | n.d. | n.d. | n.d. | n.d. | n.d. | 2.652 | n.d. | n.d. | n.d. |
| **17:1e** | **19.05** | **Mono** | n.d. | n.d. | n.d. | 0.004 | 0.007 | 0.008 | n.d. | n.d. | n.d. | n.d. | n.d. | n.d. | n.d. | n.d. | n.d. |
| **br-16:0** | **19.09** | **Br** | 0.003 | 0.130 | 0.033 | 0.007 | n.d. | 0.010 | n.d. | n.d. | n.d. | n.d. | 0.084 | 2.678 | 0.028 | 2.934 | 0.191 |
| **i-17:0** | **19.29** | **Term** | 0.003 | 0.265 | 0.012 | 0.005 | 0.008 | 0.016 | n.d. | n.d. | n.d. | n.d. | 0.086 | 2.794 | 0.044 | 3.422 | 0.255 |
| **a-17:0** | **19.40** | **Term** | n.d. | 0.259 | 0.010 | 0.004 | 0.008 | 0.011 | n.d. | n.d. | n.d. | n.d. | 0.086 | 2.898 | 0.043 | 3.576 | 0.256 |
| **17:1f** | **19.45** | **Mono** | n.d. | 0.124 | n.d. | n.d. | n.d. | n.d. | 0.001 | 0.001 | n.d. | n.d. | n.d. | n.d. | n.d. | n.d. | n.d. |
| **cy-17:0** | **19.56** | **Cyclo** | 0.003 | 0.132 | 0.049 | 0.014 | 0.008 | 0.010 | 0.001 | 0.001 | 0.001 | 0.001 | 0.084 | 2.856 | 0.031 | 3.946 | 0.238 |
| **17:1g** | **19.67** | **Mono** | n.d. | 0.033 | n.d. | n.d. | n.d. | 0.008 | n.d. | n.d. | n.d. | n.d. | n.d. | n.d. | n.d. | n.d. | n.d. |
| **17:0** | **19.78** | **Sat** | n.d. | 0.163 | 0.008 | n.d. | n.d. | 0.008 | 0.001 | 0.001 | 0.001 | 0.001 | 0.085 | 2.753 | 0.018 | 2.970 | 0.148 |
| **br-17:0** | **19.80** | **Br** | n.d. | n.d. | 0.011 | 0.005 | 0.008 | 0.009 | n.d. | n.d. | n.d. | n.d. | n.d. | n.d. | 0.022 | n.d. | 0.155 |
| **18:3 (n-6)** | **20.39** | **Poly** | n.d. | 0.050 | n.d. | n.d. | n.d. | n.d. | n.d. | n.d. | n.d. | n.d. | n.d. | n.d. | n.d. | n.d. | n.d. |
| **18:2** | **20.53** | **Poly** | n.d. | 0.065 | n.d. | n.d. | n.d. | n.d. | n.d. | n.d. | n.d. | n.d. | n.d. | n.d. | n.d. | n.d. | n.d. |
| **phytanic acid** | **20.59** | **Br** | n.d. | n.d. | 0.012 | n.d. | 0.012 | 0.014 | n.d. | n.d. | n.d. | n.d. | 0.106 | n.d. | 0.032 | n.d. | 0.264 |
| **18:1a** | **20.60** | **Mono** | 0.003 | n.d. | n.d. | n.d. | n.d. | n.d. | n.d. | n.d. | n.d. | n.d. | n.d. | n.d. | n.d. | n.d. | n.d. |
| **18:2,9,12** | **20.61** | **Poly** | n.d. | 0.152 | n.d. | n.d. | n.d. | n.d. | n.d. | n.d. | n.d. | n.d. | n.d. | 4.717 | n.d. | 4.243 | n.d. |
| **cis-18:1 (n-9)** | **20.69** | **Mono** | 0.003 | 5.771 | 0.015 | 0.008 | 0.012 | 0.039 | 0.001 | 0.001 | 0.001 | 0.002 | 0.118 | 7.871 | 0.031 | 6.263 | 0.385 |
| **trans-18:1 (n-9)** | **20.76** | **Mono** | 0.003 | 0.568 | 0.031 | 0.013 | 0.013 | 0.128 | 0.004 | 0.005 | 0.002 | 0.006 | 0.111 | 5.658 | 0.050 | 6.734 | 0.464 |
| **18:0** | **21.01** | **Sat** | 0.003 | 1.859 | 0.020 | 0.007 | 0.012 | 0.017 | 0.001 | 0.001 | n.d. | 0.002 | 0.121 | 4.341 | 0.045 | 4.687 | 0.541 |
| **19:1a** | **21.12** | **Mono** | n.d. | n.d. | n.d. | n.d. | 0.012 | 0.017 | n.d. | n.d. | n.d. | n.d. | n.d. | n.d. | n.d. | n.d. | n.d. |

| | | | | | | | | | | | | | | | | | |
|---|---|---|---|---|---|---|---|---|---|---|---|---|---|---|---|---|---|
| **19:1b** | **21.37** | **Mono** | n.d. | 0.054 | 0.012 | 0.006 | 0.012 | 0.013 | n.d. | n.d. | n.d. | n.d. | n.d. | 3.470 | 0.022 | 3.565 | 0.181 |
| **i-19:0** | **21.48** | **Term** | n.d. | 0.067 | 0.012 | 0.006 | n.d. | 0.012 | n.d. | n.d. | n.d. | n.d. | 0.104 | 3.481 | 0.023 | 3.596 | 0.190 |
| **a-19:0** | **21.51** | **Term** | n.d. | 0.079 | 0.012 | 0.006 | n.d. | 0.012 | n.d. | n.d. | n.d. | n.d. | 0.104 | 3.475 | 0.023 | 3.586 | 0.185 |
| **19:1c** | **21.66** | **Mono** | n.d. | 0.059 | n.d. | n.d. | n.d. | n.d. | n.d. | n.d. | n.d. | n.d. | n.d. | 3.488 | 0.022 | 3.572 | 0.182 |
| **19:1d** | **21.76** | **Mono** | n.d. | 0.065 | 0.012 | 0.006 | n.d. | 0.013 | n.d. | n.d. | n.d. | n.d. | 0.104 | n.d. | 0.022 | 3.575 | 0.181 |
| **19:1e** | **21.86** | **Mono** | n.d. | 0.060 | 0.012 | 0.006 | n.d. | 0.012 | n.d. | n.d. | n.d. | n.d. | n.d. | n.d. | 0.022 | 3.561 | 0.178 |
| **cy-19:0 (n-9)** | **21.98** | **Cyclo** | 0.003 | 0.077 | n.d. | n.d. | n.d. | n.d. | n.d. | n.d. | n.d. | n.d. | n.d. | n.d. | n.d. | n.d. | n.d. |
| **cy-19:0** | **22.02** | **Cyclo** | n.d. | 0.136 | 0.016 | 0.006 | n.d. | 0.012 | n.d. | n.d. | n.d. | n.d. | 0.106 | 3.654 | 0.024 | 3.756 | 0.237 |
| **19:0** | **22.19** | **Sat** | n.d. | 0.065 | 0.012 | 0.006 | n.d. | 0.012 | n.d. | n.d. | n.d. | n.d. | n.d. | n.d. | n.d. | n.d. | n.d. |
| **20:4 (n-6)** | **22.50** | **Poly** | n.d. | 0.051 | n.d. | n.d. | n.d. | n.d. | n.d. | n.d. | n.d. | n.d. | n.d. | n.d. | n.d. | n.d. | n.d. |
| **20:5 (n-3)** | **22.58** | **poly** | n.d. | 0.049 | n.d. | n.d. | n.d. | n.d. | n.d. | n.d. | n.d. | n.d. | n.d. | n.d. | n.d. | n.d. | n.d. |
| **20:1** | **22.97** | **Mono** | 0.003 | 0.066 | n.d. | n.d. | n.d. | 0.012 | n.d. | n.d. | n.d. | n.d. | n.d. | n.d. | 0.024 | n.d. | n.d. |
| **20:1** | **22.97** | **Sat** | n.d. | n.d. | n.d. | n.d. | n.d. | n.d. | n.d. | n.d. | n.d. | n.d. | n.d. | n.d. | n.d. | 0.065 | n.d. |
| **cis-20:1 (n-9)** | **23.01** | **Mono** | n.d. | 0.082 | n.d. | n.d. | n.d. | n.d. | n.d. | n.d. | n.d. | n.d. | 0.107 | 3.499 | 0.026 | 4.313 | 0.185 |
| **20:0** | **23.29** | **Sat** | 0.003 | 0.069 | 0.012 | 0.006 | n.d. | 0.012 | n.d. | n.d. | n.d. | n.d. | 0.105 | 3.491 | 0.023 | 4.290 | 0.182 |
| **22:1a** | **24.89** | **Mono** | n.d. | 0.074 | n.d. | n.d. | n.d. | n.d. | n.d. | n.d. | n.d. | n.d. | n.d. | n.d. | n.d. | n.d. | n.d. |
| **22:1b** | **25.10** | **Mono** | n.d. | 0.068 | n.d. | n.d. | n.d. | n.d. | n.d. | n.d. | n.d. | n.d. | n.d. | n.d. | n.d. | n.d. | n.d. |
| **22:0** | **25.35** | **Sat** | n.d. | 0.053 | n.d. | n.d. | n.d. | n.d. | n.d. | n.d. | n.d. | n.d. | n.d. | n.d. | n.d. | n.d. | n.d. |
| **cis-24:1 (n-9)** | **27.02** | **Mono** | n.d. | 0.053 | n.d. | n.d. | n.d. | n.d. | n.d. | n.d. | n.d. | n.d. | n.d. | n.d. | n.d. | n.d. | n.d. |

## A.3 REFERENCES


[1] Å. Frostegård, A. Tunlid, E. Bååth, Use and misuse of PLFA measurements in soils, Soil Biol Biochem. 43 (2011) 1621–1625.

[2] G.T. Hill, N.A. Mitkowski, L. Aldrich-Wolfe, L.R. Emele, D.D. Jurkonie, A. Ficke, S. Maldonado-Ramirez, S.T. Lynch, E.B. Nelson, Methods for assessing the composition and diversity of soil microbial communities, Applied Soil Ecology. 15 (2000) 25–36.

[3] Y. Zhang, N. Zheng, J. Wang, H. Yao, Q. Qiu, S.J. Chapman, High turnover rate of free phospholipids in soil confirms the classic hypothesis of PLFA methodology, Soil Biol Biochem. 135 (2019) 323–330.

[4] A.L. Brady, E. Gibbons, A. Sehlke, C.J. Renner, S.E. Kobs Nawotniak, D.S.S. Lim, G.F. Slater, Microbial community distribution in variously altered basalts: Insights into astrobiology sample site selection, Planet Space Sci. 194 (2020). https://doi.org/10.1016/j.pss.2020.105107.

[5] L. Zhang, J. Fang, R. Joeckel, Microbial biomass and community structure in alkaline lakes of the Nebraska Sand Hills, USA, Chem Geol. 356 (2013) 171–180. https://doi.org/10.1016/j.chemgeo.2013.08.017.

[6] Y.M. Zhang, C.O. Rock, Membrane lipid homeostasis in bacteria, Nat Rev Microbiol. 6 (2008) 222–233. https://doi.org/10.1038/nrmicro1839.

[7] C.D. Georgiou, D.W. Deamer, Lipids as universal biomarkers of extraterrestrial life, Astrobiology. 14 (2014) 541–549. https://doi.org/10.1089/ast.2013.1134.

[8] International Committee on Harmonization, Validation Of Analytical Procedures, in: International Council for Harmonisation of Technical Requirements for Pharmaceuticals for Human Use (ICH), 2005.

[9] J.F. Power, C.R. Carere, C.K. Lee, G.L.J. Wakerley, D.W. Evans, M. Button, D. White, M.D. Climo, A.M. Hinze, X.C. Morgan, I.R. McDonald, S.C. Cary, M.B. Stott, Microbial biogeography of 925 geothermal springs in New Zealand, Nat Commun. 9 (2018). https://doi.org/10.1038/s41467-018-05020-y.

[10] C.E. Sharp, A.L. Brady, G.H. Sharp, S.E. Grasby, M.B. Stott, P.F. Dunfield, Humboldt's spa: microbial diversity is controlled by temperature in geothermal environments, ISME J. 8 (2014) 1166–1174. https://doi.org/10.1038/ismej.2013.237.

[11] M.F. Siliakus, J. van der Oost, S.W.M. Kengen, Adaptations of archaeal and bacterial membranes to variations in temperature, pH and pressure, Extremophiles. 21 (2017) 651–670. https://doi.org/10.1007/s00792-017-0939-x.

[12] T. Kaneda, Iso-and anteiso-fatty acids in bacteria: biosynthesis, function, and taxonomic significance, Microbiol Rev. 55 (1991) 288–302.

[13] P. De Maayer, D. Anderson, C. Cary, D.A. Cowan, Some like it cold: Understanding the survival strategies of psychrophiles, EMBO Rep. 15 (2014) 508–517. https://doi.org/10.1002/embr.201338170.

# Appendix B:

# Supplementary Information for Chapter 3

Supplementary Information File for

A Case Study on Refractory Lipid Biomarkers for Mars Exploration: the Kverkfjöll Glaciovolcanic System

Gibbons E.F. [a]*, Leveille R.J. [a], Berlo K. [a], Slater G. [b]

[a] Department of Earth and Planetary Sciences, McGill University, 3450 University Street, Montreal, Quebec, Canada, H3A 0E8

[b] School of Earth, Environment & Society, McMaster University, 1280 Main Street West, Hamilton, Ontario, Canada, L8S 4K1

*Corresponding author: *erin.gibbons@mail.mcgill.ca*

## B.1 CALCULATION OF HYDROCARBON BIOMARKER INDICES

A number of indices were calculated to help characterize the biomarker distributions and elucidate their source. Details of their computation are as follows:

1) LMW/HMW was computed using the following formula:

$$\frac{LMW}{HMW} = \frac{\left(\sum_{i=j}^{23} X_i\right)}{\left(\sum_{i=24}^{k} X_i\right)}$$

Where *j i*s the length of the smallest compound, k is the length of the longest compound, *i* is the index, and *X* is the concentration in picomole/g (quantified by calibration).

2) CPI was computed using the following generic formula:

$$CPI = \frac{\left(\sum_{i=n}^{m} C_{2i+1}\right) + \left(\sum_{i=n+1}^{m+1} C_{2i+1}\right)}{2\left(\sum_{i=n+1}^{m+1} C_{2i}\right)}$$

Where *n* is the starting *n*-alkane divided by 2*, m* is the ending n-alkane divided by 2, *i* is the index, and *C* is the concentration (represented by chromatographic peak area, see below). Note, we use the formula modified by [1] which avoids issues of over-estimation associated with the original CPI defined by Bray & Evans (1961) [2] . Further, we use chromatographic peak areas for the concentration variable to facilitate direct comparisons with other studies – a recent review found that CPI outcomes using chromatographic peak areas/heights differ significantly than those using compound concentrations obtained by calibration curves. Peak area provides a more agnostic metric for comparison between studies.

In this study we calculate the CPI for two ranges. For the low molecular weight range, $<C_{23}$ ($CPI_{LMW}$), $n = 7$ and $m = 10$. For the high molecular weight range, $>C_{25}$ ($CPI_{HMW}$), $n = 12$ and $m = 14$.

3) ACL was computed using the following generic formula:

$$ACL = \frac{\left(\sum_{i=j}^{k} iX_i\right)}{\left(\sum_{i=j}^{k} X_i\right)}$$

Where *j i*s the length of the smallest compound, k is the length of the longest compound, *i* is the index, and *X* is the concentration in picomole/g (quantified by calibration).

## B.2 SUPPORTING RESULTS

### B.2.1 Sedimentological Field Observations

The northern Kverkfjöll caldera is blanketed by subglacially eroded volcanoclastic sediments. The colour of the sediments ranged from beige to brown-grey, and their distribution appeared relatively uniform across the site. The sedimentary succession within the study area had undergone recent incision, apparently driven by the erosive outflow of the overfilled, active hot spring. The extent of incision was greatest at the spring source, exposing approximately 2 meters of vertical stratigraphy, but decreased downstream such that there was no incision where the overflow stream joined lake Gengissig. This incision, which is believed to have occurred after 2011 since it was not previously documented in the study by Cousins et al. (2018) [3], provided an opportunity to observe the subsurface sedimentary structures, detailed below. During our sampling, the hot spring itself exhibited vigorous hydrothermal activity, including continuous steam emission and rapid bubbling. The immediate area featured dark cobbles coated with ~0.1-0.5 cm thick layers of calcite (see section 4.2) and a fine-grained subaqueous deposit of grey mud and minor lithics.

The sedimentary walls exposed by incision revealed an unconsolidated deposit characterized by inclined strata that sloped towards the caldera center. The contact surfaces are mostly planar with gentle undulations and evidence of slumping or soft sediment deformation. The most dominant facies were poorly sorted and consisted of a clay- to sand-sized matrix surrounding sub-rounded to angular pebbles and cobbles. The density of matrix and clast material varied both laterally and vertically. These coarser layers were sporadically interbedded with discontinuous lenses (~1-5 cm thick) of clay-rich material characterized by a distinctive grey-blue colour. Directly overlying

this matrix-supported package was an approximately 1-meter-thick assemblage of poorly sorted, predominantly clast-supported pebbles and cobbles with no obvious imbrication.

Within lake Gengissig, the sedimentary sequence showed a greater degree of physical reworking by phreatic and sedimentary processes. The proximal lake-bed sediments were composed of lapilli-sized particles with some larger blocks, while the finer-grained matrix material appeared to have been mostly removed. The milky appearance of the water suggested that at least some of the fines were suspended in the water column. Furthermore, at a distance of approximately 30 meters from the shore, the lake-bed sediments transitioned to a visually homogenous, fine-grained deposit with the same distinctive grey-blue colour observed within the subsurface shoreline sediments.

The Mud Pot area had a slightly different sedimentary expression at the surface. The quiescent pool and pots themselves were lined by thick layers of visually homogenous grey-blue fine-grained material. The surrounding ground was a mottled beige-brown and featured several shallow hollows, interpreted to be relict mud pools in various stages of desiccation. The uppermost, cracked material of these relict pools was fine-grained, brittle, and light-toned, whereas the material just below consisted of a dense, damp, homogenous layer of dark grey-blue fines. See Chapter 2 for details of the physicochemical parameters measured across the site.

### B.2.2 In-depth Mineralogical Interpretation of the Kverkfjöll Hydrothermal Assemblage

Our study site is a surface manifestation of a vigorous subglacial hydrothermal system [4]. The formation of the Fe-S hydrothermal environments, such as the subaerial/subaqueous hot springs and mud pots, begins at depth. Groundwater that has percolated through the porous volcanic edifice is heated and undergoes rapid decompression boiling when it reascends [4,5]. Upon boiling, the reservoir geothermal water experiences phase segregation, and the steam phase becomes progressively enriched in volatiles (e.g., $CO_2$, $H_2S$, and $H_2$) that can alter the host rock as the steam rises [5]. Consequently, the resultant mineralogical assemblage can provide valuable insight into the subsurface hydrothermal environment and any subsequent alteration.

In particular, clay minerals, which are widespread hydrothermal alteration products, have been identified as useful indicators of alteration extent due to their sensitivity to changes in the physicochemical conditions of hydrothermal fluids [6]. The pervasive presence of smectite in our samples is consistent with low-grade argillic alteration, which proceeds at low-temperatures

(<160°C) and relatively neutral pH conditions (~5.5–7) [6]. This low-temperature grade is validated by the universal co-occurrence of quartz and heulandite. The presence of crystalline quartz in a dominantly basaltic system is suggestive of a hydrothermal origin and is favored as the stable silica phase over opal-C at temperatures above 100°C [7]. Heulandite is generally produced at temperatures between 25°C and 150°C but may also be stable at higher temperatures [8–10]. Correspondingly, we did not observe minerals commonly associated with more advanced and hotter alteration in Icelandic hydrothermal systems, such as chlorite (>140°C), kaolinite (>150°C), epidote (>200°C), or prehnite (>200°C) [6,7]. Moreover, the pervasive presence of anatase, a low-T and low-P titanium oxide, confirms that crystallization temperatures were predominantly below 470°C, above which rutile is the favoured $TiO_2$ phase [11]. Overall, the assemblage is consistent with crystallization temperatures between 100°C and 140°C (Figure S1), suggesting that the glaciovolcanic hydrothermal conditions generated here are within the current theoretical boundaries for life (up to ~150°C) [12].

Other minerals, although not geothermometers, can reflect both hydrothermal and surficial gradients in the system. The occurrence of pyrite in these predominantly acidic and oxidizing environments implies that oxidizing conditions are probably restricted to the surface, while reducing conditions prevail at shallow depths. Alternatively, the presence of pyrite could represent a relatively recent redox change in the environment, but we do not favor this latter explanation considering that pyrite was also detected at high levels in the shoreline sediments more than a decade prior to our sampling [13]. The occurrence of gypsum – an evaporitic mineral that predominantly precipitates from brine – in the relict mud pools records ambient moisture gradients and likely reflects a later stage of subaerial alteration. Both of these phases provide evidence of local chemical-physical gradients/disequilibrium, which substantiates the claim of glaciovolcanic habitability.

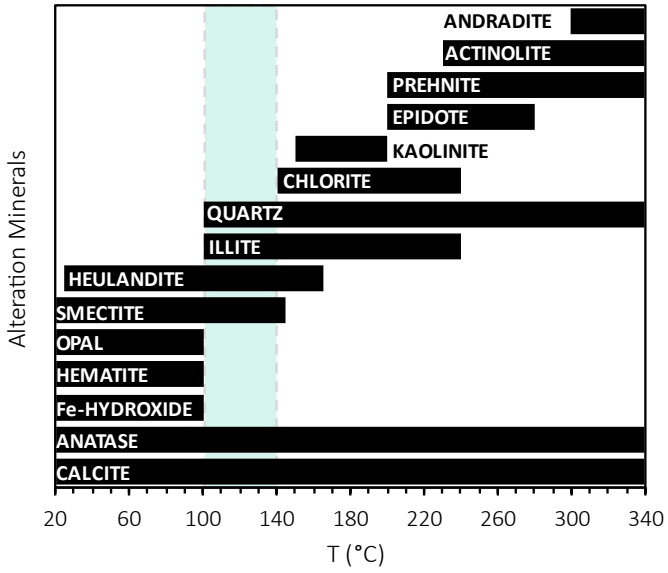


*Figure S1: Schematic of common minerals associated with Icelandic hydrothermal systems and their crystallization temperatures.*

*Data from Griffith and Shock (1995), Treibold 2011, and Fulignati 2020. The observed mineral assemblage of smectite, heulandite, low-temperature quartz, and anatase is consistent with crystallization temperatures between 100°C and 140°C.*

## B.2.3 Hydrocarbon Compound List

*Table S1:Complete list of hydrocarbons identified.*

*Compounds are listed in the order of elution and reported in ug/g of dry sediment. Normal alkanes and alkenes are labeled in the format CX:Y, where X denotes the number of carbons on the longest straight chain and Y indicates the number of unsaturations, if applicable. Branched compounds are labeled according to their chemical name, if known, or by a descriptive acronym if the branching position was not determined (DMA = dimethylalkane)*

| Compound | RT | L_60m | L_50m | L_3m | S_Distal | S_Mid_ Mat | S_Source | MP_Pool | MP_Recent _Crust | MP_Recent _Low | MP_Old_ Crust | MP_Old _Low |
|---|---|---|---|---|---|---|---|---|---|---|---|---|
| C12 | 8.00 | - | - | - | 43.3 | - | 63.8 | - | - | 60.0 | - | - |
| C13 | 9.73 | - | - | - | 50.6 | 87.5 | 49.6 | - | - | 46.5 | - | - |
| C14:1 | 11.50 | - | - | - | 70.0 | 78.1 | 42.9 | - | - | - | - | - |
| C14 | 11.66 | 22.8 | 25.7 | 27.5 | 145.0 | 202.8 | 98.8 | - | 1338.4 | 81.4 | - | 134.8 |
| C15 | 13.72 | 27.8 | 39.3 | 35.1 | 132.2 | 208.2 | 130.4 | 157.0 | 4379.7 | 81.5 | 1661.2 | 845.1 |
| C16:1 | 15.68 | 36.0 | 51.8 | 62.8 | 186.7 | 151.5 | 119.1 | - | - | 33.6 | - | - |
| C16 | 15.84 | 80.3 | 164.9 | 90.7 | 267.2 | 369.4 | 415.0 | 154.6 | 1563.2 | 97.2 | 665.9 | 301.7 |
| C17 | 17.95 | 64.2 | 163.3 | 80.5 | 235.0 | 8171.2 | 586.0 | 6430.1 | 31794.7 | 168.2 | 27965.1 | 9574.1 |
| 7-methyl-heptadecane | 18.87 | - | - | - | - | 873.4 | - | 1615.2 | 26635.6 | 122.0 | 7993.9 | 1515.7 |
| 6-methyl-heptadecane | 18.91 | - | - | - | - | 3069.5 | - | 9033.4 | 15554.2 | 73.1 | 27983.4 | 6619.8 |
| 5-methyl-heptadecane | 18.99 | - | - | - | - | 3055.4 | - | 6027.7 | 4513.5 | 65.6 | 17423.8 | 4224.6 |
| 4-methyl-heptadecane | 19.13 | - | - | - | - | 322.7 | - | 704.3 | 1499.8 | - | 1704.9 | 507.2 |
| DMA a | 19.62 | - | - | - | - | - | - | 4746.5 | 4964.0 | 68.1 | 11416.1 | 2112.8 |
| DMA b | 19.81 | - | - | - | - | - | - | 9080.9 | 5237.1 | 40.7 | 22493.2 | 3797.2 |
| C18:1 | 19.87 | 100.9 | 203.3 | 159.2 | 303.5 | - | 301.7 | - | - | - | - | - |
| 5,12-dimethylheptadecane | 19.92 | - | - | - | - | - | - | 7627.9 | 4851.7 | 52.7 | 21292.6 | 3775.4 |
| 5,13-dimethylheptadecane | 20.00 | - | - | - | - | 395.2 | - | 5912.4 | 4971.9 | 132.5 | 9558.4 | 3452.3 |
| C18 | 20.01 | 100.0 | 192.0 | 136.2 | 281.8 | - | 531.2 | - | - | - | - | - |
| 4,5-dimethylheptadecane | 20.05 | - | - | - | - | - | - | 2128.9 | 1764.8 | - | 4798.1 | 861.7 |
| DMA d | 20.15 | - | - | - | - | - | - | 1827.8 | 2574.0 | - | 4982.9 | 1540.0 |
| 4,5,13-trimethylheptadecane | 21.58 | - | - | - | - | - | - | 1472.2 | 1248.6 | 73.0 | 892.4 | - |
| C19 | 22.02 | 52.2 | 98.8 | 78.3 | 141.6 | 186.1 | 225.4 | 399.6 | 2633.2 | 88.3 | 4023.8 | 593.0 |
| C20:1 | 23.82 | 106.7 | 209.2 | 167.2 | 295.3 | 203.1 | 264.4 | - | - | 77.3 | - | - |
| C20 | 23.94 | 101.5 | 156.3 | 149.0 | 276.3 | 206.6 | 192.8 | - | - | 108.5 | - | - |
| C21 | 25.80 | 62.8 | 78.8 | 102.0 | 177.8 | 122.1 | 138.2 | - | - | 59.6 | - | - |

| | | | | | | | | | | | | |
|---|---|---|---|---|---|---|---|---|---|---|---|---|
| C22:1 | 27.48 | 60.0 | 98.2 | 94.8 | 194.3 | - | 128.2 | - | - | - | - | - |
| C22 | 27.60 | 79.7 | 123.0 | 121.9 | 238.1 | 170.6 | 178.7 | - | - | 59.9 | - | - |
| C23 | 29.29 | 45.2 | 69.7 | 65.3 | 156.6 | 60.9 | 58.3 | - | - | 43.7 | - | - |
| C24 | 30.94 | 35.8 | 34.1 | 45.7 | 91.5 | 48.1 | 42.3 | - | - | 33.5 | - | - |
| C25 | 32.52 | 34.8 | 35.8 | 44.2 | 95.3 | 45.4 | 40.7 | - | - | 30.3 | - | - |
| C26 | 34.04 | 33.4 | 30.8 | 40.7 | 81.1 | 40.5 | 34.6 | - | - | - | - | - |
| C27 | 35.51 | 32.2 | 27.6 | 37.0 | 77.4 | 37.8 | 31.6 | - | - | - | - | - |
| C28 | 36.93 | 26.8 | 24.1 | 33.6 | 71.8 | 34.5 | 29.0 | - | - | - | - | - |
| C29 | 38.30 | 25.6 | 24.2 | 31.9 | 68.3 | 34.0 | 26.2 | - | - | - | - | - |
| C30 | 39.63 | 23.4 | 21.6 | 30.6 | 66.5 | 30.8 | - | - | - | - | - | - |
| C31 | 40.91 | 18.2 | 18.5 | 27.1 | 60.0 | - | - | - | - | - | - | - |

## B.3 REFERENCES


[1] R. Marzi, B.E. Torkelson, R.K. Olson, A revised carbon preference index, Org Geochem. 20 (1993) 1303–1306.

[2] E.E. Bray, E.D. Evans, Distribution of n-paraffins as a clue to recognition of source beds, Geochim Cosmochim Acta. 22 (1961) 2–15.

[3] C.R. Cousins, M. Fogel, R. Bowden, I. Crawford, A. Boyce, C. Cockell, M. Gunn, Biogeochemical probing of microbial communities in a basalt-hosted hot spring at Kverkfjöll volcano, Iceland, Geobiology. 16 (2018) 507–521. https://doi.org/10.1111/gbi.12291.

[4] E. Ranta, S.A. Halldórsson, P.H. Barry, S. Ono, J.G. Robin, B.I. Kleine, A. Ricci, J. Fiebig, Á.E. Sveinbjörnsdóttir, A. Stefánsson, Deep magma degassing and volatile fluxes through volcanic hydrothermal systems: Insights from the Askja and Kverkfjöll volcanoes, Iceland, Journal of Volcanology and Geothermal Research. 436 (2023) 107776. https://doi.org/10.1016/j.jvolgeores.2023.107776.

[5] A. Stefánsson, N.S. Keller, J.G. Robin, H. Kaasalainen, S. Björnsdóttir, S. Pétursdóttir, H. Jóhannesson, G.Ó. Hreggvidsson, Quantifying mixing, boiling, degassing, oxidation and reactivity of thermal waters at Vonarskard, Iceland, Journal of Volcanology and Geothermal Research. 309 (2016) 53–62. https://doi.org/10.1016/j.jvolgeores.2015.10.014.

[6] P. Fulignati, Clay minerals in hydrothermal systems, Minerals. 10 (2020) 1–17. https://doi.org/10.3390/min10100919.

[7] L.L. Griffith, E.L. Shock, A geochemical model for the formation of hydrothermal carbonates on Mars, Nature. 377 (1995) 406–408. https://doi.org/10.1038/377406a0.

[8] J.G. Liou, C. de Capitani, M. Frey, Zeolite equilibria in the system CaAI2Si208 - NaAISi3O8 - SiO2 - H2O, New Zealand Journal of Geology and Geophysics. 34 (1991) 293–301. https://doi.org/10.1080/00288306.1991.9514467.

[9] A. Iijima, Geology of natural zeolites and zeolitic rocks, Pure and Apllied Chemistry. 52 (1980) 2115–2130.

[10] K. Bargar, R. Erd, T.E.C. Keith, M.H. Beeson, Dachiardite from Yellowstone National Park, Wyoming, Can Mineral. 25 (1987) 475–483.

[11] S. Triebold, G.L. Luvizotto, R. Tolosana-Delgado, T. Zack, H. von Eynatten, Discrimination of TiO2 polymorphs in sedimentary and metamorphic rocks, Contributions to Mineralogy and Petrology. 161 (2011) 581–596. https://doi.org/10.1007/s00410-010-0551-x.

[12] N. Merino, H.S. Aronson, D.P. Bojanova, J. Feyhl-Buska, M.L. Wong, S. Zhang, D. Giovannelli, Living at the extremes: Extremophiles and the limits of life in a planetary context, Front Microbiol. 10 (2019). https://doi.org/10.3389/fmicb.2019.00780.

[13] C.R. Cousins, I.A. Crawford, J.L. Carrivick, M. Gunn, J. Harris, T.P. Kee, M. Karlsson, L. Carmody, C. Cockell, B. Herschy, K.H. Joy, Glaciovolcanic hydrothermal environments in Iceland and implications for their detection on Mars, Journal of Volcanology and Geothermal Research. 256 (2013) 61–77. https://doi.org/10.1016/j.jvolgeores.2013.02.009.

# Appendix C:

# Supplementary Information for Chapter 5

Supplementary Information File for

Assessing the Feasibility of Laser Induced Breakdown Spectroscopy for Detecting Nitrogen in Martian Surface Sediments

Erin Gibbons[a*], Richard Léveillé[a1], and Kim Berlo[a1]

[a] Department of Earth and Planetary Sciences, McGill University, 3450 University Street, Montreal, Quebec, Canada, H3A 0E8

[1]These authors contributed equally to this work.

*Corresponding author: *erin.gibbons@mail.mcgill.ca*

## C.1 DOPING CHEMICALS

Table S1 lists the chemicals used to dope the Mars-analogue geological matrices with various nitrogenous phases. Nitrogen phases were selected to approximate those expected on Mars.

| Chemical | Supplier | CAS number | Lot Number | Grade / Purity |
|---|---|---|---|---|
| Sodium Nitrate | Bio Basics | 7631-99-4 | J8384561 | Certified ACS |
| Magnesium Nitrate Hexahydrate | Alfa Aesar | 13446-18-9 | Q27H019 | 98% |
| Calcium Nitrate Tetrahydrate | Fisher Scientific | 13477-34-4 | 126440 | Certified ACS, 99.7% |
| Potassium Nitrate | Fisher Scientific | 7757-79-1 | 720061 | Certified ACS |
| Iron (III) Nitrate Nonahydrate | Sigma Aldrich | 7782-61-8 | MKCC6758 | Certified ACS ≥ 98.0% |
| Ammonium Acetate | Alfa Aesar | 631-61-8 | Z23G077 | ACS, 97.0 % min |

*Table S1: Summary of chemicals used to synthesize N-bearing samples.*

## C.2 GEOCHEMISTRY AND MINERALOGY OF MATRIX MATERIALS

The bulk chemical and mineralogical properties of the Mars-analogue geological matrix materials used in our study are summarized in Table S2 and Table S3, respectively.

| Oxide | MGS-1[a] | NAu-1*[b] | NAu-2*[b] | SWy-3[c] | SAz-1[c] |
|---|---|---|---|---|---|
| $SiO_2$ | 50.8 | 51.36 | 56.18 | 62.9 | 60.4 |
| $Al_2O_3$ | 8.9 | 8.15 | 3.11 | 19.6 | 17.6 |
| MgO | 16.7 | 0.19 | 0.26 | 3.05 | 6.46 |
| $Na_2O$ | 3.4 | 0.03 | 0.14 | 1.53 | 0.06 |
| CaO | 3.7 | 3.57 | 2.34 | 1.68 | 2.82 |
| $FeO_T$ | 13.3 | 35.94 | 37.85 | 3.67 | 1.5 |
| $TiO_2$ | 0.3 | 0.02 | 0.02 | 0.09 | 0.24 |
| $K_2O$ | 0.3 | 0.01 | 0.01 | 0.53 | 0.19 |
| $P_2O_5$ | 0.4 | n.r. | n.r. | 0.05 | 0.02 |
| F | n.r. | n.r. | n.r. | 0.11 | 0.29 |
| $Cr_2O_3$ | 0.1 | n.r. | n.r. | n.r. | n.r. |
| MnO | 0.1 | n.r. | n.r. | n.r. | n.r. |
| $SO_3$ | 2.1 | n.r. | n.r. | n.r. | n.r. |
| LOI** | n.r. | n.r. | n.r. | 6.06 | 9.91 |
| Total | 100 | 99.5 | 99.9 | 99.16 | 99.2 |

*Table S2: Bulk major element chemistry (wt %) of the matrix materials used in this study, as reported by the supplier or in previous baseline characterization studies. n.r. = not reported by the reference.*

**From the Clay Minerals Society Special Clay Repository – Data for these materials are unofficial and meant to be used as guideline and not an analytical certification*
***"Loss on Ignition" at up to 1000°C*
*[a] Data from [1]*
*[b] Data from [2]*
*[c] Data from [3]*

| Matrix Material | Mineralogy |
|---|---|
| MGS-1 | 27.1% plagioclase, 22.9% basaltic glass, 20.3% pyroxene, 13.7% olivine, 5% opal, 4% Mg-sulfate, 1.9% magnetite, 1.7% ferrihydrite, 1.4% Fe-carbonate, 1.1% hematite, 0.9% anhydrite |
| NAu-1[a] | ~90% smectite, 4% kaolin, 2% quartz, <1% biotite, 3% goethite |
| NAu-2[a] | ~95% smectite, 5% plagioclase, <1% quartz, trace biotite, talc, and ilmenite |
| SWy-3[b] | ~75% smectite, 8% quartz, 16% feldspar, 1% gypsum + mica and/or illite + kaolinite(?) and/or chlorite(?) |
| SAz-1[b] | ~98% smectite, 1% quartz, 1% other |

*Table S3: Mineralogy of the matrix materials used in this study, as reported by the supplier or previous studies.*
*[a] Data from [1]*
*[b] Data from [2]*
*[c] Data from [4]*

## C.3 EXTERNAL VALIDATION OF N CONTENT

The total N content of the ammoniated clay samples, the pure nitrate salts, the MGS-1 simulant, and a subset of the salt + MGS-1 mixtures (the 5 and 30 wt.% mixtures) were validated by Activation Laboratories Ltd. (Ancaster, Ontario, Canada). The method, as described by the laboratory, is as follows: 0.2g sample is combusted in a resistance furnace at 1350 °C, using a LECO CNS-2000. Combustion gases are collected in a 4.5-liter ballast tank and then flow to the detectors. Nitrogen in the form of $N_2$ is detected by thermal conductivity detection. A Leco CNS-2000 is used for the analysis. The instrument has a detection limit of 0.01%.

Figure S1 shows that the validated N content was in good agreement with the N content expected from the mixing procedure.

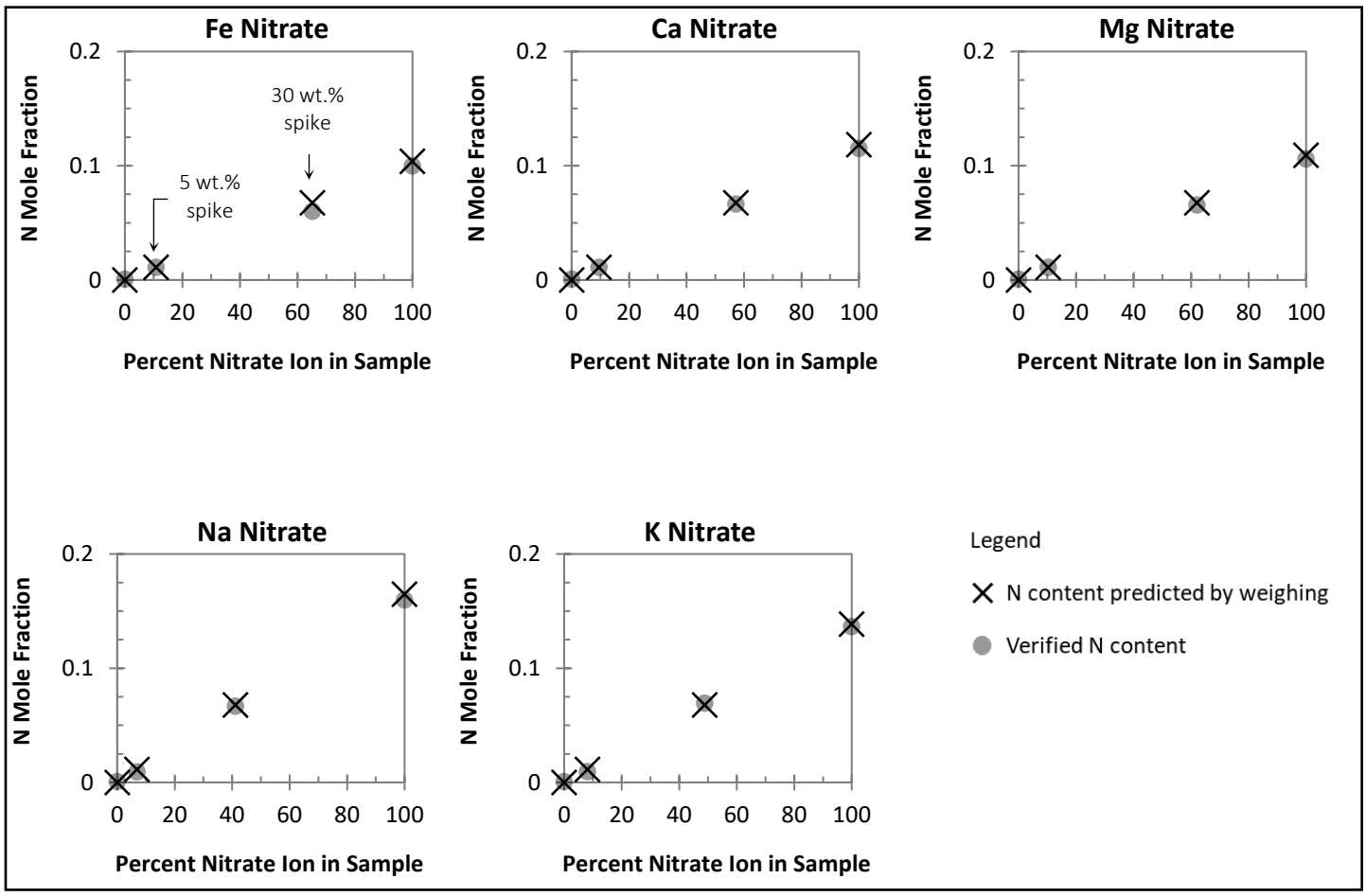


*Figure S1: Comparison of the N content determined by Actlabs relative to the expected N content determined by calculations and careful weighing. The data points at 0 and 100 % nitrate correspond to the MGS-1 (blank) and pure salt samples, repectively.*

## C.4 CALIBRATION CURVES

Table S2 notes the wavelength ranges used for local baseline correction as well as the wavelength range used for peak area summation.

| Line of Interest (nm) | Channel Range for Baseline Subtraction (nm) | Channel Range for Peak Area Integration (nm) |
|---|---|---|
| 744.2 | 742.87 - 745.67 | 743.99 - 744.44 |
| 746.8 | 745.79 - 751.35 | 746.57 - 747.13 |
| 821.6 | 819.63 - 823.50 | 821.38 - 821.86 |
| 868.0 | 866.41 - 870.00 | 867.61 - 868.21 |

*Table S4: Summary of channels used for baseline correction and peak area summation.*

Figure S2 and Figure S3 present the full range of calibration curves generated for this project – an expansion upon Figure 3 presented in the main text. The four vertical columns correspond to the four emission lines tested (to facilitate a comparison of the usefulness of each line for tracing N concentration) and the four horizontal panels correspond to the four normalization conditions tested. In each figure, the top panel presents the unnormalized data for reference, with the lower three panels showcasing the influence of the various tested normalization approaches. In each plot, different colours represent the different salt series, where the legend identifies the cationic composition of the salt used in the doping procedure. Each point is an average of the five replicate scans measured from each sample; vertical error bars represent the standard deviation across the five replicates. Horizontal error bars represent the average error between the calculated and validate N contents.

In the absence of self-absorption and matrix effects, LIBS emission intensity should increase linearly with the concentration of the analyte. Linear best-fit trend lines were therefore initially fit to each dataset (solid lines in Figure S2 and Figure S3), however, where the linear best-fit trendline failed to pass through at least 70% of the vertical error bars, we applied various curved fits (second-order polynomials, exponential functions, and power functions) and selected the function that maximized the $R^2$ statistic. This was done simply to showcase the extent of the non-linearity observed during normalization of the full dataset.

In the main text of the manuscript, we conclude that the non-linearity observed in our calibration curves is an artefact of normalizing spectra from samples with sufficiently different matrices – pure salts and salts mixed with basalt regolith. Therefore, the calibration curves were re-

generated without the pure salt samples (Figure S3). With the pure salts removed, the N emission behaviour is consistent and increases proportionally with the increasing N content. This highlights the value of restricting the range of compositions sufficiently so that each curve is trained on samples whose spectral line intensities respond similarly to changes in composition.

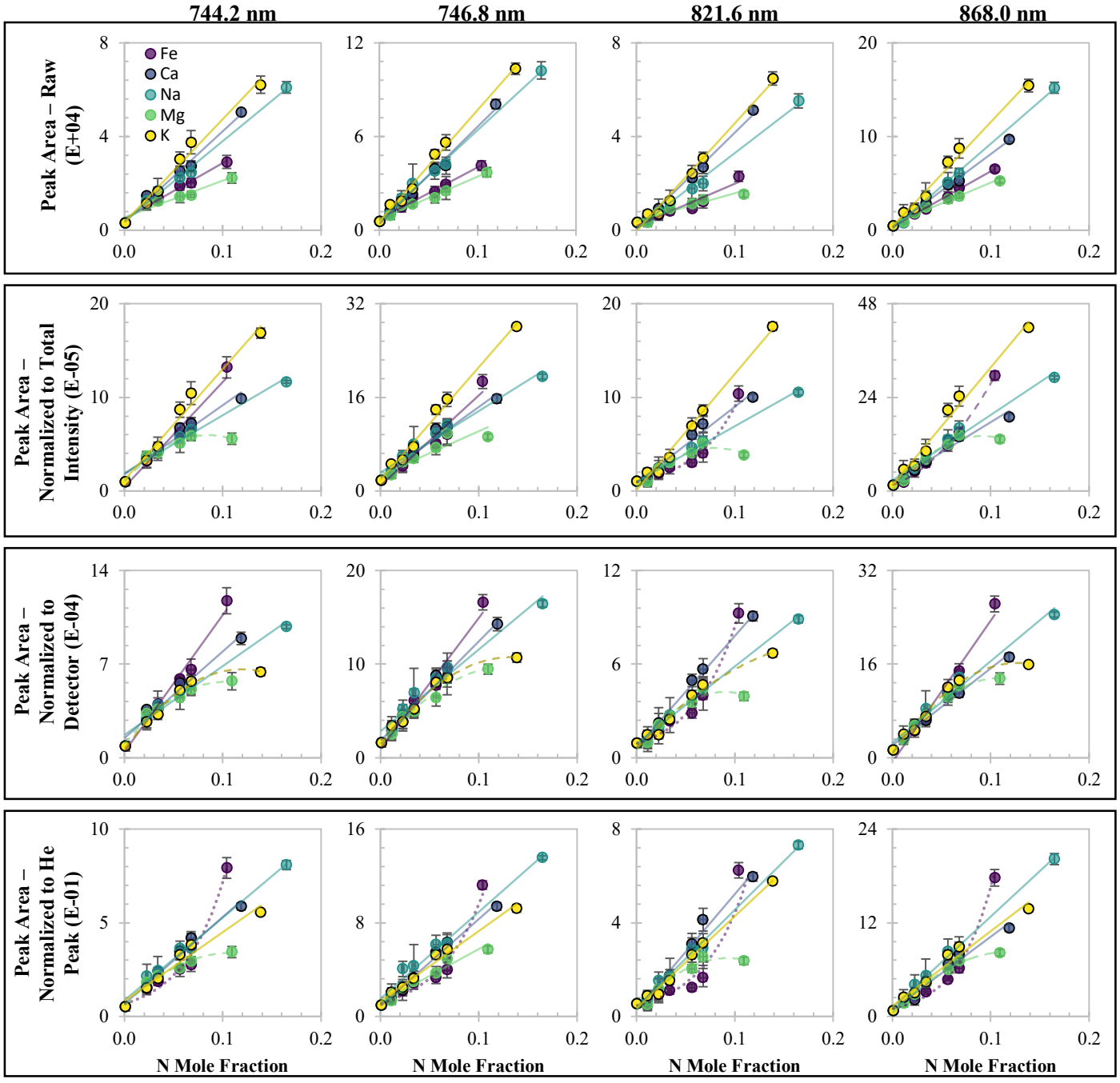


*Figure S25: Calibration Curves for the full nitrate sample suite.*

*The four vertical columns correspond to the four emission lines tested (to facilitate a comparison of the usefulness of each line for tracing N concentration) and the three horizontal panels depict selected pre-processing conditions. Different colours represent the different salt series, where the legend identifies the cationic composition of the salt used in the doping procedure. Each point is an average of the five replicate scans measured from each sample; vertical error bars represent the standard deviation across the five replicates. Horizontal error bars represent the average error between the calculated and validate N contents. Solid best-fit lines represent linear functions. Where a linear function lay outside 70% of the vertical error bars, an additional curve fitting algorithm was attempted: second order polynomial fits are represented by dashed lines and exponential fits are indicated by dotted lines.*
*Note the introduction of non-linear, and in some cases non-monotonic, behaviour into the relationship between the N peak area and the known N content.*

.

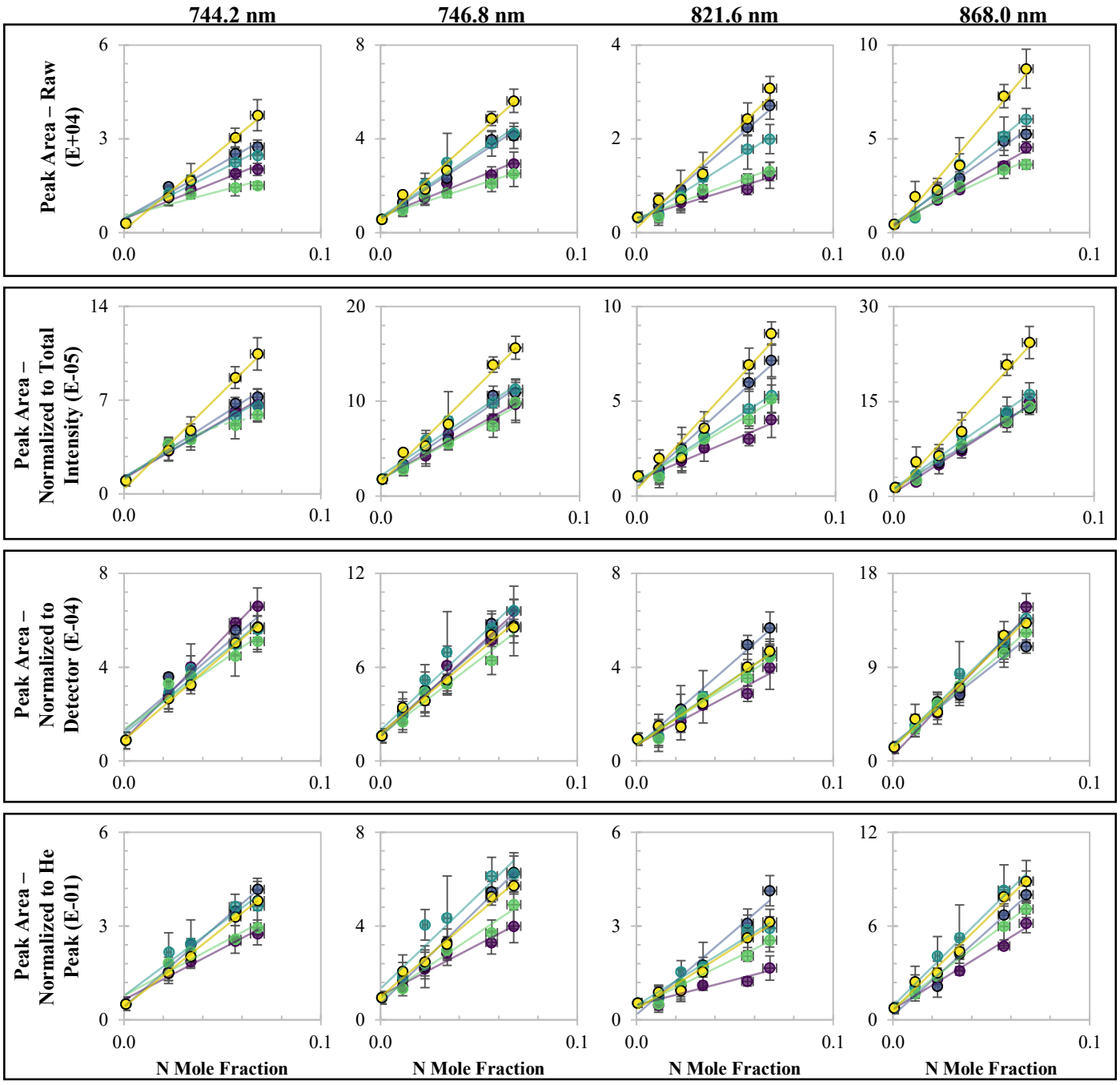


*Figure S3: Calibration Curves for only the nitrate + regolith mixtures samples (ie., salt end-members removed).*

*The four vertical columns correspond to the four emission lines tested (to facilitate a comparison of the usefulness of each line for tracing N concentration) and the three horizontal panels depict selected pre-processing conditions. Different colours represent the different salt series, where the legend identifies the cationic composition of the salt used in the doping procedure. Each point is an average of the five replicate scans measured from each sample; vertical error bars represent the standard deviation across the five replicates. Horizontal error bars represent the average error between the calculated and validate N contents. Solid best-fit lines represent linear functions. Note the consistent, monotonically-increasing linear trends*

## C.5 CALIBRATION MODELS

Considering our observation that the pure salt end-member and mixture samples exhibit dissimilar spectral behaviour, model permutation 2 and 3 were run on both the full nitrate sample suite, as well as a restricted sample set that excluded the pure salt end-members from the modeling. The performance outcomes of each model are shown graphically in a plot that compares the prediction accuracy (NRMSE) and the proportion of explained variance ($R^2$) achieved by each model (Figure S4). Values derived from the full nitrate sample suite are plotted on separate axes than those from the restricted sample set (panels A and B, respectively) to facilitate a direct assessment of the impact of using a restricted compositional range during calibration. The bars/points in Figure S4 are clustered according to the normalization pre-treatment to facilitate a direct assessment of the impact of normalization on model performance, with different colour/shading to identify the specific modelling permutation. A cross comparison of panels A and B shows that excluding the end-members yields universal improvement, with consistently lower NRMSE values and higher $R^2$ in panel B than the equivalent models in panel A. This result holds true for every model permutation and normalization condition.

It is important to note that we initially ran model permutation 3 (multivariate PLS restricted to N-relevant wavelength regions) using peak areas that had *not* been pre-treated with a baseline subtraction, see main text for details. However, these initial runs using uncorrected peak areas performed almost universally worse than each of the univariate models, generating large percentage errors and low $R^2$ values. Consequently, we re-generated these models using the same emission peaks but with the baseline correction applied (*i.e.*, the exact same data as the univariate models, but modelled simultaneously); the results are plotted alongside the other models in Figure S4.

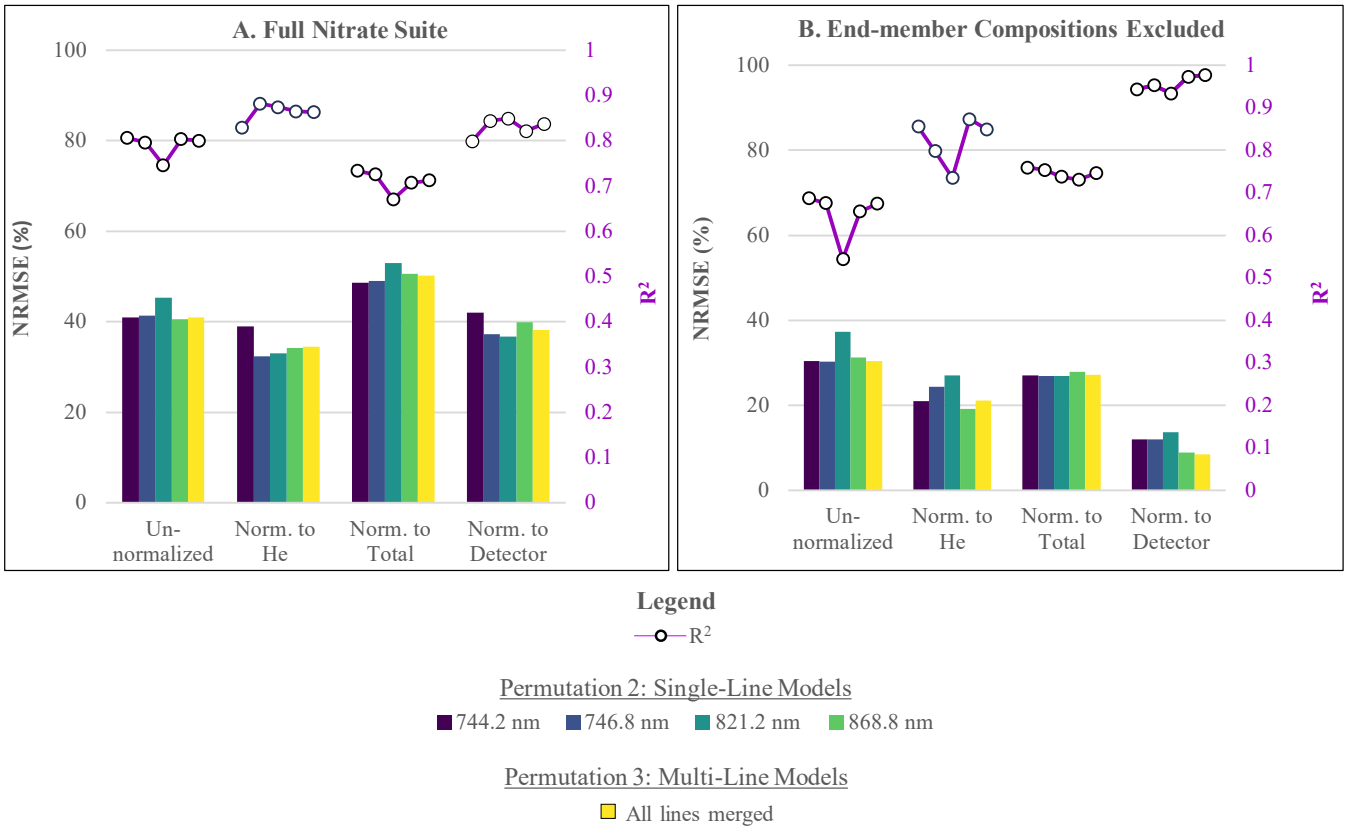


*Figure S4: Figures of merit for the single- and multi-line PLS model permutations.*

*NRMSE is the Normalized Root Mean Square Error of the PLS predictions; higher values indicate more uncertainty in the model. A) Results from the full nitrate suite. B) Results from the restricted nitrate site after the exclusion of end-member salt samples with dissimilar spectral behaviour. Bars are clustered according to the normalization ("norm.") pre-treatment, facilitating an evaluation of the influence of normalization of model performance. Bars are shaded according to the model permutation, with univariate models in colour and (wavelength-restricted) multivariate models in greyscale. Comparison of panels A and B highlights the improvement gained by restricting the compositional range of the calibration set.*

## C.6 REFERENCES


[1] K.M. Cannon, D.T. Britt, T.M. Smith, R.F. Fritsche, D. Batcheldor, Mars global simulant MGS-1: A Rocknest-based open standard for basaltic martian regolith simulants, Icarus. 317 (2019) 470–478. https://doi.org/10.1016/j.icarus.2018.08.019.

[2] J.L. Keeling, M.D. Raven, W.P. Gates, Geology and characterization of two hydrothermal nontronites from weathered metamorphic rocks at the Uley graphite mine, South Australia, Clays Clay Miner. 48 (2000) 537–548.

[3] H. van Olphen, J.J. Fripiat, Data handbook for clay materials and other non-metallic minerals, (1979).

[4] S.J. Chipera, D.L. Bish, Baseline studies of the clay minerals society source clays: Powder X-ray diffraction analyses, Clays Clay Miner. 49 (2001) 398–409. https://doi.org/10.1346/CCMN.2001.0490507.